Katalysatoren für die Wasserstoffentwicklung und CO_2-Reduktion untersucht mit Röntgenabsorptionsspektroskopie und in funktionalen Studien

im Fachbereich Physik der Freien Universität Berlin eingereichte Dissertation

von Jonathan Heidkamp

2016

Disputation am 20.5.2016

Erstgutachter: Prof. Dr. Holger Dau
Zweitgutachter: Prof. Dr. Peter Strasser

2016

Catalysts for hydrogen (H^+) and carbon dioxide (CO_2) reduction investigated by X-ray absorption spectroscopy and in functional studies

HEIDKAMP, JONATHAN

DEPARTMENT OF EXPERIMENTAL PHYSICS, FREIE UNIVERSITÄT BERLIN

CONTENTS

I. MOTIVATION

The growing world population comes along with an increasing demand for fuel and electricity. So far, the energy needs have been covered predominantly by fossil fuels and to a minor extent by nuclear power. Both energy sources possess significant drawbacks. The major disadvantages of fossil fuels are that the combustion produces carbon dioxide, a powerful greenhouse gas, and that the fossil sources will be depleted in the long run. Nuclear power, on the other hand, involves a significant risk for radioactive contamination of human habitat and a problematic disposal of nuclear waste.

Renewable energy sources like solar or wind power are potential alternatives to fossil fuels and nuclear power, as they are CO_2 neutral, sustainable (Lewis and Nocera 2006) and non-hazardous. However, solar and wind power are not as reliable as the conventional energy sources, since they vary with daytime and weather. A storage technology is required to compensate these temporal fluctuations (Lewis and Nocera 2006). The storage of the renewable energy in the form of chemical fuels is a promising approach, since fuels exhibit clearly higher energy densities than batteries (Cook, Dogutan et al. 2010).

One way to convert renewable energy into fuel is the use of electrochemical cells driven by solar or wind power. The cells can produce molecular hydrogen as a fuel through water splitting (electrolyser) (Gratzel 2001, Lewis and Nocera 2006, Cook, Dogutan et al. 2010, Walter, Warren et al. 2010, Armaroli and Balzani 2011, Reece, Hamel et al. 2011) or liquid fuels like formic acid or methanol through CO_2 reduction (Morris, Meyer et al. 2009, Appel, Bercaw et al. 2013, Centi, Quadrelli et al. 2013, Costentin, Robert et al. 2013, Kondratenko, Mul et al. 2013, Reske, Duca et al. 2013, Mistry, Reske et al. 2014, Qiao, Liu et al. 2014, Reske, Mistry et al. 2014). To regain the energy, the fuel can be combusted later on demand in a fuel cell or engine.

The water splitting as well as the CO_2 reduction rely on electro-catalysts to boost the slow kinetics of the involved chemical reactions and to lower the required electrode voltage close to the thermodynamical potential of the reactions. So far, catalysts are often based on rare and, therefore, expensive noble metals like Pt, representing an economic bottle neck for the electrochemical fuel production and combustion. The development of catalytic materials based on earth-abundant and, hence, cheap elements would remove this economic obstacle (Gordon, Bertram et al. 2006) and, thus, support the proliferation of renewable energy sources. The understanding of the catalytic mechanisms at work in these materials would help to optimize their catalytic performance.

In this thesis, we investigate the atomic structure of a variety of catalytic materials for H_2 formation and CO_2 reduction that are based on earth-abundant elements. The investigations are performed with X-ray absorption spectroscopy because of the amorphous or 'weak crystalline nature' of the materials. The following topics are addressed:

I. Methods

II. Results

1. **MoS_x catalyst** (x = 2 or 3) for H_2 formation prepared by electro-deposition and doped with Co or Ni

2. **Co-based catalyst** for H_2 formation prepared by electro-deposition

3. **Molecular Ni catalyst** for H_2 formation grafted on a carbon-nanotube support

4. **Fuel cell** with noble-metal free catalysts for H_2 oxidation and O_2 reduction

5. **Cu-based catalyst** for CO_2 reduction prepared by electro-deposition

III. Summary

In 'Methods', we give an introduction to the basics of the used measurement methods, X-ray absorption spectroscopy (XAS) and electrochemical experiments. The practical implementation of the methods is described and important experimental details are denoted. Furthermore, we provide a description of the data processing, the spectra simulation and the analytical methods applied in our XAS analysis.

In 'Results', the investigated catalytic systems are introduced in detail and the obtained results from the XAS investigations and (if conducted) electrochemical studies are presented. The results are discussed in respect of the open questions about the atomic structure and (if possible) the catalytic mechanism of the investigated catalyst. Furthermore, we provide for each catalytic system a description of the specific preparation procedure.

In 'Summary', we summarize the outcome of our investigations on the catalytic systems presented in this thesis. For each system, the crucial findings of the investigation are stated and the open questions about the atomic structure and (if possible) the catalytic mechanism are answered as conclusive as possible.

In the following, we give a brief introduction into the catalytic systems studied in this thesis and describe the objectives of our investigations.

ELECTRO-DEPOSITED MoS_X AND Co/Ni:MoS_X ELECTRODES

In the first chapter of 'Results', we study an electro-deposited molybdenum sulfide catalyst for the hydrogen-evolution reaction (HER) and the promotion of its catalytic activity by doping with Co or Ni. In general, molybdenum sulfide materials are a non-precious alternative as HER catalysts to the highly active but scarce and, hence, expensive Pt. MoS_2 crystals are known as poor catalysts (Tributsch and Bennett 1977, Jaegermann and Tributsch 1988) but nanocrystals of MoS_2 with unsaturated edge sites exhibit significant catalytic activity (Hinnemann, Moses et al. 2005, Jaramillo, Jorgensen et al. 2007, Bonde, Moses et al. 2008, Chen, Cummins et al. 2011, Li, Wang et al. 2011). The preparation of the nanocrystals, however, involves ultrahigh vacuum or thermal treatments at high temperatures of 400 – 550 °C, leading to high production costs for the catalyst. The amorphous MoS_x catalysts (x = 2 or 3) established by *Merki et al.* might be a less costly alternative, as it can be prepared by simple electro-deposition under ambient conditions and exhibits a high activity for HER (Merki, Fierro et al. 2011, Merki, Vrubel et al. 2012). The as-prepared MoS_x catalyst is a mixture of amorphous MoS_2, which is the catalytic species, and MoS_3 (Merki, Fierro et al. 2011, Merki, Vrubel et al. 2012, Lassalle-Kaiser, Merki et al. 2015). *Merki et al.* reports that the doping of the MoS_x catalyst with Co or Ni increases its catalytic activity for HER, as the dopants promote catalytic load, surface area and intrinsic activity of the catalyst (Merki, Vrubel et al. 2012). In this thesis, we analyse the doped and undoped MoS_x catalyst via X-ray absorption spectroscopy and, thus, provide insight into the atomic structure of the Mo and dopant sites during HER catalysis. From these structural insights, we derive possible implications for the catalytic HER mechanism, supported by complementary electrochemical studies. We additionally examine the MoS_x catalyst for OER activity and identify the corresponding catalytic species. A non-precious, easy-to-produce MoS_x catalyst active for HER and OER could be interesting for possible electrolyser or fuel cell devices.

CATALYTIC Co ELECTRODE ELECTRODEPOSITED UNDER REDUCTIVE CONDITIONS

In the second chapter of 'Results', we investigate an electro-deposited Co-based catalyst for HER and OER. Cobalt-based oxides have been reported as robust electro-catalysts for the oxygen-evolution reaction (OER) (Kanan and Nocera 2008, Risch, Khare et al. 2009, Dau, Limberg et al. 2010, Jiao and Frei 2010, Yin, Tan et al. 2010, Chou, Ross et al. 2011, Shevchenko, Anderlund et al. 2011, Wee, Sherman et al. 2011). For the hydrogen-evolution reaction (HER), cobalt compounds are promising as well. Several investigations reported a series of cobaloxime and diimine-dioxime compounds that show notable properties for HER at low over-potentials (Hu, Cossairt et al. 2005, Razavet, Artero et al. 2005, Baffert, Artero et al. 2007, Hu, Brunschwig et al. 2007, Jacques, Artero et al. 2009, Dempsey, Winkler et al. 2010, Fourmond, Jacques et al. 2010). However, for the application in devices, molecular catalysts have to be grafted onto an electrode material without degrading their catalytic activity (Le Goff, Artero et al. 2009). For the mentioned Co compounds, this has not been be achieved so far due to synthetic issues (Artero, Chavarot-Kerlidou et al. 2011). To avoid the complications of a grafting process, *Cobo et al.* present an convenient approach of forming a Co-based HER catalyst directly on the electrode via reductive electro-deposition from an aqueous solution of $Co(NO_3)_2{\cdot}6H_2O$ at pH 7 (Cobo, Heidkamp et al. 2012). The Co-based catalyst also exhibits catalytic activity for OER. In this thesis, we analyse this catalyst via X-ray absorption spectroscopy and provide insight into the atomic structure of the catalytic species for HER and OER.

MOLECULAR Ni CATALYST GRAFTED ON A CARBON-NANOTUBE CATHODE

In the third chapter of 'Results', we study the $[Ni(P_2^{Ph}N_2^{CH_2Pyrene})_2]^{2+}$ complex ("NiP_4") which is a molecular catalyst for H_2 formation. Its structure is inspired by the active sites of hydrogenases, enzymes for H_2 oxidation and reduction (Canaguier, Artero et al. 2007, Tard 2009). For the use in fuel cells or electrolysers, the NiP_4 complex is grafted on multi-walled carbon nanotubes (MWCNTs) to assemble electrode material (Le Goff, Artero et al. 2009). MWCNTs are advantageous as support material, as they offer high surface areas (facilitating high catalyst loading), high stability and electrical conductivity (Tasis, Tagmatarchis et al. 2006, Sgobba and Guldi 2009). For grafting the NiP_4 complex on the MWCNTs, *Tran et al.* present an approach (based on (Zhao and Stoddart 2009)) that is more suitable for application than previous ones (Le Goff, Artero et al. 2009) as it attaches the NiP_4 complex via noncovalent π–π stacking directly on the MWCNTs (Tran, Le Goff et al. 2011). The final NiP_4-MWCNTS electrode material is noble-metal free, exhibits a low over-potential and high stability for H_2 evolution or uptake and is compatible with conditions in classical proton-exchange membrane devices (Le Goff, Artero et al. 2009, Tran, Artero et al. 2010). In this thesis, we analyse the NiP_4-MWCNTs material via X-ray absorption spectroscopy and show that the grafting process can affect the structural integrity of the NiP_4 complex.

NOBLE METAL-FREE FUEL CELL

In the fourth chapter of 'Results', we investigate a fuel cell based on proton exchange membrane (PEM) technology that employs earth-abundant materials as catalysts for the H_2 oxidation and O_2 reduction reactions (HOR and ORR). PEM fuel cells can be used in a wide range of portable and automotive applications. However, so far PEM fuels cells require Pt as catalyst for the HOR and ORR. This represents an economic bottle neck for the fuel cells, as Pt is rare and, hence, expensive. The substitution of Pt by earth-abundant catalysts is a potential way to remove this economic handicap. Significant progress in the substitution of Pt was achieved for the ORR-side of the fuel cells (Bashyam and Zelenay 2006, Pylypenko, Mukherjee et al. 2008, Gong, Du et al. 2009, Lefevre, Proietti et al. 2009, Liu, Wu et al. 2010, Morozan, Jegou et al. 2011, Morozan, Jousselme et al. 2011). However, a PEM fuel cell with earth-abundant catalysts on both electrodes, ORR and HOR, has not been reported before the work of *Tran et al.* (Tran, Morozan et al. 2015). The fuel cell of *Tran et al.* utilizes as ORR catalyst a novel Cobalt/nitrogen/Vulcan (Co-N-C) material and as HOR catalyst a previously studied carbon-nanotube material functionalized with biomimetic Ni complexes (Ni-CNT) (Tran, Le Goff et al. 2011). In thesis, we analyse both catalysts, ORR and HOR, via X-ray absorption spectroscopy and show effects on the atomic structure of the catalysts by the operation conditions in a PEM fuel-cell. Furthermore, we provide first insights in the atomic structure of the ORR catalyst.

CATALYTIC Cu ELECTRODE FOR CO_2 REDUCTION

In the fifth chapter of 'Results', we study an electro-deposited Cu-based catalyst for CO_2 reduction. In recent studies, electro-catalytic material for CO_2 reduction has been investigated in non-aqueous media like organic solvents or ionic liquids (DiMeglio and Rosenthal 2013, Asadi, Kumar et al. 2014, Medina-Ramos, DiMeglio et al. 2014, Nakata, Ozaki et al. 2014, Oh, Vrubel et al. 2014). Non-aqueous media enables a higher solubility of CO_2 and a convenient control of H_2 evolution via adjusting the

water concentration. Novel catalytic materials were developed based on MoO_2 (Oh, Vrubel et al. 2014), Bi (DiMeglio and Rosenthal 2013, Medina-Ramos, DiMeglio et al. 2014) and B-doped diamond (Nakata, Ozaki et al. 2014) or consist of molecular metal complexes (Morris, Meyer et al. 2009, Appel, Bercaw et al. 2013, Costentin, Robert et al. 2013, Qiao, Liu et al. 2014) whose activity is adjustable via ligand variations. *Huan et al.* report a novel Cu material that is electro-catalytic for the reduction of CO_2 into formic acid (liquid fuel), showing remarkable activity, selectivity and stability (Huan, Andreiadis et al. 2015). The material is prepared via electro-deposition and operates in a non-aqueous medium (dimethylformamide). In thesis, we analyze the catalytic Cu material via X-ray absorption spectroscopy and provide insights in the atomic structure of the catalytic species.

II. METHODS

1. X-ray absorption spectroscopy on catalyst electrodes

BASICS

The following short introduction in X-ray absorption spectroscopy is based on the textbooks of *B. Teo*, *G. Bunker* and *S. Calvin* (Teo 1986, Bunker 2010, Calvin 2013).

In X-ray absorption spectroscopy (XAS), a sample is irradiated with a monochromatic X-ray beam and the absorption of the beam by the sample is measured. To obtain a XAS spectrum, the absorption behaviour of the sample is recorded over an interval of beam energies. Absorption appears if the beam

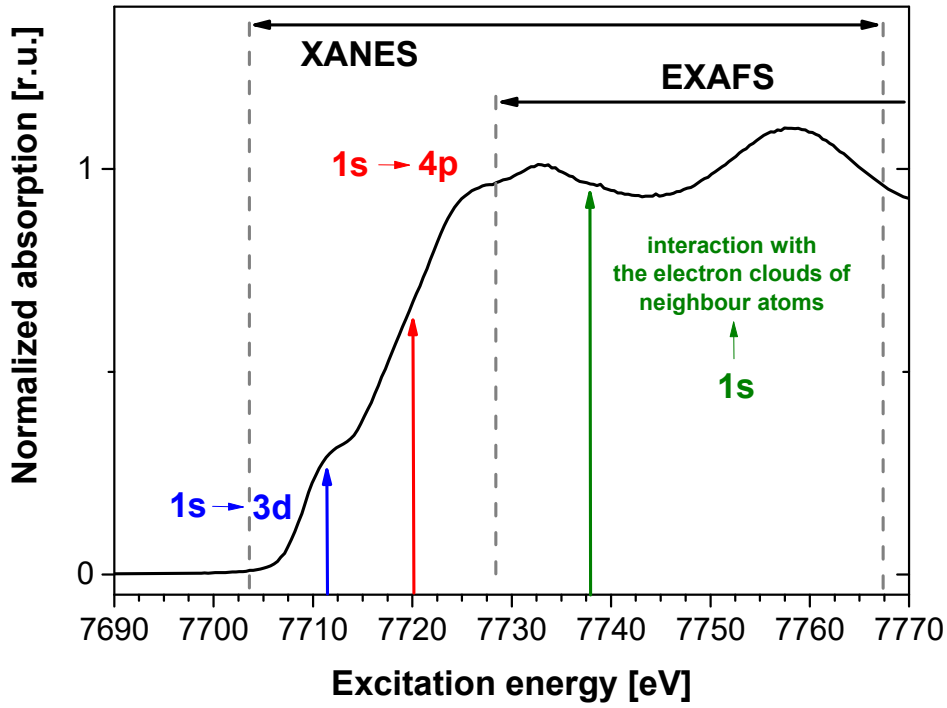

Figure 1

A representative XAS spectrum for *K*-edge absorption, here, recorded at the Co edge for Co metal. The division of the spectrum in XANES and EXAFS is marked by the vertical dashed gray lines. The XANES are created by exciting the *1s* electrons (*K* shell) via X-ray photons (excitation energy) into unoccupied *d* orbitals (pre-edge) and, at higher energies, into unoccupied *p* orbitals (main edge). The *1s* → *3d* and *1s* → *4p* transitions are indicated by vertical arrows, the former in blue and the latter in red, at their usual energy range in the spectrum. The EXAFS are created by expelling the *1s* electrons out of the absorber atom and their interactions with the electron clouds of neighbour atoms. The transition is indicated by a green arrow.

energy matches or exceeds the binding energy of core electrons of atoms in the sample. The core electrons absorb the beam photons and are excited into higher unoccupied shells or are expelled from the atom. The threshold of the binding energy is visible in the XAS spectrum as absorption edge (see **Figure 1** and **Figure 2**). The mean energy of the absorption edge (first inflection point) is specific for each chemical element (e. g. 7709 eV for Co, 8333 eV for Ni, 20000 eV for Mo, …).

In the *K*-edge absorption (see **Figure 1**), the beam is absorbed by electrons in the $1s$ orbital (*K* shell) and, obeying the selection rule for electromagnetic dipole transitions, excites them into higher p orbitals, if they are unoccupied. Transitions into unoccupied d orbitals may also happen but only if they possess a minor p character due to mixing with p orbitals. However, the probability for this transition is significantly smaller. All transitions together give rise to an abrupt absorption edge. A pre-edge may precede the main edge, if unoccupied d orbitals are available at a lower energy than unoccupied p orbtials. The spectral features of the pre-edge, the main edge and until ≈30 eV beyond are the so-called X-ray absorption near-edge structure (XANES). The XANES spectra contain information about the chemical nature of the neighbouring atoms or ligands around the absorber atom within a radius of ≈3 Å including the geometry of their coordination environment and the oxidation state of the absorber atom. Usually, it is very complicated to extract this information from the XANES in a quantitative way. Hence, most of the time a XANES spectrum is interpreted in a more qualitative way via a comparison with reference spectra where the atomic structure of the ligand environment is known.

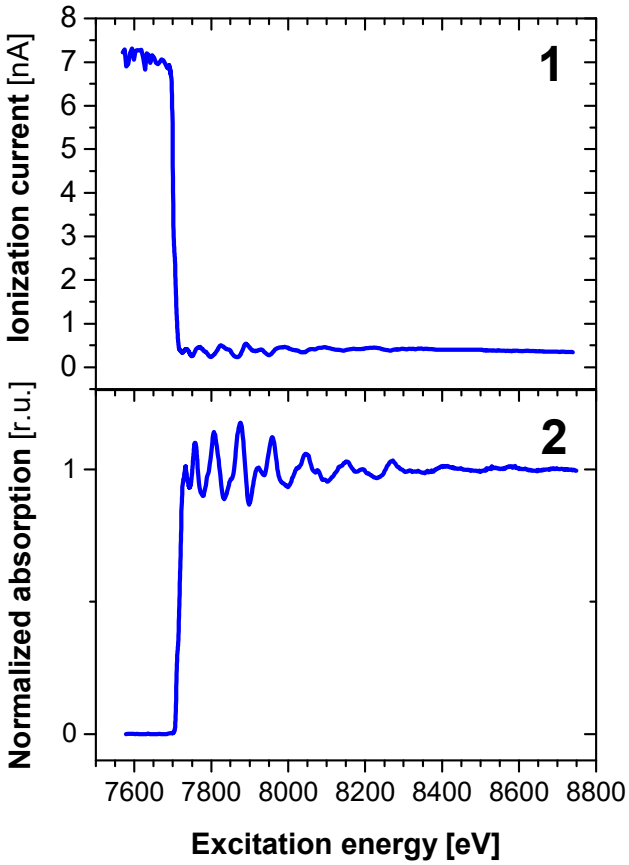

Figure 2

A representative XAS spectrum (Co metal foil) for *K*-edge absorption before (raw) and after data processing, here, recorded at the Co edge. Panel **1** shows the raw, unprocessed spectrum. The ionization current represents the beam intensity. After the sample, the beam passes through an ionization chamber. The ionization of the gas in the chamber is proportional to the beam intensity. *K*-edge absorption of the sample appears as an abrupt drop in the ionization current. Panel **2** shows the same spectrum after the complete data processing: normalization with the beam intensity before the sample, application of the negative logarithm, energy calibration, removal of the background before the edge and removal of the slope after the edge.

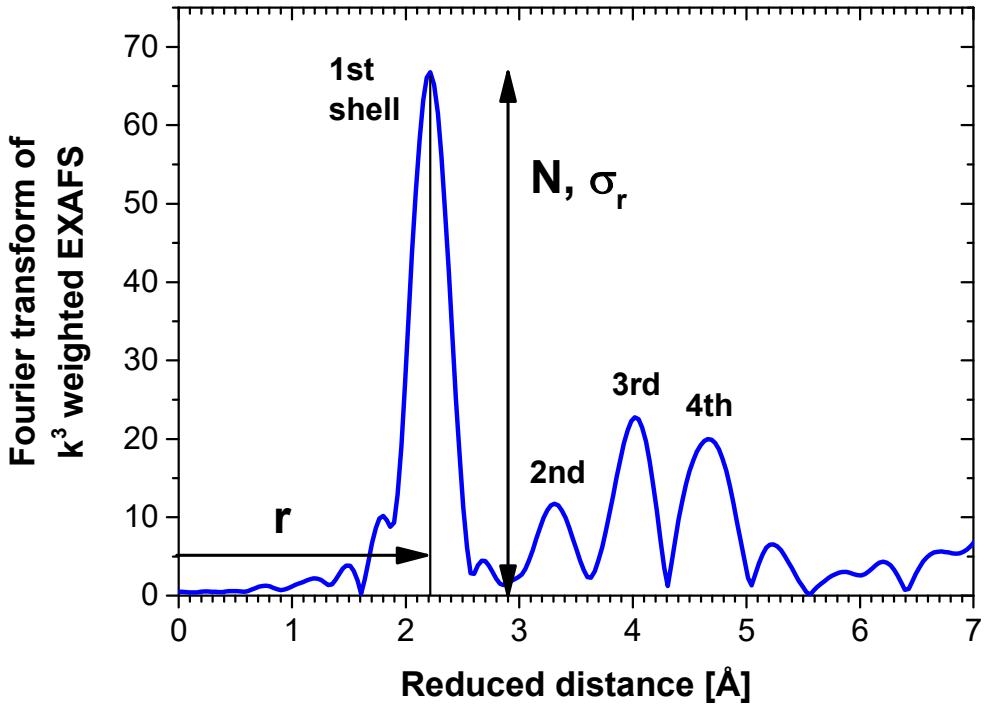

Figure 3

A representative Fourier transform (FT) of a k^3 weighted EXAFS spectrum (k = wavenumber of photo-electron wave) recorded of a Co metal foil at the Co K-edge. The original EXAFS were extracted from the spectrum shown in **Figure 2.2**. In the FT, each prominent peak represents a coordination shell of ligands or neighbour atoms around the absorber atom. The peak position corresponds to the reduced mean distance, r, between the atoms of the coordination shell and the absorber atom. The reduced distance differs up to 0.3 Å from the correct value. The peak magnitude corresponds to the coordination number, N, and the Debye-Waller parameter, σ_r, of the coordination shell. The latter is the root-mean-square (RMS) deviation from r and is a measure for the spatial order of the coordination shell. The exact values for r, N and σ_r can be determined from EXAFS simulations.

In the high end of the XANES spectrum, the extended X-ray absorption fine-structure (EXAFS) starts to emerge and expands over ≈1000 eV beyond the XANES region (see **Figure 1**). In the EXAFS region, the beam energy is sufficient to expel the excited $1s$ electron out of the atom. The probability for the electron ejection is modified by the interaction of the photo-electron with the electron clouds of neighbour atoms. The matter wave of the photo-electron is scattered by the neighbour atoms, leading to an interference between the original wave and the scattered wave. During a scan of the EXAFS region, the continuous increase in beam energy varies the wave length of the photo-electron, leading to an oscillation between constructive and destructive interference. This oscillation affects the probability for the photo-electron ejection and induces an oscillating behaviour in the EXAFS region of the absorption signal (see **Figure 2**). The EXAFS contain structural information of the atomic environment around the X-ray absorbing atom, since the phase and the amplitude of the scattered photo-electron wave are dependent on the type of the neighbour atoms and their distance to the

absorber atom. The Fourier-transform (FT) of the EXAFS is a way to make the structural information directly visible (see **Figure 3**). In the FT, each coordination shell of neighbour atoms is represented by a peak. The position of the peak corresponds to the mean distance, r, from the coordination shell to the X-ray absorbing atom; and the peak height to the coordination number, N, and the Debye-Waller parameter, σ_r, of the coordination shell. This information can be determined quantitatively via EXAFS simulations (see subsequent sections).

The X-ray absorption of the sample leads to simultaneous fluorescence, as electrons of higher atom orbitals relax into the $1s$ vacancies created by the ejected core electrons. The probability of the fluorescence emission is directly proportional to the probability of the absorption process, which created the vacancy in the $1s$ orbital. Therefore, the excitation spectrum of the fluorescence is proportional to the absorption spectrum, enabling the fluorescence detection of the absorption. However, the proportionality holds only if the optical thickness of the sample is sufficiently low to avoid re-absorption of the fluorescence photons (self-absorption). The fluorescence detection of the *K*-edge absorption can be achieved via recording the K_α fluorescence, which arises from $2p$ electrons relaxing into the unoccupied $1s$ orbitals.

MEASUREMENT DETAILS

The X-ray absorption near-edge structure (XANES) and extended X-ray absorption fine-structure (EXAFS) measurements at the Co, Ni and Cu *K*-edge were performed at the KMC-1 bending-magnet beam line of the BESSY synchrotron (Helmholtz-Zentrum Berlin for Materials and Energy). The energy of the X-ray beam (excitation energy) was adjusted by a double-crystal monochromator (Si-111). The sample was transferred into a cryostat (*Oxford instruments*) to keep it at a temperature of 20 K during the measurement. The liquid He cryostat cooled the sample via heat conduction over He gas (0.2 bar). The used sample holders provide a sample spot of 6 x 15 mm^2 for powder samples, and of 11 x 15 mm^2 for tissue and quasi in-situ electrochemical samples.

For the recording of XANES and EXAFS spectra, the X-ray beam energy was screened over a typical scan range for Co *K*-edge from 7580 to 8750 eV, for Ni from 8215 to 9375 eV and for Cu from 8840 to 10010 eV. The measurements were performed in absorption and fluorescence mode. In absorption mode (see **Figure 4**), the intensity of the X-ray beam is measured before and after the sample via ionisation chambers (containing N_2 gas). The face of the sample was oriented perpendicularly to the incoming beam. In fluorescence mode (see **Figure 4**), a fluorescence detector with 13 Ge-elements (*Canberra*) was aligned orthogonal to the X-ray beam and collected the fluorescence photons emitted by the sample. The face of the sample was oriented to the detector and the incoming beam in an angle of 45°, respectively. The distance between detector and sample was adjusted to gain optimal fluorescence counts and to prevent saturation of its elements. The energy windows of the single channel analysers for the 13 detector-elements were set to the K_α-emission line of Co, Ni or Cu, respectively. Beam scattering from the sample can lead to saturation of the detector elements. In this case, a filter foil (5 µm thick) was placed between sample and detector consisting of metallic Fe, Co or Ni when measuring Co, Ni or Cu K_α-emission, respectively. Absorption mode was applied if the sample

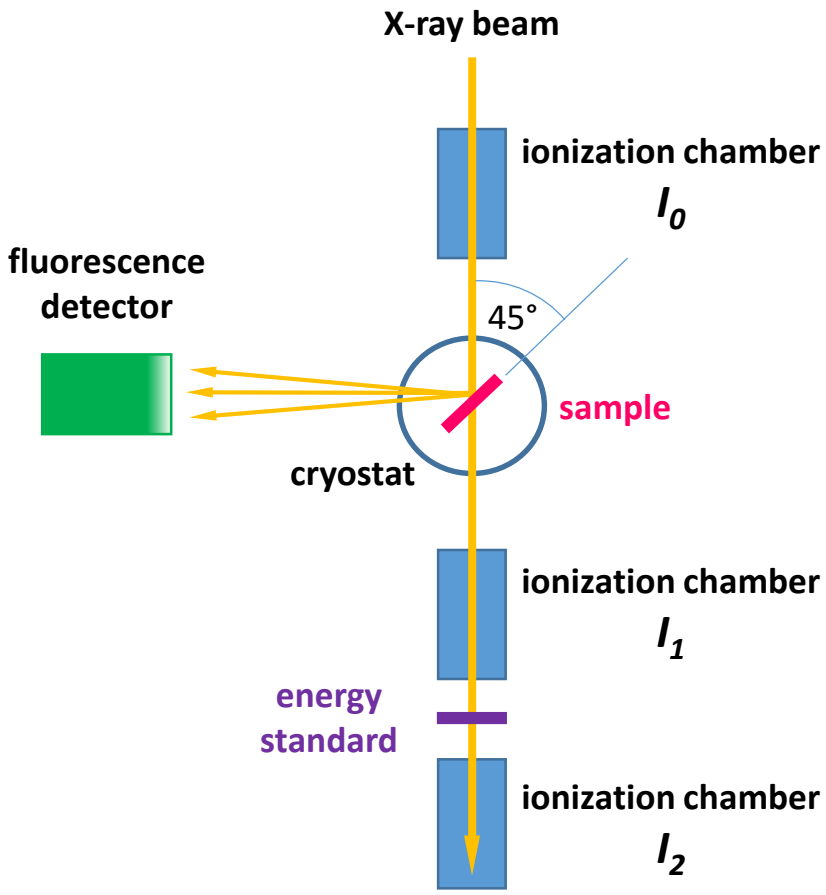

Figure 4

Schematic representation of a set-up for XANES and EXAFS spectroscopy.

absorbs ≈90 % of the X-ray beam intensity (powder samples), and fluorescence mode if the absorption is below 10 % (tissue or electrochemical quasi in-situ samples). Spectra were collected from different non-overlapping spots of the sample, then weighted by their signal to noise ratio and averaged to one sample spectrum.

For calibrating the energy axis of the sample spectrum, a reference (energy standard) with an established energy position of its absorption edge was recorded simultaneously with the sample. In the case of measurements at the Co, Ni or Cu *K*-edge, a metallic Co, Ni or Cu foil (10 µm thick) was used as reference, respectively. The first maximum in the derivative of the metal-foil spectra (= first inflexion point of their absorption edges) has an established energy position that is for Co at 7709 eV, for Ni at 8333 eV and for Cu at 8979 eV (published in (Bearden and Burr 1967)). In the experiment, the energy position of this maximum can differ from the denoted reference values. Then, the energy axis of the experimental data (foil and sample spectra) is shifted until the energy position of the maximum coincidences with the reference value.

The XANES and EXAFS measurements at the Mo *K*-edge were performed at the SAMBA bending-magnet beam line at the SOLEIL synchrotron in Paris. The excitation energy was adjusted by a double-crystal monochromator (Si-220). The typical scan-range for a measurement at the Mo *K*-edge was

19810 to 20980 eV. To record the Mo K_α-emission of the sample, a 35 Ge-elements detector (*Canberra*) was used. In case of saturation of the detector-elements due to beam scattering, a Nb or Zr foil was placed between the sample and the detector. A metallic Mo foil was used as reference for the energy axis with the established energy position of its Mo *K*-edge at 20000 eV (see (Bearden and Burr 1967)). The used set-up was analogous to the set-up at KMC-1 in BESSY as well as the applied experimental methods. At SAMBA, the same types of samples could be measured as at KMC-1, since the same sample holders could be applied.

POWDER AND TISSUES SAMPLE

The powder samples were carefully grinded and appropriately diluted with BN. The final powder was filled into a sample frame (thickness 1 mm, made of transparent poly(methyl methacrylate) (PMMA)) whose window (area 6 x 15 mm^2) on the backside was closed with *Kapton* tape (thickness 0.025 mm). After filling the sample, the front window of the sample frame was closed with *Kapton* tape as well. In the case of a tissue sample, the tissue was carefully attached onto the sticky inner side of the *Kapton* tape that closes the window (area 11 x 15 mm^2) of the sample frame from the backside. After this preparation, the powder and tissues samples were stored in liquid N_2 until the XANES/EXAFS measurement.

FREEZE-QUENCH PREPARATION

For the freeze-quench preparation of samples (see **Figure 5**), a 3 mm thick sample frame (made of transparent poly(methyl methacrylate) (PMMA)) was used with a window area of 11 x 15 mm^2. The working electrode (WE) was attached on the backside of sample frame via a silicone glue or *Kapton* tape, completely covering the window of the frame. The electrical contact of the electrode consisted of copper tape, sticking out by ≈1 cm on the bottom of the sample frame. As counter electrode (CE), a Pt wire was pierced through two holes on the side of the sample frame and formed to a single loop parallel to the surface of the WE in a distance of 3 – 5 mm. The ends of the wire, sticking out by ≈1 cm laterally from the frame, were twisted to one electrical contact. After incorporation of the Pt wire, the holes on the side of the sample frame were sealed with glue.

For the electrochemical experiment, the electrical contacts of the WE and CE were connected to a potentiostat via cables with crocodile clamps. The probe of a reference electrode (RE) was approached to the WE at a distance of 5 mm and placed in the window centre of the sample frame. Then, electrolyte was filled into the window until the Pt wire of the CE and the probe of the RE were completely immersed.

For freezing the sample at a certain potential of the WE, a two-step procedure for the electrochemical conditioning was applied. The freeze-quench sample was placed in a small tray made of polystyrene (PS). In the first step, the sample was kept at the desired WE potential for a certain time and the potential difference between WE and CE was recorded simultaneously. After that, the RE was removed

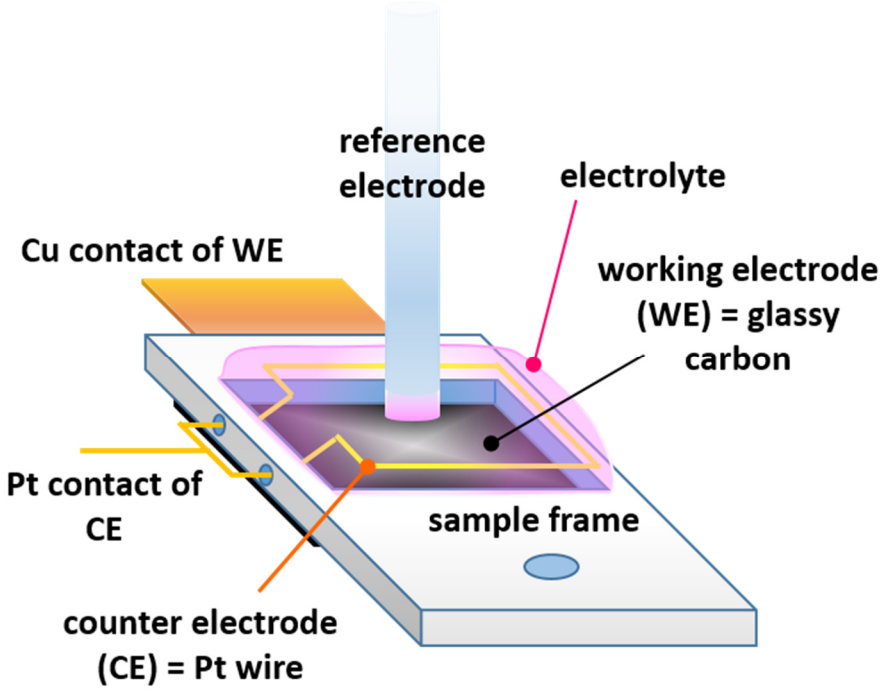

Figure 5

Schematic representation of a freeze-quench sample. The potentiostat is connected via the Cu and Pt contacts of working and counter electrode, respectively.

and its cable to the potentiostat was connected to the CE. In a second step, the equilibrium value of the beforehand determined potential difference, WE – CE, was applied as new WE potential. After 1 min, the PS stray was filled with liquid N_2 (LN_2) to freeze the sample. Then, the conditioning was stopped and the sample was stored in LN_2 until the XANES/EXAFS measurements.

The freeze-quench preparation was developed by my co-worker Marcel Risch (published in (Risch, Klingan et al. 2012)).

SPECTRA PROCESSING

All XANES/EXAFS spectra recorded from one sample were processed in the same way. The intensity of the absorption spectra, I_1, (see **Figure 6.1**) was converted into absorbance (see **Figure 6.2**) via $-\log_{10}(I_1/I_0)$ with the intensity of the X-ray beam before the sample, I_0. The photon counts of the fluorescence spectra were corrected for the number of not-detected photons due to possible dead time of the detector elements and, then, normalized with I_0. The single fluorescence spectra of all detector elements were averaged to one spectrum. After these initial steps, both types of spectra, absorbance and fluorescence, were processed in the same way.

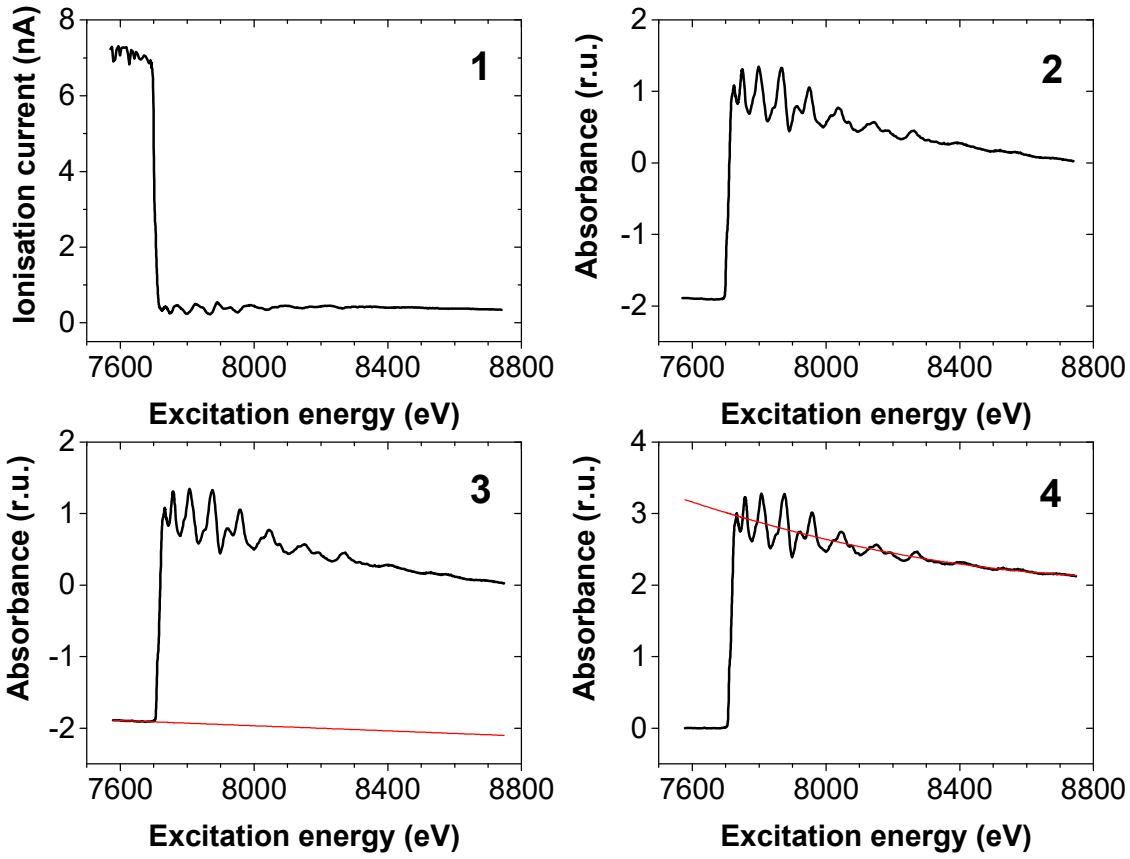

Figure 6

Data processing of a representative XAS spectrum for *K*-edge absorption (here Co edge). (**1**) raw, unprocessed spectrum. (**2**) conversion into absorbance spectrum. (**3**) removal of the background by subtracting a linear function (red line). (**4**) normalization via dividing the spectrum by a polynomial function (red line).

The energy axis of the XANES/EXAFS spectrum was corrected with the simultaneously measured reference spectra, as previously explained. Then, the background of the spectrum was removed by subtracting a linear function fitted to the range of the spectrum before the absorption edge (see **Figure 6.3**). After that, the jump of the absorption edge was normalized to one via dividing the spectrum by a polynomial function (of polynomial order = 1, 2 or 3) fitted to the range of the spectrum shortly after the edge (see **Figure 6.4**). All spectra from one sample are averaged to one sample spectrum weighted by their individual signal-to-noise ratio. The final XANES/EXAFS spectrum is shown in (see **Figure 7.1**).

For extracting the EXAFS, the range of the spectrum after the edge was fitted with a spline function (number of knots = 3 – 7) as centre line through the EXAFS oscillations (see **Figure 7.1**). Then, this part of the spectrum was cut-out and its background was removed by subtracting the spline function, yielding a so-called χ spectrum (see **Figure 7.2**). The energy axis of the spectrum, E, was substituted by an energy offset, $E - E_0$, relative to the threshold energy, E_0, of the absorption edge. After that, the energy offset was converted into an axis of the photo-electron wave vector, k, via $k = \sqrt{(2m / \hbar^2 \ (E - E_0)}$ (m … mass of the electron, $\hbar$ … Planck constant divided by 2π). The converted spectrum was weighted with k^3 to compensate the increasing damping of the EXAFS oscillations at larger k values (see **Figure 7.3**). This form of the EXAFS spectrum was fitted via EXAFS simulations to

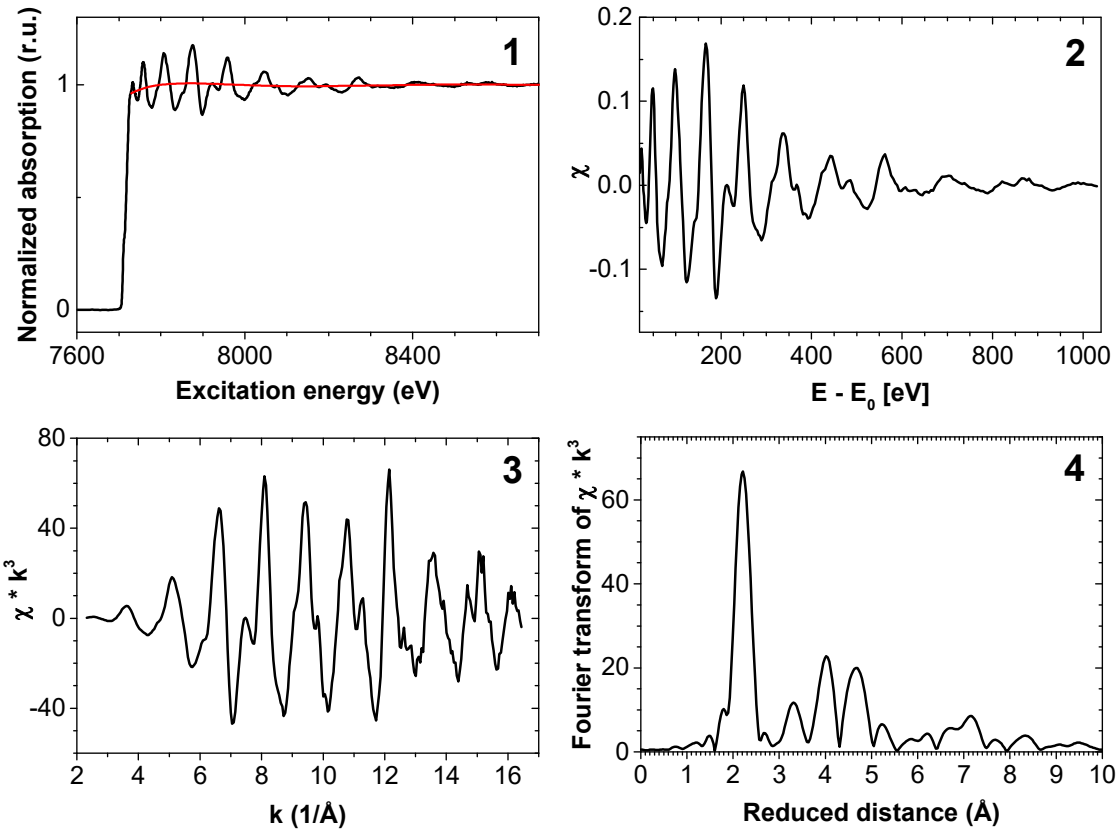

Figure 7

Extraction of the EXAFS from a representative XAS spectrum for *K*-edge absorption (here at the Co edge). (**1**) spectrum from **Figure 6** with a spline function (red line) fitted as centre line through the EXAFS oscillations. (**2**) cut-out EXAFS oscillations, the so-called χ spectrum. The energy axis is substituted by an energy offset, $E - E_0$, relative to the threshold energy, E_0, of the absorption edge. (**3**) energy offset is converted into the photo-electron wave vector k and the spectrum is weighted with k^3. (**4**) Fourier transform of **3**.

obtain the structural information from the EXAFS (see subsequent sections). In the last step, the spectrum was Fourier-transformed to make the structural information of the EXAFS directly visible (see **Figure 7.4**).

The entire processing of the XANES/EXAFS spectra was executed with the in-house software *Bessy*. A program developed by Dr. Petko Chernev.

EXAFS SIMULATIONS

The extracted and k^3 weighted EXAFS data (see **Figure 7.3**) was simulated in *k* space with the software *SimX lite* (developed by Dr. P. Chernev). For the simulation, the atomic environment around the X-ray absorbing central atom was modelled via a certain number, n_{shell}, of atomic shells. Each shell, i, consisted of atoms of the same element in a certain number, N_i, and distance, r_i, to the absorber atom. The following formular was applied to calculate the contribution of each shell to the EXAFS spectrum, $\chi(k)$, and to sum up all contributions to the final spectrum (Teo 1986, Penner-Hahn 1999, Rehr and Albers 2000):

$$\chi(k) = S_0^2 \cdot \sum_{i}^{n_{shell}} A(R_i, k)_i \cdot N_i \cdot e^{-2\sigma_i^2 \cdot k^2} \cdot \sin(2k \cdot R_i + \phi_i)$$

Equation 1

S_0^2 … amplitude reduction factor

$A(R_i, k)_i$ … scattering amplitude of the electron wave

N_i … number of neighbours in the i^{th} atomic shell

σ_i … Debye-Waller parameter of the i^{th} atomic shell

R_i … distance between the X-ray absorbing atom and the atoms in the i^{th} atomic shell

ϕ_i … phase shift experienced by the photo electron

The structural parameters N_i, σ_i and R_i as well as S_0^2 were used as fit parameters for fitting the simulation to the real spectrum. In the fitting, the simulation error, $\delta(\boldsymbol{w})$, represented by the following function was minimized via a least-square approach using a Levenberg-Marquardt algorithm:

$$\delta(\boldsymbol{w}) = \sum_{i}^{n} (\chi(k, \boldsymbol{w})_i - y_i)^2$$

Equation 2

$\boldsymbol{w}$ … vector containing all fit parameters

$\chi(k, \boldsymbol{w})_i$ … data point of simulated EXAFS spectrum

y_i … data point of experimental EXAFS spectrum (n data points)

The used phase functions, ϕ_i, in $\chi(k)$, (see **Equation 1**) were calculated with the *FEFF* program (Ankudinov, Ravel et al. 1998, Rehr and Albers 2000) (version 8.4, self-consistent field option activated). Atomic coordinates of the *FEFF* input files were generated from crystal structures of appropriate reference compounds. The scattering paths were obtained up to a radius of 12 Å for up to 'four-legged' paths.

UNCERTAINTY OF FIT PARAMETER

The uncertainty of the fit parameters $\boldsymbol{w}$ was determined by calculating the inverse Hesse matrix of the normalised simulation error via $\mathrm{d}^2\delta^{norm}(\boldsymbol{w})/\mathrm{d}\boldsymbol{w}^2$ for the optimal fit parameters $\boldsymbol{w_{min}}$. The diagonal elements c_{jj} of the inverse Hesse matrix are the squared uncertainties of the single fit parameters w_j.

The normalised simulation error was obtained via $\delta^{norm}(\boldsymbol{w}) = \delta(\boldsymbol{w})/\sigma$ using the statistically relevant (averaged) experimental error σ as norm. In the case of a reasonable simulation, the error σ can be estimated via the equation:

$$\nu = \frac{N_{idp}}{N} \cdot \frac{\delta(\boldsymbol{w_{min}})}{\sigma}$$

Equation 3

ν … degrees of freedom in the simulation

N … number of data points in the fit range

N_{idp} … number of statistically independent data points in the fit range

σ … experimental error

$\delta(\boldsymbol{w_{min}})$ … simulation error with optimal fit parameters $\boldsymbol{w_{min}}$

The degrees of freedom of a simulation are the difference, $\nu = N_{idp} - N_{fit}$, between the number of independent data points, N_{idp}, and the number of fit parameters, N_{idp}, in the simulation (Eadie, Drijard et al. 1971). In a reasonable simulation, the simulation error correlates with the degrees of freedom, since a certain number of fit parameters only enables the optimal simulation of an equal number of independent data points. Hence, the degrees of freedom weighted with the experimental error should be equal to the simulation error. This relation enables the estimation of the experimental error, under the assumption that the error is equal for all independent data points.

The number of independent data points was estimated via $N_{idp} \approx 2 \cdot \Delta k \cdot \Delta R/\pi$ (Stern 1993, IXAS 2000). Δk corresponds to the fit range in k-space and ΔR to the range of meaningful data above the noise in R-space.

MEASURE OF THE FIT QUALITY

The quality of EXAFS simulations were quantified with the filtered R_f-factor that is the relative difference between the simulated and the real EXAFS spectrum after Fourier-filtering. The simulated and the real spectrum were Fourier-transformed into *R*-space and only the *R*-range of the Fourier-transforms containing the relevant structural information was transformed back into *k*-space. Only these Fourier-filtered spectra were used for the R_f calculation via the formula:

$$R_f = 100 \times \frac{\sum_i^n |\chi(k, \boldsymbol{w})_i^* - y_i^*|}{|y_i^*|}$$

Equation 4

$\boldsymbol{w}$ … vector containing all fit parameters

$\chi(k, \boldsymbol{w})_i^*$ … data point of simulated, Fourier-filtered EXAFS spectrum

y_i^* … data point of experimental. Fourier-filtered EXAFS spectrum (n data points)

SUBTRACTION OF METAL CONTRIBUTION FROM SPECTRUM

The extended X-ray absorption fine-structure (EXAFS) spectrum of a non-metallic species can be obscured by the spectrum of a prominent metallic contribution in the sample. In this case, the metallic

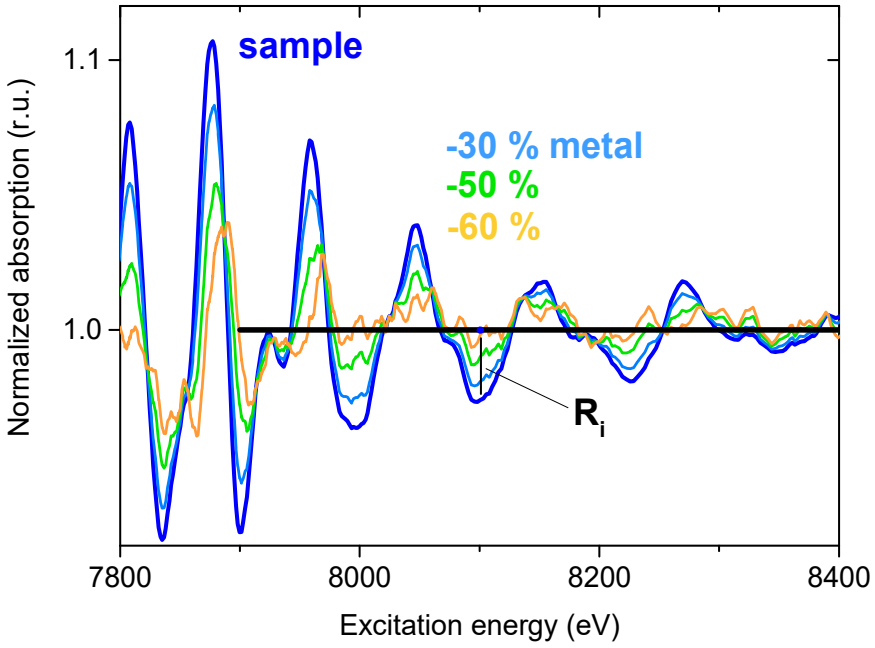

Figure 8

Demonstration of the artificial diminishment of a metallic EXAFS contribution. **Blue** line: spectrum of a sample, here *H_2-CoCat* at -0.79 V *vs.* NHE, exhibiting oscillations in the predominantly metallic range of the EXAFS (> 7900 eV). **Light blue** line: sample spectrum subtracted by a metal spectrum (here a Co metal foil) weighted with a factor of 0.30; and subsequently re-normalized. The same repeated with a weighting factor of 0.50 or 0.60 yields the **green** or **yellow** spectrum, respectively. **Black** line: ideal EXAFS spectrum without any metallic oscillations. $\mathbf{R_i}$ represents the fit residuals calculated for every point of the metal-subtracted spectrum. In a *least-squares* approach, the optimal weighting factors of the metal subtraction are determined by minimizing the sum of the squared fit residuals.

contribution can be artificially diminished (see **Figure 8**) by subtracting a weighted metal spectrum from the EXAFS of the sample:

$$metal\text{-}reduced\ spectrum = \frac{1}{1-\alpha} \times (sample\ spectrum - \alpha \times metal\ spectrum) \text{ with } \alpha < 1$$

Equation 5

The "metal-reduced" difference spectrum is re-normalized with the factor $1/(1-\alpha)$. The weighting factor α corresponds to the relative amount of metal in the sample. In the predominantly metallic range of the difference spectrum, the EXAFS oscillations are fitted to a horizontal line with amplitude one, leading to a minimization of their amplitude. In the fit procedure, the weighting factor is varied from zero to one. The fit uncertainty is estimated as the difference between the final weighting factor with a minimal sum of squared residuals and a sub-optimal weighting factor exhibiting the double sum.

LINEAR COMBINATION OF SPECTRA

The X-ray absorption near-edge structure (XANES) and extended X-ray absorption fine-structure (EXAFS) spectrum of a sample recorded at a certain absorption edge can be a composition of spectra from various species of the X-ray absorber atom present in the sample. To reassemble the sample spectrum via a linear combination of two or more reference spectra is a possible way to identify these various species of the absorber atom. The linear combination (see **Figure 9**) is a weighted addition of the reference spectra:

$$linear\ combination = \alpha_1 \times reference\ spectrum\ 1 + \alpha_2 \times reference\ spectrum\ 2 + \cdots$$

Equation 6

The weighting factors α_i (linear coefficients) correspond to the individual proportions of the reference species in the sample ($\sum_i \alpha_i = 1$ and $\alpha_i < 1$). The linear combination is fitted to the sample spectrum via a *least-squares* approach with the weighting factors as fit parameters. In the fit procedure, the weighting factors are varied from zero to one. The fit uncertainty is estimated as the difference between the final weighting factors with a minimal sum of squared residuals and sub-optimal weighting factors exhibiting the double sum

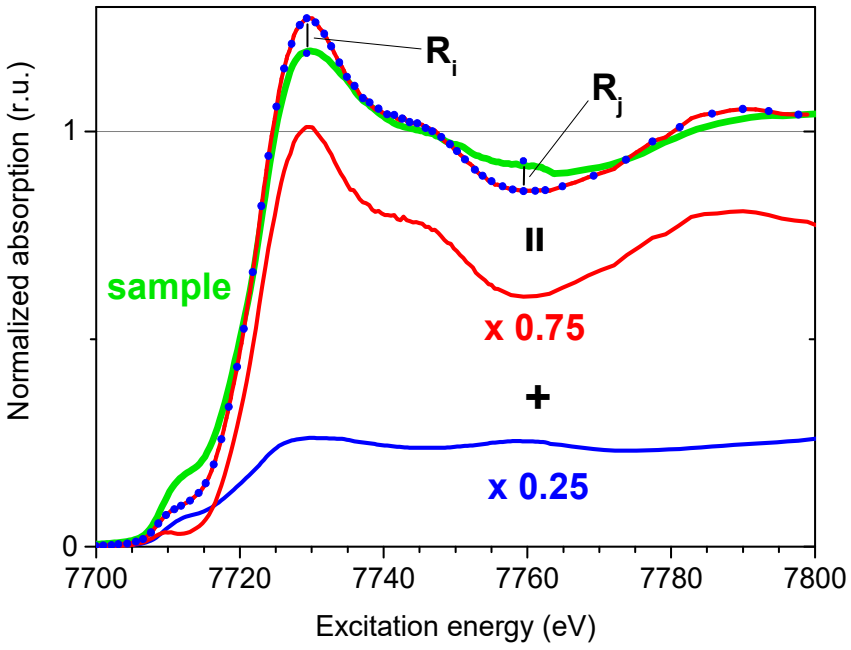

Figure 9

Demonstration of the linear combination of XANES/EXAFS spectra. **Green** line: a sample spectrum, here the *H_2-CoCat* at +1.37 V *vs.* NHE. **Red** line: first reference spectrum, here the *O_2-CoCat*, weighted with the factor 0.75. **Blue** line: second reference spectrum, here *H_2-CoCat* at -0.79 V, weighted with the factor 0.25. **Blue-dotted red** line: linear combination of the two weighted reference spectra. $\mathbf{R_i}$ and $\mathbf{R_j}$ represent the fit residuals calculated for every point of the linear-combination spectrum. In a *least-squares* approach, the optimal weighting factors of the linear combination are determined by minimizing the sum of the squared fit residuals.

.

2. Electrochemical cell and methods

THREE-ELECTRODE SYSTEM

The following short introduction in a electrochemical cell (three-electrode system) and cyclic voltammetry is based on the textbook of *A. J. Bard* and *L. R. Faulkner* and the publication of *P. T. Kissinger* and *W. R. Heineman* (Bard and Faulkner 1980, Kissinger and Heineman 1983).

In a three-electrode configuration (see **Figure 10**), an electrochemical cell consists of a working electrode, a counter electrode and a reference electrode placed in an electrolyte. The working electrode and the counter electrode are connected to an external power source provided by a

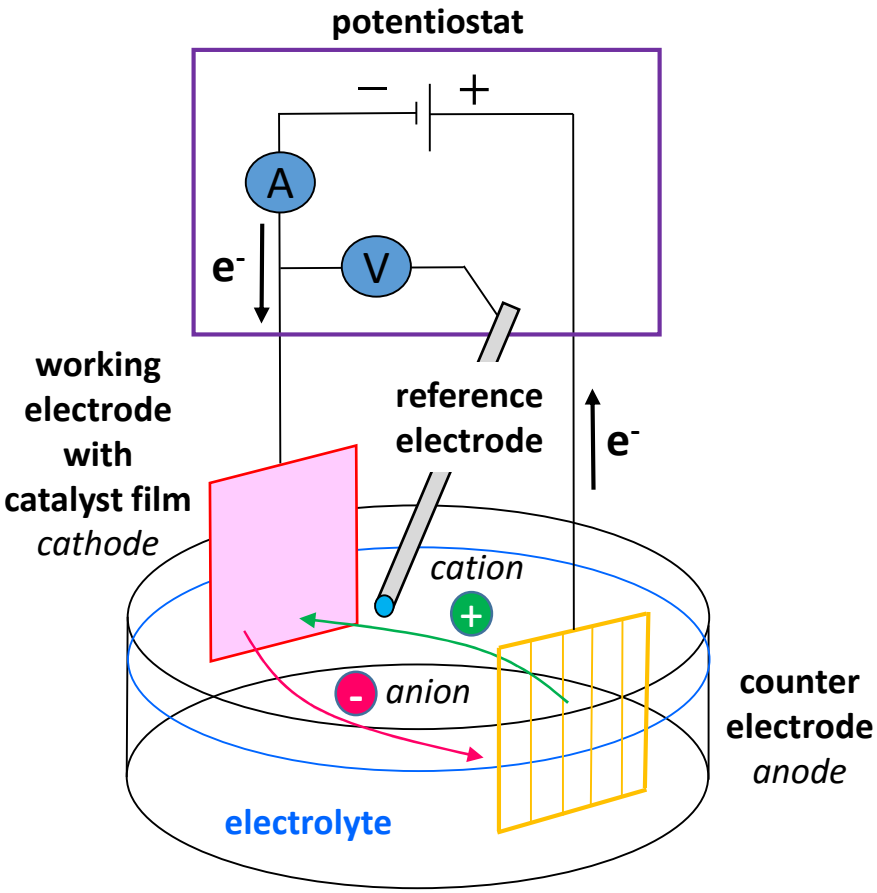

Figure 10

Set-up of an electrochemical cell with a three-electrode system connected to a potentiostat. Here, the potentiostat applies a cathodic voltage between working and counter electrode. The corresponding flow direction of the electrons in the wire as well as for the ions in the electrolyte is indicated by arrows. An anodic voltage would reverse the flow directions and the assignment of the electrodes as 'cathode' or 'anode'. 'A' and 'V' represent the ampere- and the voltmeter incorporated into the potentiostat. The electrical circuit depicted in the potentiostat is very simplified.

potentiostat and form, together with the electrolyte, a closed electric circuit (see **Figure 10**). The potentiostat is a device for controlling and measuring the electrode potential of the working electrode as well as the current flowing through the electrode. The potentiostat can adjust the potential and the current of the working electrode by modifying the voltage between working and counter electrode.

The working electrode contains the sample (in this thesis: a catalytic film on a substrate). The electrode potential and current of the working electrode are crucial probes to characterize the sample. The electrode potential arises at the interface between working electrode and electrolyte due to the transfer of charged species across the sample, specific adsorption of ions at the sample surface, and orientation of polar molecules in sample and electrolyte.

The electrode potential of the working electrode is measured against a constant equilibrium potential provided by the reference electrode. The probe of the reference electrode is located close to the surface of the working electrode and is shielded via a diaphragm to protect its electrochemical equilibrium. Almost no current is flowing through the reference electrode due to the very high ohmic resistance of the circuit of the potentiostat.

The counter electrode completes the electrical circuit formed by the potentiostat, the working electrode and the electrolyte. The function of the counter electrode is to provide the electric potential needed for maintaining a certain electric current required by the working electrode. The magnitude of the electric current is determined by electric potential and processes at the working electrode. The counter electrode must

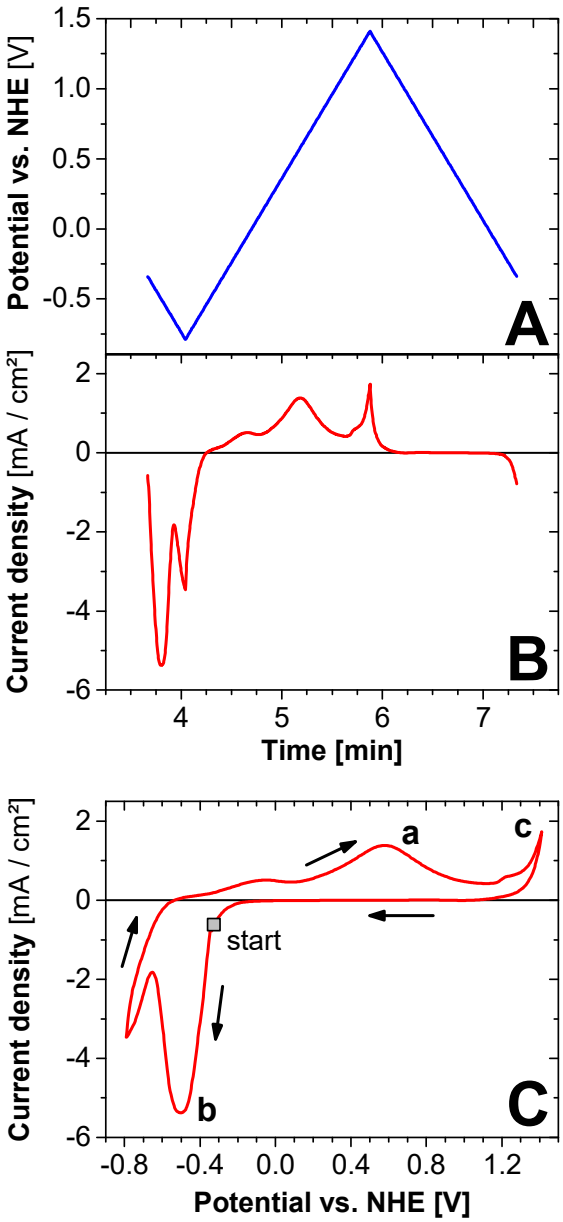

Figure 11

The principle of cyclic voltammetry (CV). (**A**) The potential of the working electrode is cycled with a constant (absolute) scan rate between a lower and an upper potential limit. (**B**) Simultaneously, the current occurring at the electrode is recorded. (**C**) In the common representation of cyclic voltammetry, the current is plotted over the potential and the time line is neglected or indicated by arrows. The CV was recorded on a Co doped MoS_x catalyst (x = 2 or 3).

not affect or limit the electrochemical reactions at the working electrode. Hence, the material of the counter electrode possesses a high surface area and exhibits a low electrical resistance.

CYCLIC VOLTAMMETRY

Cyclic voltammetry (CV) is a method for the electrochemical characterisation. In this method, the electrode potential of the working electrode is cycled with a constant scan rate between a lower and an upper potential limit (see **Figure 11A**) while the current response is simultaneously recorded (see **Figure 11B**). Positive currents correspond to anodic currents and indicate that an oxidation process takes place at the working electrode. In this process, anions are forced by the electrical potential to react chemically and to release electrons to the working electrode. Negative currents in CV correspond to cathodic currents, indicating a reduction process at the working electrode. In this process, the electrical potential forces cations to react chemically and to receive electrons from the working electrode. The sample attached to the working electrode (in this thesis, a catalytic film on a substrate) can contain chemical species (i. a. metal ions) that are involved in the oxidation and reduction processes and undergo oxidation-state changes. These species provide only a limited quantity of oxidizable or reducable atoms and, therefore, exhibit anodic or cathodic currents which decay after the initial rise as the available atoms are consumed by the oxidation or reduction. These limited anodic or cathodic currents can be visible as distinct waves in CV if an appropriate scan velocity is used (see anodic wave **a** and cathodic wave **b** in **Figure 11C**). In an aqueous electrolyte, CV can indicate catalytic hydrogen formation or water oxidation after exceeding the corresponding standard electrode potential by a steep rise in respective cathodic or anodic current (see anodic rise **c** in **Figure 11C**). These catalytic currents do not decay as their educts are abundant in an aqueous electrolyte or formed at the counter electrode.

III. RESULTS

1. Electro-deposited MoS_x and Co/Ni:MoS_x electrodes

Contents

INTRODUCTION

Molybdenum sulfide materials as catalysts for hydrogen formation are a non-precious alternative to the highly active but scarce and, hence, expensive Pt. Bulk MoS_2 crystals are known as poor catalysts (Tributsch and Bennett 1977, Jaegermann and Tributsch 1988) but nanocrystals of MoS_2 with unsaturated edge sites exhibit significant catalytic activity (Hinnemann, Moses et al. 2005, Jaramillo, Jorgensen et al. 2007, Bonde, Moses et al. 2008, Chen, Cummins et al. 2011, Li, Wang et al. 2011). The preparation of the nanocrystals, however, involves ultrahigh vacuum or thermal treatments at high temperatures of 400 – 550 °C, leading to high production costs for the catalyst. The amorphous MoS_x catalysts (x = 2 or 3) established by *Merki et al.* might be a less costly alternative, as it can be prepared by simple electro-deposition under ambient conditions and exhibits a high activity for H_2 formation (Merki, Fierro et al. 2011, Merki, Vrubel et al. 2012). The as-prepared MoS_x catalyst is a mixture of amorphous MoS_2, which is the catalytic species, and MoS_3 (Merki, Fierro et al. 2011, Merki, Vrubel et al. 2012, Lassalle-Kaiser, Merki et al. 2015).

Merki et al. reports that the doping of the MoS_x catalyst with Co or Ni increases its catalytic activity for H_2 formation, as the dopants promote the film growth leading to a higher catalytic load and a larger surface area (Merki, Vrubel et al. 2012). *Merki et al.* suggests that, under certain conditions, the dopants can additionally increase the intrinsic activity of the catalyst (Merki, Vrubel et al. 2012). At pH 7, the doped catalysts exhibit an increase in their exchange current densities (ca. 12 fold) that is significantly higher than the increase in either surface area (ca. 1.5 – 3 fold) or catalyst loading (ca. 3 fold) (all values reported in (Merki, Vrubel et al. 2012)).

Our objective is to gain insight into the atomic mechanism behind the intrinsic activity and its promotion by doping. In the first main section ***Atomic structure***, we will investigate the atomic structure of the MoS_x catalyst at the Mo, Co and Ni site with X-ray absorption spectroscopy. The atomic structure will be studied in a state of H_2 formation and in a non-catalytic state. In the second main section ***Hydrogen formation***, we will discuss possible implications of the observed atomic structure and of its structural modification during catalysis on the catalytic mechanism for H_2 formation. The magnitude of the modification could be an indicator for the catalytic activity of the corresponding site.

In the last main section ***Water oxidation***, we will additionally investigate whether the MoS_x catalysts, undoped or doped, exhibit catalytic activity for water oxidation and will try to identify the catalytic species. A non-precious, easy-to-produce MoS_x catalyst active for H_2 formation and water oxidation could be interesting for possible electrolyser or fuel cell devices.

PREPARATION

The MoS_x and Co/Ni:MoS_x electrodes (x = 2 or 3) were prepared according to the protocol of *Merki et al.* as published in (Merki, Vrubel et al. 2012). The MoS_x films were electro-deposited (three-electrode system) on glassy carbon substrates (100 µm thick, 5 - 10 Ω) via cyclic voltammetry in an aqueous solution (100 ml *milliQ* water) of 0.1 M $NaClO_4$ with 2 mM $(NH_4)_2MoS_4$. For doping the films with Co or Ni, 0.67 mM $CoCl_2{\cdot}6H_2O$ or $NiCl_2{\cdot}6H_2O$ were added to the solution, respectively. The solution was freshly prepared for each film deposition. The back side of the glassy carbon was covered by *Kapton* tape to allow film deposition only on the front side (deposition area 15 x 12 mm^2) facing the reference electrode. For film deposition, the applied cyclic voltammetry performed 25 cycles between +0.30 V and -0.80 V *vs.* normal hydrogen electrode (NHE) with a scan rate of 50 mV/s. After deposition, the electrodes were rinsed with *milliQ* water. The used type of reference electrode was mercury-sulphate with an equilibrium potential of +0.65 V *vs.* NHE. The counter electrode was a Pt mesh located in a glass compartment with a glass frit and filled with 0.1 M $NaClO_4$ solution. The used potentiostat was a *Biologic SP200* or *SP300*.

The MoS_x and Co/Ni:MoS_x electrodes were characterized by cyclic voltammetry (scan rate of 1 mV/s or 20 mV/s) in a 0.1 M KH_2PO_4/K_2HPO_4 buffer (in *milliQ* water) of pH 7. *IR* compensation was applied. The characterization was executed in the same three-electrode set-up as described for the film deposition.

Prior to the X-ray absorption spectroscopy (XAS) measurements, the MoS_x and Co/Ni:MoS_x electrodes were conditioned at -0.80 V, -0.35 V or +1.40 V *vs.* NHE for 12 min in a 0.1 M KH_2PO_4/K_2HPO_4 buffer (in milliQ water) of pH 7. After the conditioning, the electrodes were immediately frozen and stored in liquid N_2 until the XAS measurements. The conditioning and freezing were performed in a special electrochemical cell adapted for XAS measurements as described in the section *Freeze-quench preparation* of the *Methods* chapter.

The deposition, conditioning, freezing and characterization of the electrodes were executed under N_2 atmosphere. All used solutions were degassed by purging with N_2 gas prior to the experiments.

ATOMIC STRUCTURE

Mo SITE - ATOMIC STRUCTURE

RESULTS AND DISCUSSION

EXPECTED STRUCTURE

The applied preparation method for the Co-doped, Ni-doped and undoped MoS_x (x = 2 or 3) *Merki* electrodes is supposed to produce a mixture of amorphous $Mo^{IV}S_2$ and $Mo^{V}S_3$ (Merki, Fierro et al. 2011, Merki, Vrubel et al. 2012). The deposition is done by cycling the potential between -0.8 V and +0.3 V *vs.* normal hydrogen electrode (NHE) in an aqueous solution of $(NH_4)_2MoS_4$ with an additional contribution of $CoCl_2$ or $NiCl_2$ for the doping. In a potential cycle, MoS_3 is deposited between 0 V and +0.3 V and MoS_2 between -0.8 V and -0.7 V (Vrubel and Hu 2013). In the intermediate potential range, the deposited MoS_3 experiences a partial corrosion (Vrubel and Hu 2013). In general, there is evidence (Merki, Fierro et al. 2011) that MoS_3 is deposited under anodic conditions (shown for electrolysis at ≈ +0.55 V in (Belanger, Laperriere et al. 1993)) and MoS_2 under cathodic conditions (shown for electrolysis from -0.75 V to -1.15 V in (Ponomarev, Neumann-Spallart et al. 1996)). Additionally, MoS_3 can convert to MoS_2 at cathodic potentials by reducing the S_2^{2-} in MoS_3 to S^{2-} (Merki, Fierro et al. 2011, Merki, Vrubel et al. 2012). In our study, the *Merki* electrodes were conditioned and frozen at cathodic potentials, -0.8 V and -0.35 V, to capture their state during H_2 formation and inactivity, respectively. Hence, the electrodes should mainly consist of amorphous MoS_2.

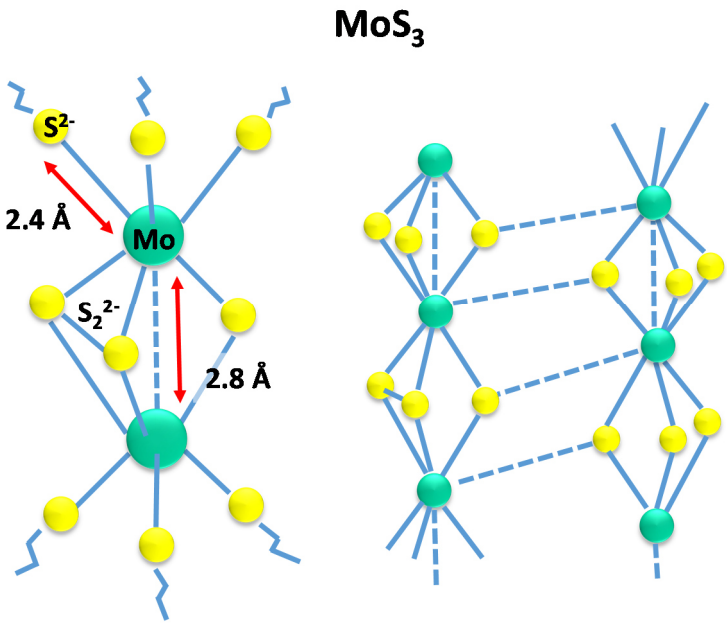

Figure 12

Left side: proposed Mo_2S_9 building block for the atomic structure of amorphous MoS_3 (scheme based on illustration in (Hibble, Rice et al. 1995)). **Right** side: chain model proposed for amorphous MoS_3 with the possible inter-connection between the chains (scheme based on illustration in (Weber, Muijsers et al. 1995)).

The atomic structure of amorphous MoS_2 is not defined but it is supposed to consist of Mo^{IV} centres coordinated to S^{2-} ligands like in crystalline MoS_2 exhibiting similar Mo-S distances. However, the number of the S ligands and their geometry is unclear. Amorphous MoS_2 does not possess a long-range order. Amorphous MoS_3 (see **Figure 12**), on the other hand, consists of Mo^{V} centres coordinated to S^{2-}

and S_2^{2-} ligands. The Mo centres form Mo_2S_9 units via a Mo-Mo coordination of 2.8 Å (see XAS studies in (Cramer, Liang et al. 1984, Scott, Jacobson et al. 1986, Hibble, Rice et al. 1995, Afanasiev and Bezverkhy 2002, Afanasiev, Jobic et al. 2009, Tang, Grauer et al. 2011)). The Mo-Mo distance is shorter than in crystalline MoS_2 with 3.2 Å. The Mo_2S_9 units of MoS_3 possibly form chain-like structures, as proposed by (Chien, Moss et al. 1984).

Mo-S COORDINATION

X-ray absorption near-edge structure (XANES) and extended X-ray absorption fine-structure (EXAFS) of the doped and undoped MoS_x *Merki* electrodes (x = 2 or 3) were recorded at the Mo *K*-edge to gain insight into the atomic structure of their Mo sites. Prior to the XANES/EXAFS measurements, the electrodes were conditioned (12 min, pH 7) and frozen either at -0.80 V or -0.35 V *vs.* normal hydrogen electrode (NHE), to study structural differences between Mo sites in a state of catalytic H_2 formation

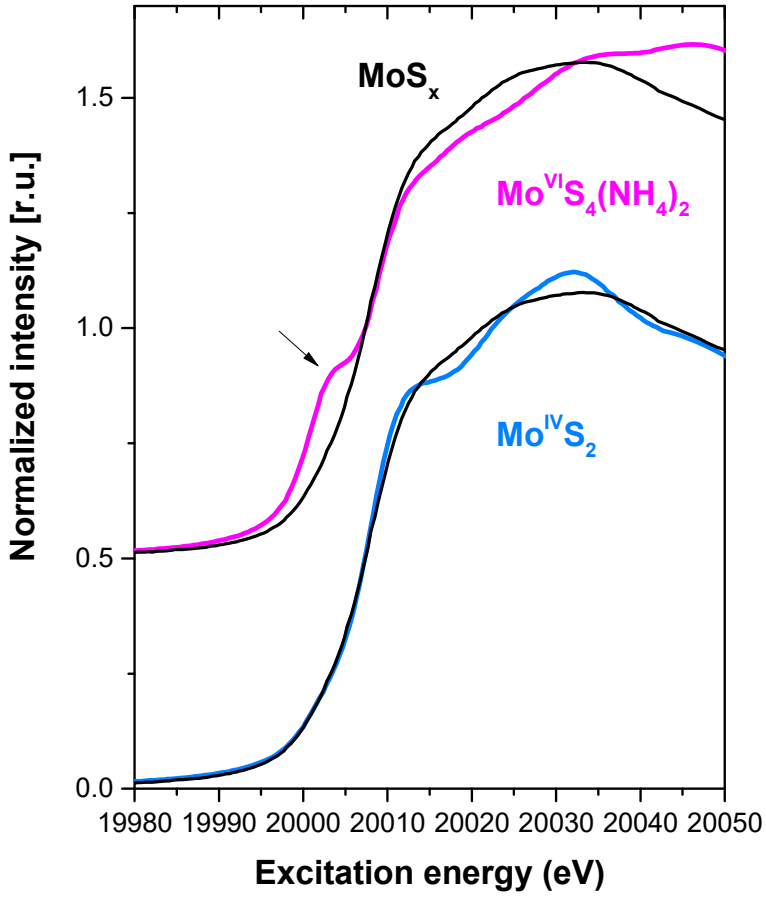

Figure 13

XANES spectra recorded at the Mo *K*-edge of the undoped MoS_x *Merki* electrode at -0.80 V *vs.* NHE (**black** line) compared to $Mo^{IV}S_2$ (**blue** line) and $Mo^{VI}S_4(NH_4)_2$ (**magenta** line). The shown electrode spectrum is representative for the doped electrodes at -0.80 V and for the electrodes at -0.35 V.

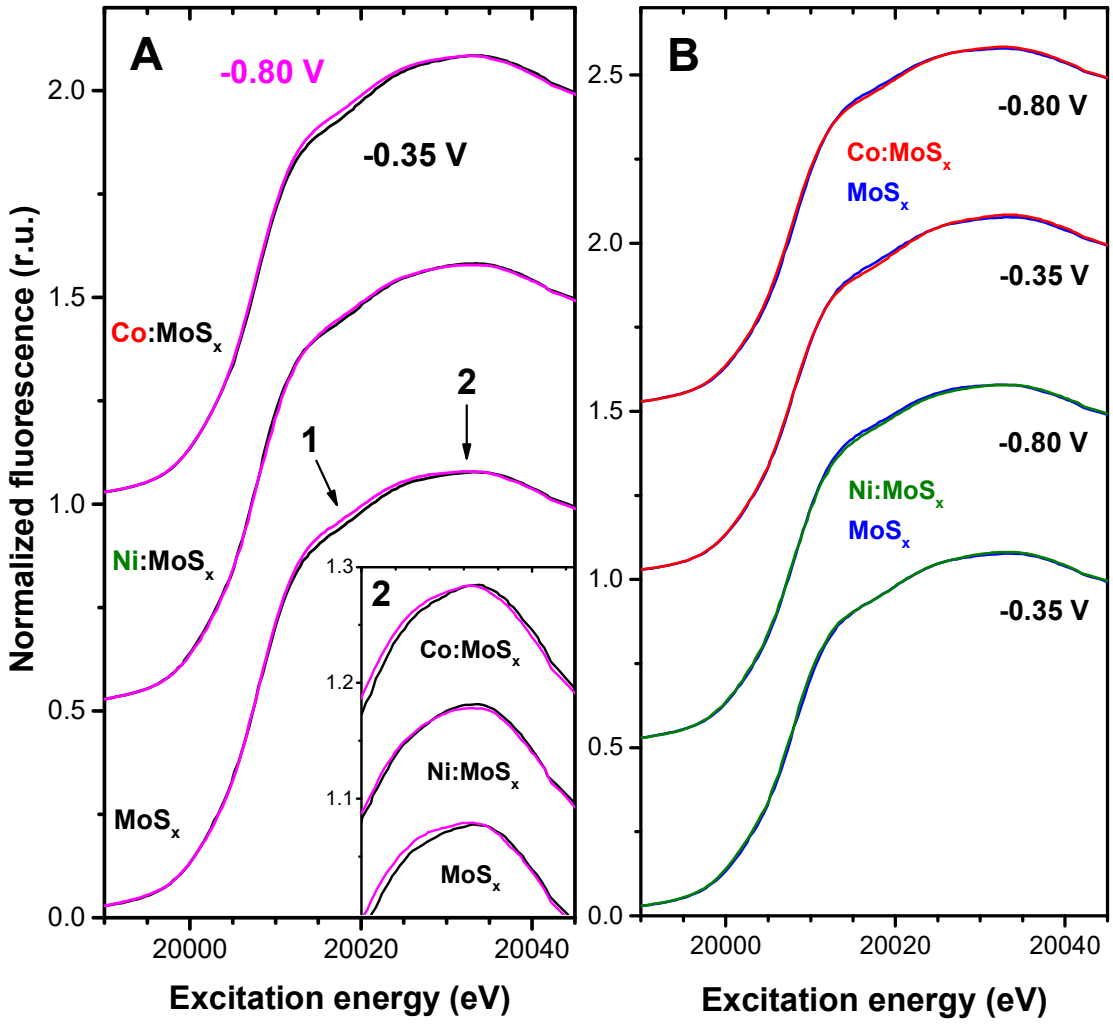

Figure 14

XANES spectra recorded at the Mo *K*-edge of the *Merki* electrodes. In **A**: doped and undoped MoS_x *Merki* electrodes at -0.80 V *vs.* NHE (**magenta** line) compared to the same electrodes at -0.35 V (**black** line). The inlet shows a magnification of the edge summit indicated by arrow **2**. In **B**: Ni doped (**green** line) and Co doped (**red** line) *Merki* electrodes compared to the undoped electrodes (**blue** line) at the same electrode potential.

(-0.80 V) and in a non-catalytic state (-0.35 V) (standard electrode potential of hydrogen reduction E^0_{H2} = -0.41 V at pH 7).

The Mo XANES of the undoped *Merki* electrodes (see **Figure 13**) are similar in shape to the spectrum of $Mo^{IV}S_2$ and show larger deviations when compared to the spectrum of $Mo^{VI}S_4(NH_4)_2$, in particular, the lack of a pre-edge (see **arrow** in **Figure 13**). This suggests that the first coordination sphere of the Mo sites in the electrodes is rather a geometry of six S ligand as in $Mo^{IV}S_2$ than a four-ligand geometry as in $Mo^{VI}S_4(NH_4)_2$. The same can be deduced for the Mo sites in the Co or Ni doped *Merki* electrodes, since their XANES are almost identical to spectra of the undoped electrodes (see **Figure 14B**). The XANES of the electrodes exhibit a position of the Mo edge close to the edge of $Mo^{IV}S_2$ (see **Table 1**),

indicating a mean oxidation state of about IV for the Mo sites in the electrodes. The alteration in electrode potential from -0.35 V to -0.80 V leads only to small modifications in the XANES of the electrodes. At -0.80 V, the XANES exhibit a small shift in the summit of the edge towards lower excitation energies by 0.3 – 0.7 eV (see arrow **2** and inlet in **Figure 14A**) as well as an analogue shift in the upper half of the edge by 0.3 – 0.4 eV (except for the Ni doped electrode) (see arrow **1** in **Figure 14A**). Both shifts (see **Table 1**) suggest that, at -0.80 V, a small fraction of Mo^{IV} ions is reduced to Mo^{III}. Similar but smaller shifts are visible between the undoped and doped electrodes (see **arrow** in **Figure 14B**), suggesting a weaker reduction effect for the Mo^{IV} ions in the doped electrodes. The Ni doped electrodes exhibits the smallest modifications in the XANES, suggesting more inert Mo ions than in the other electrodes.

Mo edge	**Edge position** [eV]	**Summit position** [eV]
MoS_x -0.35V	**20011.8**	**20032.3**
MoS_x -0.80V	-0.3	-0.7
MoS_x:Ni -0.35V	**20011.6**	**20032.4**
MoS_x:Ni -0.80V	-0.0	-0.3
MoS_x:Co -0.35V	**20011.9**	**20034.6**
MoS_x:Co -0.80V	-0.4	-0.6
References		
$Mo^{IV}S_2$	**20011.9**	**20031.8**
$Mo^{VI}S_4(NH_4)_2$	20013.2	20045.9

Table 1

Mo *K*-edge positions of the *Merki* electrodes at -0.80 V and -0.35 V *vs.* NHE. The edge positions were determined with the integral method as described in (Dau, Liebisch et al. 2003) but with an smaller interval of integration from 0.5 to 1.0 of normalized absorption to exclude pre-edges. The summit position of the edges (indicated by arrow **2** in **Figure 14**) were determined by a weighted addition of the excitation energies in the summit range. The weighting factors are the normalized absorption per excitation energy divided by the total absorption of the summit range.

The Mo EXAFS of the undoped and doped *Merki* electrodes exhibit the two prominent peaks **1** and **2** in the Fourier transforms (see **Figure 15**). When compared to the spectrum of $Mo^{IV}S_2$, peak **1** can be assigned to a Mo-S coordination similar to MoS_2. The nature of peak **2** remains unclear but is possibly a Mo-Mo coordination, see section *Mo-metal coordination*. For all electrodes, EXAFS simulations (see **Figure 17** and **Figure 18**) of peak **1** yield the same Mo-S distance between 2.37 – 2.38 Å (see **Table 3**), showing no effect of the doping or the electrode potential. The S distance can be found in MoS_2 (see **Figure 15**) with 2.35 – 2.41 Å and is too short for MoS_3 (2.41 – 2.44 Å) and too long for $Mo^{VI}S_4(NH_4)_2$ (2.17 – 2.18 Å) (see **Figure 15**). This supports the deduction from the XANES analysis that the Mo sites in the electrodes possess a MoS_2-like S coordination with more than four ligands.

Peak **1** of the electrodes exhibits a smaller amplitude than in MoS_2 (see **Figure 15**). The amplitude of the peak is presumably damped by a high spatial disorder of the S shells in the electrodes. EXAFS simulations of peak **1** indeed yield a clearly higher Debye-Waller factor of σ_S = ±0.08 Å for the electrodes than for crystalline MoS_2 with σ_S = ±0.03 Å. The Debye-Waller factor is a measure for the spatial disorder of a ligand shell, as the factor corresponds to the root-mean-square deviation of the mean distance between ligand and central atom.

For all *Merki* electrodes, EXAFS simulations of peak **1** (see **Figure 17** and **Figure 18**) yield a mean S coordination number close to five at both electrode potentials (see **Table 4**). This suggests that the Mo sites in the doped and undoped electrodes possess presumably five S ligands in the first coordination

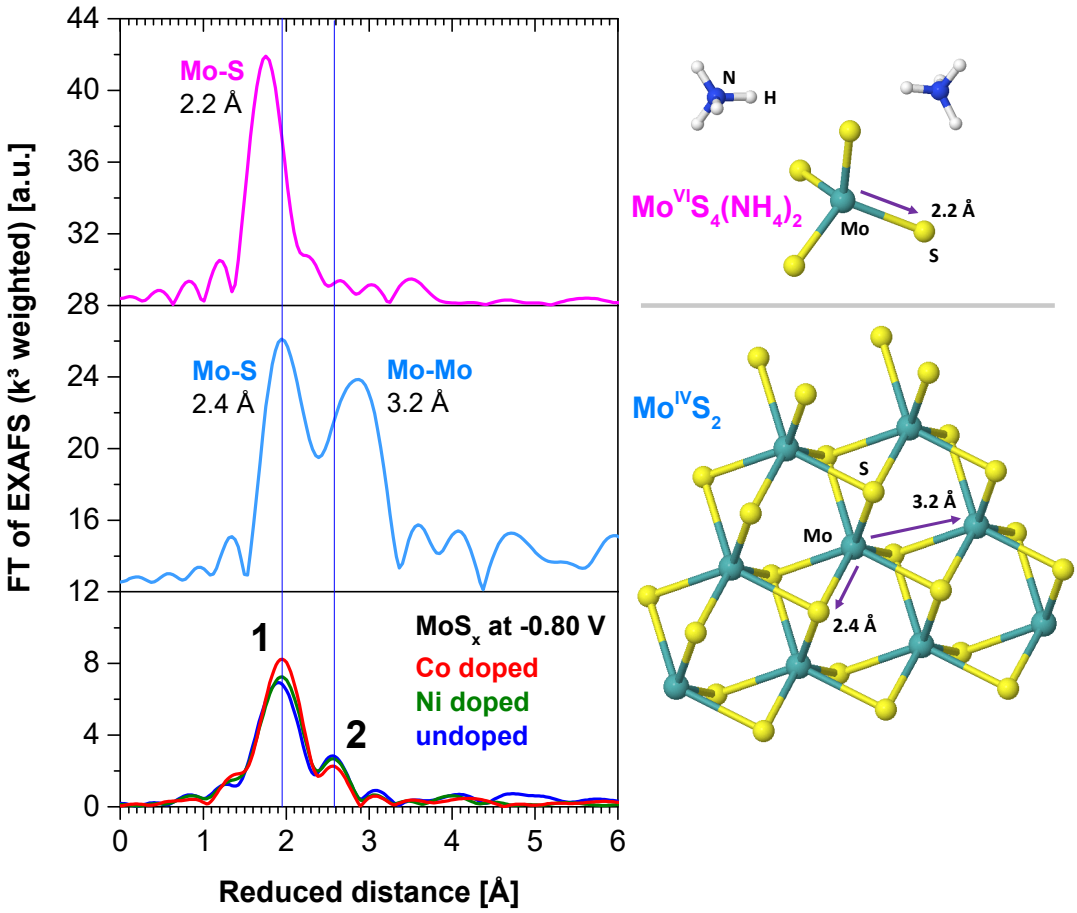

Figure 15

Left side: Fourier transforms of k^3 weighted EXAFS spectra (k range = 3 - 12 Å^{-1}) recorded at the Mo *K*-edge: Co doped (**red** line), Ni doped (**green** line) and undoped (**dark blue** line) MoS_x *Merki* electrodes at -0.80 V *vs.* NHE compared to $Mo^{IV}S_2$ (**light blue** line) and $Mo^{VI}S_4(NH_4)_2$ (**magenta** line). The main peaks of MoS_2 and $MoS_4(NH_4)_2$ are labelled with the corresponding Mo-S and Mo-Mo distances. For this comparison, the -0.80 V *Merki* electrodes are representative for the not shown electrodes at -0.35 V (similar spectra). **Right** side: Schematic structures of $Mo^{IV}S_2$ (layered structure, top view on single layer) and $Mo^{VI}S_4(NH_4)_2$. Characteristic Mo-S and Mo-Mo distances are indicated. The images are based on crystal data published for MoS_2 (Dickinson and Pauling 1923) and for $MoS_4(NH_4)_2$ (Hill, Lerner et al. 2010).

sphere. A possible six fold S coordination of the Mo sites as in crystalline $Mo^{IV}S_2$ is not favoured by the simulations but cannot be excluded. Analogue EXAFS simulations with a S coordination number of six exhibit an increase in R_f-factor by 20 – 50 % (= degradation of simulation quality) but the simulation quality is still reasonable with an R_f-factor below 20 % (see **Table 2**). The doped electrodes show a smaller increase in R_f-factor by 1.5 – 3.3 than the undoped electrodes with 4.7 – 5.1 (see **Table 2**), suggesting a higher likelihood for a six fold S coordination in the doped electrodes. For all electrodes,

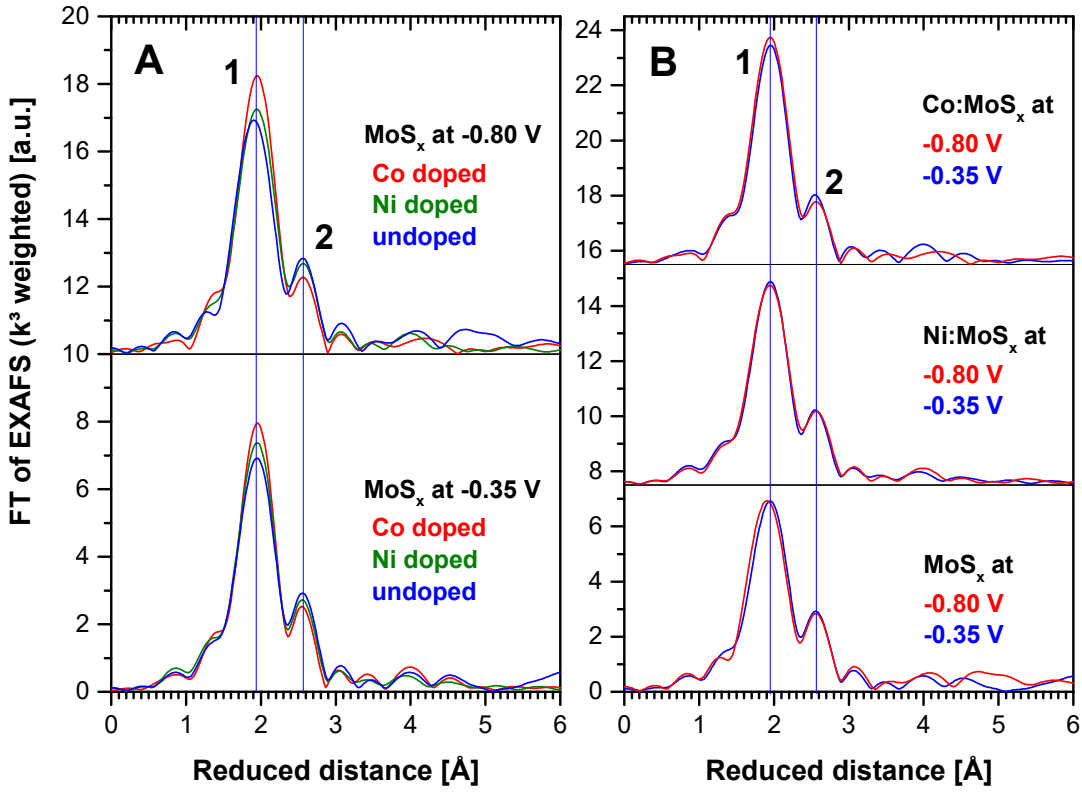

Figure 16

Fourier transforms of k^3 weighted EXAFS spectra (k range = 3 - 12 Å^{-1}) recorded at the Mo *K*-edge. In **A**: Co doped (**red** line), Ni doped (**green** line) and undoped (**blue** line) MoS_x *Merki* electrodes at -0.80 V *vs.* NHE (**top**) and at -0.35 V (**bottom**). In **B**: Co doped (**top**), Ni doped (**middle**) and undoped (**bottom**) MoS_x *Merki* electrode at -0.80 V *vs.* NHE (**red** line) compared to the same electrode at -0.35 V (**blue** line). In **A** and **B**, the main peaks of the *Merki* electrodes are labelled with **1** and **2** and can be assigned to a Mo-S and a Mo-Mo coordination, respectively.

the simulated Debye-Waller parameters for a possible six-fold S coordination are larger than for a fivefold coordination (see **Table 2**), suggesting a higher spatial disorder for the S_6 shell.

The alteration in electrode potential from -0.35 V to -0.80 V does not significantly affect peak **1** (see **Figure 16B**). The doping of the electrodes, however, seems to have an effect on the amplitude of peak **1**. At both electrode potentials (-0.35 V and -0.80 V), the Co doped electrode exhibits the largest amplitude, followed by the Ni doped and then the undoped electrode (see **Figure 16A**). The EXAFS simulations in **Table 4** reflect that and exhibit slightly larger S coordination numbers for the doped electrodes, in particular with Co, than for the undoped electrodes. However, the increase in amplitude of peak **1** is small, showing a maximal difference of only 10 % between peak **1** of the Co doped and the undoped electrode at -0.80 V. This suggests that the doping does not affect the number of five S ligands per Mo site but decreases the spatial disorder of the S shell in the doped electrodes. This interpretation

Mo-S coordination		$N_S \approx 5$		$N_S = 6$	
		R_f [%]	σ_S x 10^3 [Å^2]	R_f [%]	σ_S x 10^3 [Å^2]
MoS_x	**-0.80 V**	13.9	13	18.6	18
MoS_x:Ni	**-0.80 V**	9.2	14	12.5	17
MoS_x:Co	**-0.80 V**	8.1	12	9.6	14
MoS_x	**-0.35 V**	10.3	14	15.4	18
MoS_x:Ni	**-0.35 V**	11.0	14	13.6	17
MoS_x:Co	**-0.35 V**	10.3	12	12.5	16

Table 2

Quality of EXAFS simulations (= filtered R-factor, R_f) for the Mo sites in the *Merki* electrodes in dependence of the simulated mean S coordination number, N_S. Additionally, the simulated Debye-Waller parameters, σ_S, of the Mo-S coordination are listed. **Middle** column: mean S coordination number close to five, $N_S \approx 5$. The complete details of the EXAFS simulations are shown in **Table 3** and **Table 4. Right** column**:** analogue EXAFS simulations but mean S coordination number fixed at six, $N_S = 6$. R_f was determined over a R-range of 1 – 3 Å.

is possible due to the direct correlation in the EXAFS between the coordination number of a ligand shell and its Debye-Waller factor (= measure for the spatial disorder).

The high spatial disorder of the Mo-S coordination in the *Merki* electrodes, in comparison to crystalline MoS_2, suggests that the S shells of their Mo sites contain a significant number of coordinatively unsaturated S sites. Furthermore, the Mo sites exhibit a mean S coordination number that is presumably lower than in crystalline MoS_2, suggesting that coordinatively unsaturated Mo sites are present as well. The presence of these unsaturated sites in the electrodes was already proposed by *Merki et al*. (Merki, Vrubel et al. 2012). The doping of the electrodes with Co or Ni slightly increases the mean S coordination number of the Mo sites and/or decreases the spatial disorder of their S shells. Hence, the doping seems to have a slight impeding effect on the formation of unsaturated S and Mo sites in the electrodes.

The Mo sites in the electrodes do not possess O, N or C ligands (or CN^- and CO ligands) to a significant extent. In the Mo EXAFS, prominent peaks of correspondingly short Mo-ligand distances (shorter than the distance of peak **1**) are not visible (see **Figure 16**). The left shoulder of peak **1** is part of the side lobes of the Mo-S peak as shown by the EXAFS simulations (see **Figure 17** and **Figure 18**).

		mean **Mo-ligand distance** [Å]			
		S	**Mo**		EXAFS
MoS_x	**-0.80 V**	2.37 ± 0.01	2.81 ± 0.01		
MoS_x:Ni	**-0.80 V**	2.37 ± 0.01	2.81 ± 0.01		
MoS_x:Co	**-0.80 V**	2.38 ± 0.01	2.81 ± 0.01		
MoS_x	**-0.35 V**	2.38 ± 0.01	2.80 ± 0.01		
MoS_x:Ni	**-0.35 V**	2.38 ± 0.01	2.79 ± 0.01		
MoS_x:Co	**-0.35 V**	2.38 ± 0.01	2.79 ± 0.01		
References[a)]		**S**	**Mo**		XRD
$Mo^{IV}S_2$		2.35 – 2.41	3.14 – 3.16		
$Mo^{VI}S_4(NH_4)_2$		2.17 – 2.18			
Amorphous MoS_3[b)]		**S**	**Mo**		EXAFS
MoS_3, *min - max*		2.41 – 2.44	2.75 – 2.78		
Cubane structure[a)]		**S**	**Mo**	**Ni**	XRD
$[Mo_3S_4(H_2O)_9]^{4+}$		2.28 – 2.34	2.73 – 2.74		
$[Mo_3NiS_4(H_2O)_{10}]^{4+}$ $[Mo_3NiS_4Cl(H_2O)_9]^{3+}$		2.30 – 2.35	2.74 – 2.80	2.63 – 2.67	

Table 3

Mo-ligand distances of the S shell and Mo coordination in the MoS_x *Merki* electrodes during catalytic H_2 formation (-0.80 V *vs.* NHE) and in the non-catalytic state (-0.35 V). Denoted as references are the crystal structures[a)] of MoS_2, $MoS_4(NH_4)_2$, $[Mo_3S_4(H_2O)_9]^{4+}$, $[Mo_3NiS_4(H_2O)_{10}]^{4+}$ and $[Mo_3NiS_4Cl(H_2O)_9]^{3+}$; and the structural parameters[b)] of various amorphous MoS_3. For the *Merki* electrodes, the structural parameters were obtained from fitting their Mo EXAFS spectra with S and Mo phase functions calculated from the crystal structure of MoS_2. The simulations of all electrodes were performed with the same Debye-Waller parameter for Mo ($2\sigma_{Mo}^2$ = 0.005 Å^2), the same energy offset (E_0 = 3.8 eV) and the same amplitude reduction factor (S_0^2 = 0.85). The values of σ_{Mo} and E_0 were determined from a previous simulation of the undoped electrode at -0.35 V and the value of S_0 from a simulation of MoS_2 with a fixed S coordination number of six. In all simulations, the coordination numbers of the ligands and the Mo-ligand distances were free to move. The Debye-Waller parameter of S was free as well and yielded, at -0.80 V and -0.35 V, $2\sigma_S^2$ = 0.012 Å^2 for the Co doped electrode and $2\sigma_S^2$ = 0.014 Å^2 for the Ni doped and undoped electrode. The simulated EXAFS spectra are presented in **Figure 17** and **Figure 18**.

a) Crystal structure data for MoS_2 was obtained from (Dickinson and Pauling 1923, Hassel 1925, Wyckoff 1963, Schonfeld, Huang et al. 1983), for $MoS_4(NH_4)_2$ from (Bélougne, Chezeau et al. 1976, Hill, Lerner et al. 2010), for $[Mo_3S_4(H_2O)_9]^{4+}$ from (Akashi, Shibahara et al. 1990, Taniguchi, Imamura et al. 1999), for $[Mo_3NiS_4(H_2O)_{10}]^{4+}$ from (Shibahara, Yamasaki et al. 1991) and for $[Mo_3NiS_4Cl(H_2O)_9]^{3+}$ from (Shibahara, Yamasaki et al. 1991, Taniguchi, Imamura et al. 1999).

b) The structural parameters of amorphous MoS_3 were extracted from EXAFS results reported in (Cramer, Liang et al. 1984, Scott, Jacobson et al. 1986, Hibble, Rice et al. 1995, Afanasiev and Bezverkhy 2002, Afanasiev, Jobic et al. 2009).

		mean **Coordination number**			
		S	**Mo**		EXAFS
MoS_x	**-0.80 V**	4.7 ± 0.5	0.9 ± 0.1		
MoS_x:Ni	**-0.80 V**	5.0 ± 0.4	1.0 ± 0.1		
MoS_x:Co	**-0.80 V**	5.3 ± 0.3	0.8 ± 0.1		
MoS_x	**-0.35 V**	4.7 ± 0.4	1.0 ± 0.1		
MoS_x:Ni	**-0.35 V**	5.1 ± 0.5	0.9 ± 0.1		
MoS_x:Co	**-0.35 V**	5.0 ± 0.4	0.7 ± 0.1		
References[a)]		**S**	**Mo**		XRD
$Mo^{IV}S_2$		6	6		
$Mo^{VI}S_4(NH_4)_2$		4			
Amorphous MoS_3[b)]		**S**	**Mo**		EXAFS
MoS_3, *min – max*		5.4 – 6.1	0.9 – 2.3		
Cubane structure[a)]		**S**	**Mo**	**Ni**	XRD
$[Mo_3S_4(H_2O)_9]^{4+}$		3	2		
$[Mo_3NiS_4(H_2O)_{10}]^{4+}$ $[Mo_3NiS_4Cl(H_2O)_9]^{3+}$		3	2	1	

Table 4

Coordination numbers of the S shell and Mo coordination in the MoS_x *Merki* electrodes during catalytic H_2 formation (-0.80 V *vs.* NHE) and in the non-catalytic state (-0.35 V). Denoted as references are the crystal structures[a)] of MoS_2, $MoS_4(NH_4)_2$, $[Mo_3S_4(H_2O)_9]^{4+}$, $[Mo_3NiS_4(H_2O)_{10}]^{4+}$ and $[Mo_3NiS_4Cl(H_2O)_9]^{3+}$; and the structural parameters[b)] of various amorphous MoS_3. For the *Merki* electrodes, the structural parameters were obtained from fitting their Mo EXAFS spectra with S and Mo phase functions calculated from the crystal structure of MoS_2. The simulations of all electrodes were performed with the same Debye-Waller parameter for Mo ($2\sigma_{Mo}^2$ = 0.005 Å^2), the same energy offset (E_0 = 3.8 eV) and the same amplitude reduction factor (S_0^2 = 0.85). The values of σ_{Mo} and E_0 were determined from a previous simulation of the undoped electrode at -0.35 V and the value of S_0 from a simulation of MoS_2 with a fixed S coordination number of six. In all simulations, the coordination numbers of the ligands and the Mo-ligand distances were free to move. The Debye-Waller parameter of S was free as well and yielded, at -0.80 V and -0.35 V, $2\sigma_S^2$ = 0.012 Å^2 for the Co doped electrode and $2\sigma_S^2$ = 0.014 Å^2 for the Ni doped and undoped electrode. The simulated EXAFS spectra are presented in **Figure 17** and **Figure 18**.

a) Crystal structure data for MoS_2 was obtained from (Dickinson and Pauling 1923, Hassel 1925, Wyckoff 1963, Schonfeld, Huang et al. 1983), for $MoS_4(NH_4)_2$ from (Belougne, Chezeau et al. 1976, Hill, Lerner et al. 2010), for $[Mo_3S_4(H_2O)_9]^{4+}$ from (Akashi, Shibahara et al. 1990, Taniguchi, Imamura et al. 1999), for $[Mo_3NiS_4(H_2O)_{10}]^{4+}$ from (Shibahara, Yamasaki et al. 1991) and for $[Mo_3NiS_4Cl(H_2O)_9]^{3+}$ from (Shibahara, Yamasaki et al. 1991, Taniguchi, Imamura et al. 1999).

b) The structural parameters of amorphous MoS_3 were extracted from EXAFS results reported in (Cramer, Liang et al. 1984, Scott, Jacobson et al. 1986, Hibble, Rice et al. 1995, Afanasiev and Bezverkhy 2002, Afanasiev, Jobic et al. 2009).

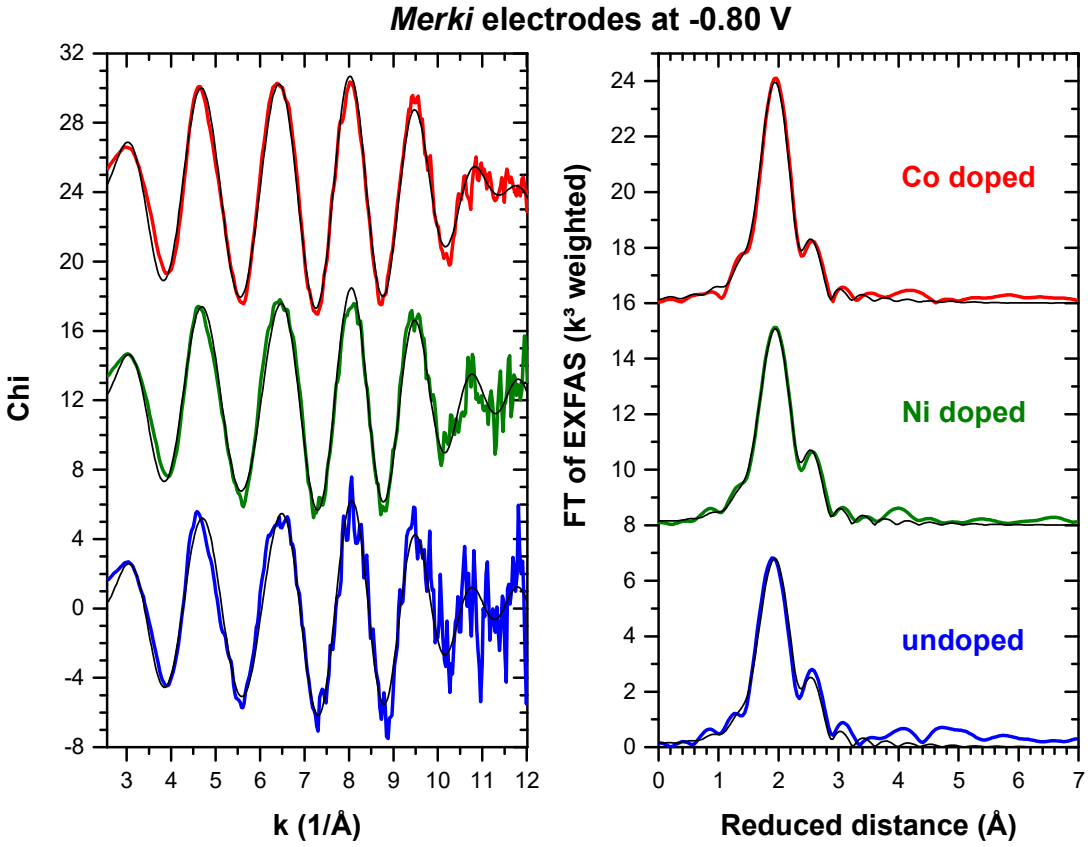

Figure 17

EXAFS simulations (**black** line) of the experimental spectra of the undoped (**blue** line), Ni doped (**green** line) and Co doped (**red** line) *Merki* electrode at -0.80 V *vs.* NHE. **Left** side: the EXAFS represented as χ spectra. **Right** side: Fourier transforms of the k^3 weighted EXAFS spectra. The EXAFS simulations and Fourier transforms were performed over the *k* range shown on the left side. The EXAFS simulations correspond to the structural parameters presented in **Table 3** and **Table 4**.

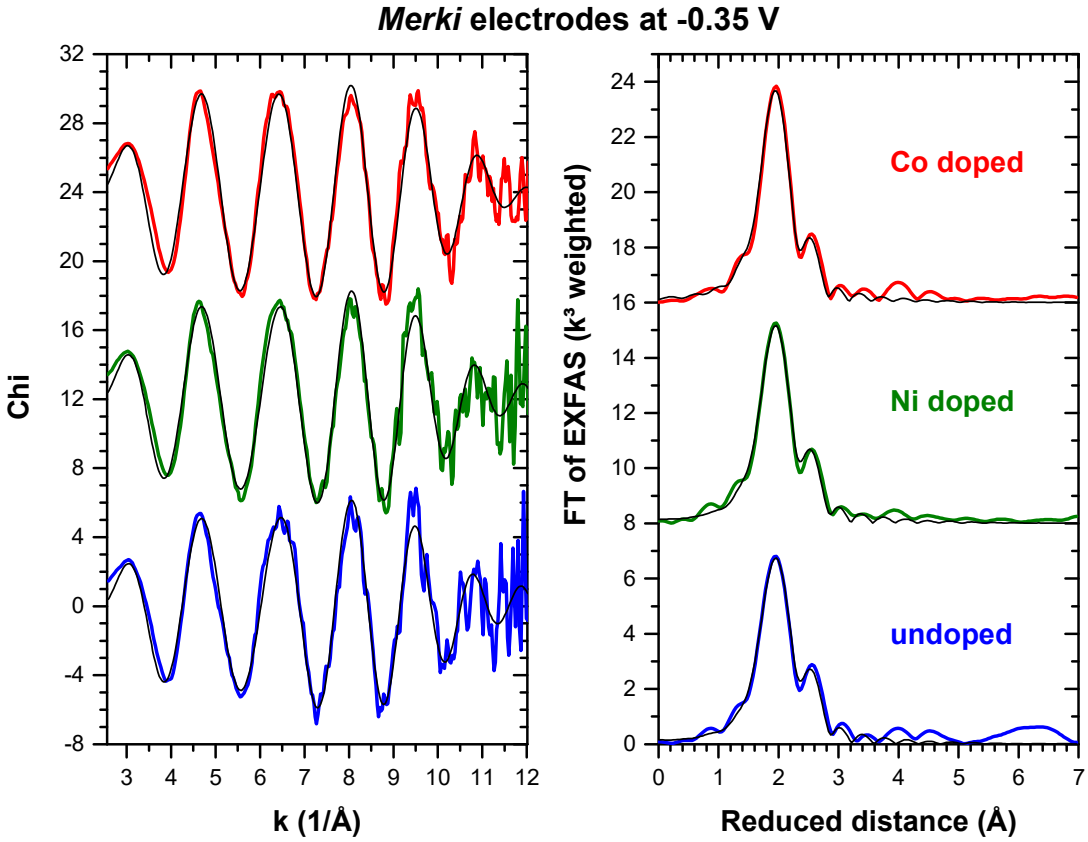

Figure 18

EXAFS simulations (**black** line) of the experimental spectra of the undoped (**blue** line), Ni doped (**green** line) and Co doped (**red** line) *Merki* electrode at -0.35 V *vs.* NHE. **Left** side: the EXAFS represented as χ spectra. **Right** side: Fourier transforms of the k^3 weighted EXAFS spectra. The EXAFS simulations and Fourier transforms were performed over the *k* range shown on the left side. The EXAFS simulations correspond to the structural parameters presented in **Table 3** and **Table 4**.

Mo-METAL COORDINATION

The Mo sites in the *Merki* electrodes exhibit, besides the $Mo^{IV}S_2$-like Mo-S coordination, also structural features that can be assigned to amorphous $Mo^{V}S_3$.

The Mo EXAFS of the electrodes contain, besides the peak for the Mo-S coordination, a second prominent peak (marked as **2** in **Figure 15**)**.** A comparison with EXAFS studies of amorphous MoS_3 from (Cramer, Liang et al. 1984, Scott, Jacobson et al. 1986, Hibble, Rice et al. 1995, Afanasiev and Bezverkhy 2002, Afanasiev, Jobic et al. 2009, Tang, Grauer et al. 2011) suggests that peak **2** can be assigned to a Mo-Mo coordination that can be found in the Mo_2S_9 building blocks of MoS_3 (see structural scheme in **Figure 12**). EXAFS simulations of peak **2** (see **Figure 17** and **Figure 18**) support this assignment to a MoS_3-like Mo-Mo coordination. For all electrodes, the simulations indicate a Mo-Mo distance of 2.79 – 2.81 Å that is close to the distance in MoS_3 of 2.75 – 2.78 Å (see **Table 3**). The simulated Mo coordination number of 0.7 – 1.0 suggests that the majority of the Mo sites in the electrodes is coordinated to a neighbouring site. This is also similar to MoS_3 which shows Mo coordination numbers in the range of 0.9 - 2.3 (see **Table 4**). Compared to MoS_2, the Mo-Mo coordination of the electrodes is too short (3.2 Å Mo-Mo distance in MoS_2, see **Table 3**) and its coordination number too low (six Mo ligands in MoS_2, see **Table 4**).

In **Figure 16A**, peak **2** of the electrodes exhibits small variations in amplitude that suggest a doping effect. At both electrode potentials, the Co doped electrode shows the smallest amplitude, followed by the Ni doped electrode and then the undoped electrode. EXAFS simulations of peak **2** also show, in tendency, a smaller Mo coordination number for the Co doped electrode than for the other electrodes (see **Table 4**). However, the difference of 0.1 – 0.2 between their Mo coordination numbers is small and suggests only a slightly weaker occurrence of the Mo-Mo coordination in the Co doped electrode or a Mo coordination that is a bit more spatially disordered. Considering the electrode potential, peak

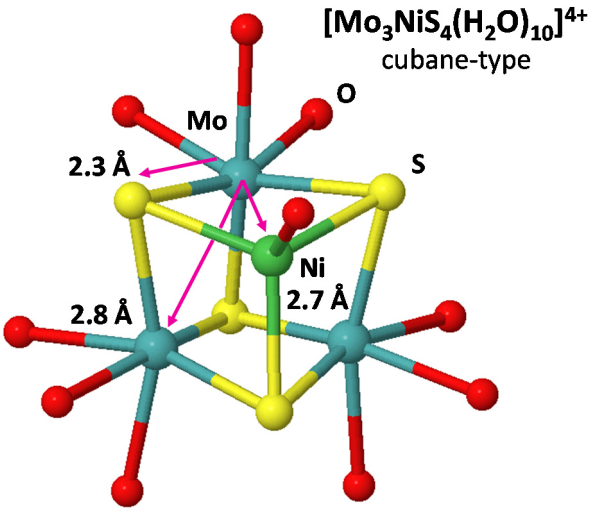

Figure 19

Schematic structure of the cubane-type $[Mo_3NiS_4(H_2O)_{10}]^{4+}$ cluster with denoted Mo-S, Mo-Mo and Mo-Ni distances. The image is based on crystal data published for $[Mo_3NiS_4(H_2O)_{10}]^{4+}$ in (Shibahara, Yamasaki et al. 1991).

2 does not show significant differences between the -0.80 V and -0.35 V electrodes, except for the Co doped electrode (see **Figure 16B**). There, the amplitude of peak **2** decreases at -0.80 V but EXAFS simulations do not suggest a significant modification in the Mo coordination number (see **Table 4**). The EXAFS simulations also show that the Mo-Mo distances of the electrodes are not significantly affected by the doping or the alteration in electrode potential (see **Table 3**). In conclusion, the Mo sites of all electrodes exhibit the same Mo-Mo coordination.

In contrast to MoS_2, the Mo EXAFS of the electrodes lack significant peaks at longer distances than 3 Å (see **Figure 15**). This indicates that the Mo sites in the electrodes do not possess a prominent long-range order as found in MoS_2. The atomic structure of the electrodes seems to be amorphous.

The Ni doped *Merki* electrodes could contain a Mo-Ni coordination as in the cubane-type complexes, $[Mo_3NiS_4(H_2O)_{10}]^{4+}$ (Shibahara, Yamasaki et al. 1991) and $[Mo_3NiS_4Cl(H_2O)_9]^{3+}$ (Shibahara, Yamasaki et al. 1991, Taniguchi, Imamura et al. 1999) (see **Figure 19**). The complexes possess a mixed S/O ligand environment with a shorter Mo-S coordination (Mo-S distance of 2.30 – 2.35 Å) than the electrodes but their Mo-Mo coordination is similar (Mo-Mo distance of 2.74 – 2.80 Å and two Mo ligands) (see **Table 3** and **Table 4**). The latter suggests that peak **2** in the EXAFS of the Ni doped electrode might contain a cubane-type Mo-Ni coordination with a distance of 2.63 – 2.67 Å that is obscured by the dominant Mo-Mo coordination. However, EXAFS simulations of peak **2** with a mixed Mo-Mo/Ni coordination cannot confirm that. For the Co doped electrode, analogue simulations support an obscured Mo-Co coordination neither. Aside from the cubane structure, other known Mo-Ni/Co distances are longer than 3 Å. The Ni or Co doped electrode do not exhibit prominent peaks at that distance (see **Figure 16B**), indicating the absence or a weak occurrence of Mo-Ni/Co coordinations. The latter is the case as shown in the sections *Co-metal coordination* and *Ni-metal coordination*.

SUMMARY

The Co doped, Ni doped and undoped MoS_x *Merki* electrodes (x = 2 or 3) (preparation as in (Merki, Vrubel et al. 2012)) were investigated with X-ray absorption spectroscopy (XAS) at the Mo *K*-edge to gain insight into the atomic structure of their Mo sites. Prior to the XAS measurements, the electrodes were conditioned (12 min, pH 7) and frozen either at -0.80 V or -0.35 V *vs.* normal hydrogen electrode (NHE), to study structural differences between Mo sites in a state of catalytic H_2 formation (-0.80 V) and in a non-catalytic state (-0.35 V) (standard electrode potential of hydrogen reduction E^0_{H2} = -0.41 V at pH 7).

The Mo sites of the electrodes (see **Figure 20**) consist of Mo^{IV} ions coordinated to presumably five S ligands in their first coordination sphere with a mean Mo-S distance of 2.37 – 2.38 Å typical for $Mo^{IV}S_2$ (see **Table 3** and **Table 4**). The change in electrode potential from -0.35 V to -0.80 V possibly leads to the reduction of a small fraction of Mo^{IV} ions to Mo^{III} (see **Figure 14A**) but does not affect the Mo-S coordination significantly. The fivefold S coordination of the Mo sites is favoured by the EXAFS simulations but a possible six fold S coordination as in $Mo^{IV}S_2$ cannot be excluded. Simulations with a S coordination number of six exhibit a 20 – 50 % higher R_f-factor (= degradation in simulation quality) but their simulation quality is still reasonable with a R_f-factor below 20 % (see **Table 2**). The high spatial disorder of the Mo-S coordination in the *Merki* electrodes (Debye-Waller factor of σ_S = ±0.08 Å) compared to crystalline MoS_2 (with σ_S = ±0.03 Å) suggests that the S shells of their Mo sites contain a significant number of coordinatively unsaturated S sites. Furthermore, the Mo sites exhibit a mean S coordination number that is presumably lower than in crystalline MoS_2, suggesting that coordinatively unsaturated Mo sites are present as well. The presence of these unsaturated sites in the electrodes was already proposed by *Merki et al*. (Merki, Vrubel et al. 2012). The doping of the electrodes with Co or Ni slightly increases the mean S coordination number of the Mo sites by 0.3 – 0.6 (see **Table 4** and increase in S peak in **Figure 16A**) and/or decreases the spatial disorder of their S shells. Hence, the doping seems to have a slight impeding effect on the formation of unsaturated S and Mo sites in the electrodes.

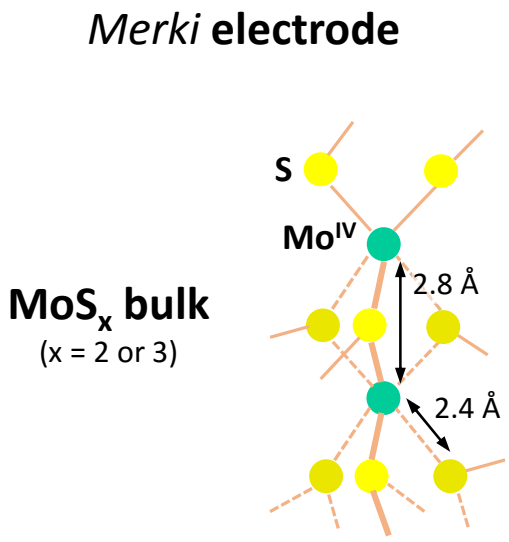

Figure 20

Schematic representation of a possible Mo-site structure in the undoped, Ni doped and Co doped *Merki* electrodes at -0.80 V and at -0.35 V *vs.* NHE.

The Mo sites in the electrodes do not exhibit O, N or C ligands (or CN^- and CO ligands) to a significant extent. The correspondingly short Mo-ligand distances are absent in the Mo EXAFS of the electrodes (see **Figure 16**).

The majority of the Mo sites in the *Merki* electrodes is coordinated to a neighbouring site with a mean Mo-Mo distance of 2.79 – 2.81 Å (see **Table 3**). The Mo_2S_9 building blocks of amorphous $Mo^{V}S_3$ (see

Figure 12) exhibit a similar Mo-Mo coordination (see **Table 3**). The doping of the electrodes or the alteration in electrode potential hardly affects the Mo-Mo coordination (see **Figure 16**). In the doped electrodes, the Mo sites might possess an additional Mo-Ni/Co coordination as in the cubane-type complexes, $[Mo_3NiS_4(H_2O)_{10}]^{4+}$ (Shibahara, Yamasaki et al. 1991) and $[Mo_3NiS_4Cl(H_2O)_9]^{3+}$ (Shibahara, Yamasaki et al. 1991, Taniguchi, Imamura et al. 1999) (see **Figure 19**), that is obscured in the Mo XAS by the dominant Mo-Mo coordination. Beyond the Mo-Mo coordination, the Mo sites of the electrodes do not exhibit a prominent long-range order in their atomic structure as in $Mo^{IV}S_2$ (see **Figure 15**).

The *Merki* electrodes were conditioned under a cathodic regime and, hence, are supposed to consist of amorphous $Mo^{IV}S_2$, according to *Merki et al.* (Merki, Fierro et al. 2011, Merki, Vrubel et al. 2012). The XAS analysis, however, indicates that Mo sites in the electrodes combine a $Mo^{IV}S_2$-like Mo-S coordination with a Mo-Mo coordination typical for amorphous $Mo^{V}S_3$. The atomic structure of the sites possibly builds up from Mo_2S_9 blocks as in MoS_3, based on the same Mo-Mo coordination, but with Mo^{IV} centres as in MoS_2. As suggested by *Merki et al.* (Merki, Fierro et al. 2011, Merki, Vrubel et al. 2012), the Mo sites seem to have only S^{2-} ligands as in MoS_2 (Mo-S distance of 2.4 Å) and no additional S_2^{2-} ligands as in MoS_3 (with a Mo-S distance of 2.6 Å (Hibble, Rice et al. 1995)).

Tang et al. reports a MoS_3 catalyst that after H_2 formation exhibits a diminished S coordination number of 3.1 – 4.1 and a shortened Mo-S distance of 2.35 – 2.36 Å (Tang, Grauer et al. 2011). The *Merki* electrodes in our study exhibit similar values (see **Table 3** and **Table 4**). *Tang et al.* suggests that the S_2^{2-} ligands of the original MoS_3 species are reduced and transformed into S-H ligands (Tang, Grauer et al. 2011). This may be also the case for some S ligands of the *Merki* electrodes.

Co SITE - ATOMIC STRUCTURE

RESULTS AND DISCUSSION

Co-S COORDINATION

X-ray absorption near-edge structure (XANES) and extended X-ray absorption fine-structure (EXAFS) of the Co doped MoS_x *Merki* electrodes (x = 2 or 3) were recorded at the Co *K*-edge to gain insight into the atomic structure of their Co sites. Prior to the XANES/EXAFS measurements, the electrodes were conditioned (12 min, pH 7) and frozen either at -0.80 V or -0.35 V *vs.* normal hydrogen electrode (NHE), to study structural differences between Co sites in a state of catalytic H_2 formation (-0.80 V) and in a non-catalytic state (-0.35 V) (standard electrode potential of hydrogen reduction E^0_{H2} = -0.41 V at pH 7).

The Co absorption edge in the XANES of the *Merki* electrodes (see **Figure 21**) shows a position close to the Co edge of the $Co^{II}S_2$ reference. This indicates that the mean oxidation state of the Co ions in the electrodes is close to II as in the reference. The quantitative edge positions of the electrodes (see **Table 5**) are slightly shifted to higher excitation energies than in $Co^{II}S_2$. The electrode at -0.35 V exhibits the largest shift with +1.5 eV. This indicates that the Co ions in the electrodes are more oxidized than in

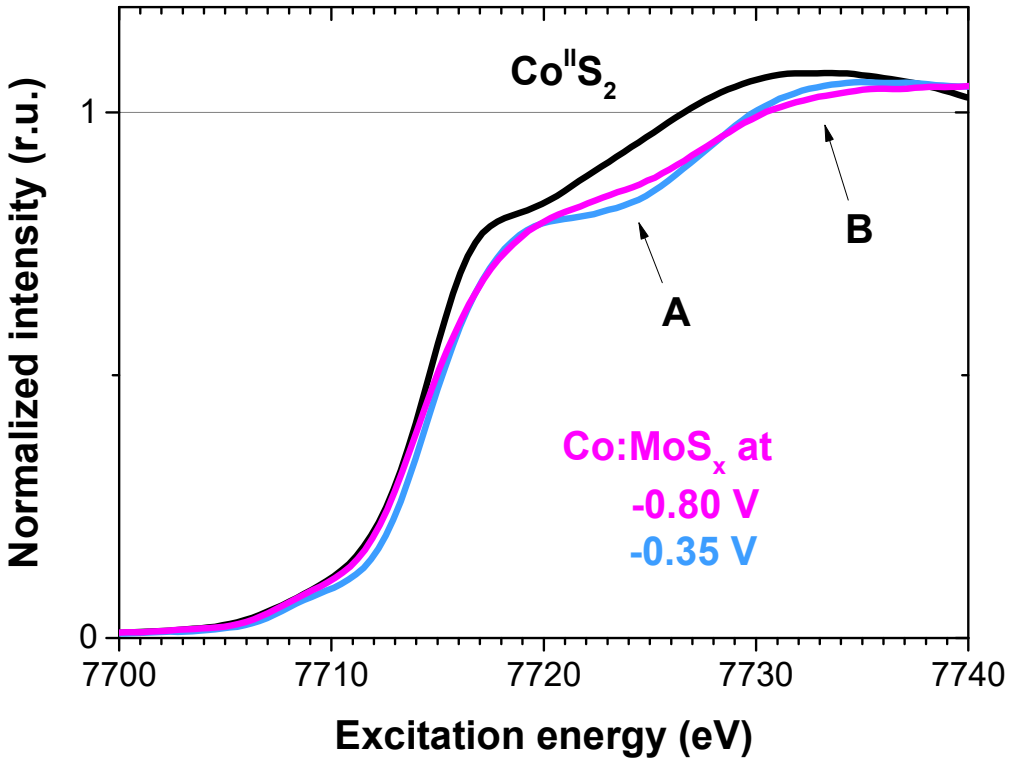

Figure 21

XANES spectra recorded at the Co *K*-edge of the Co doped MoS_x *Merki* electrode at -0.80 V *vs.* NHE (**magenta** line) and at -0.35 V (**blue** line) compared to $Co^{II}S_2$ (**black** line).

$Co^{II}S_2$ and, hence, their mean oxidation state is a bit larger than II, in particular for the -0.35 V electrode. The more oxidized Co oxidation state in the -0.35 V electrode compared to the -0.80 V electrode is most likely an effect of the less reductive electrode potential. The XANES of the electrodes show a flattened absorption edge as CoS_2. This feature is typical for Co coordinated to S atoms in its first coordination sphere. The arrows **A** and **B** in **Figure 21** mark modifications of the electrode XANES that are possibly related to the different electrode potential as well, and could indicate structural differences in the S coordination sphere.

Co edge	**Edge position** [eV]	**Mean oxidation state**
$Co:MoS_x$ -0.80 V	7717.6	> 2
$Co:MoS_x$ -0.35 V	7717.9	> 2
$Co^{II}S_2$	7716.4	2

Table 5

Co *K*-edge positions of the Co doped *Merki* electrodes at -0.80 V and -0.35 V *vs.* NHE and their corresponding mean oxidation states for Co. The edge positions were determined with the integral method as described in (Dau, Liebisch et al. 2003) with an interval of integration from 0.15 to 1.0 of normalized fluorescence.

The Co EXAFS of the Co doped *Merki* electrodes, at both potentials, exhibit two prominent peaks, labelled as **1** and **2** in **Figure 22**. When compared to the spectrum of $Co^{II}S_2$ (see structure in **Figure 24**), peak **1** of the electrodes can be assigned to a Co-S coordination. Peak **2**, however, is difficult to assign but is possibly a Co-Mo or Co-Co coordination, see section *Co-metal coordination*. The low amplitude of peak **2** as well as the lack of peaks beyond 3 Å indicates that the Co-S species in the electrodes has no significant long-range order as in $Co^{II}S_2$.

In both electrodes, EXAFS simulations of peak **1** (see **Figure 23**) yield a mean S distance of 2.25 – 2.26 Å that is -0.07 Å shorter than in CoS_2 (see **Table 6**). The shortening of the distances could be due to the stronger oxidized Co ions in the electrodes. In the -0.35 V electrode, peak **1** exhibits an amplitude comparable to CoS_2, suggesting a S coordination number of six as in the reference. This is confirmed by EXAFS simulations yielding a coordination number of 6.2 (see **Table 6**). At -0.80 V, the amplitude of peak **1** significantly decreases by 25 %. EXAFS simulations indicate a lowering of the S coordination number to 5.3 (see **Table 6**). However, the subsidence of peak **1** is small and, hence, could be alternatively interpreted as an increase in the spatial disorder of the S_6-ligand shell. This is possible due to the direct correlation in the EXAFS between the coordination number of a ligand shell and its Debye-Waller factor (= measure for the spatial disorder). The observed differences in the XANES between the -0.35 V and -0.80 V electrode (see arrow **A** and **B** in **Figure 21**) could be related to the structural modifications in the S shell.

The electrodes exhibit a different Co-S coordination than CoS_2. Considering other Co-S compounds, the Co-S distance of the electrodes can be found in octahedral CoS_6 clusters of $Co^{II,\,III}{}_3S_4$ (no XAS spectrum recorded) (see structure in **Figure 24**). Co_3S_4 also possesses tetrahedral CoS_4 clusters with a S distance of 2.20 Å. This distance is close to the mean Co-S distance of the electrodes. Hence, it could be possible that the electrodes contain a mixture of $Co\text{-}S_4$ and $Co\text{-}S_6$ species. At -0.35 V, the mixture is dominated by the octahedral species, leading to a coordination number of S close to six. At -0.80 V, the tetrahedral species becomes more prominent and lowers the average S coordination number to five. The structural

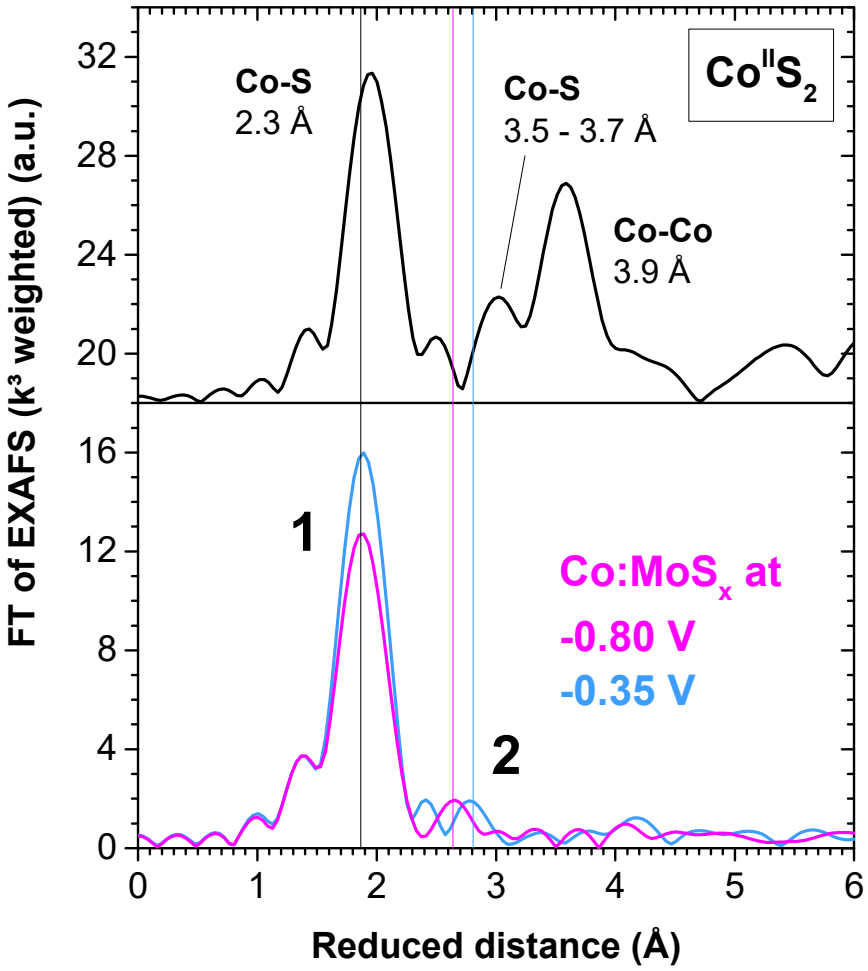

Figure 22

Fourier transforms of k^3 weighted EXAFS spectra (k range = 3 – 13 Å^{-1}) recorded at the Co *K*-edge: Co doped MoS_x *Merki* electrode at -0.80 V *vs.* NHE (**magenta** line) and at -0.35 V (**blue** line) compared to $Co^{II}S_2$ (**black** line). The main peaks of the latter are labelled with the corresponding Co-S and Co-Co distances.

similarities with $Co^{II,\,III}{}_3S_4$ suggest, in concordance with the XANES analysis, that the Co ions in the electrodes exhibit a mean oxidation state between II and III.

Another interpretation for the low S coordination number could be that the CoS_6 species in the -0.80 V electrode contains coordinatively unsaturated Co sites where one or two S ligands are missing. *Merki et al.* already suggested the presence of coordinatively unsaturated Mo and S sites in the electrodes (Merki, Vrubel et al. 2012). The unsaturated Co sites mainly occur in the -0.80 V electrode and, hence, could be produced by the catalytic reaction, as proposed in (Miller, Marschall et al. 2001).

The Co sites in the electrodes do not possess O, N or C ligands (or CN^- and CO ligands) to a significant extent. In the Co EXAFS, prominent peaks of correspondingly short Co-ligand distances (shorter than the distance of peak **1**) are not visible (see **Figure 22**). The left shoulder of peak **1** is part of the side lobes of the Co-S peak as shown by the EXAFS simulations (see **Figure 23**).

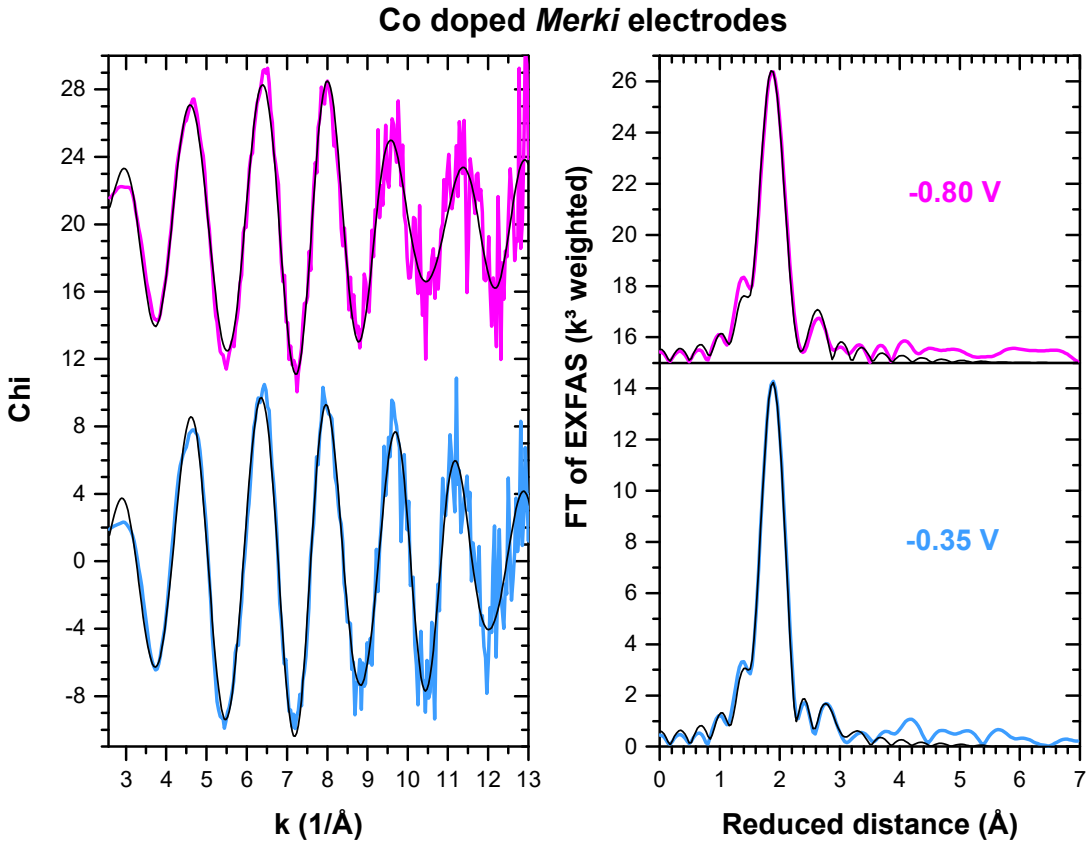

Figure 23

EXAFS simulations (**black** line) of the experimental spectra of the Co doped Merki electrode at -0.80 V *vs.* NHE (**magenta** line) and -0.35 V (**blue** line). **Left** side: the EXAFS represented as k^3 weighted χ spectra. **Right** side: Fourier transforms of the k^3 weighted EXAFS spectra. The EXAFS simulations and Fourier transforms were performed over the *k* range shown on the left side. The EXAFS simulations correspond to the structural parameters presented in **Table 6**.

mean **Co-ligand distance**				
Co edge	**Co-S** [Å]		**Co-Mo** [Å]	EXAFS
Co:MoS_x -0.80 V	2.25 ± 0.01		2.72 ± 0.01	
Co:MoS_x -0.35 V	2.26 ± 0.01		3.19 ± 0.01	
References[a)]				
$Co^{I,II}{}_9S_8$	2.15	2.48	-	XRD
$Co^{II}S$	2.33 – 2.34		-	
$Co^{II}S_2$	2.33 – 2.36		-	
$Co^{II,III}{}_3S_4$	2.04 – 2.20	2.26 – 2.35	-	
Co-Mo-S phase[b)]	2.18 – 2.26		2.75 – 2.82	EXAFS
mean **Coordination number**				
Co edge	**Co-S**		**Co-Mo**	EXFAS
Co:MoS_x -0.80 V	5.3 ± 0.3		0.9 ± 0.1	
Co:MoS_x -0.35 V	6.2 ± 0.3		0.9 ± 0.2	
References[a)]				
$Co^{I,II}{}_9S_8$	4	6	-	XRD
$Co^{II}S$	6		-	
$Co^{II}S_2$	6		-	
$Co^{II,III}{}_3S_4$	4	6	-	
Co-Mo-S phase[b)]	4.0 – 6.2		0.5 – 2.0	EXAFS

Table 6

Structural parameters of the Co ligand environment in the Co doped *Merki* electrodes at -0.80 V and -0.35 V *vs.* NHE, compared to the crystal structures[a)] of Co_9S_8, CoS, CoS_2, Co_3S_4 and the Co-Mo-S phase[b)] of various $CoMoS_2$ catalyst for hydrodesulphurization. For the *Merki* electrodes, the structural parameters were obtained from fitting their Co EXAFS spectra with S and Mo phase functions calculated from the crystal structure[a)] of CoS and $CoMoO_4$. The simulations of both electrodes were performed with the same Debye-Waller parameter for Mo ($2\sigma_{Mo}^2$ = 0.009 Å^2), the same energy offset (E_0 = 3.9 eV) and the same amplitude reduction factor (S_0^2 = 0.70). The values of σ_{Mo} and E_0 were determined from a previous simulation of the -0.35 V electrode with a fixed Mo coordination number of one. The value of S_0 was established in (Risch, Khare et al. 2009). In all simulations, the coordination numbers of the ligands and the Co-ligand distances were free to move. The Debye-Waller parameter of S was free as well and yielded $2\sigma_S^2$ = 0.009 Å^2 for the -0.80 V electrode and 0.008 Å^2 at -0.35 V. The simulated EXAFS spectra are presented in **Figure 23**.

a) Crystal structure data for Co_9S_8 was obtained from (Lindqvist 1936), for CoS from (Alsen 1925, Wyckoff 1963), for CoS_2 from (Wyckoff 1931, Nowack, Schwarzenbach et al. 1989, Nowack, Schwarzenbach et al. 1991), for Co_3S_4 from (Lundqvist 1938, Brown 1973) and for Co:MoO_4 from (Smith and Ibers 1965).

b) The structural parameters of the Co-Mo-S phase of various $CoMoS_2$ catalyst for hydrodesulphurization were extracted from EXAFS results reported in (Bouwens, van Veen et al. 1991, Craje, Louwers et al. 1992, Eijsbouts 1997, de Bont, Vissenberg et al. 1998, Miller, Marschall et al. 2001, Kadono, Kubota et al. 2006, Okamoto, Kato et al. 2009, Dugulan, van Veen et al. 2013).

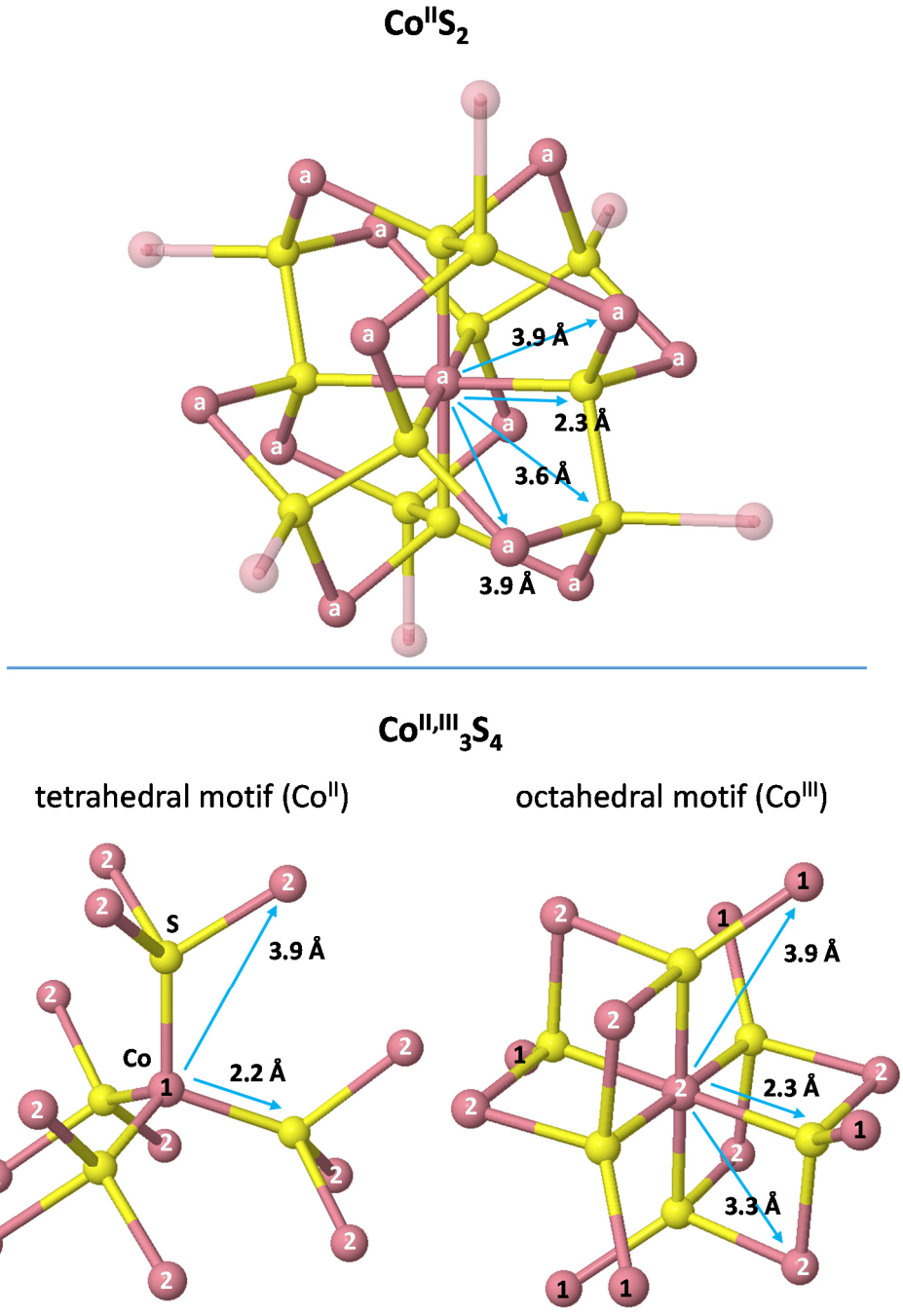

Figure 24

Schematic structures of the Co ligand environment in bulk $Co^{II}S_2$ and $Co^{II,III}{}_3S_4$ with denoted Co-S and Co-Co distances. Co atoms with a ligand environment of the same atomic structure are labelled with the same letter ("a") or number ("1" or "2"). The images are based on crystal data published for CoS_2 in (Nowack, Schwarzenbach et al. 1989) and for Co_3S_4 in (Lundqvist 1938).

Co-Mo-S PHASE

In the Co doped *Merki* electrodes, the structural incorporation of the Co-S species into the amorphous MoS_x (x = 2 or 3) bulk could form a "Co-Mo-S" phase (structure) similar to the phase known from various $CoMoS_2$ catalysts for hydrodesulphurization (a selection of XAS studies for these catalysts can be found in (Bouwens, van Veen et al. 1991, Craje, Louwers et al. 1992, de Bont, Vissenberg et al. 1998, Miller, Marschall et al. 2001, Kadono, Kubota et al. 2006, Okamoto, Kato et al. 2009, Dugulan, van Veen et al. 2013)). There, the Co-Mo-S phase consists of Co sulphide clusters located on the edge of small MoS_2 crystallites. The clusters contain Co ions coordinated to five or six S ligands. The Co ions can be connected via S bridges to the Mo of the crystallites or to neighbouring Co atoms in its cluster. According to (Okamoto, Kato et al. 2009, Dugulan, van Veen et al. 2013), it seems to be generally accepted that the Co-Mo-S phase is the catalytic (or active) phase in the $CoMoS_2$ catalysts.

The Co-S coordination of the *Merki* electrodes exhibits S distances and coordination numbers that fall into the range of values reported for the Co-Mo-S phase of the $CoMoS_2$ catalysts (see **Table 6**). This suggests that the electrodes might possess a similar Co-Mo-S phase.

For the Co-Mo-S phase of the $CoMoS_2$ catalysts, (Miller, Marschall et al. 2001) proposes that the S ligands at the Co site have a shorter distance of 2.18 Å, when they are incorporated into a Co-(μ-S)$_2$-Mo bridge, and a longer distance of 2.26 Å, when they are terminal. However, these two distances are usually difficult to resolve in the EXAFS. The model of (Miller, Marschall et al. 2001) (see illustration in **Figure 25**) suggests a number of four bridging S ligands and one or two terminal ligands per Co site.

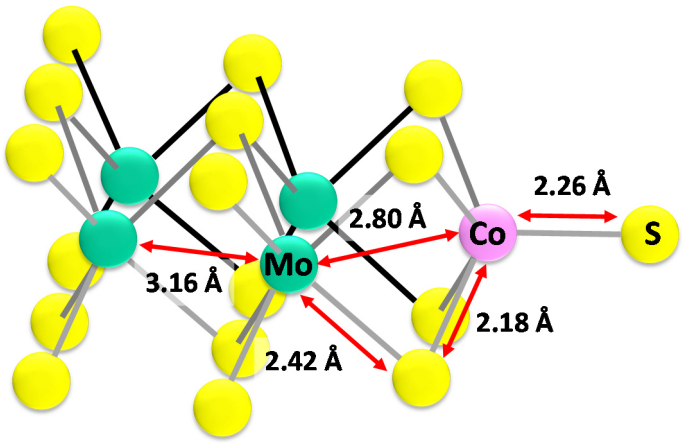

Figure 25

Atomic structure of the Co-Mo-S phase consisting of CoS_5 clusters at the edges of crystalline MoS_2 as proposed by (Miller, Marschall et al. 2001). The scheme is a modified reproduction from an illustration in (Miller, Marschall et al. 2001).

In **Table 7**, the *Merki* electrodes are simulated with two S shells at the Co site, one for the bridging S ligands and one for the terminal ligands. The yielded distances of 2.21 – 2.22 Å and 2.27 – 2.30 Å, respectively, are similar to the proposed distances of (Miller, Marschall et al. 2001). The simulated number of bridging ligands, however, is with 1.8 – 2.9 lower than in the model of (Miller, Marschall et al. 2001). The mean Co-S distance of the electrodes matches the one of the terminal ligands and, hence, underlines their higher abundance. Therefore, it seems that, in the electrodes, the connection between the Co-S clusters and the MoS_x bulk is more loose than in the Co-Mo-S phase of the $CoMoS_2$ catalysts. A reason for this difference and others could be that the Co-Mo-S phases in the literature were characterized on crystalline MoS_2 whereas the electrodes consist of amorphous MoS_x that exhibits a very different long-range structure.

mean **Co-ligand distance**				
Co edge	**Co-S** [Å]		**Co-Mo** [Å]	EXAFS
	bridging	terminal		
Co:MoS_x -0.80 V	2.22 ± 0.01	2.27 ± 0.01	2.72 ± 0.01	
Co:MoS_x -0.35 V	2.21 ± 0.01	2.30 ± 0.01	3.19 ± 0.01	
Co-Mo-S phase	bridging	terminal		EXAFS
model of (Miller, Marschall et al. 2001)	2.18	2.26	2.80	
mean **Coordination number**				
Co edge	**Co-S**		**Co-Mo**	EXAFS
	bridging	terminal		
Co:MoS_x -0.80 V	1.8 ± 0.5	3.5 ± 0.4	1.0 ± 0.3	
Co:MoS_x -0.35 V	2.9 ± 0.5	3.1 ± 0.4	0.9 ± 0.3	
Co-Mo-S phase	bridging	terminal		EXAFS
model of (Miller, Marschall et al. 2001)	4	1 - 2	2	

Table 7

Structural parameters of the Co ligand environment in the Co doped *Merki* electrodes at -0.80 V and -0.35 V *vs.* NHE, compared to the Co-Mo-S phase of a $CoMoS_2$ catalyst for hydrotreating, published in (Miller, Marschall et al. 2001) (atomic model shown in **Figure 25**). For the *Merki* electrodes, the structural parameters were obtained from fitting their Co EXAFS spectra with S and Mo phase functions calculated from the crystal structure of CoS (Alsen 1925, Wyckoff 1963) and $CoMoO_4$ (Smith and Ibers 1965). The simulations of both electrodes were performed with the same Debye-Waller parameter for Mo ($2\sigma_{Mo}^2$ = 0.010 Å^2), the same energy offset (E_0 = 3.6 eV) and the same amplitude reduction factor (S_0^2 = 0.70). The values of σ_{Mo} and E_0 were determined from a previous simulation of the -0.35 V electrode with a fixed Mo coordination number of one. The value of S_0 was established in (Risch, Khare et al. 2009). In all simulations, the coordination numbers of the ligands and the Ni-ligand distances were free to move. The Debye-Waller parameter of S was free as well but restrained to be the same for the bridging and terminal S ligands. For the -0.80 V electrode the yielded parameter was $2\sigma_S^2$ = 0.008 Å^2 and, for the -0.35 V electrode, $2\sigma_S^2$ = 0.002 Å^2.

The EXAFS simulation of the Co-S coordination in the electrodes with two S hells instead of one does not significantly improve the simulation quality (= R_f-factor decreases only by 5 % over R range = 1 – 3 Å). This suggests that the actual Co-S coordination in the electrodes consists most likely of one S shell.

Co-METAL COORDINATION

Peak **2** in the Co EXAFS of the Co doped *Merki* electrodes (see **Figure 22**) is difficult to assign via the reference spectrum of CoS_2. However, if the electrodes possess a similar Co-Mo-S phase as observed in various $CoMoS_2$ catalysts for hydrodesulphurization (see previous section), then peak **2** might represent Mo atoms in the Co-$(\mu\text{-}S)_2$-Mo bridges between Co-S cluster and MoS_x bulk, or neighbouring Co atoms within the Co-S cluster.

Under the assumption of a Co-Mo coordination, the EXAFS simulations (see **Figure 23**) yield a Co-Mo distance of 2.72 Å at -0.80 V and a longer distance of 3.19 Å at -0.35 V (see **Table 6**). The coordination number of Mo can be simulated with a value close to one for both potentials, suggesting that the majority of the Co sites in the electrodes possesses a coordination to a Mo atom. The short Co-Mo distance at -0.80 V is similar (Δ = -0.03 Å) to the 2.75 – 2.82 Å of the Co-$(\mu\text{-}S)_2$-Mo bridge in the Co-Mo-S phase of hydrodesulphurization catalysts (see **Table 6**). The longer Co-Mo distance at -0.35 V can be found in Co-$(\mu^4\text{-}O)_2$-Mo bridges of $CoMoO_4$. This might indicate for the -0.35 V electrode the presence of Co-S-Mo bridges similar to the O bridges of $CoMoO_4$.

If the Co-Mo coordination is substituted by a Co-Co coordination, then the simulations yield a Co-Co distance of 2.89 Å at -0.80 V and a longer distance of 3.34 Å at -0.35 V (see **Table 8**). The coordination number of the Co-Co coordination can be simulated with a value close to one as well, suggesting that the majority of the Co sites in the electrodes exhibit a coordination to a neighbouring Co site. The Co-Co distances of the electrodes are unusual, as they cannot be found in the crystalline Co-S references: Co_9S_8, CoS, CoS_2 and Co_3S_4. However, the Co-Mo-S phase of hydrodesulphurization catalysts contains Co-S clusters that can exhibit Co-Co distances similar to the ones simulated for the electrodes (see **Table 8**).

The shorter Co-Mo/Co distance of the -0.80 V electrode in comparison to the -0.35 V electrode could be due to the smaller number of S ligands at the Co sites, which diminishes the effective dimensions of the sites and enables them to get closer to the MoS_x bulk (shorter Co-Mo distance) or to each other (shorter Co-Co distance).

It is complicated to decide whether a Co-Mo or a Co-Co coordination is actual present in the electrodes. Corresponding data of the electrodes recorded at the Mo *K*-edge cannot help to differentiate. In the case of an existing Mo-Co coordination, only a very low coordination number of 0.3 for Co would be visible at the Mo edge, which is difficult to detect with EXAFS. This low coordination number arises from the small Co : Mo stoichiometry of 1 : 4 in the electrodes (as reported in (Merki, Vrubel et al. 2012) and indicated by our elemental analysis in **Table 12**). The EXAFS simulations, however, favour the existence of a Co-Mo coordination by yielding a significantly higher simulation quality (= decrease in R_f-factor by 30 – 40 % over *R* range = 1 – 3 Å) than for the Co-Co coordination. Furthermore, it is more reasonable to assume that the Co-Mo coordination exists, since Mo is more abundant in the electrodes than Co.

Alternative EXAFS simulations of peak **2** in the spectrum of the electrodes (see **Figure 22**) with other ligands like S or O yielded a significantly lower simulation quality and/or more unassignable distances than with Mo or Co.

mean **Absorber-ligand distance**			
Co edge	**Co-Co** [Å]		EXAFS
Co:MoS_x -0.80 V	2.89 ± 0.02		
Co:MoS_x -0.35 V	3.34 ± 0.02		
References[a)]			XRD
Co_9S_8	2.48	3.51	
CoS	2.58	3.37	
CoS_2	3.92 – 3.99		
Co_3S_4	3.32		
Co-Mo-S phase[b)]	2.53 – 2.60, 2.90, 3.13 – 3.35		EXAFS
mean **Coordination number**			
Co edge	**Co-Co**		EXAFS
Co:MoS_x -0.80 V	0.9 ± 0.2		
Co:MoS_x -0.35 V	0.8 ± 0.3		
References[a)]			XRD
Co_9S_8	1.5	3	
CoS	2	6	
CoS_2	12		
Co_3S_4	3		

Table 8

Structural parameters of a possible Co-Co coordination in the Co doped *Merki* electrodes at -0.80 V and -0.35 V *vs.* NHE, compared to the first and second shortest Co-Co coordinations in Co_9S_8, CoS, CoS_2, Co_3S_4 and the Co-Mo-S phase of various $CoMoS_2$ catalysts for hydrodesulphurization. For the *Merki* electrodes, the structural parameters were obtained from fitting their Co EXAFS spectra with S and Co phase functions calculated from the crystal structure[a)] of CoS and $CoMoO_4$. The simulations of both electrodes were performed with the same Debye-Waller parameter for Co ($2\sigma_{Co}^2$ = 0.009 Å^2), the same energy offset (E_0 = 3.9 eV) and the same amplitude reduction factor (S_0^2 = 0.70). The values of σ_{Co} and E_0 were determined from a previous simulation of the -0.35 V electrode with a fixed Co coordination number of one. The value of S_0 was established in (Risch, Khare et al. 2009). In all simulations, the coordination numbers of the ligands and the Co-ligand distances were free to move.

a) Crystal structure data for Co_9S_8 was obtained from (Lindqvist 1936), for CoS from (Alsen 1925, Wyckoff 1963), for CoS_2 from (Wyckoff 1931, Nowack, Schwarzenbach et al. 1989, Nowack, Schwarzenbach et al. 1991), for Co_3S_4 from (Lundqvist 1938, Brown 1973) and for Co:MoO_4 from (Smith and Ibers 1965).

b) The structural parameters of the Co-Mo-S phase of various $CoMoS_2$ catalyst for hydrodesulphurization were extracted from EXAFS results reported in (Bouwens, van Veen et al. 1991, Craje, Louwers et al. 1992, Eijsbouts 1997, de Bont, Vissenberg et al. 1998, Miller, Marschall et al. 2001, Kadono, Kubota et al. 2006, Okamoto, Kato et al. 2009, Dugulan, van Veen et al. 2013).

SUMMARY

The Co doped MoS_x *Merki* electrodes (x = 2 or 3) (preparation as in (Merki, Vrubel et al. 2012)) were investigated with X-ray absorption spectroscopy (XAS) at the Co *K*-edge to gain insight into the atomic structure of their Co sites. Prior to the XAS measurements, the electrodes were conditioned (12 min, pH 7) and frozen either at -0.80 V or -0.35 V *vs.* normal hydrogen electrode (NHE), to study structural differences between Co sites in a state of catalytic H_2 formation (-0.80 V) and in a non-catalytic state (-0.35 V) (standard electrode potential of hydrogen reduction E^0_{H2} = -0.41 V at pH 7).

The Co sites in the electrodes (see **Figure 26**) consist of Co ions with a mean oxidation state between II and III. At -0.80 V, the oxidation state is more reduced than at -0.35 V, possibly an effect of the more reductive electrode potential (see **Table 5** and Co XANES of the electrodes in **Figure 21**). The Co ions are coordinated to S atoms in their first coordination sphere, presumably with a coordination number of five at -0.80 V and of six at -0.35 V (see **Table 6** and peak **1** in **Figure 22**). At both potentials, the mean Co-S distance is 2.25 – 2.26 Å (see **Table 6**) which can be found in octahedral CoS_6 species of $Co^{II, III}{}_3S_4$ (see **Figure 24**). This could be the main Co-S species in the electrodes. At -0.80 V, the tetrahedral form of Co_3S_4 might be present as well, indicated by a mean S coordination number lower than six. The low S coordination number could also indicate that, in the -0.80 V electrode, the CoS_6 species contains coordinatively unsaturated Co sites where one or two S ligands are missing. *Merki et al.* already suggests the presence of unsaturated Mo sites in the electrodes (Merki, Vrubel et al. 2012). The unsaturated Co sites mainly occur in the -0.80 V electrode and, hence, might be produced by the catalytic reaction, as proposed in (Miller, Marschall et al. 2001). However, the decrease in the S coordination number at -0.80 V is small and allows the alternative interpretation that the S shell retains

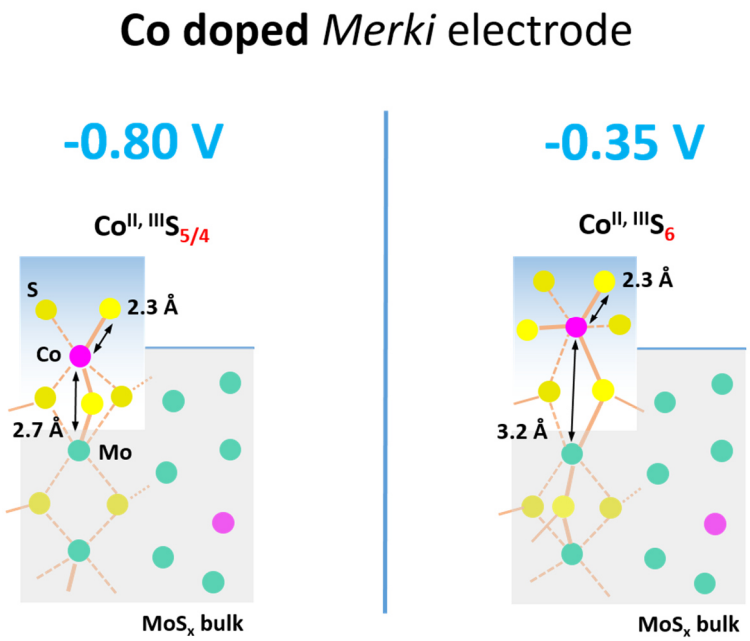

Figure 26

Schematic representation of a possible Co-site structure in the Co doped *Merki* electrode at -0.80 V and at -0.35 V *vs.* NHE.

all six ligands and, instead, the spatial disorder of the shell increases. This interpretation is possible due to the direct correlation in the EXAFS between the coordination number of a ligand shell and its Debye-Waller factor (= measure for the spatial disorder).

The Co sites in the electrodes do not exhibit O, N or C ligands (or CN^- and CO ligands) to a significant extent. The correspondingly short Co-ligand distances are absent in the Co EXAFS of the electrodes (see **Figure 22**).

The majority of the Co sites in the electrodes possesses a coordination to a neighbouring Mo atom (see peak **2** in **Figure 22**). This Co-Mo coordination exhibits a short distance of 2.72 Å at -0.80 V and a longer one of 3.19 Å at -0.35 V (**Table 6**). The EXAFS simulations would also support a Co-Co coordination. However, this is less likely in the electrodes due to the four-times higher abundance of Mo (as reported in (Merki, Vrubel et al. 2012) and indicated by our elemental analysis in **Table 12**). Besides this Co-metal coordination, the Co sites exhibit no significant long-range order.

The Co sites in the electrodes, in particular at -0.80 V, exhibit an atomic structure similar to the so-called "Co-Mo-S" phase (structure) observed in various $CoMoS_2$ catalysts for hydrodesulphurization (a selection of XAS studies for these catalysts can be found in (Bouwens, van Veen et al. 1991, Craje, Louwers et al. 1992, de Bont, Vissenberg et al. 1998, Miller, Marschall et al. 2001, Kadono, Kubota et al. 2006, Okamoto, Kato et al. 2009, Dugulan, van Veen et al. 2013)). The Co-Mo-S phase consists of Co-S clusters located at the edges of MoS_2 crystallites. The clusters contain Co ions coordinated to five or six S ligands. According to (Okamoto, Kato et al. 2009, Dugulan, van Veen et al. 2013), it is generally accepted that the Co-Mo-S phase is the catalytic or active phase in the $CoMoS_2$ catalysts.

Miller et al. proposes for the Co-Mo-S phase that the Co ions in the Co-S clusters exhibit two types of S ligands, terminal and bridging (see **Figure 25**) (Miller, Marschall et al. 2001). The latter are incorporated into the Co-$(\mu\text{-}S)_2$-Mo bridges between Co-S cluster and MoS_2 bulk and exhibit a shorter Co-S distance of 2.18 Å than the terminal ligands with 2.26 Å. When the model of (Miller, Marschall et al. 2001) is applied to the Co site in the *Merki* electrodes, similar distances can be resolved but with a lower number of bridging ligands. This indicates a more loose connection between the Co-S clusters and the MoS_x bulk than in the Co-Mo-S phase of the $CoMoS_2$ catalysts.

In the context of the Co-Mo-S phase, the Co-Mo coordination of the *Merki* electrodes represents the Co-$(\mu\text{-}S)_2$-Mo bridges between the Co-S cluster and the MoS_x bulk. At -0.35 V, the Co-Mo distance of the electrodes is unusually long in comparison to a typical Co-Mo-S phase in the $CoMoS_2$ catalysts. At -0.80 V, the Co-Mo coordination of the *Merki* electrodes contracts indicating that the Co sites approach closer to the MoS_x bulk. This could have been enabled by a reduction in the effective dimensions of the Co sites caused by the loss of an S ligand. If the Co-Mo coordination of the electrodes is considered as a Co-Co coordination (comparable quality of the corresponding EXAFS simulations), a contraction of the Co-Co distance from 3.3 Å to 2.9 Å analogue to the Co-Mo distance can be observed as well. The Co-Co contraction at -0.80 V could indicate the formation of spots in the electrode where the Co sites are spatially more concentrated.

The differences between the Co-Mo-S phase of the $CoMoS_2$ catalysts and the one of the *Merki* electrodes could arise from the fact that the former is based on MoS_2 crystallites while the electrodes consist of amorphous MoS_x, which exhibits a different long-range structure.

Ni SITE - ATOMIC STRUCTURE

RESULTS AND DISCUSSION

Ni-S COORDINATION

X-ray absorption near-edge structure (XANES) and extended X-ray absorption fine-structure (EXAFS) of the Ni doped MoS_x *Merki* electrodes (x = 2 or 3) were recorded at the Ni *K*-edge to gain insight into the atomic structure of their Ni sites. Prior to the XANES/EXAFS measurements, the electrodes were conditioned (12 min, pH 7) and frozen either at -0.80 V or -0.35 V *vs.* normal hydrogen electrode (NHE), to study structural differences between Ni sites in a state of catalytic H_2 formation (-0.80 V) and in a non-catalytic state (-0.35 V) (standard electrode potential of hydrogen reduction E^0_{H2} = -0.41 V at pH 7).

The Ni absorption edge of in the XANES of the *Merki* electrodes (see **Figure 27**) exhibits a similar shape as the Ni edge of $Ni^{I,II}{}_3S_2$ (heazlewoodite). This suggests that the Ni sites in the electrodes have a first coordination sphere similar to Ni_3S_2 where each Ni atom is tetrahedrally coordinated to four S ligands.

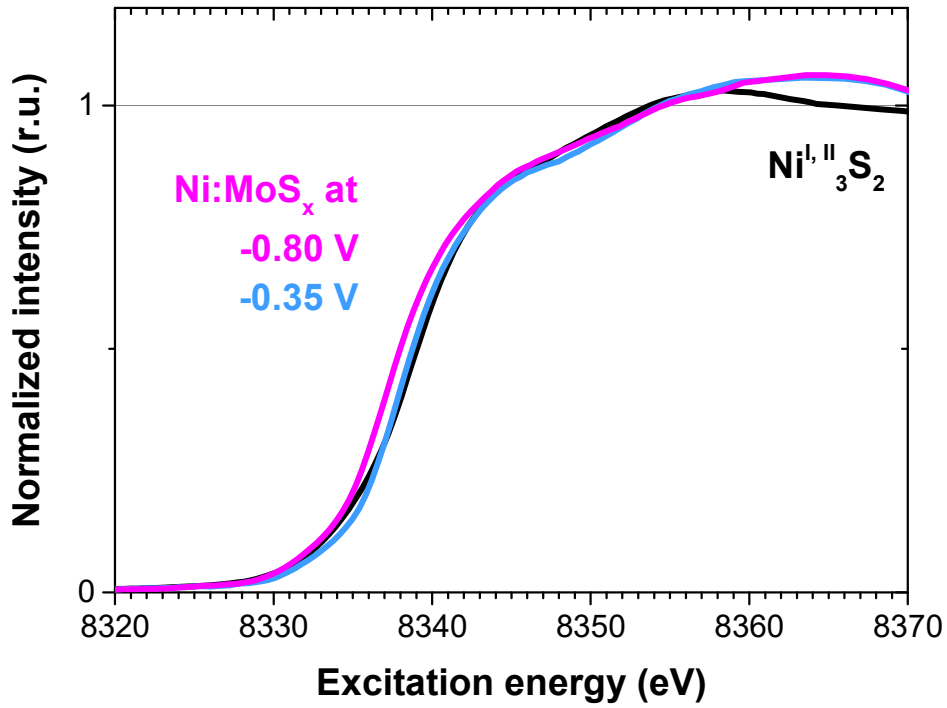

Figure 27

XANES spectra recorded at the Ni *K*-edge: Ni doped *Merki* MoS_x electrode at -0.80 V vs. NHE (**magenta** line) and at -0.35 V (**blue** line); crystalline $Ni^{I,II}{}_3S_2$ (**black** line).

Furthermore, the edge position of the -0.35 V electrode is close to the one of $Ni^{I,II}{}_3S_2$ suggesting that the Ni ions in the electrode, as in Ni_3S_2, exhibit a mean oxidation state of ≈ +1.3 (see **Table 9**). The edge position of the -0.80 V electrode is shifted to lower excitation energies by -0.8 eV indicating that the Ni ions have a more reduced mean oxidation state than at -0.35 V.

Ni edge	**Edge Position** [eV]	**Mean oxidation state**
Ni:MoS_x -0.80 V	8340.3	< 1.3
Ni:MoS_x -0.35 V	8341.1	≈ 1.3
$Ni^{I,II}{}_3S_2$	8340.9	1.3

Table 9

Ni *K*-edge positions of Ni doped *Merki* electrodes at -0.80 V and -0.35 V *vs.* NHE and their corresponding mean oxidation states for Ni. The edge positions were determined with the integral method as described in (Dau, Liebisch et al. 2003) with an interval of integration from 0.15 to 1.0 of normalized fluorescence.

The Ni EXAFS spectra of *Merki* electrodes, at both potentials, exhibit two prominent peaks, labelled as **1** and **2** in **Figure 28**. A comparison with the spectrum of Ni_3S_2 (see structure in **Figure 30**) indicates that peak **1** can be assigned to a Ni-S coordination. The nature of peak **2** remains unclear but is possibly a Ni-Mo coordination, see section *Ni-metal coordination*. EXAFS simulations of peak **1** (see **Figure 29**) yield a Ni-S distance of 2.22 Å (see **Table 11**), which is a bit shorter than in Ni_3S_2 with 2.27 ± 0.01 Å (see **Table 10**). The simulated S coordination number for peak **1** is close to four (= S coordination number of Ni_3S_2) but fluctuates with the electrode potential. From -0.35 V to -0.80 V, the coordination number decreases from 4.3 to 3.7 (see **Table 11**). The corresponding subsidence of peak **1** by 10 % (see **Figure 28**) is small and allows the alternative interpretation that the S shell retains all four ligands and, instead, the spatial disorder of the shell increases. This interpretation is possible due to the direct correlation in the EXAFS between the coordination number of a ligand shell and its Debye-Waller factor (= measure for the spatial disorder). The observed differences in the XANES between the -0.35 V and -0.80 V electrode (see **Figure 27**) could be related to the structural modifications in the S shell.

	mean **Ni-S distance** [Å]					
S coordination number	$Ni^{I,II}{}_3S_2$	$Ni^{I,II}{}_9S_8$	$Ni^{II}S$	$Ni^{II,III}{}_3S_4$	$Ni^{IV}S_2$	XRD
4	2.27 ± 0.01	2.23 ± 0.03		2.15 ± 0.06		
5		2.31 ± 0.04	2.31 ± 0.05			
6				2.34 ± 0.07	2.40 ± 0.01	

Table 10

Ni-S distances for various ligand environments of Ni with four, five or six S atoms. The denoted distances for each Ni-S compound (Ni_3S_2, Ni_9S_8, NiS, Ni_3S_4 and NiS_2) are mean values for a certain S-ligand geometry averaged from one or several crystal structures of the compound.

The crystal structure for Ni_3S_2 is published in (Westgren 1938, Fleet 1977, Parise 1980), for Ni_9S_8 in (Fleet 1987), for NiS (Millerite) in (Alsen 1925, Grice and Ferguson 1974, Rajamani and Prewitt 1974), for Ni_3S_4 in (Wyckoff 1931, Lundqvist 1974) and for NiS_2 in (Furuseth, Kjekshus et al. 1969, Nowack, Schwarzenbach et al. 1989, Nowack, Schwarzenbach et al. 1991).

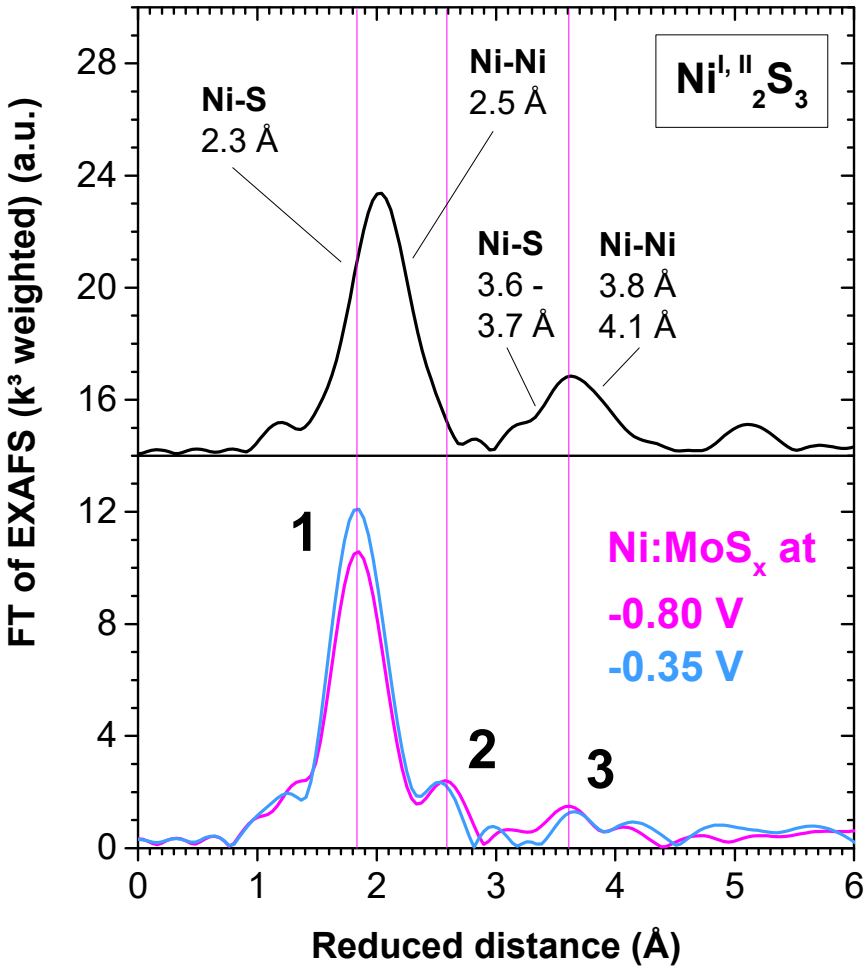

Figure 28

Fourier transforms of k^3 weighted EXAFS spectra (k range = 3 -13 Å^{-1}) recorded at the Ni *K*-edge: Ni doped *Merki* MoS_x electrodes at -0.80 V vs. NHE (**magenta** line) and at -0.35 V (**blue** line); crystalline $Ni^{I, II}_3S_2$ (**black** line). The main peaks of Ni_3S_2 are labelled with the corresponding Ni-ligand coordination and distance.

A comparison with various Ni-S compounds (see **Table 10**) suggests that the Ni-S distance of the *Merki* electrodes, which is the same at both potentials, exclusively corresponds to a geometry of four S ligands in the first coordination sphere. In particular, the tetrahedral NiS_4 species of Ni_9S_8 (see structure in **Figure 30**) (no XAS spectrum recorded) shows a S distance coincident with the electrodes. This suggests for the electrodes that the small drop in the simulated S coordination number from -0.35 V to -0.80 V (see **Table 11**) is rather due to an increase in spatial disorder of the S shell than due to a change in ligand number.

On the other hand, the *Merki* electrodes could contain coordinatively unsaturated Ni sites at -0.80 V where one or two S ligands are missing. This would decrease the mean S coordination number below four. *Merki et al.* already suggests the presence of coordinatively unsaturated Mo sites in the electrodes (Merki, Vrubel et al. 2012).

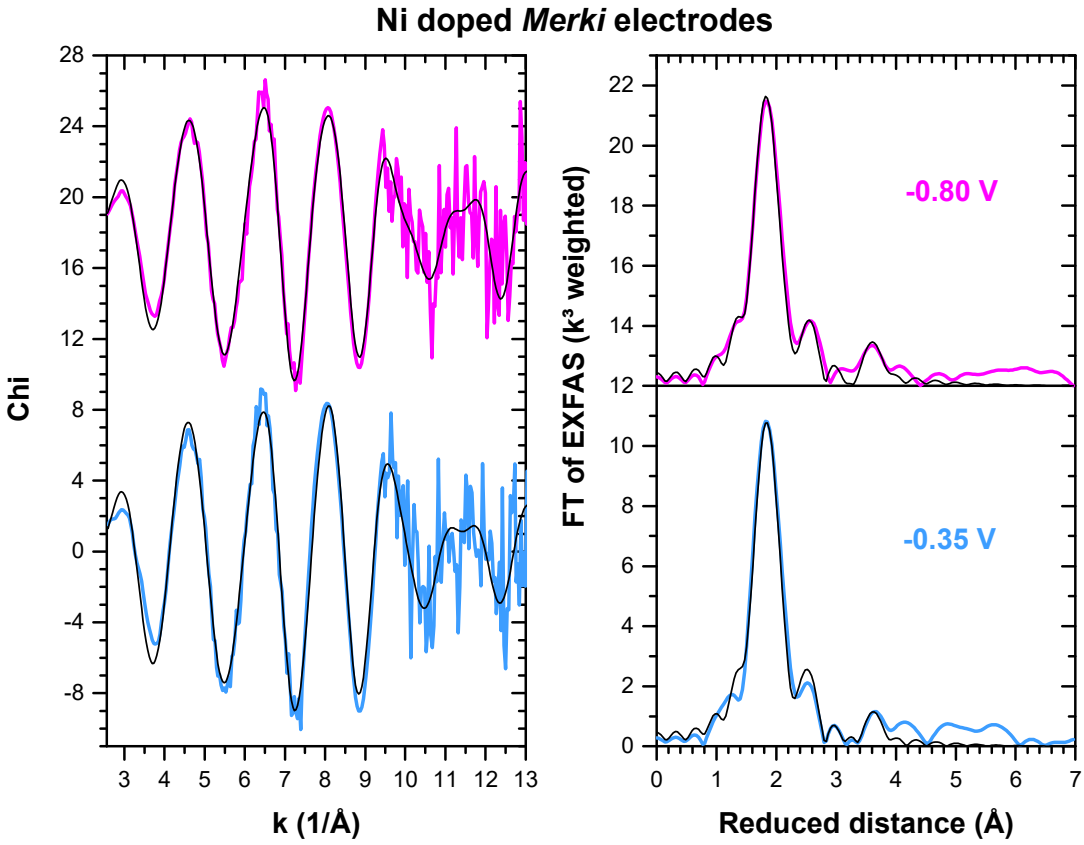

Figure 29

EXAFS simulations (**black** line) of the experimental spectra of the Ni doped Merki electrode at -0.80 V *vs.* NHE (**magenta** line) and -0.35 V (**blue** line). **Left** side: the EXAFS represented as k^3-weighted χ spectra. **Right** side: Fourier transforms of the k^3 weighted EXAFS spectra. The EXAFS simulations and Fourier transforms were performed over the k range shown on the left side. The EXAFS simulations correspond to the structural parameters presented in **Table 11**.

The Ni sites in the electrodes do not possess O, N or C ligands (or CN^- and CO ligands) to a significant extent. In the Ni EXAFS, prominent peaks of correspondingly short Ni-ligand distances (shorter than the distance of peak **1**) are not visible (see **Figure 28**). The left shoulder of peak **1** is part of the side lobes of the Ni-S peak as shown by the EXAFS simulations (see **Figure 29**).

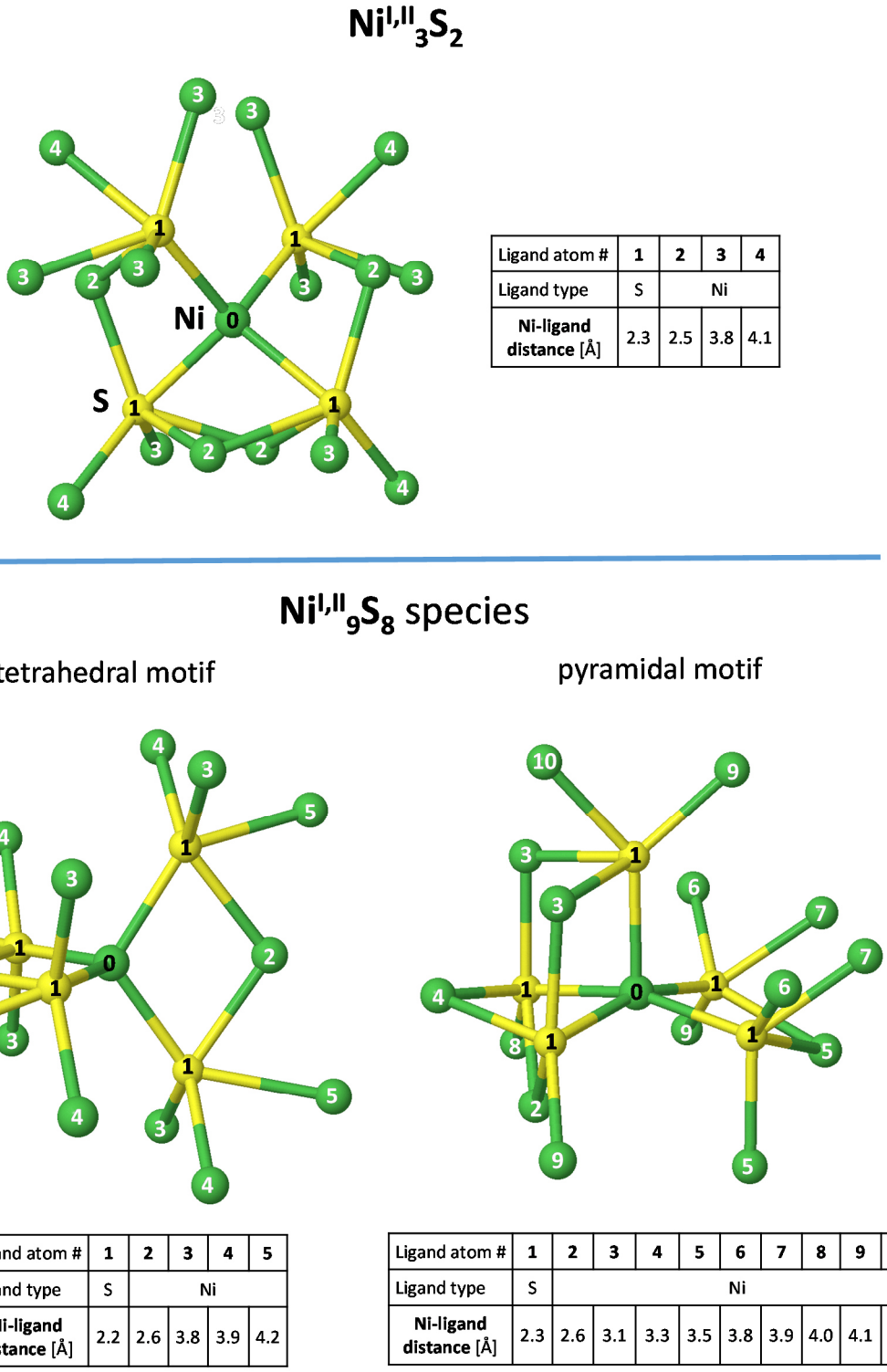

Ligand atom #	1	2	3	4
Ligand type	S	Ni		
Ni-ligand distance [Å]	2.3	2.5	3.8	4.1

Ligand atom #	1	2	3	4	5
Ligand type	S	Ni			
Ni-ligand distance [Å]	2.2	2.6	3.8	3.9	4.2

Ligand atom #	1	2	3	4	5	6	7	8	9	10
Ligand type	S	Ni								
Ni-ligand distance [Å]	2.3	2.6	3.1	3.3	3.5	3.8	3.9	4.0	4.1	4.3

Figure 30

Schematic structures of the Ni ligand environment in bulk $Ni^{I,II}{}_3S_2$ and $Ni^{I,II}{}_9S_8$. For each structure, the central Ni atom is indicated as "0". The numbering of the S/Ni ligand atoms increases with their distance from the central atom. Ligand atoms with the same number have the same distance. The concrete distance for each number is listed in the corresponding table next to the structure. The shown structures for Ni_9S_8 are a representative selection from the various Ni ligand environments present in this compound. The images are based on crystal data published for Ni_3S_2 in (Westgren 1938) and for Ni_9S_8 in (Fleet 1987).

mean **Ni-ligand distance**				
Ni edge	Ni-S [Å]	Ni-Mo [Å]	Ni-Ni [Å]	EXAFS
Ni:MoS_x -0.80 V	2.22 ± 0.01	2.67 ± 0.01	3.85 ± 0.02	
Ni:MoS_x -0.35 V	2.22 ± 0.01	2.67 ± 0.01	3.87 ± 0.03	
Cubane structure[a] $[Mo_3NiS_4(H_2O)_{10}]^{4+}$ $[Mo_3NiS_4Cl(H_2O)_9]^{3+}$	2.20 – 2.22	2.63 – 2.67	-	XRD
"Ni-Mo-S" phase[b]	2.12 – 2.29	2.81 – 2.85	2.53, 2.81	EXAFS
mean **Coordination number**				
Ni edge	Ni-S	Ni-Mo	Ni-Ni	EXAFS
Ni:MoS_x -0.80 V	3.7 ± 0.3	0.9 ± 0.2	1.2 ± 0.4	
Ni:MoS_x -0.35 V	4.3 ± 0.3	0.9 ± 0.2	0.8 ± 0.4	
Cubane structure[a] $[Mo_3NiS_4(H_2O)_{10}]^{4+}$ $[Mo_3NiS_4Cl(H_2O)_9]^{3+}$	3	3	-	XRD
"Ni-Mo-S" phase[b]	1.5 – 6.7	0.5 – 2.0	0.8 – 1.2	EXAFS

Table 11

Structural parameters of the Ni ligand environment in the Ni doped *Merki* electrodes at -0.80 V and -0.35 V *vs.* NHE, compared to the cubane-type structures[a] $[Mo_3NiS_4(H_2O)_{10}]^{4+}$ and $[Mo_3NiS_4Cl(H_2O)_9]^{3+}$ and the Ni-Mo-S phase[b] of various $NiMoS_2$ catalyst for hydrodesulphurization. For the *Merki* electrodes, the structural parameters were obtained from fitting their Ni EXAFS spectra with S, Mo and Ni phase functions calculated from the crystal structure[a] of Ni_3S_2 and Ni:$MoO_4 \cdot H_2O$. The simulations of both electrodes were performed with the same Debye-Waller parameters for Mo and Ni ($2\sigma_{Mo}^2$ = 0.009 Å² and $2\sigma_{Ni}^2$ = 0.009 Å²), the same energy offset (E_0 = 2.7 eV) and the same amplitude reduction factor (S_0^2 = 0.90). The values of σ_{Mo}, σ_{Ni} and E_0 were determined from a previous simulation of the -0.35 V electrode with a fixed Mo coordination number of one. The value of S_0 was established in (Haumann, Porthun et al. 2003). In all simulations, the coordination numbers of the ligands and the Ni-ligand distances were free to move. The Debye-Waller parameter of S was free as well and yielded $2\sigma_S^2$ = 0.010 Å² for the -0.80 V electrode and 0.011 Å² at -0.35 V. The simulated EXAFS spectra are presented in **Figure 29**.

a) The crystal structure data for $[Mo_3NiS_4(H_2O)_{10}]^{4+}$ was obtained from (Shibahara, Yamasaki et al. 1991), for $[Mo_3NiS_4Cl(H_2O)_9]^{3+}$ from (Shibahara, Yamasaki et al. 1991, Taniguchi, Imamura et al. 1999), for Ni_3S_2 from (Westgren 1938, Fleet 1977, Parise 1980) and for Ni:$MoO_4 \cdot H_2O$ from (Eda, Kato et al. 2010).

b) The structural parameters of the Ni-Mo-S phase of various $NiMoS_2$ catalyst for hydrodesulphurization were extracted from EXAFS results reported in (Bouwens, Koningsberger et al. 1990, Niemann, Clausen et al. 1990, Medici and Prins 1996, Eijsbouts 1997).

Ni–METAL COORDINATION

For peak **2** in the Ni EXAFS of the *Merki* electrodes (see **Figure 28**), EXAFS simulations (see **Figure 29**) suggest a Ni-Mo coordination. Simulations with a Ni-Ni coordination show less agreement with the electrode spectra (increase in the filtered *R*-factor by 50-60 %, *R* range = 1 – 3 Å). The Mo coordination number can be simulated with a value close to one, suggesting that the majority of the Ni sites in the electrodes are coordinated to a Mo atom. The simulated Ni-Mo distance of 2.67 Å (see **Table 11**) can be found in cubane-type bimetallic sulphide clusters as $[Mo_3NiS_4(H_2O)_{10}]^{4+}$ (Shibahara, Yamasaki et al. 1991) and $[Mo_3NiS_4Cl(H_2O)_9]^{3+}$ (Shibahara, Yamasaki et al. 1991, Taniguchi, Imamura et al. 1999) (see **Figure 19**) where the Ni-Mo distances are between 2.63 – 2.67 Å. The clusters also possess a Ni-S coordination with a S distance of 2.20 – 2.22 Å (see **Table 11**) that is similar to the one simulated for the *Merki* electrodes. Hence, the Ni sites in the electrodes might similar S bridges between Ni and Mo as in the clusters. However, cubane-type structures are probably not formed between the Ni sites and the MoS_x bulk of the electrodes, since the Ni sites do not achieve a three-fold Mo coordination as in the clusters (see **Table 11**). The Mo coordination of the Ni sites is not visibly affected by the alteration of the electrode potential from -0.35 V to -0.80 V.

Peak **3** in the Ni EXAFS of the electrodes indicates the presence of a weak long-range structure (see **Figure 28**). At -0.35 V, the long-range structure is not as evident as at -0.80 V, since the amplitude of peak **3** is closer to the noise level. In EXAFS, peaks at such long distances as peak **3** (≈3.7 Å) most likely correspond to heavy backscatterers like metal atoms. In the case of the Ni doped *Merki* electrodes, the possible metals are Ni or Mo. EXAFS simulations of peak **3** support a Ni-Ni coordination (see **Figure 29**) as well as a Ni-Mo coordination. Both coordinations result in the same simulation quality. In case of a Ni-Ni coordination, the simulations yield a Ni-Ni distance of 3.85 – 3.87 Å (see **Table 11**) which can be found in Ni-μ^4-S-Ni bridges of Ni_9S_8 or Ni_3S_2 (see structure in **Figure 30**). The former would be in concordance with the Ni_9S_8-like Ni-S coordination of peak **1** (see **Figure 28**). In case of a Ni-Mo coordination, the simulations of peak **3** yield a Ni-Mo distance of 3.69 – 3.72 Å which is unusual and prevents an assignment to a certain structural motif. For both coordinations, Ni-Ni and Ni-Mo, the simulated coordination numbers are close to one (for Ni-Ni see **Table 11**) and indicate only a weak occurrence of this long-range structure. The Ni doped *Merki* electrodes possibly contain only spots where either the Ni sites are more concentrated or the MoS_x bulk exhibits a higher structural order. This could lead to a higher spatial correlation between remote metal sites and would sum up to a corresponding long-range feature in the EXAFS.

The Ni sites in the electrodes exhibit only a weak similarity with the so-called “Ni-Mo-S” phase (structure) of $NiMoS_2$ catalysts for hydrodesulphurization (a selection of XAS studies for these catalysts can be found in (Bouwens, Koningsberger et al. 1990, Niemann, Clausen et al. 1990, Medici and Prins 1996, Eijsbouts 1997)). This is interesting, since the Co sites in the electrodes share common features with the “Co-Mo-S” phase of analogue $CoMoS_2$ catalysts. The Ni-Mo-S phase consists of Ni-S clusters on the edges of MoS_2 crystallites and, according to (Eijsbouts 1997), contains the active site of the catalysts or a part of it. The S shell of the Ni sites in the electrodes exhibits a Ni-S distance and coordination number that falls in the range of observed values for the Ni-Mo-S phase (see **Table 11**). However, the Ni-metal coordinations of the sites significantly deviate from the Ni-Mo-S structure. The amorphicity of the MoS_x bulk in the electrodes could affect the formation of the Ni-Mo-S phase leading to a different atomic structure than on crystalline MoS_2.

SUMMARY

The Ni doped MoS_x *Merki* electrodes (x = 2 or 3) (preparation as in (Merki, Vrubel et al. 2012)) were investigated with X-ray absorption spectroscopy (XAS) at the Ni *K*-edge to gain insight into the atomic structure of their Ni sites. Prior to the XAS measurements, the electrodes were conditioned (12 min, pH 7) and frozen either at -0.80 V or -0.35 V *vs.* normal hydrogen electrode (NHE), to study structural differences between Ni sites in a state of catalytic H_2 formation (-0.80 V) and in a non-catalytic state (-0.35 V) (standard electrode potential of hydrogen reduction E^0_{H2} = -0.41 V at pH 7).

The Ni sites in the electrodes (see **Figure 31**) consist of Ni ions with a mean oxidation state close to +1.3. At -0.80 V, the Ni ions are more reduced than at -0.35 V due to the more reductive electrode potential (see **Table 9** and Ni XANES of the electrodes in **Figure 27**). The Ni ions are coordinated to S atoms in their first coordination sphere with a mean Ni-S distance of 2.22 Å (see **Table 11**). The mean S coordination number is close to four but fluctuates with the electrode potential. From -0.35 V to -0.80 V, the coordination number decreases from 4.3 to 3.7 (see **Table 11** and subsidence of peak **1** in **Figure 28**). The Ni-S distance and S coordination number indicate that the Ni-S species in the electrodes is similar to tetrahedral species present in $Ni^{I,\,II}{}_9S_8$ (see structure in **Figure 30**). The lower S coordination number at -0.80 V could originate from coordinatively unsaturated Ni sites where one or two S ligands are missing. *Merki et al.* already suggests the presence of unsaturated Mo sites in the electrodes (Merki, Vrubel et al. 2012). The unsaturated Ni sites mainly occur in the -0.80 V electrode and, hence, could be produced by the catalytic reaction, as proposed in (Miller, Marschall et al. 2001). However, the decrease in the S coordination number at -0.80 V is small and allows the alternative interpretation that the S shell retains all four ligands and, instead, the spatial disorder of the shell

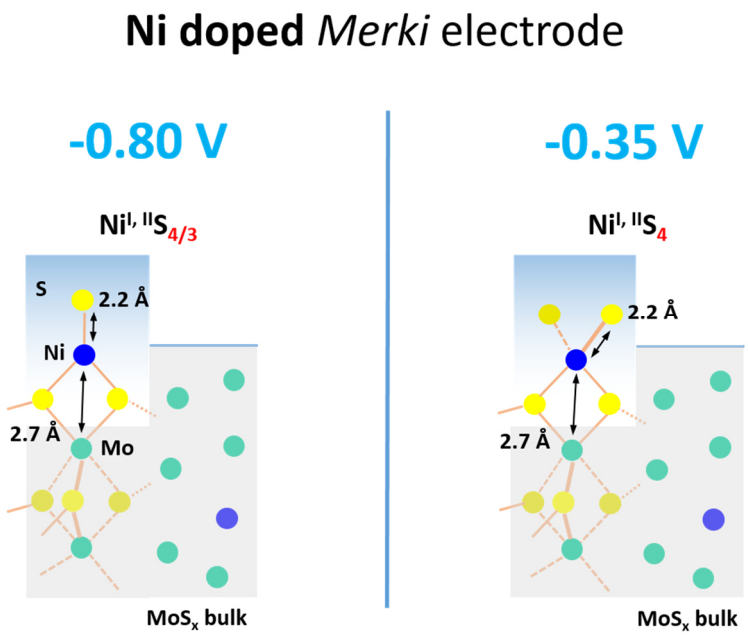

Figure 31

Schematic representation of a possible Ni-site structure in the Ni doped *Merki* electrode at -0.80 V and at -0.35 V *vs.* NHE.

increases. This interpretation is possible due to the direct correlation in the EXAFS between the coordination number of a ligand shell and its Debye-Waller factor (= measure for the spatial disorder).

The Ni sites in the electrodes do not exhibit O, N or C ligands (or CN^- and CO ligands) to a significant extent. The correspondingly short Ni-ligand distances are absent in the Ni EXAFS of the electrodes (see **Figure 28**).

The majority of the Ni sites in the electrodes possess a single Ni-Mo coordination with a Ni-Mo distance of 2.67 Å (see **Table 11** and peak **2** in **Figure 28**). The Ni-Mo coordination is not affected by the alteration of the electrode potential from -0.35 V to -0.80 V. The distance of the Ni-Mo coordination can be found in the cubane-type bimetallic sulphur clusters $[Mo_3NiS_4(H_2O)_{10}]^{4+}$ (Shibahara, Yamasaki et al. 1991) and $[Mo_3NiS_4Cl(H_2O)_9]^{3+}$ (Shibahara, Yamasaki et al. 1991, Taniguchi, Imamura et al. 1999) (see **Figure 19**). The clusters also possess a Ni-S coordination similar to the one observed for the Ni sites of the electrodes (see **Table 11**). Hence, the Ni sites might exhibit similar S bridges between Ni and Mo as in the clusters. However, cubane-type structures are probably not formed between the Ni sites and the MoS_x bulk of the electrodes, since the Ni sites do not achieve a three-fold Mo coordination as in the bimetallic sulphide clusters (see **Table 11**). In (Taniguchi, Imamura et al. 1999), the cubane-type cluster $[Mo_3NiS_4Cl(H_2O)_9]^{3+}$ is applied as precursor for hydrodesulphurization catalysts. Hence, the structural similarity between the Ni sites of the *Merki* electrodes and the cluster could be a reason for the catalytic activity of the sites.

The Ni sites exhibit a weak long-range structure consisting of a Ni-Ni or Ni-Mo coordination longer than 3 Å (peak **3** in **Figure 28**). The potential Ni-Ni coordination would exhibit a Ni-Ni distance of 3.85 – 3.87 Å (see **Table 11**) which can be found in Ni-μ^4-S-Ni bridges of Ni_9S_8 and would be in concordance with the Ni_9S_8-like Ni-S coordination of the Ni sites. The potential Ni-Mo coordination would show an unusual Ni-Mo distance of 3.69 – 3.72 Å which prevents an assignment to a certain structural motif. For both coordinations, Ni-Ni and Ni-Mo, the coordination numbers are close to one (for Ni-Ni see **Table 11**) indicating only a weak occurrence of the long-range structure. It seems that the Ni doped *Merki* electrodes contain only spots where either the Ni sites are more concentrated or the MoS_x bulk exhibits a higher structural order. The former could lead to a weak long-range coordination between Ni sites and the latter between Ni and Mo sites.

In various $NiMoS_2$ catalysts for hydrodesulphurization, a so-called “Ni-Mo-S” phase (structure) is observed (a selection of XAS studies for these catalysts can be found in (Bouwens, Koningsberger et al. 1990, Niemann, Clausen et al. 1990, Medici and Prins 1996, Eijsbouts 1997)). This phase contains the active sites of the catalysts or parts of it. The Ni sites in the electrodes exhibit a Ni-S coordination suitable for a possible Ni-Mo-S phase but their Ni-Mo coordination does not match. This is interesting, since the Co sites in the electrodes show a high similarity with the analogous “Co-Mo-S” phase of $CoMoS_2$ catalysts for hydrodesulphurization.

In the Mo EXAFS of the same electrodes, the Mo-Ni distances are hardly visible due to the low stoichiometric ratio between Ni and Mo of about 1 : 5 (as reported in (Merki, Vrubel et al. 2012) and indicated by our elemental analysis in **Table 12**).

HYDROGEN FORMATION – MECHANISTIC IMPLICATIONS

DISCUSSION

XAS MEASUREMENTS ON THE MERKI ELECTRODES

The Co doped, Ni doped and undoped MoS_x *Merki* electrodes (x = 2 or 3) were investigated with X-ray absorption spectroscopy (XAS) at the Mo *K*-edge to gain insight into the atomic structure of their Mo sites. For the doped electrodes, additional XAS measurements were performed at the Co or Ni *K*-edge to obtain information about the atomic structure of the Co or Ni sites. The XAS spectra were recorded at electrode potentials of -0.80 V and -0.35 V *vs.* normal hydrogen electrode (NHE) under neutral conditions (pH 7), to study structural differences between Mo, Co and Ni sites in a state of catalytic hydrogen-evolution reaction (HER) (-0.80 V) and in a non-catalytic state (-0.35 V) (standard electrode potential of hydrogen reduction E^0_{H2} = -0.41 V at pH 7).

HER MECHANISM OF MoS_2 CATALYSTS

Amorphous MoS_2 is proposed as the catalytic Mo species for hydrogen evolution reaction (HER) in the *Merki* electrodes while a non-catalytic MoS_3 species can be present as well (Merki, Fierro et al. 2011, Merki, Vrubel et al. 2012, Lassalle-Kaiser, Merki et al. 2015). Our X-ray absorption spectroscopy (XAS) investigations of the electrodes support that and indicate that the Mo sites of the electrodes combine a $Mo^{IV}S_2$-like Mo-S coordination (= S^{2-} ligands) with a 2.8 Å Mo-Mo coordination typical for amorphous $Mo^{V}S_3$ (see chapter *Mo site – Atomic structure*). The atomic structure of the sites possibly builds up from Mo_2S_x blocks (x = 7, 8 or 9) similar to the Mo_2S_9 building blocks of MoS_3 (see **Figure 12**), based on the same Mo-Mo coordination, but with Mo^{IV} centres as in MoS_2. The Mo sites do not show a long-range order comparable to crystalline MoS_2 with a 3.2 Å Mo-Mo coordination (see chapter *Mo site – Atomic structure*). The missing long-range order suggests an amorphous character for the Mo-S species of the electrodes.

A tentative model for catalyst in the *Merki* electrodes could be MoS_2 crystals (as proposed by (Merki, Vrubel et al. 2012)), as they exhibit significant catalytic activity for HER in form of nanocrystals (Jaramillo, Jorgensen et al. 2007) and possess structural similarities with the Mo-S species of the electrodes. The catalytic sites of the MoS_2 crystals are the edges while the basal planes of the crystals are inactive (Jaramillo, Jorgensen et al. 2007). A bulk MoS_2 crystal possesses a hexagonal morphology leading to two types of edge sites: the Mo (10$\underline{1}$0) edge and the S ($\underline{1}$010) edge (see **Figure 32A**) (Bollinger, Jacobsen et al. 2003). The Mo edge is the catalytically active site (Jaramillo, Jorgensen et al. 2007) and is sulfided, presumably with a S monomer (see **Figure 32B**) (Bollinger, Jacobsen et al. 2003). Crystalline MoS_2 nanoparticles exhibit a higher catalytic activity than bulk crystals, as their truncated triangular shape (see **Figure 32C**) leads to a predominance of Mo edges (Jaramillo, Jorgensen et al. 2007).

The doping of MoS_2 nanocrystals with Co can increase their catalytic activity for HER (Bonde, Moses et al. 2008). The Co atoms exclusively bind to the S edges (Raybaud, Hafner et al. 2000, Schweiger, Raybaud et al. 2002, Lauritsen, Kibsgaard et al. 2007) and transform them into catalytically active sites (Bonde, Moses et al. 2008). This leads to a higher number of active sites in the Co doped MoS_2

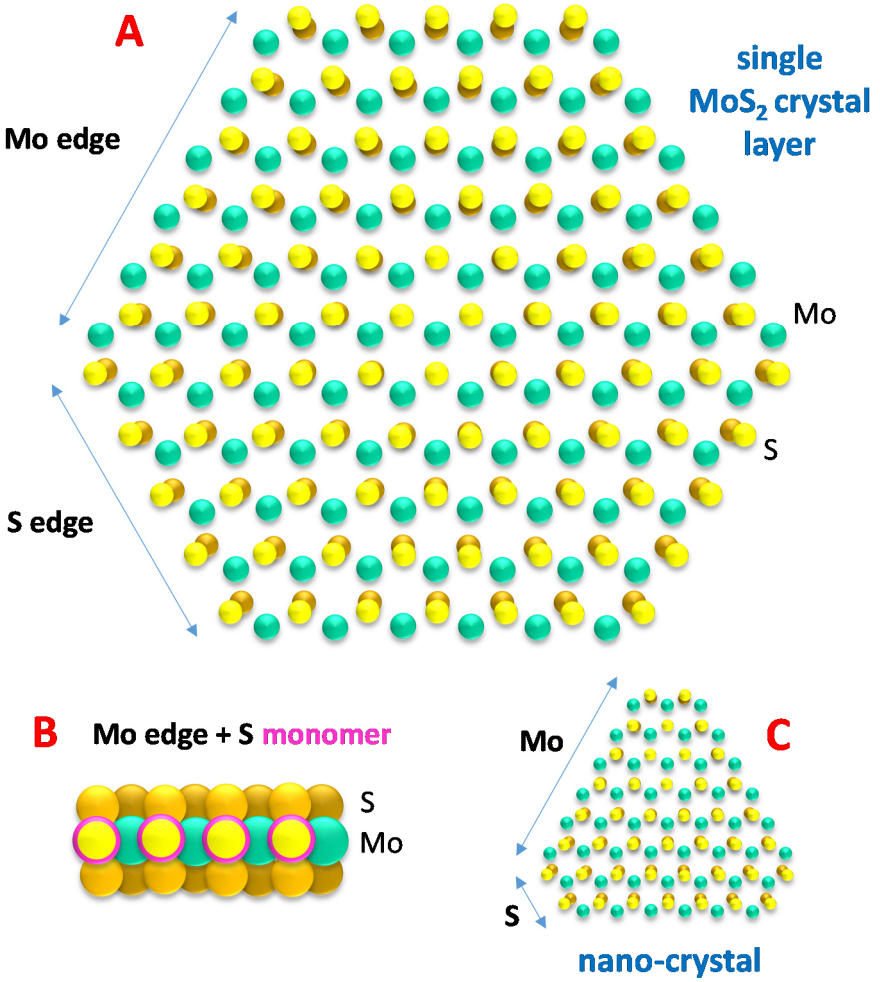

Figure 32

A: Schematic structure of the Mo and S edges of a single MoS_2 crystal layer (view on basal plane). **B**: Mo edge covered by a S monomer. **C**: MoS_2 nano-crystal. Schemes are based on illustrations in (Bollinger, Jacobsen et al. 2003, Bonde, Moses et al. 2008).

nanoparticles compared to the undoped particles. For the doping with Ni, analogue promotion effects on MoS_2 nanoclusters were observed (Kibsgaard, Tuxen et al. 2010).

The Gibbs free energy, ΔG_H, for atomic hydrogen adsorption on a specific atomic site is a measure of its catalytic activity. The smaller the value of ΔG_H (closer to zero) the higher the activity or exchange current density, respectively. Density functional theory (DFT) calculations of ΔG_H for the MoS_2 nanocrystals yield a lower value of +0.08 eV for the Mo edges than for the S edges with +0.18 eV (Bonde, Moses et al. 2008), suggesting a higher catalytic activity for the Mo edges. The ΔG_H calculations propose that, at room temperature, the S monomer of the Mo edge is the most attractive adsorption site for atomic hydrogen (Hinnemann, Moses et al. 2005). The doping of the MoS_2 nanocrystals with Co does not affect ΔG_H of the Mo edges but lowers the value of ΔG_H for the S edges to +0.10 eV (Bonde, Moses et al. 2008), suggesting that the Co-binding S edges possess a catalytic activity comparable to the Mo edges.

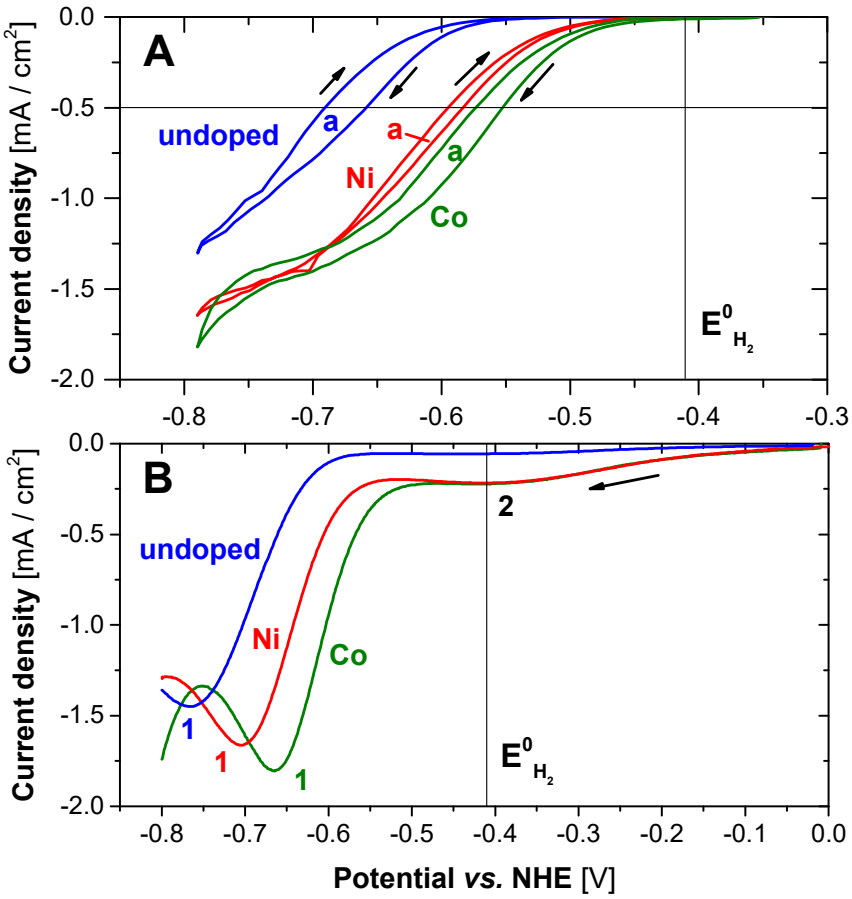

Figure 33

Cyclic voltammetry (CV) of the *Merki* electrodes in 0.1 M potassium phosphate at pH 7.0: (**blue** line) undoped, (**red** line) Ni doped and (**green** line) Co doped electrode. The scan direction is indicated by the arrows. Before cyclic voltammetry, the electrolyte was degassed via flushing with N_2. The measurement was performed under N_2 atmosphere. In (**A**), the 4th cycle of the CV is shown with a scan rate of 1 mV/s. The forward traces are in good agreement with analogue measurements reported by *Merki et al.* in (Merki, Vrubel et al. 2012). In (**B**), the as-prepared *Merki* electrodes were slowly ramped up from the open-circuit voltage (non-catalytic conditions) to -0.80 V *vs.* NHE (HER conditions) with a scan rate of 5 mV/s. The ramp-up is part of the electrode conditioning for the XAS measurements and was performed in a *freeze-quench* configuration (for a detailed description see chapter *Methods*). The standard potential $\mathbf{E^0_{H2}}$ of hydrogen reduction at pH 7.0 is marked by the vertical line for both measurements, **A** and **B**.

The edge sites in the MoS_2 crystals can be considered as defect sites and/or unsaturated sites. The configuration of the Mo and S atoms at the edge sites breaks the symmetry of the crystal lattice (Bollinger, Jacobsen et al. 2003) leading to edge atoms that are coordinatively unsaturated. This enables the edge sites to adsorb hydrogen and to mediate HER. The *Merki* electrodes do not possess such well-defined Mo edge sites as the MoS_2 crystals but they still exhibit a catalytic activity comparable to other MoS_2-based catalysts (Merki and Hu 2011). The hypothesis of *Merki et al.* is that the amorphous MoS_2 character of the electrodes leads to a significant amount of defect sites and, thereby, coordinatively unsaturated Mo and S atoms where HER may take place (Merki, Vrubel et al. 2012). The Co or Ni dopants can enhance the activity of these unsaturated sites (Merki, Vrubel et al.

2012) and/or create new ones as observed in the MoS_2 nanocrystals (transforming S edges into active sites). The dopant sites themselves could be potential reaction sites for HER as well.

DFT calculations of ΔG_H suggest that the unsaturated S sites are the most suitable sites for HER in the *Merki* electrodes, as they require the lowest energy to adsorb atomic hydrogen (Hinnemann, Moses et al. 2005). Unsaturated Mo, Co and Ni sites form stronger bonds with atomic hydrogen which could impede HER via a slow hydrogen-release step (Hinnemann, Moses et al. 2005). However, the Mo, Co and Ni sites could support HER by providing an additional source of bound atomic hydrogen. This might happen in analogy to the catalytic mechanism in hydrogenase where molecular hydrogen is formed by the interplay between a hydride-binding metal site and a proton-binding pendant base in close proximity (Lubitz, Ogata et al. 2014). In the case of the *Merki* electrodes, the unsaturated Mo, Co and Ni sites would bind the hydride and the unsaturated S sites the proton. In the *Merki* electrodes, this mechanism could operate in parallel to a mechanism solely based on unsaturated S sites.

ELECTROCHEMICAL EFFECTS BY THE DOPING OF THE *MERKI* ELECTRODES

Cyclic voltammetry (CV) on the *Merki* electrodes, at pH 7, indicates a correlation between the doping with Co or Ni and the over-potential of the electrodes for HER and the redox currents occurring under HER conditions. The CV scans of the electrodes in **Figure 33A** (scan rate 1 mV/s) show that the doping with Co or Ni shifts the rise of the catalytic HER current to lower electrode potentials: for the Co doped electrode, the catalytic current reaches -0.5 mA/cm^2 at -0.55 V *vs.* normal hydrogen electrode (NHE), for the Ni doped electrode at -0.58 V and for the undoped electrode at -0.66 V. This indicates that the doping, in particular with Co, lowers the over-potential of the electrodes for HER (standard electrode potential of hydrogen reduction, E^0_{H2} = -0.41 V *vs.* NHE at pH 7.0) (the doping effect on the over-potential was already reported in (Merki, Vrubel et al. 2012)). The *Merki* electrodes exhibit significant redox currents under HER conditions. These currents are indicated in the CV scans of the electrodes by the difference area "**a**" between forward and backward trace in **Figure 33A** (scan rate 1 mV/s) and by the occurrence of the cathodic current wave "**1**" in **Figure 33B** (scan rate 5 mV/s). In both cases, the doping with Co or Ni effects that the redox-currents occur at less negative potentials than in the undoped electrode. This suggests that doping enables a provision of redox equivalents for HER closer to E^0_{H2} than in the undoped electrode. The occurrence of the redox currents and their midpoint potential do not degrade over time as shown by the one-hour CV measurements in **Figure 34**.

The occurrence of redox currents under HER conditions indicate that a fraction of the Mo, Co, Ni and/or S atoms in the *Merki* electrodes undergo oxidation state changes and, hence, participate as redox-equivalents in the catalytic reaction and/or in the formation of the catalytic state. The number

Elemental analysis			
	Co:MoS_x [nmol / cm^2]	**Ni:MoS_x** [nmol / cm^2]	**MoS_x** [nmol / cm^2]
Co	50		
Ni		20	
Mo	200	90	50
S	430	200	90
Mo [µg / cm^2]	19	9	4
Co : Mo	1 : 4		
Ni : Mo		1 : 5	
S : Mo	2 : 1	2 : 1	2 : 1
Redox equivalents			
	Co:MoS_x [nmol / cm^2]	**Ni:MoS_x** [nmol / cm^2]	**MoS_x** [nmol / cm^2]
	200	60	130

Table 12

Top: elemental analysis of the Co:MoS_x, Ni:MoS_x and MoS_x *Merki* electrodes via inductively coupled plasma – optical emission spectrometry (ICP-OES). Prior to analysis, the electrodes were digested in mixtures of concentrated HNO_3 : HCl in a 1 : 3 ratio for ≈ 2 h. The measurement was executed and evaluated by Mikaela Görlin of the group of Prof. Strasser at the Technical University of Berlin. Our results, in particular the proportions between Co, Ni and Mo, are in good agreement with analogue measurements reported by *Merki et al.* in (Merki, Vrubel et al. 2012). **Bottom**: numbers of redox equivalents present in the doped and undoped *Merki* electrodes under HER conditions. The numbers were determined by calculating the difference integral between the forward and backward trace of the 4th cyclic-voltammetry cycle shown in **Figure 33A** and by dividing the result by two to compensate for the catalytic current.

of the redox-equivalents can be estimated from the integration of the redox currents in **Figure 33A** (= difference area "**a**" between forward and backward trace). However, it is complicated to correctly separate the catalytic current from the redox currents and, therefore, the determined numbers for the redox equivalents are uncertain. The rough approach used for **Figure 33A** assumes that the catalytic current corresponds to the midline between the forward and backward trace of the CVs and, hence, can be compensated by diminishing the integral of the redox currents by a factor of two.

For the undoped *Merki* electrode, the determined number of redox equivalents approximately matches the number of all Mo and S atoms present in the electrode (see **Table 12**). This suggests that, besides the surface, the MoS_x bulk of the electrode participates in HER, involving a significant fraction of its S and Mo atoms. However, XAS analysis indicates only oxidation state changes around one or smaller for Mo (see **Table 1**), suggesting that S (no XAS recorded at S *K*-edge) is stronger involved in HER than Mo. In the Co and Ni doped electrodes, the MoS_x bulk presumably exhibits a comparable catalytic behaviour, since its atomic structure is similar to the one of the undoped electrode (see chapter *Mo site – Atomic structure*) and the observed oxidation-state changes for Mo are around one or smaller as well.

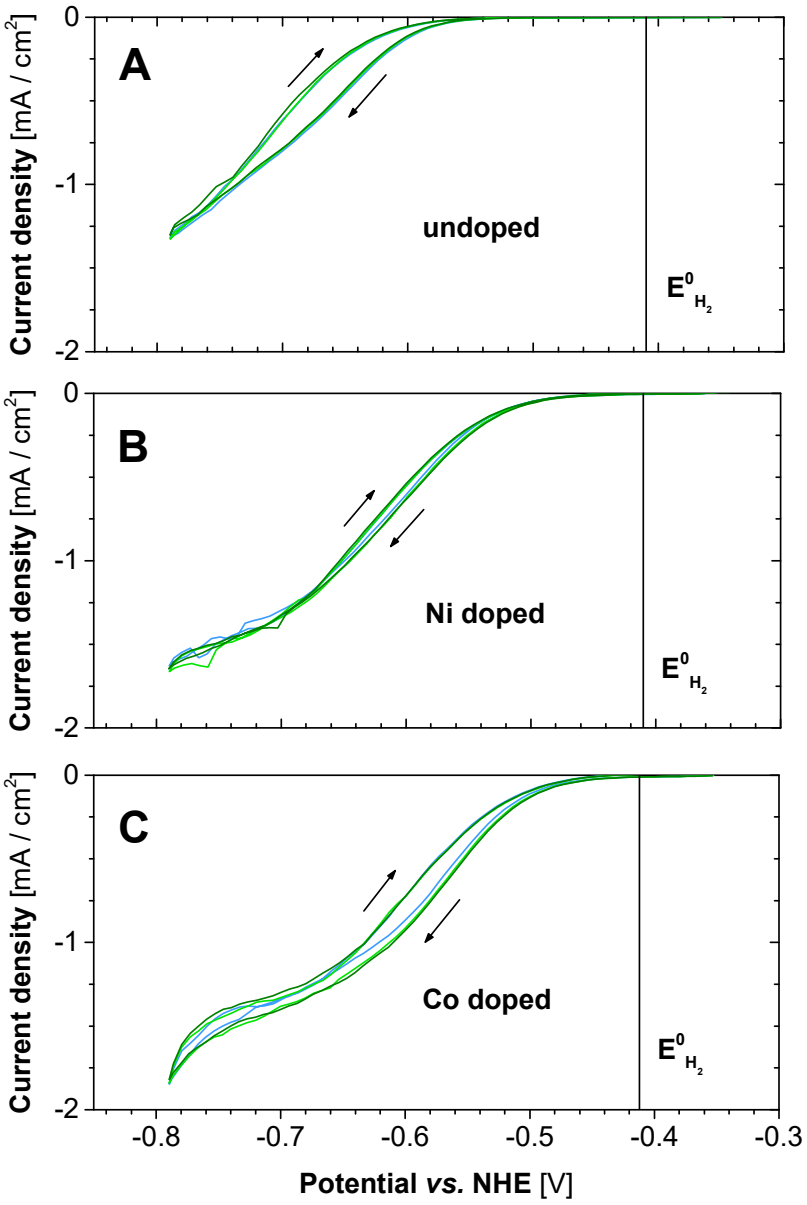

Figure 34

Cyclic voltammetry of the *Merki* electrodes with a scan rate of 1 mV/s: (**A**) undoped, (**B**) Ni doped and (**C**) Co doped. Shown are the 2nd (**blue** line), 3rd (**light green** line) and 4th cycle (**dark green** line). The standard potential $\mathbf{E^0_{H2}}$ of hydrogen reduction at pH 7.0 is marked by the vertical line. The scan direction is indicated by the arrows. The used electrolyte is 0.1 M potassium phosphate at pH 7.0. Before cyclic voltammetry, the electrolyte was degassed via flushing with N_2. The measurement was performed under N_2 atmosphere.

For the Co/Ni doped *Merki* electrodes, the determined number of redox equivalents seems to correlate with the number of dopant atoms present in the electrodes. The Co doped electrode exhibits a larger number of redox equivalents and of dopant atoms than the Ni doped electrode while the proportion between dopant atoms and redox equivalents is similar for both electrodes (see **Table 12**). This effect and the observed shift of the redox currents to less negative electrode potentials in the doped electrodes (see **Figure 33A** and **B**) suggest a direct involvement of the dopant atoms in the HER

catalysis. This dopant-related catalysis, however, is not solely based on the dopants and involves other catalytic sites as S and/or Mo sites, since the turnover of redox equivalents for the doped electrodes exceeds the number of available dopant atoms by a factor of three or four (see **Table 12**). The involvement of other catalytic sites is also supported by XAS analysis, indicating only moderate oxidation states changes for Co and Ni during HER with an estimated magnitude of one or smaller (see **Table 5** and **Table 9**).

The *Merki* electrodes possibly form a S-hydride whose activity and/or formation is promoted by the doping with Co or Ni. The observed redox currents of the electrodes under HER conditions (difference area "**a**" between forward and backward trace in **Figure 33A** and current wave "**1**" in **Figure 33B**) are probably dominated by redox processes of the S-hydride. The origin of the pre-wave "**2**" in **B** is unclear but possibly arises from the partial reduction of Mo^{IV} to Mo^{III} ions in the electrodes.

Mo SITES OF THE *MERKI* ELECTRODES

Our XAS analysis of the *Merki* electrodes at pH 7 supports the hypothesis of *Merki et al.* that the amorphicity of the electrodes leads to coordinatively unsaturated Mo and S sites where HER can take place. Our XAS analysis, however, provides mainly information for the Mo sites. The analysis indicates that the Mo sites in the electrodes (see **Figure 35**) exhibit a MoS_2-character (oxidation state close to IV and a Mo-S distance typical for MoS_2, see chapter *Mo site – Atomic structure*) but presumably a mean S coordination number of five which is smaller than in MoS_2 (six S ligands per Mo atom) (see **Table 12**). This suggests that a major fraction of the Mo sites in the bulk of the electrodes are coordinatively unsaturated (missing S ligands). These sites could be accessible for HER via proton diffusion into the electrode bulk (proposed by (Casalongue, Benck et al. 2014)) supported by the porosity of the electrodes (Merki, Vrubel et al. 2012). The participation of the electrode bulk in HER is also suggested by the amount of charges involved in the redox currents of the undoped electrode in **Figure 33** which approximately matches the number of all Mo and S atoms present in the electrode (see **Table 12**). The involvement of the unsaturated Mo sites in HER would require a mechanism where molecular hydrogen is formed by the recombination of a sulphur-bound proton with a neighbouring metal-bound hydride as observed in hydrogenase (Lubitz, Ogata et al. 2014). The one-to-one Mo-Mo coordination present in the electrodes (see **Figure 35**) could be considered as a double-metal active site in analogy to the sulphur-bridged Ni-Fe or Fe-Fe active sites in hydrogenase (Lubitz, Ogata et al. 2014).

The determination of the mean S coordination number to a value below six for the Mo sites is not definite. In the EXAFS (extended X-ray absorption fine-structure), the coordination number of a ligand shell and its Debye-Waller factor (= measure for spatial disorder) are directly correlated, rendering a definite determination of the coordination number very problematic. Our EXAFS simulations favour a S_5 shell over a stronger spatially disordered S_6 shell, as the latter exhibits 20 – 50 % higher R_f-factors (= degradation in simulation quality, see **Table 2**). However, this is not sufficient to completely exclude the presence of the S_6-shell, as the quality of the corresponding simulations is still reasonable with a R_f-factor below 20 % (see **Table 2**). Therefore, the *Merki* electrodes could possess a significant contribution of coordinatively saturated Mo sites with a six-fold S coordination.

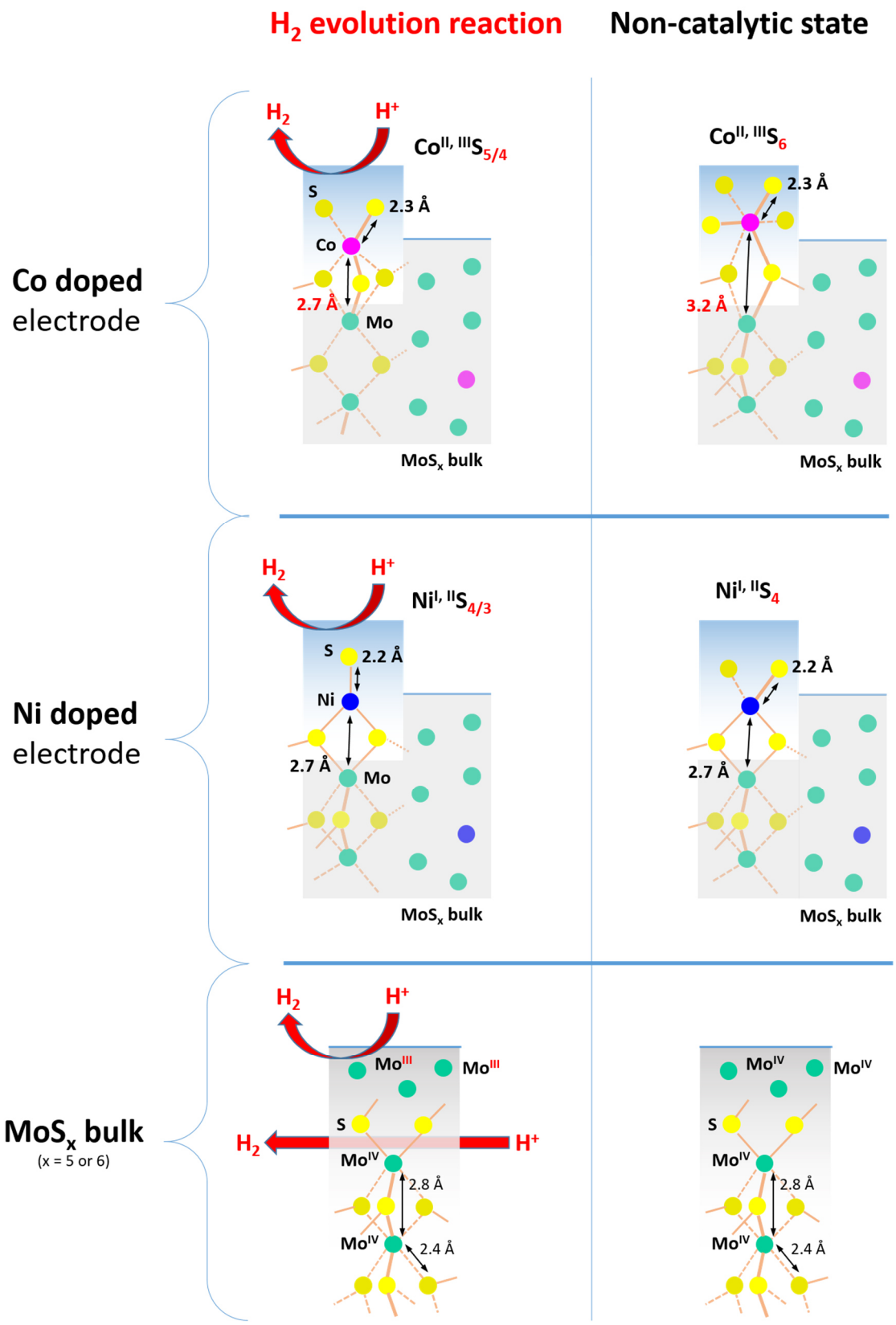

Figure 35

Schematic representation of possible Mo-, Co. and Ni-site structures in the undoped, Ni doped and Co doped *Merki* electrodes during H_2 evolution reaction (-0.80 V *vs.* NHE) and in the non-catalytic state (-0.35 V).

The S shell of the Mo sites exhibits a high spatial disorder (Debye-Waller factor of σ_S = ±0.08 Å) in comparison to crystalline MoS_2 (with σ_S = ±0.03 Å). This suggests that, in the *Merki* electrodes, the S shells of the Mo sites contain a significant number of coordinatively unsaturated S sites. As discussed in the previous section *HER mechanism of MoS_2 catalysts*, the unsaturated S sites are potential catalytic sites for HER. The high abundance of the unsaturated S sites in the electrodes is possibly a reason for their higher HER activity in comparison to bulk crystalline MoS_2.

Lassalle-Kaiser et al. proposed that the surface catalysis of the *Merki* electrodes for HER is carried by Mo^{III} ions that are located in the surface layer and possess terminal disulphide ligands (S_2^{2-}) (Lassalle-Kaiser, Merki et al. 2015). The disulphide ligands serve as adsorption sites for atomic hydrogen via the formation of thiol groups (SH) (Lassalle-Kaiser, Merki et al. 2015). Our XAS analysis of the electrodes under HER conditions indicates a partial reduction of the Mo sites from oxidation state IV to III (see **Table 1**). According to *Lassalle-Kaiser et al.*, this partial reduction can be assigned to the formation of catalytically active Mo^{III} ions in the surface layer (Lassalle-Kaiser, Merki et al. 2015).

The formation of single metal-hydrogen coordinations in the *Merki* electrodes is difficult to verify directly with XAS analysis, since H ligands are very weak backscatterers and, hence, hardly detectable in EXAFS when not occurring in a large coordination number.

Co AND Ni SITES OF THE *MERKI* ELECTRODES

The doping of the *Merki* electrodes at pH 7 with Co or Ni leads to a significant promotion of their catalytic HER activity, indicated by a significant increase in exchange current density and decrease in over-potential (Merki, Vrubel et al. 2012). Furthermore, the doping affects the magnitude of the redox currents occurring during HER (see **Figure 33**). At pH 0, the increase in catalytic activity of the doped electrodes can be solely attributed to the promotion of film growth and surface area by the doping (Merki, Vrubel et al. 2012). At pH 7, these promotion effects alone (3 fold increase in film growth and 1.5 – 3 fold increase in surface area) are not sufficient to account for the observed increase in exchange current density (12 fold), indicating that the doping improves the intrinsic activity as well (Merki, Vrubel et al. 2012). *Merki et al.* assumed that the dopants in the electrodes enhance the HER activity of the coordinatively unsaturated Mo and S sites in an analogous way as in crystalline MoS_2.

Our XAS analysis of the Co and Ni doped *Merki* electrodes at pH 7 does mainly provide information about the Mo, Co and Ni sites. The analysis indicates that the doping with Co or Ni does not affect the atomic structure of the Mo sites besides a tendency to increase the S coordination number of the Mo sites or the spatial order of their S shells. The small effect is only qualitatively visible in the EXAFS spectrum (see **Figure 37**) and is more prominent for the Co doping than for the Ni doping. This increase in S coordination number or spatial order for the S shell of the Mo sites suggests that the doping slightly diminishes the density of coordinatively unsaturated Mo or S sites, respectively, and, hence, could impede Mo-carried bulk catalysis to a small extent.

The CoS_6 and NiS_4 sites of the doped *Merki* electrodes (see **Figure 35**) experience under HER conditions (-0.8 V *vs.* NHE at pH 7) a decrease in mean S coordination number (lowering of S peak in the Co and Ni EXAFS, see **Figure 37**). The Co sites exhibit the largest decrease with 0.9 (from 6.2 ± 0.3 to 5.3 ± 0.3) followed by the Ni sites with 0.6 (from 4.3 ± 0.3 to 3.7 ± 0.3) (see **Table 14**). The S ligands might be

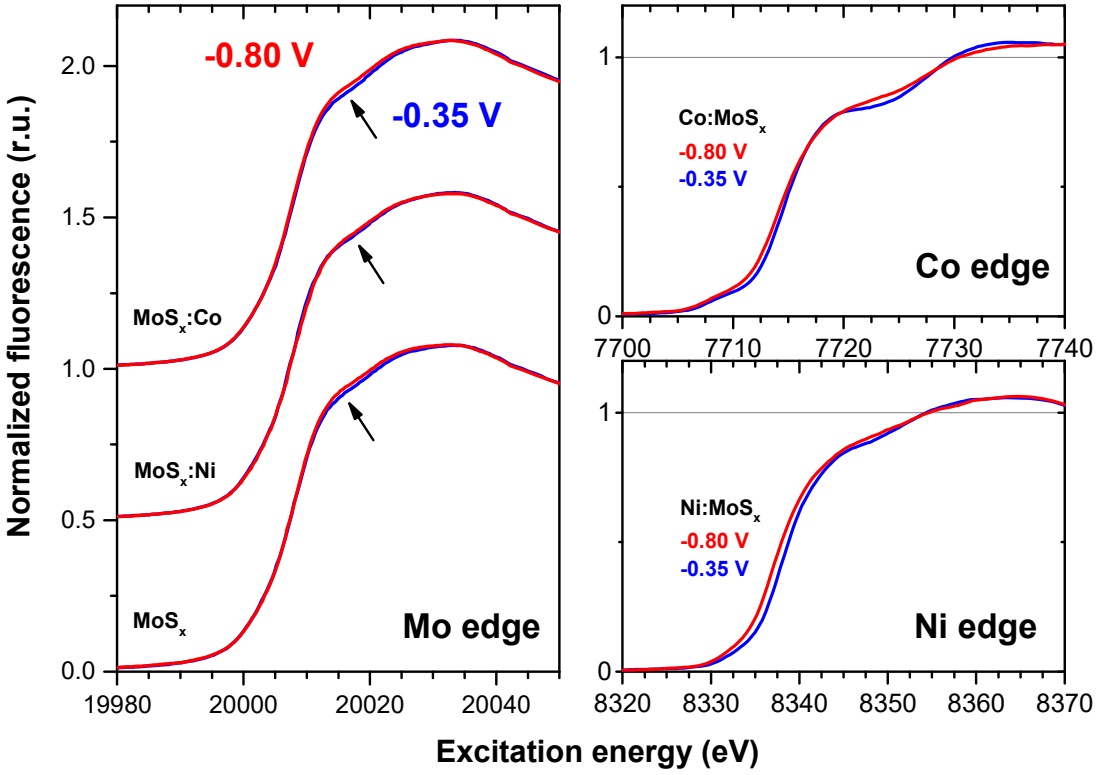

Figure 36

XANES spectra of the *Merki* electrodes at -0.80 V *vs.* NHE (H_2 evolution reaction) (**red** line) and -0.35 V (non-catalytic state) (**blue** line). **Left** side: XANES recorded at the Mo *K*-edge of the Co doped (left **top**), Ni doped (left **middle**) and undoped electrode (**left bottom**). **Right** side: XANES of the Co doped electrode recorded at the Co *K*-edge (**right top**) and of the Ni doped electrode recorded at the Ni *K*-edge (**right bottom**).This figure is a selective compilation of **Figure 14**, **Figure 21** and **Figure 27**.

removed from the dopant sites via H_2S formation during HER (as observed for Mo-S nano-particles by (Stellmach 2015)). The loss in S ligands at the dopant sites creates coordinatively unsaturated Co and Ni sites. These sites could improve the catalytic activity of the electrode as they are potential adsorption sites for atomic hydrogen. As for the unsaturated Mo sites, the possible HER mechanism might be analogous to the one of hydrogenase (Lubitz, Ogata et al. 2014). The unsaturated Co and Ni sites could bind hydrides and fuse them with protons adsorbed to neighbouring S ligands to form molecular hydrogen. Furthermore, the majority of the Co and Ni sites possesses a metal-metal coordination to a neighbouring Mo atom (see **Table 14**) that could be interpreted as a double-metal active site as present in NiFe or FeFe hydrogenases (Lubitz, Ogata et al. 2014). However, the decrease in S coordination number during HER is small, in particular for Ni, and could be also interpreted as an increase in spatial disorder of the S shell while the ligand number remains unmodified. In this case, the Co and Ni sites presumably promote the formation of coordinatively unsaturated S sites during catalysis which leads to an increase in the spatial disorder of their S shells. The dopant sites could stabilize unsaturated S sites via charge compensation (in analogy to the observed stabilization of catalytically active O defects via Fe ions in TiO_2-Fe systems (Wu and van de Krol 2012)).

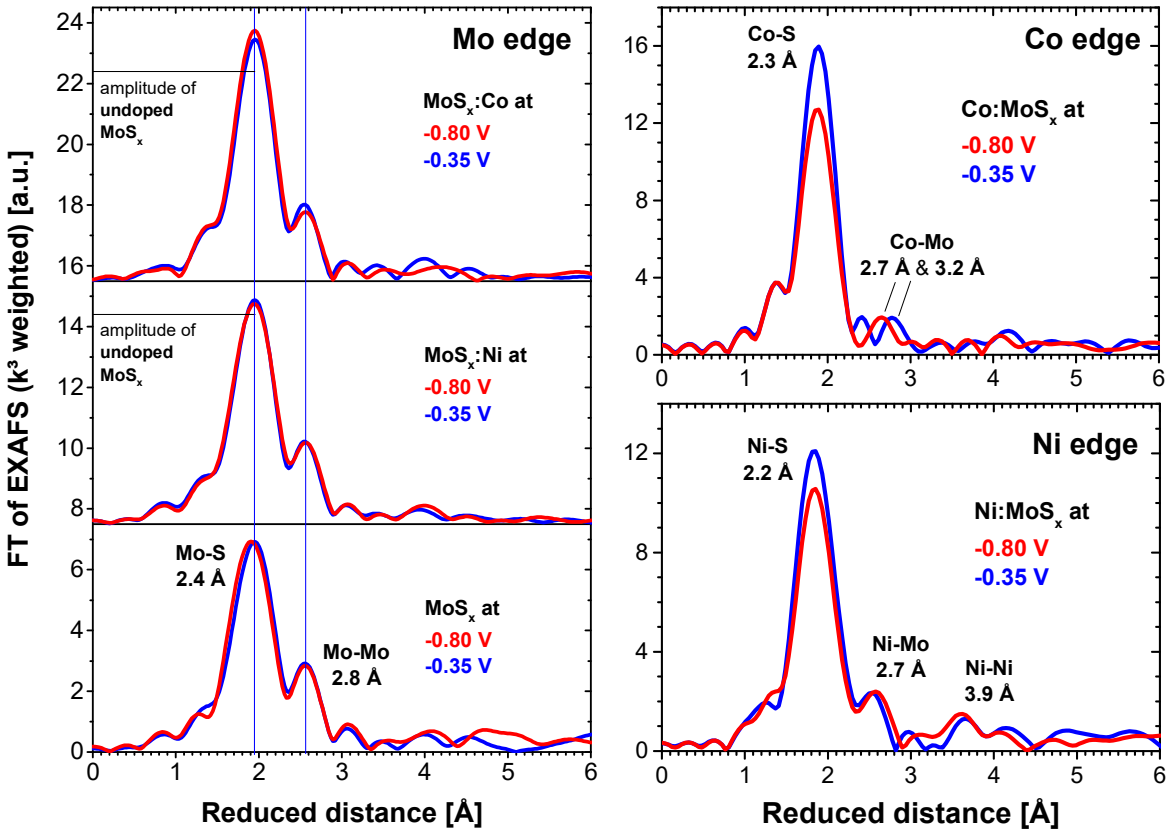

Figure 37

Fourier transforms (FT) of the k^3-weighted EXAFS spectra of the *Merki* electrodes at -0.80 V *vs.* NHE (H_2 evolution reaction) (**red** line) and -0.35 V (non-catalytic state) (**blue** line). **Left** side: EXAFS (*k* range = 3 – 12 $Å^{-1}$) recorded at the Mo *K*-edge of the Co doped (**left top**), Ni doped (**left middle**) and undoped electrode (**left bottom**). **Right** side: EXAFS (*k* range = 3 – 13 $Å^{-1}$) of the Co doped electrode recorded at the Co *K*-edge (**right top**) and of the Ni doped electrode recorded at the Ni *K*-edge (**right bottom**). This figure is a selective compilation of **Figure 16**, **Figure 22** and **Figure 28**.

The dopant sites exhibit more significant structural modifications under HER conditions (-0.80 V *vs.* NHE at pH 7) than the Mo sites. Additional to the modifications in the S shell, the dopant sites show a significant reduction of the Co and Ni ions (see alterations of Co and Ni XANES (X-ray absorption near-edge structure) in **Figure 36**). The Mo sites, however, exhibit no significant modifications of their Mo-S and Mo-Mo coordination (no significant alteration in Mo EXAFS, see **Figure 37**) and only a slight reduction of the Mo ions (see **arrow** in Mo XANES in **Figure 36**). This suggests an involvement of the Co and Ni sites in the HER catalysis and a higher reactivity for these sites than for the Mo sites. The Co and Ni doped electrodes could contain a smaller density of unsaturated Mo or S sites than the undoped electrode but, at pH 7, compensate this loss in catalytically active sites with the superior reactivity of their dopant sites.

The dopant sites, Co and Ni, exhibit shorter S distances with 2.22 – 2.26 Å than the Mo sites with 2.37 – 2.38 Å (see **Table 13**). This difference could affect the catalytic activity of the sites, since the S shell

	***Merki* film**	mean **S distance** [Å]	
		-0.80 V *vs.* NHE	**-0.35 V**
Mo	**Undoped**	**2.37** ± 0.01	**2.38** ± 0.01
	Ni doped	**2.37** ± 0.01	**2.38** ± 0.01
	Co doped	**2.38** ± 0.01	**2.38** ± 0.01
Ni	**Ni doped**	**2.22** ± 0.01	**2.22** ± 0.01
Co	**Co doped**	**2.25** ± 0.01	**2.26** ± 0.01

	***Merki* film**	mean **Mo distance** [Å]	
		-0.80 V *vs.* NHE	**-0.35 V**
Mo	**Undoped**	**2.81** ± 0.01	**2.80** ± 0.01
	Ni doped	**2.81** ± 0.01	**2.79** ± 0.01
	Co doped	**2.81** ± 0.01	**2.79** ± 0.01
Ni	**Ni doped**	Mo: **2.67** ± 0.01 Ni: **3.85** ± 0.02	Mo: **2.67** ± 0.01 Ni: **3.87** ± 0.03
Co	**Co doped**	**2.72** ± 0.01	**3.19** ± 0.01

Table 13

Distances to S, Mo and Ni at the Mo, Ni and Co site in the *Merki* electrodes. This table is a selective compilation of **Table 3**, **Table 11** and **Table 6**. The presented values were determined via EXAFS simulations. For more details, see the description at the source tables.

is significantly involved in HER. The dopant sites also possess shorter Mo distances with 2.67 - 2.72 Å (under HER conditions) than the Mo site with 2.79 – 2.81 Å (see **Table 13**). This could affect their activity as well, since Co/Ni-Mo coordinations, according to (Eijsbouts 1997) and (Taniguchi, Imamura et al. 1999), are involved in the catalytic mechanism.

The Co and Ni sites show different behaviour in XAS during HER (= doped *Merki* electrodes at -0.80 V *vs.* NHE). The Co sites exhibit a stronger modification of their S coordination in the EXAFS (see **Figure 37**) than the Ni sites while the latter show a more prominent reduction of their metal ions in the XANES (see **Figure 36**). This suggests that the catalytic mechanism of HER and/or its effectivity differ between the Co and Ni sites. A reason for that could be the difference in atomic structure between the two dopant sites.

The Co sites exhibit an atomic structure that is similar to the "Co-Mo-S" phase (see **Figure 25**), responsible for the major catalytic activity of hydrodesulphurization (HDS) $CoMoS_2$ catalysts (selection of XAS studies in (Bouwens, van Veen et al. 1991, Craje, Louwers et al. 1992, de Bont, Vissenberg et al.

	Merki film	mean **S coordination number**	
		-0.80 V *vs.* NHE	**-0.35 V**
Mo	**Undoped**	**4.7** ± 0.5	**4.7** ± 0.4
	Ni doped	**5.0** ± 0.4	**5.1** ± 0.5
	Co doped	**5.3** ± 0.3	**5.0** ± 0.4
Ni	**Ni doped**	**3.7** ± 0.3	**4.3** ± 0.3
Co	**Co doped**	**5.3** ± 0.3	**6.2** ± 0.3

	Merki film	mean **Mo coordination number**	
		-0.80 V *vs.* NHE	**-0.35 V**
Mo	**Undoped**	**0.9** ± 0.1	**1.0** ± 0.1
	Ni doped	**1.0** ± 0.1	**0.9** ± 0.1
	Co doped	**0.8** ± 0.1	**0.7** ± 0.1
Ni	**Ni doped**	Mo: **0.9** ± 0.2 Ni: **1.2** ± 0.4	Mo: **0.9** ± 0.2 Ni: **0.8** ± 0.4
Co	**Co doped**	**0.9** ± 0.1	**0.9** ± 0.2

Table 14

Coordination numbers of S, Mo and Ni for the Mo, Ni and Co site in the *Merki* electrodes. This table is a selective compilation of **Table 4**, **Table 11** and **Table 6**. The presented values were determined via EXAFS simulations. For more details, see the description at the source tables.

1998, Miller, Marschall et al. 2001, Kadono, Kubota et al. 2006, Okamoto, Kato et al. 2009, Dugulan, van Veen et al. 2013)). There, the phase consists of Co ions coordinated to five or six S ligands that form Co-S clusters on the edge of MoS_2 crystallites. The structural similarity between the Co sites and the Co-Mo-S phase suggests that the catalytic mechanisms in both structures might be similar as well. For the Co-Mo-S phase, the review of (Eijsbouts 1997) presents several hypotheses for the basic catalytic mechanisms. One of the hypotheses is that an electron transfer takes place from the Co to the Mo site, removing antibonding electrons from the Co site. Thus, the Co site can offer more binding spots for reactants. Another hypothesis is the contact synergy model (Eijsbouts 1997). The Co and Mo sites in this model are part of two distinct phases that have an intimate contact to each other. Due to this contact, the Mo site is provided with over-spill hydrogen from the Co site, enhancing the catalytic activity of the Mo site. Both hypotheses for the catalytic mechanism of the Co-Mo-S phase require a strong interaction between the Co and Mo sites. The Co-Mo coordination of the *Merki* electrodes during HER is similar to the Co-Mo-S phase (see **Table 6**) and, hence, could enable a comparable Co-Mo interaction.

The Ni sites of the *Merki* electrodes exhibit an atomic structure similar to cubane-type NiMo sulphide clusters as $[Mo_3NiS_4(H_2O)_{10}]^{4+}$ (Shibahara, Yamasaki et al. 1991) and $[Mo_3NiS_4Cl(H_2O)_9]^{3+}$ (Shibahara, Yamasaki et al. 1991, Taniguchi, Imamura et al. 1999) (see **Figure 19**). (Taniguchi, Imamura et al. 1999) uses the latter of the sulphide clusters as pre-cursor for the preparation of HDS catalysts; and shows that the Ni-Mo-S linkage of the cluster is preserved in the catalysts and enhances their activity. A fraction of the Ni sites in the *Merki* electrodes possesses a Ni-Mo-S linkage as in the sulphide clusters (see **Table 11**), leading to a higher catalytic activity of the Ni doped electrode in comparison to the undoped electrode. The Ni-Mo-S linkage might play a similar role in the catalytic mechanism as the Co-Mo coordination of the Co sites.

In contrast to the Co sites, the Ni sites exhibit a direct metal-metal coordination to neighbouring Ni sites. The distance of the Ni-Ni coordination is longer than 3 Å (see **Table 13**), indicating a long-range order for the atomic structure of the Ni site. This suggests a more cohesive and, hence, more distinct phase for the Ni sites than for the Co sites. Hence, the catalytic mechanism of the Ni sites could be more similar to the contact synergy model of the Co-Mo-S phase (described in the review of (Eijsbouts 1997)) than the one of the Co sites.

CONCLUSIONS

The Co doped, Ni doped and undoped *Merki* MoS_x electrodes were investigated with X-ray absorption spectroscopy (XAS) at the Mo *K*-edge to gain insight into the atomic structure of their Mo sites. For the doped electrodes, additional XAS measurements were performed at the Co or Ni *K*-edge to obtain information about the atomic structure of the Co and Ni sites. The XAS spectra were recorded at electrode potentials of -0.80 V, -0.35 V and +1.40 V *vs.* normal hydrogen electrode (NHE) under neutral conditions (pH 7), to study structural differences between Mo, Co and Ni sites in a state of catalytic hydrogen-evolution reaction (HER) (-0.80 V), in a non-catalytic state (-0.35 V) and under conditions of water-oxidation (+1.40 V) (standard electrode potential of hydrogen reduction E^0_{H2} = -0.41 V and of water-oxidation E^0_{O2} = +0.82 V at pH 7).

Our XAS analysis indicates that the bulk of the Co/Ni doped and undoped *Merki* electrodes at pH 7 (Merki, Vrubel et al. 2012) comprises an amorphous MoS_x species (x = 2 or 3). For all electrodes, the atomic structure of the species is composed of Mo^{IV} ions coordinated to presumably five S atoms in the first coordination sphere and to a proximate Mo atom in the second sphere (see **Figure 35**). The Mo sites of the electrodes combine structural features of $Mo^{IV}S_2$ and MoS_3, as the mean Mo-S distance of 2.37 – 2.38 Å is typical for $Mo^{IV}S_2$ while the mean Mo-Mo distance of 2.79 – 2.81 Å as well as the low Mo coordination number are characteristic for MoS_3. The Mo-S coordination in the *Merki* electrodes exhibits a higher spatial disorder of the S coordination sphere (Debye-Waller parameter σ_S = ±0.08 Å) than in crystalline $Mo^{IV}S_2$ (σ_S = ±0.03 Å), suggesting a higher abundance of coordinatively unsaturated S sites. Furthermore, the Mo sites in the *Merki* electrodes seem to possess less S ligands (mean S coordination number N_S = 4.7 – 5.3) than in crystalline $Mo^{IV}S_2$ (N_S = 6), suggesting the presence of coordinatively unsaturated Mo sites. A six-fold S coordination of the Mo sites is not favoured by EXAFS simulations (EXAFS = extended X-ray absorption fine structure) (see **Table 2**) but cannot be excluded. The unsaturated S and Mo sites are possible adsorption sites for atomic hydrogen and, therefore, potential catalytic sites for HER. The higher density of unsaturated S and Mo sites in the *Merki* electrodes compared to bulk crystalline $Mo^{IV}S_2$ could explain the higher catalytic activity of the electrodes (Merki, Fierro et al. 2011, Merki, Vrubel et al. 2012). The presence of these unsaturated sites throughout the bulk of the *Merki* electrodes suggests that the bulk participates in the HER catalysis. This could be enabled via proton diffusion into the bulk (proposed by *Casalongue et al.*) supported by the porosity of the electrodes (Merki, Vrubel et al. 2012, Casalongue, Benck et al. 2014).

Our electrochemical studies on the *Merki* electrodes under neutral conditions (pH 7) also suggest a participation of the MoS_x bulk in HER catalysis. Cyclic voltammetry of the undoped *Merki* electrode (= pure MoS_x) under HER conditions shows redox currents (see **Figure 33**) that indicate the occurrence of redox equivalents approximately equal (order of magnitude estimate) in number to Mo and S atoms present in the electrode (see **Table 12**). Rather than the Mo ions itself, S sites appear to be crucial for the redox chemistry, since XAS analysis indicates only a minor change in mean oxidation state for the Mo ions when comparing non-catalytic and catalytic potentials (see **arrow** in **Figure 36**). This sub-stoichiometric reduction of Mo^{IV} ions to Mo^{III} could be related to HER catalysis at the electrode surface as previously suggested by *Lassalle et al.* (Lassalle-Kaiser, Merki et al. 2015).

In the Co/Ni doped *Merki* electrodes, the MoS_x bulk is permeated by Co or Ni sites. Our XAS analysis indicates that the Co sites consist of $Co^{II,III}$ ions coordinated to six S atoms in the first coordination sphere while the Ni sites consist of $Ni^{I,II}$ ions coordinated to four S atoms (see **Figure 35**). The majority

of the Co and Ni sites is directly coordinated to a neighbouring Mo atom, suggesting an incorporation of the sites in the MoS_x bulk. During HER catalysis at pH 7, the Co and Ni sites exhibit a decrease in S coordination number (see **Table 14**) and/or spatial order of the S coordination sphere, suggesting the formation of coordinatively unsaturated dopant sites and/or S sites. These sites are potential catalytic sites for HER, in analogy to the unsaturated S and Mo sites of the MoS_x bulk. This is especially evident for the Co sites, as their atomic structure likely is similar to the catalytic site of $CoMoS_2$ catalysts for hydrodesulphurisation. A direct involvement of the Co and Ni sites in HER catalysis is also supported by our electrochemical studies on the doped *Merki* electrodes, since cyclic voltammetry suggests (i) an influence of the dopant ions (Ni or Co) on the number of reducing equivalents accumulated when comparing catalytic with non-catalytic potentials (see **Table 12**), and (ii) a clear shift in the midpoint potential of the corresponding redox transition to less negative value by doping with Co or Ni ions (see **Figure 33**). The Co and Ni sites may be directly involved in active-site formation at catalytic potentials, since our XAS analysis suggests more significant structural modifications and oxidation state changes for the dopant sites than for the Mo sites (see **Figure 36** and **Figure 37**). The effect of the Co/Ni doping on the atomic structure of the MoS_x bulk material is small, leading only to a slight diminishment in density of unsaturated Mo or S sites for the doped *Merki* electrodes.

The intrinsic HER activity of the *Merki* electrodes under neutral conditions (pH 7) can be promoted by the doping with Co or Ni (Merki, Vrubel et al. 2012). The promotion effect in the doped electrodes could arise from the additional presence of unsaturated dopant and/or S sites and from the superior reactivity of the dopant sites in comparison to the Mo sites. The *Merki* electrodes possibly form a S-bound hydride whose reactivity and/or formation is promoted by the doping with Co or Ni. The HER mechanism of the electrodes most likely involves coordinatively unsaturated metal ions (Mo, Co and Ni) and S sites and could be analogous to the one in hydrogenases where molecular hydrogen is formed by the interplay between a hydride-binding metal site and a proton-binding pendant base in close proximity (Lubitz, Ogata et al. 2014).

WATER OXIDATION

RESULTS AND DISCUSSION

X-ray absorption near-edge structure (XANES) and extended X-ray absorption fine-structure (EXAFS) of the Co doped, Ni doped and undoped MoS_x *Merki* electrodes (x = 2 or 3) were recorded at the Mo *K*-edge to gain insight into the atomic structure of their Mo sites. To study the structure of the sites under conditions for water-oxidation, the electrodes were conditioned (12 min, pH 7) and frozen at +1.40 V

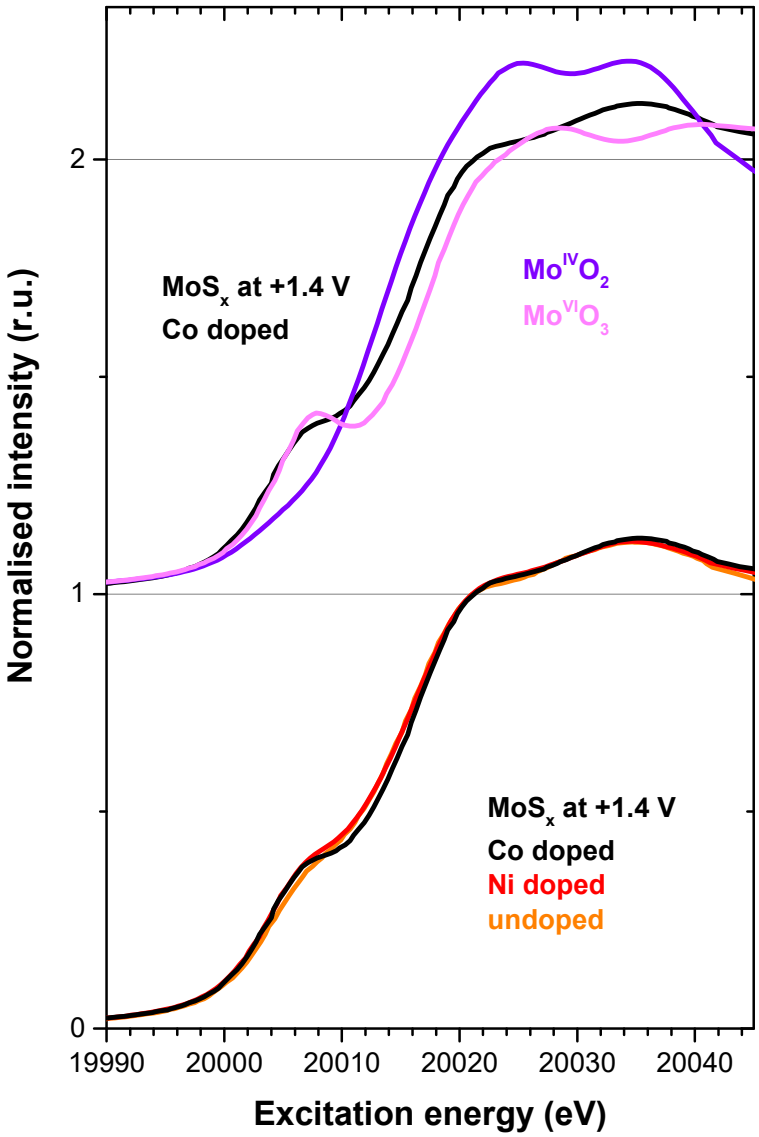

Figure 38

XANES spectra recorded at the Mo *K*-edge: Co doped (**black** line), Ni doped (**red** line) and undoped (**orange** line) MoS_x *Merki* electrodes at +1.40 V *vs.* NHE; $Mo^{IV}O_2$ (**violet** line) and $Mo^{VI}O_3$ (**pink** line).

vs. normal hydrogen electrode (NHE) (standard electrode potential of water oxidation = +0.82 V at pH 7).

Under water-oxidation conditions (+1.40 V *vs.* NHE), the X-ray absorption near-edge structure (XANES) spectra of the *Merki* electrodes exhibit a position of the Mo absorption edge located between the edges of $Mo^{IV}O_2$ and $Mo^{VI}O_3$ (see **Figure 38**). This indicates that the electrodes at +1.40 V consist of Mo ions with a mean oxidation state between IV and VI. Using the $Mo^{IV}O_2$ and $Mo^{VI}O_3$ edge positions as reference, a quantitative determination yields a Mo oxidation state of five (see **Table 15**). The XANES of the +1.4 V electrodes exhibit an edge shape similar to MoO_3, in particular the presence of a pre-edge (see **Figure 38**). This suggests that the Mo ions in the electrodes are coordinated to O ligands, possibly in a six-ligand geometry similar to MoO_3.

	Edge position [eV]	**Oxidation state**
MoS_3 at **+1.4V**	20016.1	4.8
MoS_3:Ni at **+1.4V**	20016.2	4.8
MoS_3:Co at **+1.4V**	20016.6	5.0
$Mo^{IV}O_2$	20014.7	4.0
$Mo^{VI}O_3$	20018.3	6.0

Table 15

Mo *K*-edge positions of the *Merki* electrodes at +1.40 V *vs.* NHE and their corresponding mean oxidation states for Mo. The oxidation states were interpolated via a linear function of the edge position calibrated with the edge positions of the $Mo^{IV}O_2$ and $Mo^{VI}O_4$ reference. The edge positions were determined with the integral method as described in (Dickinson and Pauling 1923, Dau, Liebisch et al. 2003) but with a different interval of integration. The interval started at a higher normalized intensity of 0.5 to exclude possible pre-edges from integration.

The extended X-ray absorption fine-structure (EXAFS) of all +1.4 V electrodes exhibit three prominent peaks, labelled as **1**, **2** and **3** (see **Figure 40**). A comparison with the spectrum of MoO_3 suggests that peak **1** can be assigned to a Mo-O coordination and peak **3** possibly to a Mo-Mo coordination (see **Figure 40**). Both peaks presumably belong to a Mo-O species similar to MoO_3. A comparison with the spectrum of a *Merki* electrode indicates that peak **2** can be assigned to a Mo-S coordination similar to the one present in the electrodes at -0.8 V or -0.35 V (see **Figure 40**). Therefore, the +1.4 V electrodes seem to contain two Mo species, a Mo-S and a Mo-O species. In all +1.4 V electrodes, the latter is the predominate species, since peak **1** exhibits a larger amplitude than peak **2** (see **Figure 40**).

In the EXAFS simulations, peak **1** (see **Figure 41**) can be simulated by two O coordination shells, one with a mean Mo-O distance of 1.70 – 1.71 Å (O1) and the other with a mean O distance of 1.99 – 2.04 Å (O2) (see **Table 16**). Both distances can be found in the O_6 octahedra of MoO_3 (see structure in **Figure 39**). The simulations of peak **2** (see **Figure 41**) yield a mean Mo-S distance of 2.36 – 2.40 Å (S1) (see **Table 16**) that matches with the Mo-S distances of the -0.8 V and -0.35 V electrodes (see **Table 3**). The sum of the simulated coordination numbers for O and S (= O1 + O2 + S1, see **Table 16**) are close to six, suggesting a mixture of two Mo species, one with six O ligands as in MoO_3 and the other with five to six S ligands as in the -0.8 V and -0.35 V electrodes. The EXAFS simulations of peak **3** (see **Figure 41**) suggest that the peak can be assigned rather to a Mo-S coordination than to a Mo-Mo coordination. The simulated Mo-S coordination contains two types of S ligands, one with a mean Mo-S distance of

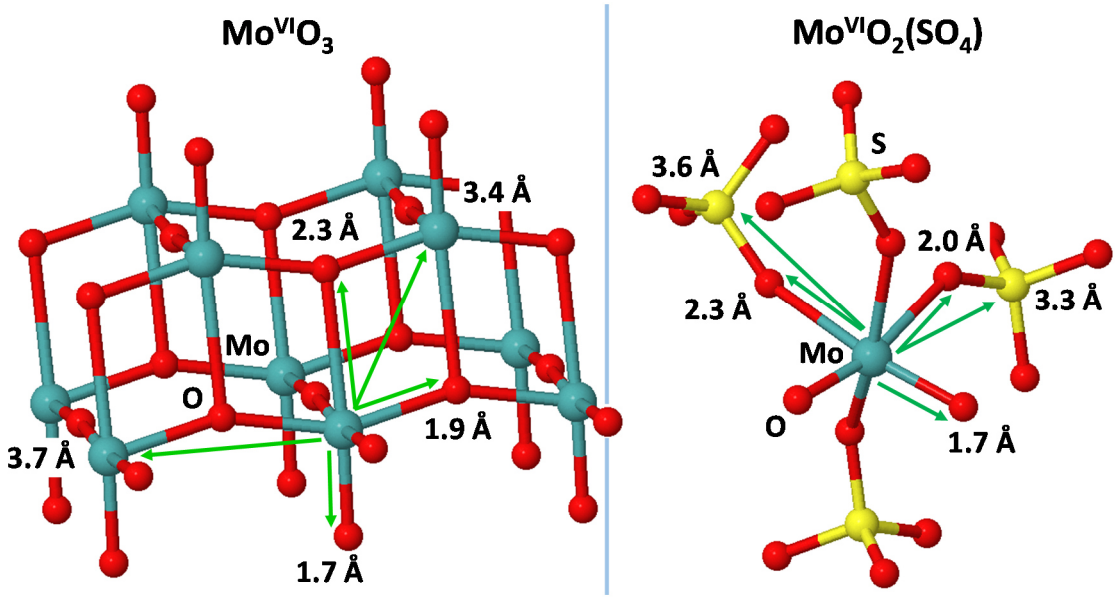

Figure 39

Schematic structures of $Mo^{VI}O_3$ (layered structure, side view on layer) and $Mo^{VI}O_2(SO_4)$ with denoted Mo-O, Mo-Mo and Mo-S distances. The images are based on crystal data published for MoO_3 in (Sitepu, O'Connor et al. 2005) and for $MoO_2(SO_4)$ in (Betke and Wickleder 2011).

3.33 – 3.34 Å (S2) and the other with a mean S distance of 3.64 – 3.65 Å (S3) (see **Table 16**). Both distances are close to the two types of Mo-μ-O-SO_4 bridges in $Mo^{VI}O_2(SO_4)$ (see **Figure 39**) (no XANES/EXAFS spectrum recorded). This suggests that, during the oxidation of the original Mo-S species in the electrodes, the S ligands are displaced from the first coordination sphere by O and form nearby SO_x groups similar to $MoO_2(SO_4)$. A long-range structure as in MoO_3 based on Mo-μ-O-Mo and Mo-(μ^3-O)$_2$-Mo bridges is probably not formed. In conclusion, the EXAFS simulations suggest that peak **1** and **3** can be assigned to a Mo-O species consisting of O_6 octahedra with a coordination to SO_x groups; and that peak **2** can be assigned to a Mo-S species similar to the one present in the -0.8 V and -0.35 V electrodes.

The Mo-O species presumably exhibits a Mo oxidation state of VI as MoO_3 and $MoO_2(SO_4)$ while the Mo-S species exhibits an oxidation state of IV as in the -0.8 V and -0.35 V electrodes. This results in an average oxidation state of Mo around five matching the estimated oxidation state from the XANES analysis (see **Table 15**).

The doping of the +1.4 V electrodes seems to effect the amplitudes of peak **1**, **2** and **3**. The Co doped electrode exhibits the largest amplitudes for peak **1** and **3**, followed by the Ni doped electrode and then the undoped electrode (see **Figure 40**). For peak **2,** the opposite behaviour is observed. This suggests that the Mo-O species, represented by peak **1** and **3**, is more prominent in the doped +1.4 V electrodes. The undoped electrode, instead, exhibits a stronger occurrence of the Mo-S species, represented by peak **2**. The doping, in particular with Co, seems to promote the presence of the Mo-O species in the +1.4 V electrodes.

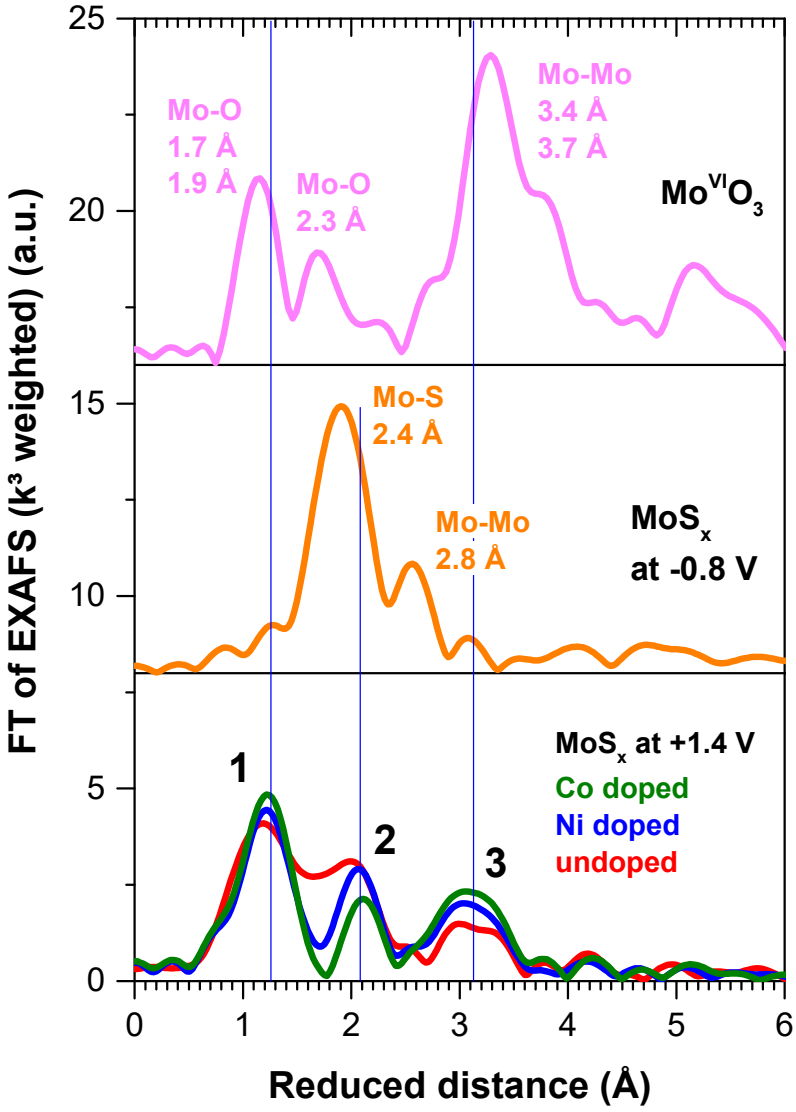

Figure 40

Fourier transforms (FT) of k^3 weighted EXAFS spectra (k range = 3 – 12 Å^{-1}) recorded at the Mo K-edge: Co doped (**green** line), Ni doped (**blue** line) and undoped (**red** line) *Merki* MoS_x electrodes at +1.40 V *vs.* NHE compared to $Mo^{VI}O_3$ (**pink** line) and the undoped *Merki* electrode at -0.80 V (**orange** line). The main peaks of MoO_3 and the undoped -0.8 V electrode are labelled with the corresponding Mo-ligand distances.

EXAFS simulations support these qualitative indications for a doping effect. The coordination number of S1 representing the original Mo-S species decreases by trend from the Co doped electrode, over the Ni doped electrode to the undoped electrode (see **Table 16**). Simultaneously, the coordination number of S2 and S3 representing the SO_x groups increases in the same order. This suggests that the conversion of the original Mo-S species into the Mo-O species is promoted by the doping, in particular with Co.

	mean **Mo-ligand distance [Å]**					
	O1	**O2**	**S1**	**S2**	**S3**	EXAFS
MoS_3:Co +1.4V	1.71 ± 0.01	2.00 ± 0.01	2.40 ± 0.01	3.33 ± 0.01	3.65 ± 0.01	
MoS_3:Ni +1.4V	1.70 ± 0.01	1.99 ± 0.01	2.38 ± 0.01	3.34 ± 0.01	3.64 ± 0.01	
MoS_3 +1.4V	1.70 ± 0.01	2.04 ± 0.03	2.36 ± 0.01	3.34 ± 0.03	3.65 ± 0.04	
$Mo^{VI}O_3$	1.67 – 2.47 Å					XRD
$Mo^{VI}O_2(SO_4)$	1.67 – 1.68 Å	2.03 – 2.05 Å 2.22 – 2.38 Å		3.29 – 3.37 Å	3.51 – 3.61 Å	
	mean **coordination number**					
	O1 + O2		**S1**	**S2 + S3**		EXAFS
MoS_3:Co +1.4V	4.9 ± 0.3		1.2 ± 0.1	3.2 ± 0.4		
MoS_3:Ni +1.4V	4.6 ± 0.5		1.7 ± 0.2	2.9 ± 0.5		
MoS_3 +1.4V	4.7 ± 0.9		1.9 ± 0.4	1.9 ± 1.0		
$Mo^{VI}O_3$	6					XRD
$Mo^{VI}O_2(SO_4)$	2	4		4		

Table 16

Structural parameters of the Mo ligand environment in the Co doped, Ni doped and undoped *Merki* electrodes at +1.40 V *vs.* NHE (conditions of water-splitting), compared to the crystal structure of MoO_3 (Sitepu, O'Connor et al. 2005, Sitepu 2009) and $MoO_2(SO_4)$ (Betke and Wickleder 2011). For the *Merki* electrodes, the structural parameters were obtained from fitting the Mo EXAFS spectra with O and S phase functions calculated from the crystal structure of MoO_3 (Sitepu, O'Connor et al. 2005, Sitepu 2009) and MoS_2 (Dickinson and Pauling 1923). To enable a direct comparison, the simulations of all electrodes were performed with the same Debye-Waller factors for O and S ($2\sigma_O^2$ = 0.016 Å^2 for O1 and O2, $2\sigma_S^2$ = 0.014 Å^2 for S1 and $2\sigma_S^2$ = 0.008 Å^2 for S2 and S3), the same amplitude reduction factor (S_0^2 = 0.93) and the same energy offset (E_0 = 1.4 eV). The value of σ_S for S1 was established by simulations of the -0.8 V and -0.35 V electrodes (see **Table 3**). The values of σ_O for O1 and O2, σ_S for S2 and S3 and E_0 were initially determined from a simulation of the Ni doped +1.4 V electrode. The value of S_0 was determined from a simulation of MoO_3 with a fixed O coordination number of six. The simulated EXAFS spectra are presented in **Figure 41**.

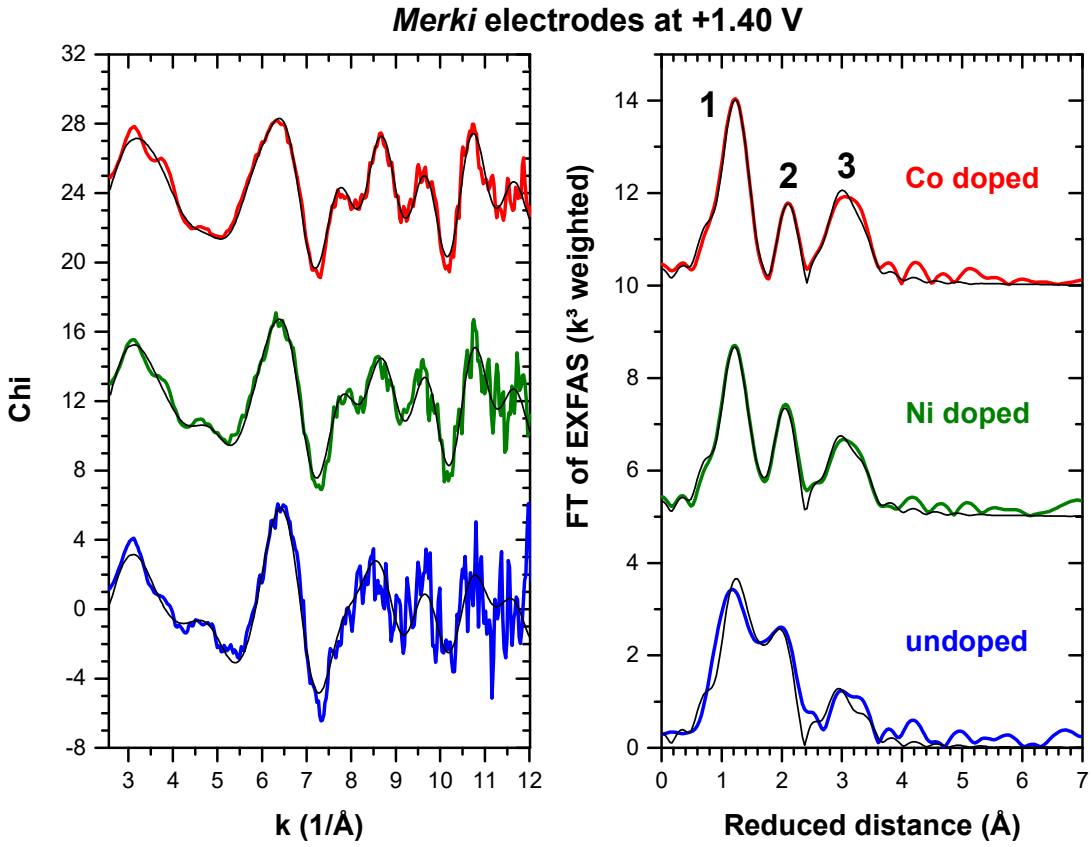

Figure 41

EXAFS simulations (**black** line) of the experimental spectra of the undoped (**blue** line), Ni doped (**green** line) and Co doped (**red** line) *Merki* electrode at +1.40 V *vs.* NHE. **Left** side: the EXAFS represented as χ spectra. **Right** side: Fourier transforms of the k^3 weighted EXAFS spectra. The EXAFS simulations and Fourier transforms were performed over the *k* range shown on the left side. The EXAFS simulations correspond to the structural parameters presented in **Table 16**.

SUMMARY

X-ray absorption near-edge structure (XANES) and extended X-ray absorption fine-structure (EXAFS) of the Co doped, Ni doped and undoped MoS_x *Merki* electrodes (x = 2 or 3) were recorded at the Mo *K*-edge to gain insight into the atomic structure of their Mo sites. To study the structure of the sites under conditions for water-oxidation, the electrodes were conditioned (12 min, pH 7) and frozen at +1.40 V *vs.* normal hydrogen electrode (NHE) (standard electrode potential of water oxidation E^0_{O2} = +0.82 V at pH 7).

Under conditions of water oxidation (+1.40 V *vs.* NHE), the *Merki* electrodes exhibit a dominant Mo-O contribution besides the original Mo-S species present in the electrodes at -0.80 V (H_2 formation) and -0.35 V (non-catalytic state but cathodic conditions). The oxide contribution of the +1.4 V electrode consists of Mo^{VI} ions coordinated to six O atoms in their first coordination sphere and to SO_x groups in the second sphere. The Mo-O coordination exhibits to mean O distances of 1.70 – 1.71 Å and 1.99 – 2.04 Å that can be found in the O_6 octahedra of $Mo^{VI}O_3$ (see **Figure 39**). The coordination to the SO_x groups shows mean Mo-S distances of 3.33 – 3.34 Å and 3.64 – 3.65 Å that are close to the distances of Mo-μ-O-SO_4 bridges present in $Mo^{VI}O_2(SO_4)$ (see **Figure 39**). A long-range structure as in MoO_3 based on Mo-μ-O-Mo and Mo-$(\mu^3\text{-O})_2$-Mo bridges is probably not present in the Mo-O contribution of the electrodes.

The doped +1.4 V electrodes contain a larger Mo-O contribution than the undoped electrode. In the extended X-ray absorption fine-structure (EXAFS), the doped electrodes, in particular when doped with Co, exhibit larger peaks for the Mo-O coordination and for the coordination to the SO_x groups than the undoped electrode (see peak **1** and **3** in the Fourier transform of the EXAFS in **Figure 40**). The undoped +1.4 V electrode, on the other hand, exhibits a larger peak for the original Mo-S species as present in the electrodes under conditions of H_2 formation (see peak **2** in **Figure 40**). This suggests that the Mo-S species is transformed into the Mo-O contribution and that the transformation is promoted by the doping, in particular with Co.

During the oxidation of the electrodes at +1.4 V, S is possibly displaced from the first coordination sphere by O and forms nearby SO_x groups. EXAFS simulations indicate a total coordination number of the first coordination sphere close to six for the doped and undoped electrodes (sum of O1 + O2 + S1 in **Table 16**) while the proportion between O and S ligands varies among the electrodes.

The mean oxidation state of the Mo ions in the +1.4 V electrodes is V and, thereby, an average between the Mo^{IV} ions of the original Mo-S species and the Mo^{VI} ions of the formed Mo-O contribution (see **Table 15**).

RESULTS AND DISCUSSION

X-ray absorption near-edge structure (XANES) and extended X-ray absorption fine-structure (EXAFS) of the Co doped MoS_x *Merki* electrodes (x = 2 or 3) were recorded at the Co *K*-edge to gain insight into the atomic structure of their Co sites. To study the structure of the sites under conditions for water-oxidation, the electrodes were conditioned (12 min, pH 7) and frozen at +1.40 V *vs.* normal hydrogen electrode (NHE) (standard electrode potential of water oxidation = +0.82 V at pH 7).

Under water-oxidation conditions (+1.40 V *vs.* NHE), the X-ray absorption near-edge structure (XANES) of the Co doped *Merki* electrode at the Co *K*-edge (see **Figure 42**) is almost identical in shape and edge position with the spectrum of the *CoCat*, a well-known amorphous Co-oxide catalyst for water oxidation (Kanan, Surendranath et al. 2009, Risch, Khare et al. 2009). This indicates that the Co species in the electrode consists of $Co^{2+/3+}$ ions with a ligand environment of O and Co like in the *CoCat* (see **Figure 45**). However, the congruence between the electrode and *CoCat* spectrum is not perfect. A linear combination of the *CoCat* spectrum with the spectrum of the Co doped *Merki* electrode at -0.8 V

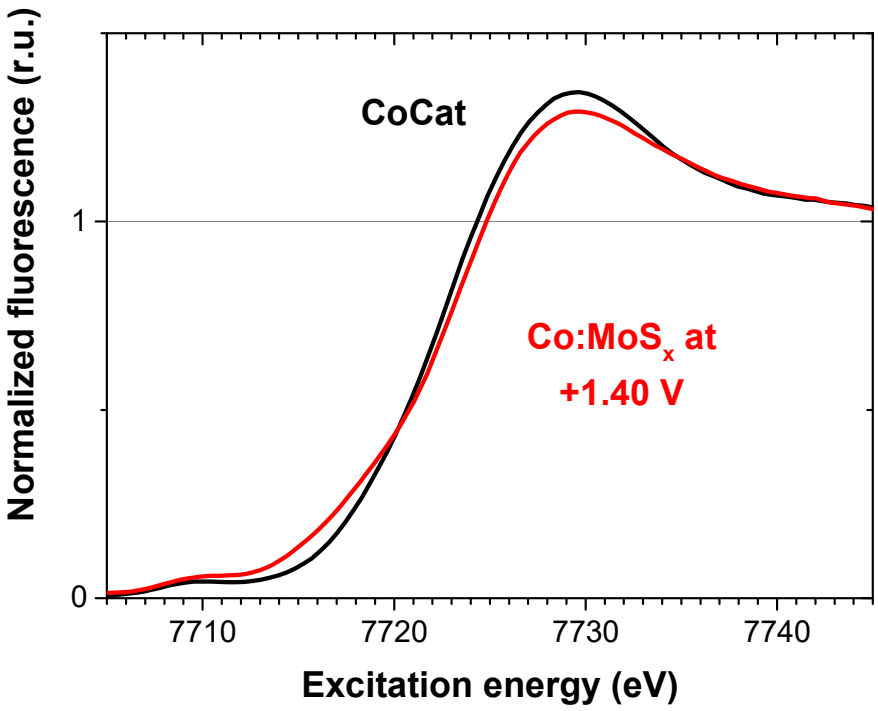

Figure 42

XANES spectra recorded at the Co *K*-edge: Co doped MoS_x *Merki* electrode at +1.40 V vs. NHE (**red** line); *CoCat*, amorphous Co-oxide catalyst for water-splitting (**black** line). The XANES data of the *CoCat* was recorded, analysed and published by Marcel Risch (Dickinson and Pauling 1923, Risch, Khare et al. 2009).

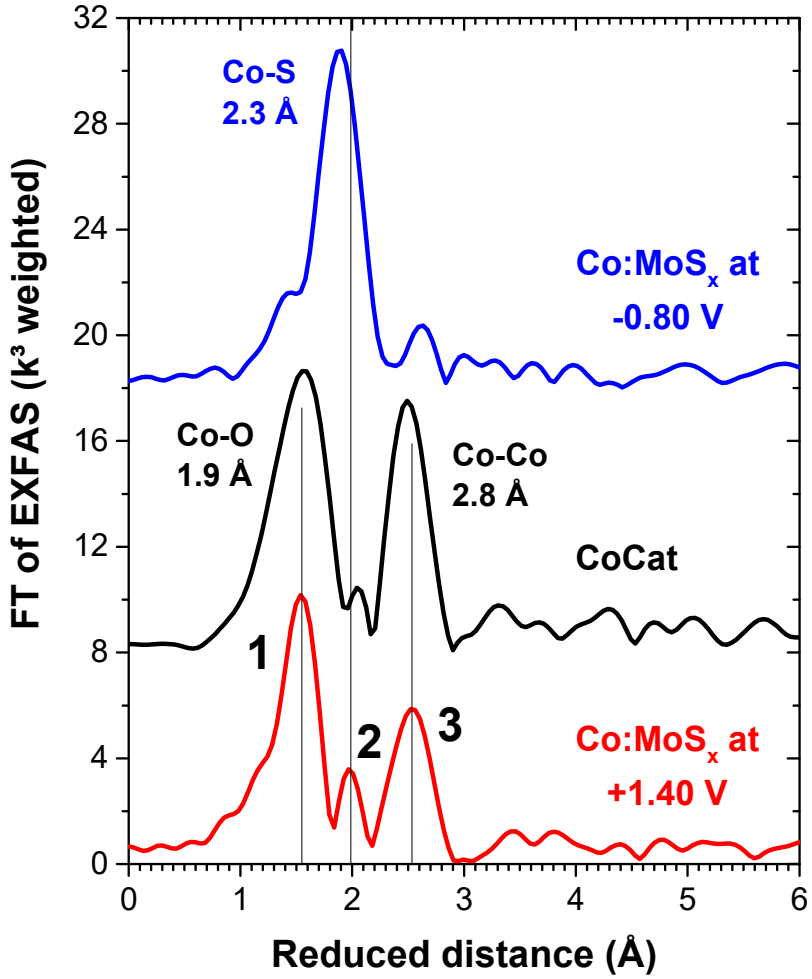

Figure 43

Fourier transforms (FT) of k^3 weighted EXAFS spectra (k range = 3 – 14 Å^{-1}) recorded at the Co *K*-edge: Co doped MoS_x *Merki* electrode at +1.40 V vs. NHE (**red** line) and at -0.80 V (**blue** line); *CoCat*, amorphous Co-oxide catalyst for water-splitting (**black** line). The EXAFS data of the *CoCat* was recorded, analysed and published by Marcel Risch (Hassel 1925, Risch, Khare et al. 2009). The main peaks of the -0.80 V *Merki* electrode and the *CoCat* are labelled with the corresponding Co-ligand coordination and distance.

yields a better coincidence with the +1.4 V spectrum than the *CoCat* spectrum alone. This indicates that the +1.4 V electrode still contains a fraction of the Co-S species which is characteristic for the -0.8 V electrode. However, suggested by the corresponding linear coefficient, this contribution is small accounting only for ≈10 % of the Co absorbers in the +1.4 V electrode. In conclusion, it seems that the conditioning of the electrode at +1.40 V oxidizes the original Co-S species to the well-known *CoCat* catalyst. However, a residual Co-S contribution is still present, since the oxidation is not completed during the conditioning.

The extended X-ray absorption fine-structure (EXAFS) confirms the conclusions from the XANES analysis. The Co EXAFS spectrum (see **Figure 43**) of the Co doped *Merki* electrode at +1.4 V exhibits three prominent peaks, labelled as **1**, **2** and **3**. When compared to the EXAFS of the *CoCat*, it seems

mean **absorber-ligand distance**				
Co edge	**Co-O** [Å]	**Co-S** [Å]	**Co-Co** [Å]	EXFAS
$Co:MoS_3$ +1.40 V	1.90 ± 0.01	2.27 ± 0.02	2.82 ± 0.01	
CoCat	1.88 – 1.90		2.79 – 2.82	
mean **coordination number**				
Co edge	**Co-O**	**Co-S**	**Co-Co**	
$Co:MoS_3$ +1.40 V	4.7 ± 0.3	1.0 ± 0.2	2.7 ± 0.3	
CoCat	5.2 – 6.2		3.1 – 6.1	

Table 17

Structural parameters of the Co ligand environment in the Co doped *Merki* electrode at +1.40 V *vs.* NHE (water-oxidation) compared to the corresponding parameters of the *CoCat* (published in (Risch, Khare et al. 2009)), an amorphous Co oxide catalyst for water oxidation. Listed are the type of the ligands, their Co-ligand distances and coordination numbers. The structural parameters were obtained from fitting the EXAFS spectrum of the +1.4 V electrode with S and Mo phase functions calculated from the crystal structure of $Co:MoO_4$, $Co:MoO_4 \cdot nH_2O$ and CoS. In the simulation, the amplitude reduction factor was fixed at $S_0^2 = 0.70$, a value established for the EXAFS simulations of the CoCat in (Risch, Khare et al. 2009). The Debye-Waller factors of O and Co were taken from (Risch, Khare et al. 2009) as well and were fixed at $\sigma_O = 0.051$ Å and $\sigma_{Co} = 0.069$ Å, respectively. The Debye-Waller factor of S was taken from simulations of the Co doped *Merki* electrode at cathodic potentials and was fixed at $\sigma_S = 0.063$ Å. The simulated EXAFS spectra are presented in **Figure 44**.

Crystal structure data for $Co:MoO_4$ obtained from (Smith and Ibers 1965), for $Co:MoO_4 \cdot nH_2O$ from (Eda, Uno et al. 2005) and for CoS from (Wyckoff 1963) and (Alsen 1925, Teo 1986, Penner-Hahn 1999).

that peak **1** and **3** of the electrode can be assigned to a Co-O and Co-Co coordination as present in this water-splitting catalyst. EXAFS simulations (see **Figure 44**) yield a Co-O distance of 1.90 Å and a Co-Co distance of 2.82 Å that are the same as reported in (Risch, Khare et al. 2009) for the *CoCat* (see **Table 17** and **Figure 45**). The simulated coordination numbers of O and Co with 4.7 and 2.7, respectively, are a bit lower than in the *CoCat* (see **Table 17**). Considering peak **2** of the +1.4 V electrode, a comparison with the EXAFS of the original -0.8 V electrode (see **Figure 43**) indicates that peak **2** can be assigned to a Co-S coordination. EXAFS simulations (see **Figure 44**) yield a mean S distance of 2.27 Å that is close to the one of the Co-S species in the -0.8 V electrode with 2.25 - 2.26 Å (see **Table 6**). The simulated coordination number of S is only 1.0 (see **Table 17**).

In conclusion, the EXAFS suggest, as the XANES analysis, a transformation of the original Co-S species into the *CoCat* catalyst. However, the Co-S peak (= **2** in **Figure 43**) in the +1.4 V electrode indicates that the transformation is not complete and, hence, a residual fraction of the original Co-S species is still present. This is also reflected in the *CoCat*-contribution of the +1.4 V electrode with an O and Co coordination number lower than in the *CoCat*.

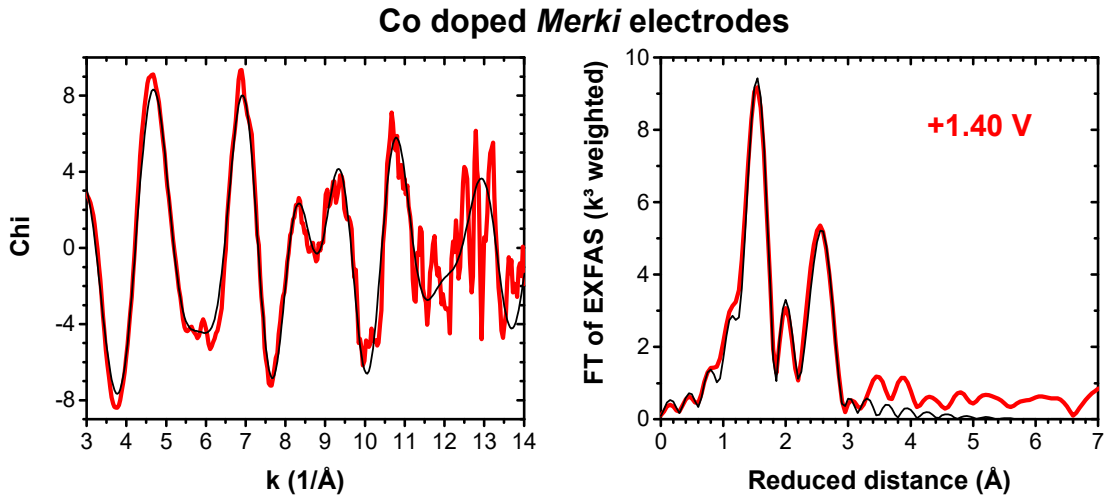

Figure 44

EXAFS simulations (**black** line) of the experimental spectra of the Co doped *Merki* electrode at +1.40 V *vs.* NHE (**red** line). **Left** side: the EXAFS represented as χ spectra. **Right** side: Fourier transforms of the k^3 weighted EXAFS spectra. The EXAFS simulations and Fourier transforms were performed over the *k* range shown on the left side. The EXAFS simulations correspond to the structural parameters presented in **Table 17**.

SUMMARY

X-ray absorption near-edge structure (XANES) and extended X-ray absorption fine-structure (EXAFS) of the Co doped MoS_x *Merki* electrodes (x = 2 or 3) were recorded at the Co *K*-edge to gain insight into the atomic structure of their Co sites. To study the structure of the sites under conditions for water-oxidation, the electrodes were conditioned (12 min, pH 7) and frozen at +1.40 V *vs.* normal hydrogen electrode (NHE) (standard electrode potential of water oxidation E^0_{O2} = +0.82 V at pH 7).

Under water-oxidation conditions (+1.40 V *vs.* NHE), the Co doped MoS_x *Merki* electrode (x = 2 or 3) experiences a transformation of the original Co-S species, present under cathodic conditions, into the well-known *CoCat* (Kanan, Surendranath et al. 2009, Risch, Khare et al. 2009), an amorphous Co-oxide catalyst for water-splitting (see **Figure 42** and **Figure 45**). In the +1.4 V electrode, the Co-O and Co-Co distance of 1.90 Å and 2.82 Å, respectively, (see **Table 17** and **Figure 43**) are the same as in the *CoCat*. However, the coordination number of O and Co in the +1.4 V electrode are a bit lower than in the *CoCat* (see **Table 17**). The difference is close to the S coordination number of the residual Co-S species in the +1.4 V electrode. The presence of this Co-S species indicates that the transformation into the *CoCat* has not been completed during the conditioning of the electrode at +1.40 V. The residual Co-S species exhibits a S distance of 2.27 Å that is close to the one of the original species in the Co doped *Merki* electrode at -0.80 V (see **Table 6**).

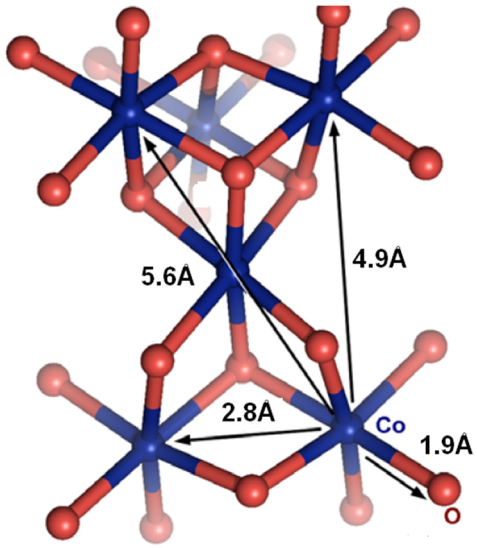

Figure 45

Atomic structure of the bulk *CoCat* proposed by (Risch, Khare et al. 2009). The here presented scheme was also produced by Marcel Risch.

CONCLUSIONS

X-ray absorption spectroscopy (XAS) spectra of the Co doped, Ni doped and undoped MoS_x *Merki* electrodes (x = 2 or 3) were recorded at the Mo *K*-edge to gain insight into the atomic structure of their Mo sites. For the Co and Ni doped electrodes, additional XAS spectra were recorded at the Co and Ni *K*-edge to obtain information about the atomic structure of their Co and Ni sites, respectively. To study the structure of the sites under conditions for water oxidation, the electrodes were conditioned (12 min, pH 7) and frozen at +1.40 V *vs.* normal hydrogen electrode (NHE) (standard electrode potential of water oxidation E^0_{O2} = +0.82 V at pH 7).

Under conditions for water oxidation, only the Co doped *Merki* electrode shows activity in form of an anodic current wave at +1.25 V *vs.* normal hydrogen electrode (NHE) in cyclic voltammetry (CV) (see wave **C** in **Figure 46**). The reason is that the Co sites in the electrode form the *CoCat* (established by (Kanan and Nocera 2008, Risch, Khare et al. 2009)), an amorphous Co-oxide catalyst for water oxidation. X-ray absorption near-edge structure (XANES) (see **Figure 42**) and extended X-ray absorption fine-structure (EXAFS) (see **Figure 43**) of the Co doped electrode at +1.4 V clearly indicate the formation of this catalyst. In the Ni doped electrode, under the same conditions (exposure to +1.4 V for 12 min), no analogous Ni oxide is formed, since X-ray absorption spectroscopy (XAS) indicates that all Ni is dissolved.

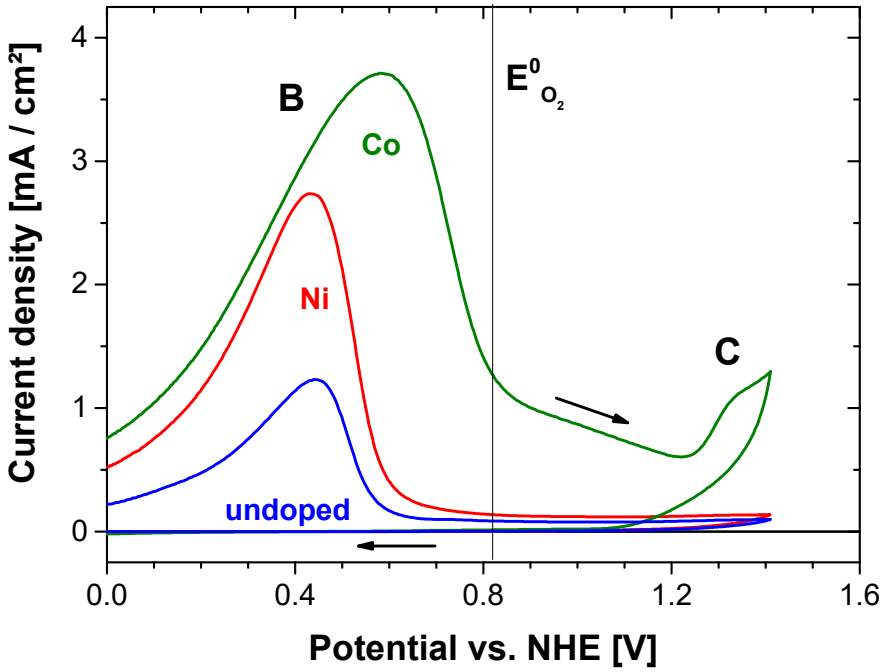

Figure 46

Cyclic voltammetry of the MoS_x *Merki* electrodes with a scan rate of 20 mV/s. Shown is the 1st cycle recorded on the (**blue** line) undoped, (**red** line) Ni doped and (**green** line) Co doped electrode (zoom-in from **Figure 47**). The standard potential of water oxidation, $\mathbf{E^0_{O2}}$, at pH 7.0 is marked by a vertical line. The scan direction is indicated by the arrows. The used electrolyte is 0.1 M potassium phosphate at pH 7.0. Before the cyclic voltammetry measurement, the electrolyte was degassed via flushing with N_2 and kept under N_2 atmosphere during the measurements.

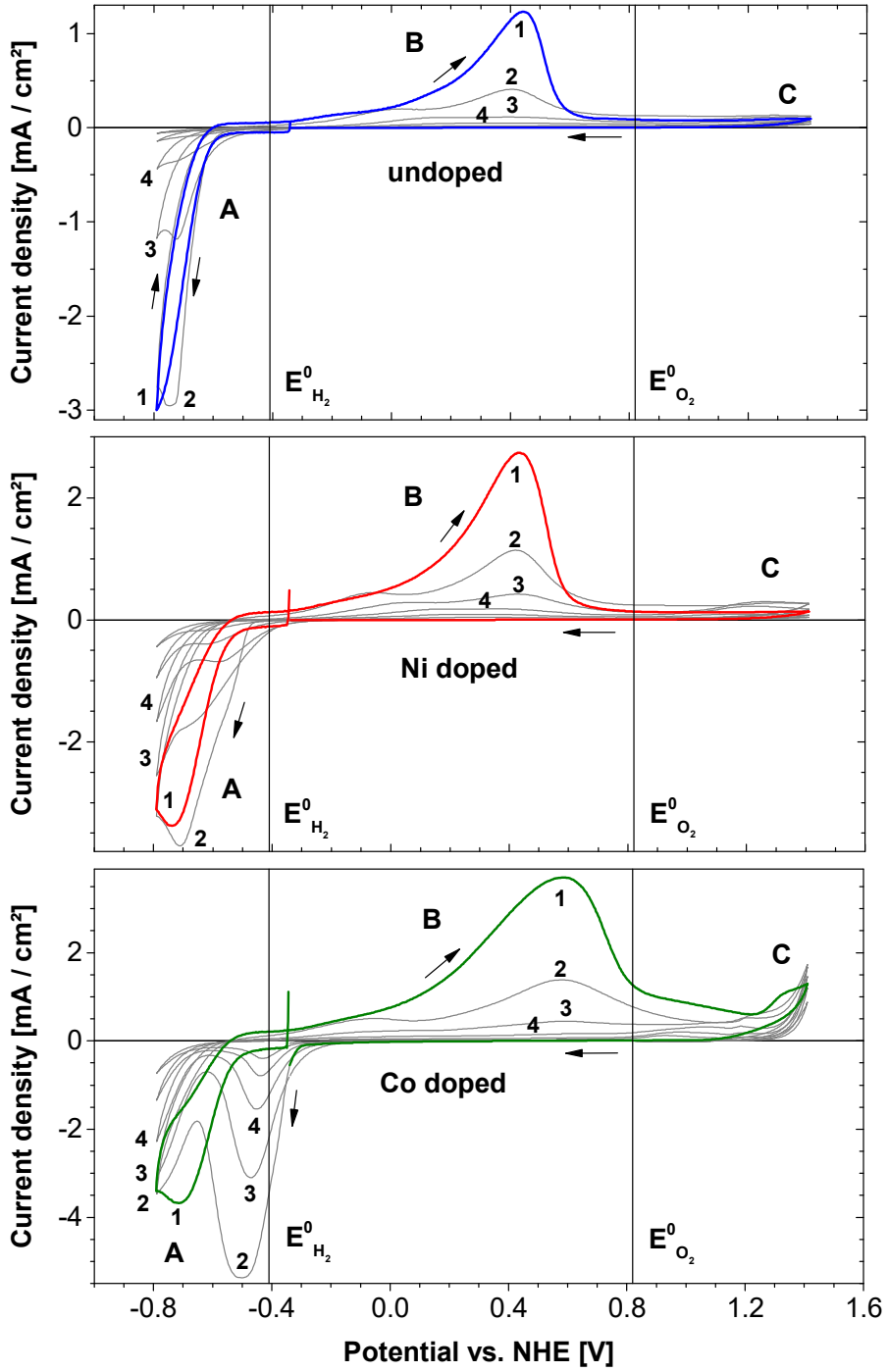

Figure 47

Cyclic voltammetry of the MoS_x *Merki* electrodes with a scan rate of 20 mV/s. Shown are all six cycles recorded on the (**blue** line) undoped, (**red** line) Ni doped and (**green** line) Co doped electrode. The 1st cycle is highlighted as coloured line and the residual cycles are shown as grey lines. All cycles are numbered in chronological order. The standard potential of water oxidation, $\mathbf{E^0_{O2}}$, and of hydrogen reduction, $\mathbf{E^0_{H2}}$, at pH 7.0 are marked by vertical lines. The scan direction is indicated by the arrows. The used electrolyte is 0.1 M potassium phosphate at pH 7.0. Before the cyclic voltammetry measurement, the electrolyte was degassed via flushing with N_2 and kept under N_2 atmosphere during the measurements.

The Mo sites in the *Merki* electrodes do not show a catalytic activity for water oxidation. In all +1.4 V electrodes, the XANES (**Figure 38**) and EXAFS (**Figure 40**) indicate that the Mo sites experience a partial transformation of the original Mo-S species into a Mo-O species ($Mo^{VI}O_6$ octahedra coordinated to SO_x groups). The doped electrodes possess a larger contribution of the Mo-O species than the undoped electrode. However, both Mo species seem to be inactive under water oxidation conditions, since the Ni doped electrode as well as the undoped electrode do not exhibit an anodic current wave comparable to the one of the Co doped electrode (see **Figure 46**).

The transformation of the original Mo-S species of the *Merki* electrodes into a Mo-O species can be assigned to the anodic current wave **B** around +0.5 V (see **Figure 46** and **Figure 47**) that originates from a partial oxidation of the sulphur presumably via the following reaction: $MoS_2 + 7H_2O \rightarrow MoO_3 + SO_4^{2-} + ½\ S_2^{2-} + 14H^+ + 11e^-$ (Bonde, Moses et al. 2008). The magnitude of the wave **B** correlates with the amount of Mo-S species present in the electrodes and, therefore, is larger for the doped electrodes than for the undoped electrode (see elemental analysis in **Table 12**). The transformation process is irreversible and leads to a dissolving of the Mo film on the electrodes when the electrode potential is cycled between -0.8 V and +1.4 V (see **Figure 47**). The film dissolution is indicated by a successive decrease in magnitude of wave **B** and of cathodic currents occurring under hydrogen evolution conditions (see **A** in **Figure 47**).

2. Catalytic Co electrode electrodeposited under reductive conditions

The X-ray absorption spectroscopy (XAS) data and analysis shown in this chapter are published in (Cobo, Heidkamp et al. 2012):

"A Janus cobalt-based catalytic material for electro-splitting of water"
Saioa Cobo, Jonathan Heidkamp, Pierre-André Jacques, Jennifer Fize, Vincent Fourmond, Laure Guetaz, Bruno Jousselme, Valentina Ivanova, Holger Dau, Serge Palacin, Marc Fontecave and Vincent Artero
Nature Materials 2012, **Vol 11**, 802-807
http://dx.doi.org/10.1038/nmat3385

Contributions:

- J. Heidkamp – X-ray absorption spectroscopy: entire data analysis, all measurements and sample preparations (incl. electro-deposition and conditioning of the Co electrodes)
- Co-workers - sample preparation, measurement and data analysis for all other used techniques aside from XAS

INTRODUCTION

Fuel cells and electrolysers typically require electro-catalysts based on noble metals like Pt or Ir. These metals are rare and, hence, expensive. The substitution of the noble metals in the catalysts with earth-abundant and, therefore, cheaper elements is necessary to improve the economic viability and to promote application.

For the oxygen-evolution reaction (OER), cobalt-based oxides (Kanan and Nocera 2008, Risch, Khare et al. 2009, Dau, Limberg et al. 2010, Jiao and Frei 2010, Yin, Tan et al. 2010, Chou, Ross et al. 2011, Shevchenko, Anderlund et al. 2011, Wee, Sherman et al. 2011), nickel (Dincă, Surendranath et al. 2010) and manganese-based oxides (Jiao and Frei 2010, Zaharieva, Najafpour et al. 2011) have been reported as robust electro-catalysts. Cobalt compounds, in particular, enabled innovative breakthroughs in the field of OER electro-catalysts in the past decade (Artero, Chavarot-Kerlidou et al. 2011).

For the hydrogen-evolution reaction (HER), cobalt compounds are promising as well. Several investigations reported a series of cobaloxime and diimine-dioxime compounds that show notable properties for HER at low over-potentials (Hu, Cossairt et al. 2005, Razavet, Artero et al. 2005, Baffert, Artero et al. 2007, Hu, Brunschwig et al. 2007, Jacques, Artero et al. 2009, Dempsey, Winkler et al. 2010, Fourmond, Jacques et al. 2010). However, for the application in devices, molecular catalysts have to be grafted onto an electrode material without degrading their catalytic activity (Le Goff, Artero et al. 2009). For the mentioned Co compounds, this has not been be achieved so far due to synthetic issues (Artero, Chavarot-Kerlidou et al. 2011).

To avoid the complications of a grafting process, we present an approach of forming a Co-based HER catalyst directly on the electrode via reductive electro-deposition (Cobo, Heidkamp et al. 2012). This method has been successfully applied for the preparation of MoS_2-based (Jaramillo, Jorgensen et al. 2007, Merki and Hu 2011) or NiMo-based (McKone, Warren et al. 2011, Reece, Hamel et al. 2011) HER catalysts as well. In *Cobo et al.*, an electro-catalytic Co-based material for HER and OER is electro-deposited from a solution of $Co(NO_3)_2{\cdot}6H_2O$ in an aqueous phosphate buffer at pH 7 onto an electrode made of fluorine tin-oxide or glassy carbon (Cobo, Heidkamp et al. 2012). The electro-deposition is convenient and the deposited catalyst is robust.

We perform X-ray absorption spectroscopy on the Co-based catalysts to gain insight into the atomic structure of the catalytic species at HER and OER.

This introduction text is based on a co-authored article (Cobo, Heidkamp et al. 2012).

PREPARATION

Preparation of Co electrode (*H_2-CoCat*) for XAS measurement

The *H_2-CoCat* for our X-ray absorption spectroscopy (XAS) studies was electrodeposited at -0.79 V *vs.* normal hydrogen electrode (NHE) on a glassy carbon (100 µm thick, 5 – 10 Ω) substrate for 3 h. The deposition solutions contained 0.5 mM $Co(NO_3)_2$ in a 0.5 M KH_2PO_4/K_2HPO_4 (KP_i) buffer (in *milliQ* water) at pH 7. For the conditioning, the *H_2-CoCat* was kept for 4 min at -0.79 V or +1.37 V in a cobalt-free 0.5 M KP_i buffer at pH 7, and then rapidly frozen in liquid N_2. *IR* compensation was applied. The deposition and conditioning were directly performed in an electrochemical cell (three-electrode system) embedded in a sample holder for XAS studies. A detailed description of this way of preparation is presented in the section *Freeze-quench preparation* of the *Methods* chapter. The used type of reference electrode was mercury-sulphate with an equilibrium potential of +0.65 V *vs.* NHE. The counter electrode was a Pt wire. The applied potentiostat was a *Biologic SP200* or *SP300*.

The *H_2-CoCat* was investigated by measurement and analysis of the Extended X-ray absorption fine-structure (EXAFS) and X-ray absorption near-edge structure (XANES) at the Co *K*-edge, to gain insight into the atomic structure of the material during H_2 formation and water oxidation. Therefore, the *H_2-CoCat* was conditioned and frozen prior to X-ray absorption spectroscopy (XAS) at electrode potentials of -0.79 V or +1.37 V *vs.* normal hydrogen electrode (NHE), respectively.

At both potentials, the Co EXAFS at the Co *K*-edge of the *H_2-CoCat* (see Fourier transforms in **Figure 48**) exhibit a strong contribution of a hexagonal close-packed phase of metallic Co (see structure scheme in **Figure 48**), indicated by the presence of peaks corresponding to metallic Co-Co coordinations. However, the amplitude of the metal peaks in the *H_2-CoCat* is ≈40 % lower in than in the metal reference. The damping of the peaks indicates the presence of a non-metallic Co species. The *H_2-CoCat* at +1.37 V additionally exhibits a non-metallic peak at 1.6 Å (see **arrow A** in **Figure 48**) and a shoulder at 2.6 Å (see **arrow B** in **Figure 48**). The former indicates the presence of a Co-O/N/C coordination and the latter the possible appearance of a non-metallic Co-Co peak. The non-metallic features of the *H_2-CoCat* EXAFS are more prominent at +1.37 V than at -0.79 V, indicating a larger non-metallic contribution at +1.37 V. The non-metallic contribution is crucial for the catalytic activity of the *H_2-CoCat*, since its electrochemical performance is much higher than of an electrode consisting of pure Co metal. Tafel analysis for the *H_2-CoCat* (performed and analysed by co-workers (Cobo, Heidkamp et

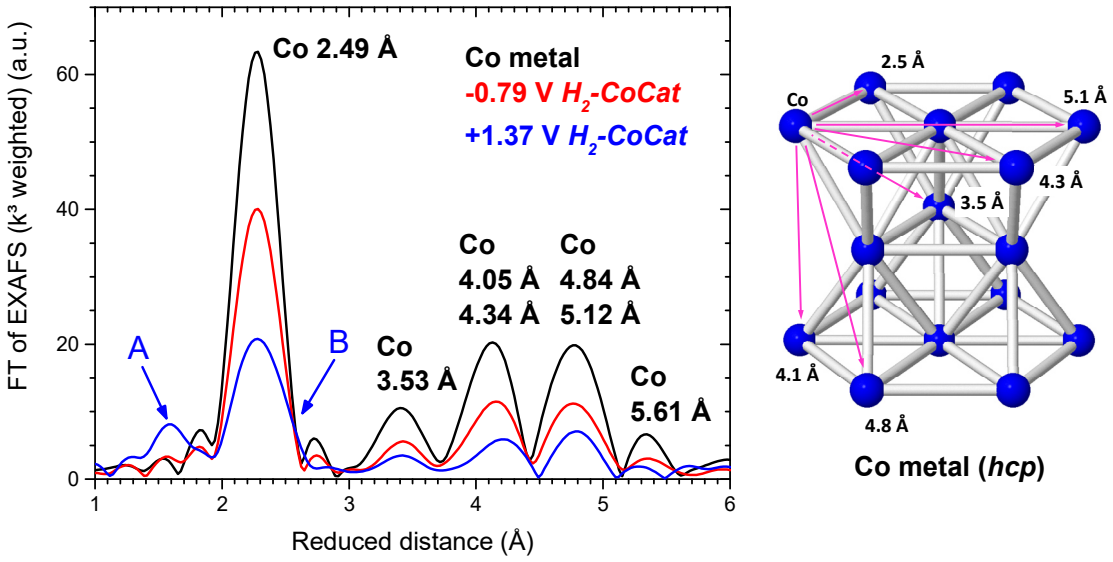

Figure 48

Left side: Fourier-transformed EXAFS spectra (k^3 weighted, *k* range = 3 – 16 $Å^{-1}$) recorded at the Co *K*-edge. **Red** trace: *H_2-CoCat* conditioned at -0.79 V *vs.* NHE. **Blue** trace: *H_2-CoCat* conditioned at +1.37 V. **Black** trace: Co metal foil (hexagonal close-packed state). The blue **arrows**, "A" and "B", mark features that are assignable to the contribution (≈50%, **Figure 52**) of a phase of edge-sharing CoO_6 octahedra in the *H_2-CoCat* at +1.37 V. The peaks of the Co metal are labelled with the corresponding Co-Co distances. **Right side:** Schematic structure of metallic Co^0 in the hexagonal close-packed phase (hcp). Image based on crystal data of Co metal published in (Wyckoff 1963).

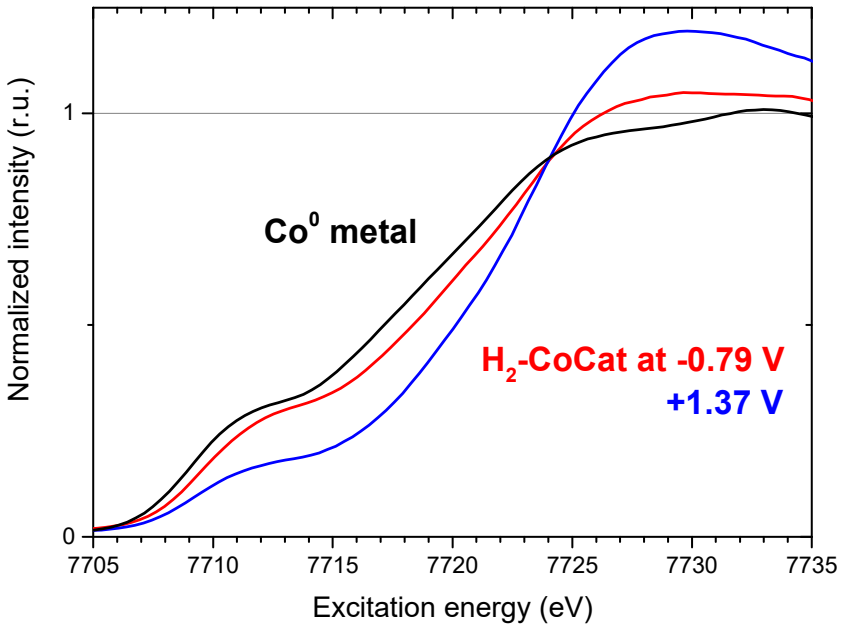

Figure 49

XANES spectra recorded at the Co *K*-edge. **Red** trace: *H_2-CoCat* conditioned at -0.79 V *vs.* NHE. **Blue** trace: *H_2-CoCat* conditioned at +1.37 V. **Black** trace: Co metal foil (hexagonal close-packed state).

al. 2012)) results in exchange current densities of $10^{-5.5}$ A/cm^2 that are three-times higher than for a comparable electrode of pure Co metal with 10^{-6} A/cm^2.

The Co XANES of the *H_2-CoCat* (see **Figure 49**) exhibits significant deviations from the spectrum of Co metal, indicating the presence of a non-metallic contribution. At both potentials, the amplitude of the absorption edge is higher than in the metal spectrum. Usually, a pronounced amplitude correlates with the occurrence of an O/N contribution. Furthermore, the edge position of the *H_2-CoCat* is shifted to excitation energies higher than in the metal spectrum, indicating the presence of a Co species with a less reduced oxidation state than in metallic Co^0. At +1.37 V, the deviations from the metal spectrum and the shift of the edge positions are larger than at -0.79 V. Hence, the non-metallic contribution is more prominent in the *H_2-CoCat* at +1.37 V than at -0.79 V and the Co ions are more oxidized.

In **Figure 50**, the metallic Co contribution in the EXAFS of the *H_2-CoCat* at -0.79 V is subtracted, to elucidate the non-metallic Co contribution (minor metal contribution may still be present). The metal-reduced spectrum exhibits a non-metallic peak at 1.7 Å which can be assigned to a coordination of the Co atom to light atoms (O, N or C) in its first coordination sphere (see **Figure 53**). However, the noise level of the spectrum and the uncertainties of the approach used for subtraction of the metallic contribution prevent reasonable EXAFS simulations to determine the Co-O/N/C distance and coordination number.

In XAS, metallic contributions can overshadow other contributions as they consist of heavy backscattering atoms and exhibit a significant long-range order. The minimization of the metal

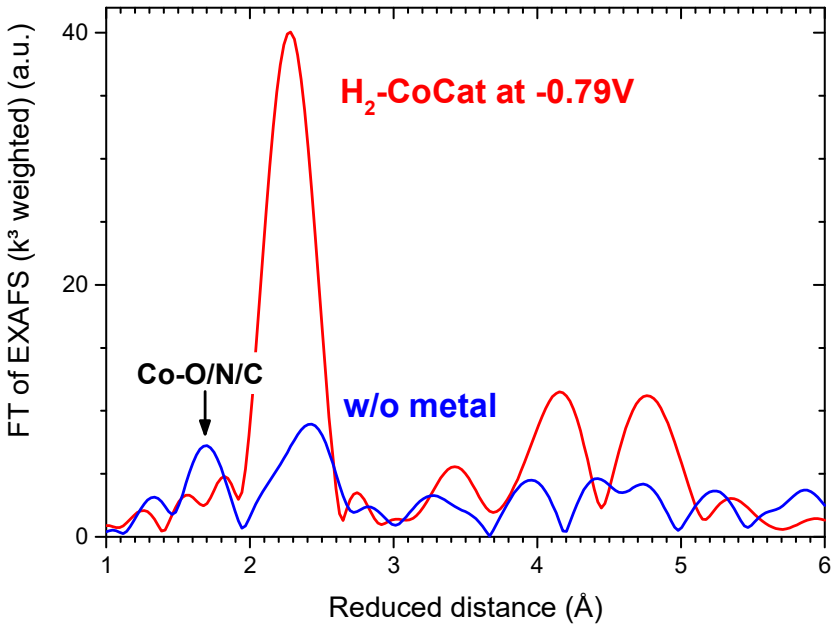

Figure 50

Fourier-transformed Co EXAFS (k^3 weighted, k range = 3 – 16 Å^{-1}) of the *H_2-CoCat* before (**red** line) and after subtraction of the Co metal contribution (**blue** line). The most prominent non-metallic peak is marked with "Co-O/N/C". The diminishment of the metal contribution was achieved by subtracting a weighted spectrum of Co metal spectrum from the original *H_2-CoCat* spectrum and renormalizing the difference spectrum (see **Equation 5**). The optimal weighting factor was determined by minimizing the oscillations in the metallic energy range of the *H_2-CoCat* spectrum.

contribution in the -0.79 V *H_2-CoCat* was achieved by subtracting the original electrode spectrum (not Fourier-transformed) by a weighted spectrum of Co metal and a subsequent renormalization of the difference spectrum (see **Equation 5**). The weighting factor of the metal spectrum was set to a value that minimizes the metal oscillations of the difference spectrum in the energy range from 7900 to 8750 eV. In this range, only metal oscillations are present, since the damping of the non-metallic contribution is stronger and the corresponding oscillations already disappear at lower energies (for a more detailed description of the metal-subtraction method, see section *Subtraction of metal contribution from spectrum* in chapter *Methods*). The optimal weighting factor for the *H_2-CoCat* was determined to 0.59 and indicates that ≈60 % of the Co species in the *H_2-CoCat* at -0.79 V are metallic and ≈40 % non-metallic (see **table** in **Figure 51**). Together with XPS measurements showing a spectrum comparable to $Co_3(PO_4)_2 \cdot xH_2O$ (performed and analysed by co-workers in (Cobo, Heidkamp et al. 2012)), it can be assumed that the *H_2-CoCat* is a combination of a Co^{II} phosphate with a Co oxo/hydroxo species formed on the surface of metallic Co.

The XANES/EXAFS of the *H_2-CoCat* at +1.37 V are well reassembled by a linear combination (in the energy range from 7680 to 8455 eV) (see **Figure 51**) of the -0.79 V spectrum and the spectrum of the well-known *O_2-CoCat* (see **Figure 51**), an amorphous Co oxide catalyst for water oxidation (established and well-studied by (Kanan and Nocera 2008, Risch, Khare et al. 2009)). This suggests that the catalytic

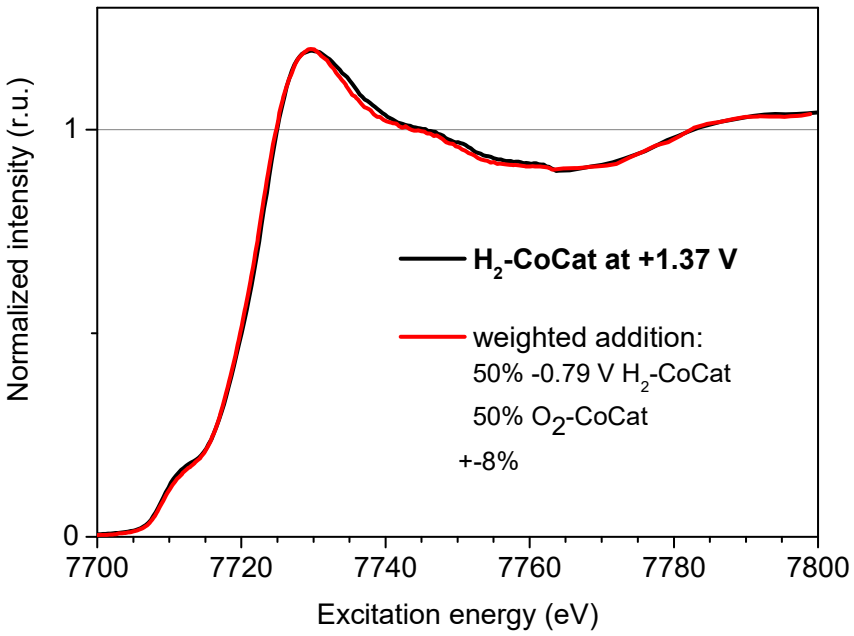

H_2-CoCat	
at -0.79 V	at +1.37 V
60% metallic Co^0 40% non-metallic Co species	30% metallic Co^0 20% non-metallic Co species 50% O_2-CoCat

Figure 51

The Co XANES of *H_2-CoCat* at +1.37 V *vs.* NHE (**black** line) are fitted with a linear combination (**red** line) of the *H_2-CoCat* spectrum at -0.79 V and the spectrum of the *O_2-CoCat* (recorded by M. Risch), an amorphous Co oxide catalyst for water oxidation (established and well-studied by (Kanan and Nocera 2008, Risch, Khare et al. 2009)). The optimal linear coefficients are ≈0.5 for both spectra. **Table**: Composition of Co species in the *H_2-CoCat* at -0.79 V and at +1.37 V as deduced from the XANES and EXAFS spectra.

Co species in the +1.37 V *H_2-CoCat* is similar to the *O_2-CoCat,* and that residuals of the -0.79 V *H_2-CoCat* are still present at +1.37 V. It seems that the *H_2-CoCat* transforms into the *O_2-CoCat*. The determined coefficients (see **Equation 6**) of the linear combination indicate a proportion between these two contributions of 1 : 1 after 4 min of conditioning at +1.37 V (see *H_2-CoCat* at +1.37 V in **Figure 51**). After the subtraction of the -0.79 V contribution, the renormalized EXAFS of the *H_2-CoCat* at +1.37 V (see **Figure 52**) exhibit a Co-O and Co-Co peak as in the *O_2-CoCat*. This confirms that *H_2-CoCat* at +1.37 V contains an *O_2-CoCat*-like Co species consisting of clusters of edge-sharing $Co^{III}O_6$ octahedra. For a more detailed description of the linear-combination method, see section *Linear combination of spectra* in chapter *Methods*.

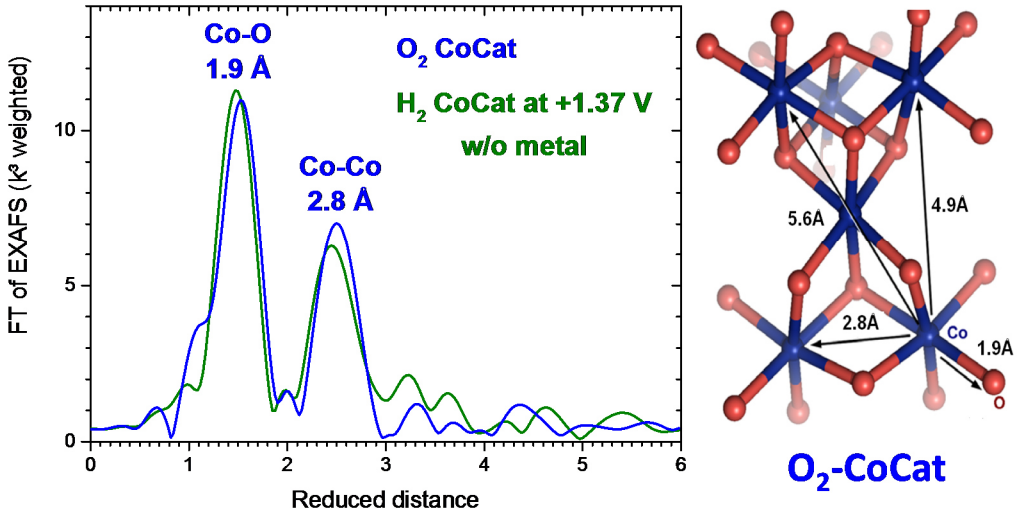

Figure 52

Fourier-transformed Co EXAFS (k^3 weighted, k range = 2 – 13 Å^{-1}) of the *H_2-CoCat* at +1.37 V *vs.* NHE after subtraction of the Co metal contribution (**green** line). The metal-reduced spectrum is compared to the spectrum of the *O_2-CoCat* (**blue** line, recorded by M. Risch, and **structure scheme** of M. Risch), an amorphous Co oxide catalyst for water oxidation (established and well-studied by (Kanan and Nocera 2008, Risch, Khare et al. 2009)). The *O_2-CoCat* peaks of its characteristic Co-O and Co-Co coordination are labelled with "Co-O" and "Co-Co", respectively. The diminishment of the metal contribution was achieved by subtracting a Co metal spectrum weighted with a factor of 0.5 from the *H_2-CoCat* spectrum at +1.37 V. The resulting difference spectrum was renormalized. The weighting factor was determined by fitting a linear combination consisting of the *H_2-CoCat* spectrum at -0.79 V and the *O_2-CoCat* spectrum to the *H_2-CoCat* spectrum at +1.37 V.

CONCLUSIONS

The *H_2-CoCat* is a Co-based material electro-deposited under reductive conditions (deposition potential of -0.79 V *vs.* normal hydrogen electrode (NHE)) and exhibits a catalytic evolution of H_2 at -0.79 V and of O_2 at +1.37 V as verified by gas chromatography measurements (performed and analysed by our co-workers in France (Cobo, Heidkamp et al. 2012)). The *H_2-CoCat* can be switched multiple times from catalytic H_2 to O_2 evolution and back, while maintaining its activity (shown by co-workers (Cobo, Heidkamp et al. 2012)). X-ray diffraction (XRD) measurements of the *H_2-CoCat* (performed and analysed by co-workers (Cobo, Heidkamp et al. 2012)) indicate a non-crystalline character of its Co species. This prevents further structural investigation of the *H_2-CoCat* by XRD and suggests a continuation with X-ray absorption spectroscopy (XAS).

Our XAS investigation show that, in the state of H_2 evolution, about 60 % of the *H_2-CoCat* consists of a hexagonal close-packed phase of metallic Co^0 (see **Figure 48**) and about 40 % of a non-metallic species with Co ions coordinated to O, N or C ligands in their first coordination sphere (see **Figure 53**). The non-metallic contribution is crucial for the catalytic activity of the *H_2-CoCat*, since its electrochemical performance is much higher than of a pure metallic electrode (Cobo, Heidkamp et al. 2012). Together with evidence from X-ray photoelectron spectroscopy (XPS) measurements (performed and analysed by our co-workers (Cobo, Heidkamp et al. 2012)), it can be assumed that the *H_2-CoCat* is a combination of a Co^{II} phosphate with a Co oxo/hydroxo species formed on the surface of metallic Co. In the state of O_2 evolution, XAS shows that the *H_2-CoCat* (partly) transforms into a Co species similar to the *O_2-CoCat* (see **Figure 52**), an amorphous Co oxide catalyst for water oxidation (Kanan and Nocera 2008, Risch, Khare et al. 2009). The *O_2-CoCat*-like Co species consists of clusters of edge-sharing $Co^{III}O_6$ octahedra.

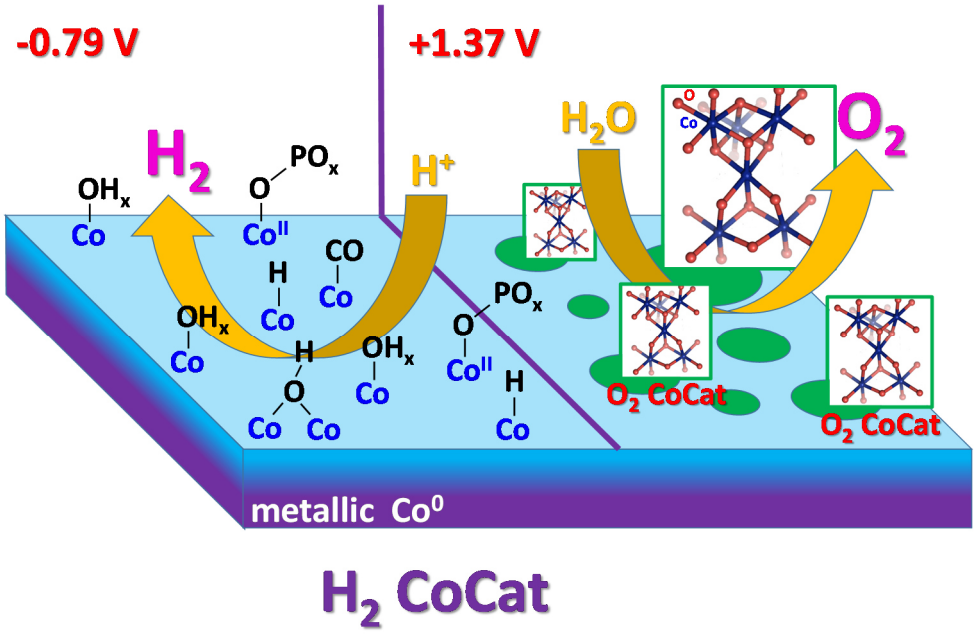

Figure 53

Schematic representation of the *H_2-CoCat* structure and, at +1.37 V *vs.* NHE, its conversion into the *O_2-Cocat*.

3. Molecular Ni catalyst grafted on a carbon-nanotube cathode

The X-ray absorption spectroscopy (XAS) data and analysis shown in this chapter are published in (Tran, Le Goff et al. 2011):

"Noncovalent Modification of Carbon Nanotubes with Pyrene-Functionalized Nickel Complexes: Carbon Monoxide Tolerant Catalysts for Hydrogen Evolution and Uptake"
Phong D. Tran, Alan Le Goff, Jonathan Heidkamp, Bruno Jousselme, Nicolas Guillet, Serge Palacin, Holger Dau, Marc Fontecave and Vincent Artero
Angewandte Chemie International Edition 2011, **Vol 50**, 1371-1374
http://dx.doi.org/10.1002/anie.201005427

Contributions:

- J. Heidkamp – X-ray absorption spectroscopy: entire data analysis and all measurements (samples were provided by co-workers)
- Co-workers – synthesis of molecular Ni catalyst and grafting of catalyst on a carbon-nanotube cathode (development and execution); sample preparation, measurement and data analysis for all other used techniques aside from XAS

INTRODUCTION

The $[Ni(P_2^{Ph}N_2^{Ar})_2]^{2+}$ complex ("NiP_4") is a molecular catalyst for H_2 formation (see structure in **Figure 56** with Ar = CH_2Pyrene). Its structure is inspired by the active sites of hydrogenases, enzymes for H_2 oxidation and reduction (Canaguier, Artero et al. 2007, Tard 2009). The complex combines a nickel centre in an electron-rich environment with proton relays provided by a pendant base. The former can be found in *NiFe* hydrogenases and the latter mimics the putative azapropanedithiolato cofactor of *FeFe* hydrogenases.

For the use in fuel cells or electrolysers, the NiP_4 complex is grafted on multi-walled carbon nanotubes (MWCNTs) to assemble electrode material (Le Goff, Artero et al. 2009). MWCNTs are advantageous as support material, as they offer high surface areas (facilitating high catalyst loading), high stability and electrical conductivity (Tasis, Tagmatarchis et al. 2006, Sgobba and Guldi 2009). The NiP_4-MWCNTS electrode material is noble-metal free and exhibits a low over-potential and high stability for H_2 evolution or uptake (Le Goff, Artero et al. 2009, Tran, Artero et al. 2010).

To graft the NiP_4 complex onto the MWCNTs, a polyphenylene layer bearing amino groups was formed on the MWCNTs and, then, an activated ester derivative of the complex (with Ar = phtalimide ester moiety) was attached to the layer via amide linkage (Le Goff, Artero et al. 2009). However, as current manufacturing techniques for active layers for fuel cells or electrolysers rely on standard deposition or printing of an ink containing the electroactive material, this procedure has practical and technical drawbacks.

Tran et al. presents an approach (based on (Zhao and Stoddart 2009)) that is more suitable for application as it attaches the NiP_4 complex (with Ar = CH_2Pyrene) via noncovalent π–π stacking directly on the MWCNTs (see **Figure 56**) (Tran, Le Goff et al. 2011). The resulting electrode material is compatible with conditions in classical proton-exchange membrane (PEM) devices. In addition, the material exhibits CO tolerance, as its catalytic activity for H_2 uptake is sustained in the presence of CO, a major impurity in H_2 fuels derived from reformed hydrocarbons or biomass. This is an advantage in comparison to Pt electro-catalysts that suffer from CO poisoning in PEM fuel cells (Baschuk and Li 2001).

We perform X-ray absorption spectroscopy on the NiP_4-MWCNTs electrode material to look for possible effects of the grafting process on the structural integrity of the NiP_4 complex.

This introduction text is based on a co-authored article (Tran, Le Goff et al. 2011).

PREPARATION

The synthesis of the [Ni($P_2^{Ph}N_2^{CH_2Pyrene}$)$_2$]-(BF_4)$_2$ complex, a molecular Ni catalyst for H_2 formation, was performed and developed by co-workers (Tran, Le Goff et al. 2011) as well as the grafting of the catalyst on a cathode, a gas diffusion layer (GDL) with a surface of multi-walled carbon-nanotubes (MWCNTs). The grafting procedure is described in the following:

Immobilisation of the nickel bisdiphosphine complex

Solution of [Ni($P_2^{Ph}N_2^{CH_2Pyrene}$)$_2$]-(BF_4)$_2$ (1 mmol/l) in dichloromethane (10 ml) was slowly filtered over a MWCNTs/GDL electrode (15 cm^2). The electrode was washed with acetonitrile (2 × 15 ml) to remove any un-immobilized nickel complex. The functionalized MWCNTs/GDL electrodes were then air-dried for 2h.

Membrane-electrode assembly preparation

The MWCNTs/GDL electrodes (14 mm disc diameter) and Nafion® NRE 212 CS membrane (DuPont™) were directly bonded together by hot-pressing process (4 MPa at 135°C for 2 minutes and 30 seconds).

Sample preparation for X-ray absorption spectroscopy

Microcrystalline [Ni($P_2^{Ph}N_2^{CH_2Pyrene}$)$_2$]-(BF_4)$_2$ ("NiP_4") was carefully grinded and thoroughly mixed with boron nitride to obtain homogeneous samples of appropriate optical thickness. The same was done with a powder of the NiP_4 complex grafted on MWCNTs that was removed from the GDL.

RESULTS AND DISCUSSION

To assemble an electrode for H_2 formation, the catalytic $[Ni(P_2^{Ph}N_2^{CH_2Pyrene})_2](BF_4)_2$ complex (= NiP_4) was grafted on the multi-walled carbon nanotube (MWCNTs) surface of a gas-diffusion layer (GDL). X-ray absorption near-edge structure (XANES) and extended X-ray absorption fine-structure (EXAFS) of the functionalized MWCNTs/GDL electrode and the original NiP_4 complex were recorded at the Ni *K*-edge, to check for possible effects of the grafting process on the structure of the complex.

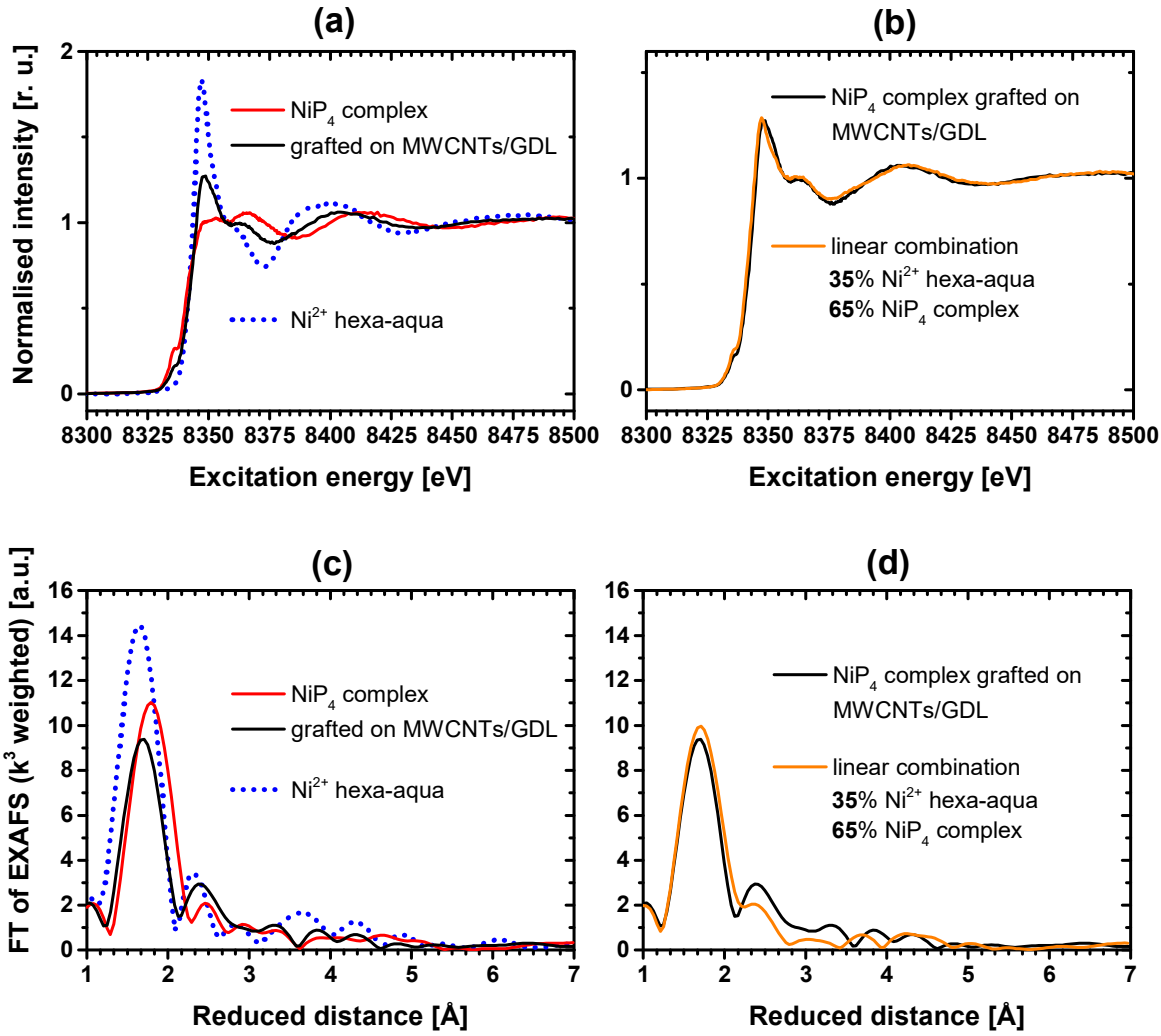

Figure 54

(a) XANES/EXAFS spectra collected at the Ni *K*-edge of the catalytic $[Ni(P_2^{Ph}N_2^{CH_2Pyrene})_2]$-$(BF_4)_2$ complex (**red** line) and of the complex after grafting onto the MWCNTs/GDL (**black** line). The spectra are compared to the reference spectrum of $[Ni^{II}(OH_2)_6]^{2+}$ (**blue-dotted** line). (b) linear combination of the spectra of the $[Ni(P_2^{Ph}N_2^{CH_2Pyrene})_2]$-$(BF_4)_2$ complex and of the $[Ni^{II}(OH_2)_6]^{2+}$ reference (**orange** line) with the respective linear coefficients of 0.65 and 0.35. The linear combination is compared to the spectrum of the complex after grafting onto the MWCNTs/GDL (**black** line). (c) and (d) Fourier transforms (FT) of the EXFAS spectra in (a) and (b) weighted with k^3 (k range = 2 – 11 $Å^{-1}$).

The Ni XANES of the functionalized electrode differ from the spectrum of the original NiP_4 complex (see **Figure 54a**). The electrode XANES show an increased amplitude of the absorption edge and a decreased amplitude of the pre-edge. A comparison with the reference spectrum of $[Ni^{II}(OH_2)_6]^{2+}$ ($NiCl_2$ in aqueous solution) suggests that these features correlate with the occurrence of a Ni coordination to six O/N atoms. The edge in the electrode XANES reaches the half of its amplitude at almost the same excitation energy as the edge of the $Ni^{II}(OH_2)_6$ reference, indicating that the mean oxidation state of the Ni ions grafted on the electrode is II as in the original NiP_4 complex before grafting.

Analogue to the XANES, the Ni EXAFS of the MWCNTs/GDL electrode functionalized with the NiP_4 complex deviates from the original complex (see Fourier transform in **Figure 54c**). The Ni-P peak of the original complex, representing the P_4 ligand environment, shifts to shorter distances after grafting on the MWCNTs from 1.8 to 1.7 Å and coincides in position with the Ni-O peak of the $Ni(OH_2)_6$ reference. This suggests that, after grafting, the Ni-P peak contains an additional Ni-O/N contribution. EXAFS simulations of the peak indicate, for the Ni-P contribution, a Ni-P distance of 2.23 Å as in the original NiP_4 complex and, for the Ni-O/N contribution, a Ni-O/N distance of 2.04 Å as in the $Ni(OH_2)_6$ reference (see **Table 18**). The simulated P coordination number of 1.9 is lower than in the original NiP_4 complex, indicating that the complex constitutes only a fraction of the Ni species on the electrode or that the ligand environment in the complex is modified towards a mixture of P and O/N atoms (simulated O coordination number is 2.0) (see **Table 18**).

In summary, XANES and EXAFS indicate that, after grafting on the MWCNTs/GDL electrode, the planar tetrahedral P_4 ligand environment of the NiP_4 complex incorporates O/N ligands or that a separate Ni-O/N species with octahedral ligand geometry similar to $Ni(OH_2)_6$ is formed. The Ni-O/N coordination could arise from a fraction of NiP_4 complexes binding to water molecules, carboxylate, or hydroxo defects present at the surface of MWCNTs as well as from the oxidation of a diphosphine ligand of the NiP_4 complex, either through the phosphine oxide function or through the amine function, as shown recently in a similar system (Yang, Bullock et al. 2010).

The XANES/EXAFS spectrum of the functionalized MWCNTs/GDL electrode is well reassembled by a linear combination of the spectrum of the original NiP_4 complex (crystalline powder) and the $Ni(OH_2)_6$ spectrum (in the energy range from 8300 to 8780 eV, see **Figure 54b**). The same can be observed of the EXAFS part of the linear combination (see Fourier transform in **Figure 54d**). At larger distances, there are deviations that could be explainable by differences in higher coordination spheres between the $Ni(OH_2)_6$ reference, a complex in aqueous solution, and the actual Ni-O species on the MWCNTs. The good agreement between the linear combination and the XANES/EXAFS spectra confirms that the Ni species on the MWCNTs is a mixture of the original NiP_4 complex with an octahedral NiO_6 species or that the NiP_4 complex incorporates O/N ligands. The linear coefficients (see **Equation 6**) suggest that 35 ± 15 % of the NiP_4 complexes transform into a Ni-O species or that a majority of the complexes incorporate one or two O ligands in their ligand environment. For a more detailed description of the linear-combination method, see section *Linear combination of spectra* in chapter *Methods*.

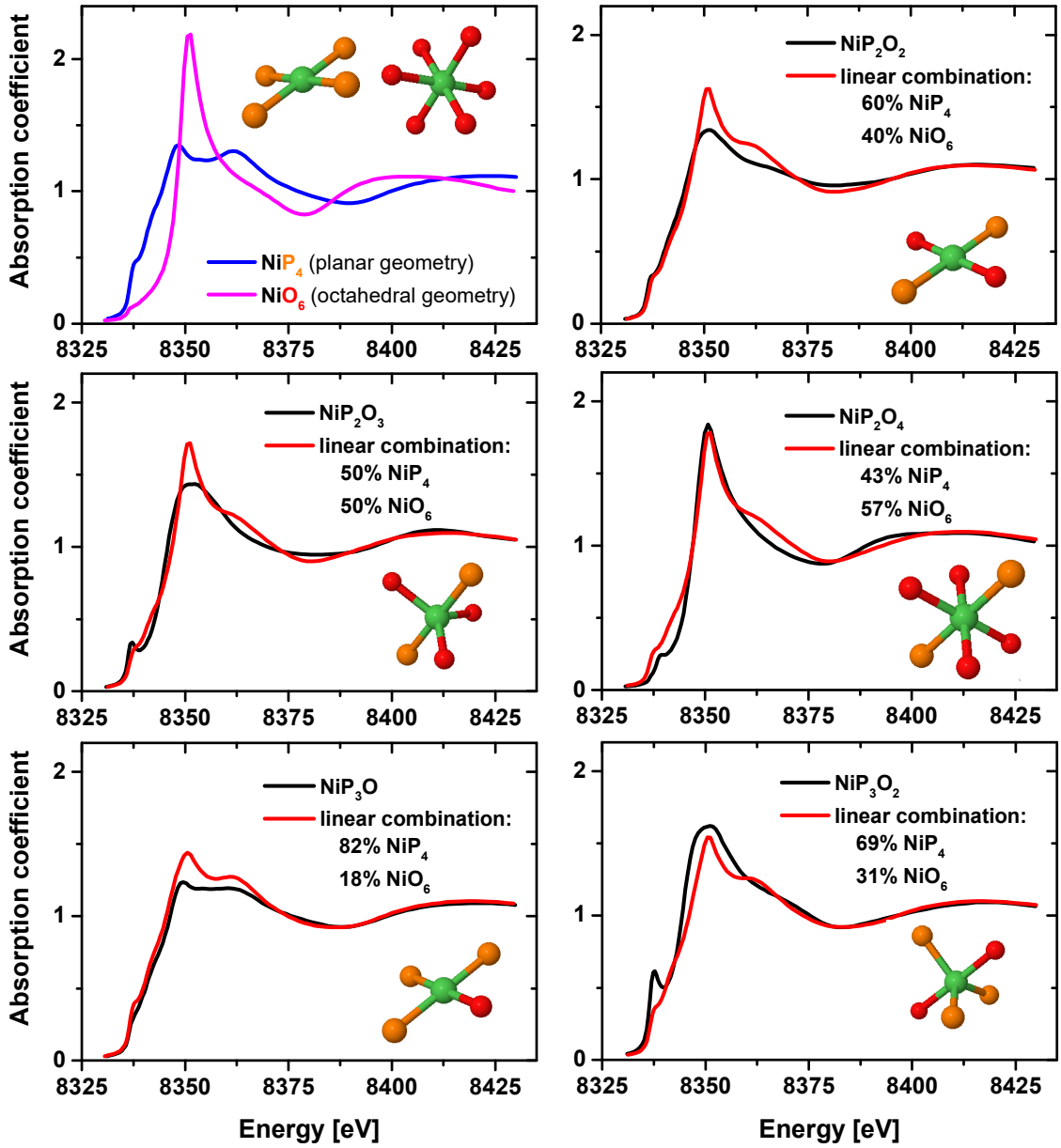

Figure 55

Simulated XANES spectra at the Ni *K*-edge of a NiP_mO_n model structure with a mixed P and O ligand environment of various $\boldsymbol{m/n}$ ratios (**black** line), compared to corresponding linear combinations (**red** line) of the simulated spectra of a planar-tetrahedral NiP_4 (**blue** line) and a octahedral NiO_6 model structure (**magenta** line). In the linear combination, the P/O ratio per Ni atom matches the $\boldsymbol{m/n}$ ratio of the corresponding NiP_mO_n structure. The linear coefficients for NiP_4 and NiO_6 are calculated by $\boldsymbol{n/4 \times 1/(n/4 + m/6)}$ and $\boldsymbol{m/6 \times 1/(n/4 + m/6)}$, respectively. All XANES simulations were carried out with *feff 9.05* (Rehr, Kas et al. 2009) using self-consistent muffin-tin potentials and full multiple-scattering calculations.

XANES simulations (see **Figure 55**) suggest that the formation of a Ni species on the MWCNTs with mixed P and O ligand is less likely than the formation of separate Ni-P and Ni-O species. The XANES of a species with mixed ligands can be simulated from a NiP_nO_m model structure for various ratios n/m between the P and O ligands. The XANES of the separate Ni species can be emulated by simulating the spectra of a planar tetrahedral NiP_4 and an octahedral NiO_6 model structure and combining them in a weighted addition. The weighting factors set the percentage of Ni ions in the sample having either a P_4 or an O_6 ligand environment. If one averages the number of P and O ligands over all Ni ions, then one can determine a mean P/O ratio per Ni ion for each weighted addition of NiP_4 and NiO_6. In **Figure 55**, the XANES of NiP_nO_m for various ratios n/m are compared to additions of NiP_4 and NiO_6 spectra with the same P/O ratio per Ni ion. The corresponding weighting factors for NiP_4 and NiO_6 are calculated by $n/4 \times 1/(n/4 + m/6)$ and $m/6 \times 1/(n/4 + m/6)$, respectively. The comparison in **Figure 55** shows that the NiP_nO_m spectra deviate significantly from the corresponding additions of NiP_4 and NiO_6. This suggests that, for the Ni species grafted on the MWCNTs, the real spectrum should look significantly different in the case of possessing a mixed P/O ligand environment than in the case of forming a separate Ni-P and Ni-O species. The sufficient resemblance of the spectrum of the Ni-MWCNTs species via a weighted addition of the NiP_4 complex with the $Ni(OH_2)_6$ spectrum (see **Figure 54b** and **d**) suggests that the case of a separate Ni-P and NI-O species is more likely. The spectrum of a possible Ni-MWCNTs species with a mixed P/O ligand environment should significantly differ from the addition of the NiP_4 and $Ni(OH_2)_6$ spectra and, therefore, differ from the actual spectrum of the Ni-MWCNTs species.

CONCLUSIONS

The $[Ni(P_2^{Ph}N_2^{CH_2Pyrene})_2]^{2+}$ complex ("NiP_4") is a molecular catalyst for H_2 formation (see **Figure 56**). Its structure is bioinspired by the active sites of hydrogenases, enzymes for H_2 oxidation and reduction. The NiP_4 complex is grafted on the multi-walled carbon-nanotubes (MWCNTs) surface of a gas diffusion layer (GDL) via noncovalent π-π stacking. The resulting noble-metal-free electro-catalytic nanomaterial is suitable for the use in fuel cells; and is not affected by CO poisoning as observed in Pt-based electro-catalysts. Our X-ray absorption near-edge structure (XANES) and extended X-ray absorption fine-structure (EXAFS) investigations monitor the structure of the NiP_4 complex during the grafting on the MWCNTs/GDL electrode.

The Ni XANES/EXAFS of the MWCNTs/GDL electrode functionalised with the NiP_4 complex (see **Figure 54a** and **c**) indicate that one third of the complexes incorporates O/N ligands or transforms into an octahedral Ni^{2+} species with a coordination to six light atoms (O, N or C) similar to $[Ni^{II}(OH_2)_6]^{2+}$ (see **Figure 56**). The other two third maintain their original planar-tetrahedral P_4 ligand system. The spectrum of the functionalised MWCNTs/GDL electrode is well reassembled by a linear combination of the XANES/EXAFS of the original NiP_4 complex and the $Ni(OH_2)_6$ reference ($NiCl_2$ in aqueous solution) (see **Figure 54b** and **d**). The optimal linear coefficients indicate that 35 ± 15 % of the original NiP_4 complexes transform into an octahedral Ni^{2+}-O/N species; or that a majority of the NiP_4 complexes

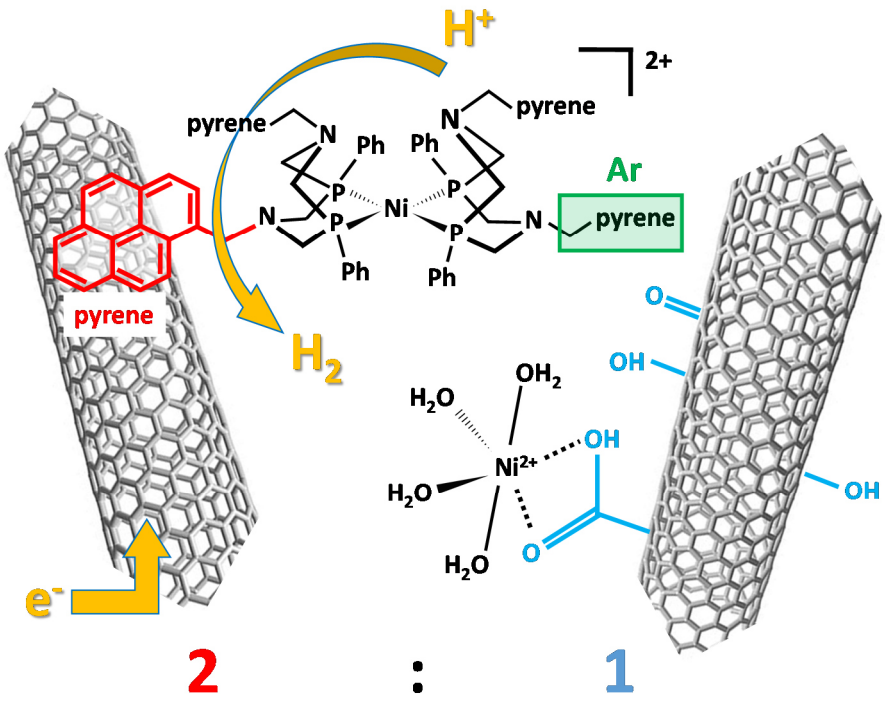

Figure 56

The molecular Ni catalyst, $[Ni(P_2^{Ph}N_2^{CH_2Pyrene})_2]^{2+}$, grafted a on cathode with a multi-walled carbon-nanotubes surface. During grafting, one third of the Ni catalysts converts into an octahedral $Ni^{II}(O/N)_6$ species.

incorporates one or two O/N ligands in their structure. XANES simulations (see **Figure 55**) suggest that the former is more likely, resulting into the formation of separate Ni-P and Ni-O species without mixed P/O ligand environments on the MWCNTs. The Ni-O/N coordination could arise from a fraction of the NiP_4 complexes binding to water molecules, carboxylate, or hydroxo defects present at the surface of MWCNTs. Furthermore, the oxidation of a diphosphine ligand in the NiP_4 complex, either through the phosphine oxide function or through the amine function, could also lead to a Ni-O/N coordination as recently shown in a similar system (Yang, Bullock et al. 2010).

4. Noble metal-free fuel cell

The X-ray absorption spectroscopy (XAS) data and analysis shown in this chapter are published in (Tran, Morozan et al. 2015):

"A noble metal-free proton-exchange membrane fuel cell based on bio-inspired molecular catalysts"
P. D. Tran, A. Morozan, S. Archambault, J. Heidkamp, P. Chenevier, H. Dau, M. Fontecave, A. Martinent, B. Jousselme and V. Artero
Chemical Science 2015, **Vol 6**, 2050-2053
http://dx.doi.org/10.1039/c4sc03774j

Published by The Royal Society of Chemistry.
http://www.rsc.org/

Contributions:

- J. Heidkamp – X-ray absorption spectroscopy: entire data analysis and all measurements (samples were provided by co-workers)
- Co-workers – synthesis of catalyst material and fabrication of fuel cell (development and execution); sample preparation, measurement and data analysis for all other used techniques aside from XAS

INTRODUCTION

Fuel cells based on proton exchange membrane (PEM) technology (see **Figure 65**) can be used in a wide range of portable and automotive applications. However, PEM fuels cells require Pt as catalyst for the H_2 oxidation and O_2 reduction reactions (HOR and ORR). Pt is rare and, hence, expensive, representing an economic bottle neck for the fuel cells. This represents an economic bottle neck for the fuel cells, as Pt is rare and, hence, expensive. The substitution of Pt by earth-abundant catalysts is a potential way to remove this economic handicap. Significant progress in the substitution of Pt was achieved for the ORR-side of the fuel cells (Bashyam and Zelenay 2006, Pylypenko, Mukherjee et al. 2008, Gong, Du et al. 2009, Lefevre, Proietti et al. 2009, Liu, Wu et al. 2010, Morozan, Jegou et al. 2011, Morozan, Jousselme et al. 2011). However, a PEM fuel cell with earth-abundant catalysts on both electrodes, ORR and HOR, has not been reported before the work of *Tran et al.* (Tran, Morozan et al. 2015). The fuel cell of *Tran et al.* utilizes as ORR catalyst a novel Cobalt/nitrogen/Vulcan (Co-N-C) material, and as HOR catalyst a previously studied carbon-nanotube material functionalized with biomimetic Ni complexes (Ni-CNT) (see chapter *Molecular Ni catalyst grafted on a carbon-nanotube cathode*) (Tran, Le Goff et al. 2011).

The Co-N-C material is prepared by an adaptation of the procedure from (Morozan, Jegou et al. 2011, Matsubara, Fujita et al. 2012). The catalytic activity of the material can be assigned to pyridinic-N functional groups located at the surface of the carbon matrix and binding cobalt ions as well as metallic cobalt nanoparticles (Morozan, Jegou et al. 2011).

The fuel cell of *Tran et al.* consists of a layer of Ni-CNT material attached to a layer of Co-N-C material via an interfacing *Nafion* membrane only permeable for protons (Tran, Morozan et al. 2015). The electrical contacts of the fuel cell are gas-permeable Au layers evaporated onto the outside of the Ni-CNT and Co-N-C layers. The performance of the noble metal-free fuel cell is comparable to PEM fuel cells based on Pt, as demonstrated by co-workers in (Tran, Morozan et al. 2015).

We perform X-ray absorption spectroscopy on the ORR and HOR catalysts to monitor possible effects of the operation conditions in a PEM fuel-cell on the atomic structure of the catalysts. Furthermore, we provide first insights in the atomic structure of the novel ORR catalyst.

This introduction text is based on a co-authored article (Tran, Morozan et al. 2015).

PREPARATION

The synthesis and preparation of the Ni-CNT material, the Co-N-C material, the catalyst inks as well as the fabrication of the fuel-cell were performed and developed by co-workers (Tran, Morozan et al. 2015). The procedures are described in the following:

Ni-CNT material

Anode catalyst was prepared by suspending $[Ni(P_2^{Ph}N_2^{CH_2Pyrene})_2](BF_4)_2$ (40 mg) and MWCNTs (30 mg) in CH_3CN (100 ml). After 10 min sonication, Vulcan XC-72 (30 mg) was added to the solution and the suspension was sonicated for 5 more min. The solvent was then evaporated in vacuum.

Co-N-C material

Cobalt/nitrogen/Vulcan (Co-N-C) cathode catalyst (12 wt. % is the nominal weight percentage of Co over the TAPy-CNTs mixture, 2/1 is the mass ratio of TAPy to CNTs) was prepared as follows. 1H-1,2,3-triazolo[4,5-b]pyridine (TAPy) (400 mg) was added to a solution of $Co(NO_3)_2{\cdot}6H_2O$ (355.1 mg) in ethanol (30 ml) and the solution was stirred for 2 h at 60 °C. Then, a dispersion of Vulcan XC-72 (200 mg) in ethanol (100 ml) was ultra-sonicated for 30 min and added to the previous solution. The mixture was heated under reflux at 60 °C for 5 h. Ethanol was removed under reduced pressure to give a black Co–TAPy-Vulcan powder which was subsequently placed for 2 h in a tube furnace under a flux of Ar to remove residual air, heated at 5 °C/min until 700 °C, held at this temperature for 1 h and then cooled at 5 °C/min until room temperature. The whole procedure was executed under in a flowing Ar atmosphere.

Catalyst ink

Inks were prepared by mixing anode or cathode catalyst with 5wt. % Nafion® solution in hydro-alcoholic solution. The mixtures were sonicated for 1 h. Isopropanol was added to the catalyst ink which was sonicated again for 30 min. The Nafion® polymer and the catalyst are respectively 20-30 wt. % and 70-80 wt. % of the total solid content of the catalyst inks.

Fuel cell - Membrane electrode assembly (MEA) fabrication

The catalyst suspensions are directly sprayed using an air brush (Harder and Stenbeck) to both sides on NRE-212 Nafion® perfluorosulfonic acid membranes commercialised by DuPont™. The membrane is used without pre-treatment steps and attached on glass with adhesive tape. The deposition is carried out at 60-80 °C on a hot plate in order to evaporate both the water in the membrane and the solvent in the catalyst ink. Both sides are subsequently sprayed and the resultant MEA is dried for one night in the air at room temperature. The MEA is then pressed at 50 °C under a pressure of 0.2 MPa for 3 min. The active electrode area was 5.76 cm^2. Gold was deposited by physical vapour deposition, thin enough to let H_2 and O_2 reach catalysts sites but thick enough to ensure a good collect of current.

Sample preparation for X-ray absorption spectroscopy (XAS)

Microcrystalline $[Ni(P_2^{Ph}N_2^{CH_2Pyrene})_2](BF_4)_2$, as-prepared Ni-CNT material, as-prepared microcrystalline Co-N-C material, $LiCo^{III}O_2$ and $[Co^{II}(OH_2)_6](NO_3)_2$ were thoroughly mixed with boron nitride to obtain homogeneous samples of appropriate optical thickness. $Ni(OH_2)_6]^{2+}$ was prepared by solving $NiCl_2$ in deionized water (10 mM) and freezing the solution in liquid nitrogen. The anode catalyst (Ni-CNT) was deposited onto gas-diffusion layers (same preparation as previously described but without application of the Nafion® membrane). These electrodes were characterized as-prepared and after electrochemical equilibration in 0.5 M H_2SO_4 aqueous solution (by repeating 5 potential cycles (potential scan rate of 2 mV/s) from –0.3 V to +0.5 V *vs.* reversible hydrogen electrode (RHE)) or extended turnover for H_2 oxidation (at +0.25 V *vs.* RHE) or evolution (at –0.3 V *vs.* RHE). Then the sample was taken out from the gas-diffusion layer and mixed with boron nitride as described above for XAS measurement. *The electrochemical conditioning of the XAS samples was performed by co-workers (Tran, Morozan et al. 2015).*

Ni CATALYST FOR H_2 OXIDATION

X-ray absorption spectroscopy (XAS) investigations on the Ni-CNT material directly embedded in the fuel-cell turned out to be impossible, hence the Ni-CNT material (CNT = carbon nanotubes) was characterised in a better accessible half-cell configuration.

The X-ray absorption near-edge structure (XANES) of the catalytic Ni-CNT material (Ni *K*-edge, see **Figure 57**) can be interpreted as a combination of the spectra from two separate Ni^{II} species present on the CNTs. One possesses a planar-tetrahedral P_4 ligand environment as in the original molecular Ni catalyst, a $[Ni(P_2^{Ph}N_2^{CH_2Pyrene})_2]^{2+}$ complex (= "NiP_4"), and the other an octahedral coordination to six light ligands (O or N) similar in structure to $[Ni(OH_2)_6]^{2+}$ (= "NiO_6") (see **Figure 65**). In the as-prepared Ni-CNT material, the NiP_4 species represents the majority of the Ni species on the CNTs (about 2/3rd). The XAS analysis of the as-prepared material is discussed in detail in the chapter *Molecular Ni catalyst grafted on a carbon-nanotube cathode* and is also reported in (Tran, Le Goff et al. 2011). During H_2 oxidation, the features in the spectrum of the Ni-CNT material corresponding to the $Ni(O/N)_6$ species

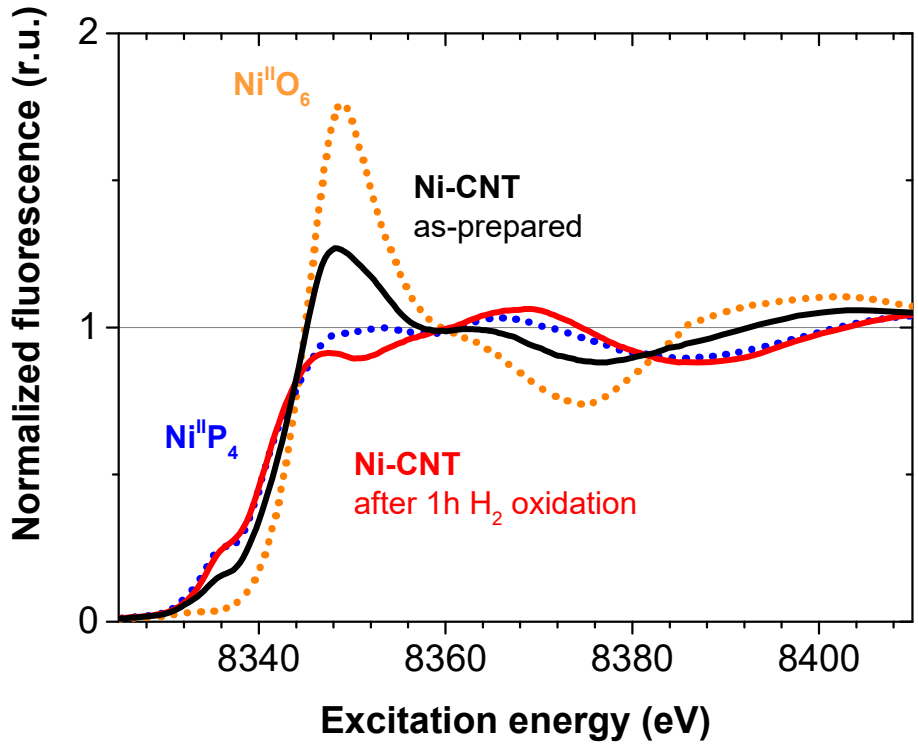

Figure 57

XANES/EXAFS spectra collected at the Ni *K*-edge for the Ni–CNT material as prepared (**black** solid line), and after 1 h of H_2 oxidation (**red** solid line). The spectra of pristine $[Ni(P_2^{Ph}N_2^{CH_2Pyrene})_2]^{2+}$ (**blue** dotted line) and of $[Ni(OH_2)_6]^{2+}$ (**orange** dotted line) are shown for comparison.

diminish and the ones of the NiP_4 species become more prominent. This can be deduced from a comparison with the XANES spectra of $[Ni(P_2^{Ph}N_2^{CH_2Pyrene})_2]^{2+}$ and $[Ni(OH_2)_6]^{2+}$ (see **Figure 57**). The comparison shows that, in the Ni-CNT spectrum, the pronounced summit of the Ni absorption edge, which is a characteristic of the NiO_6 spectrum, vanishes after 1h of H_2 oxidation while the pre-edge, a characteristic of the NiP_4 spectrum, becomes more prominent. Furthermore, the EXAFS oscillations of the Ni-CNT material after 1 h of H_2 oxidation (starting at ≈8360 eV and extending to higher energies) are close to the NiP_4 spectrum while before H_2 oxidation they tend to contour the NiO_6 spectrum. Altogether, it seems that, during H_2 oxidation, the $Ni(O/N)_6$ species is removed from the Ni-CNT material.

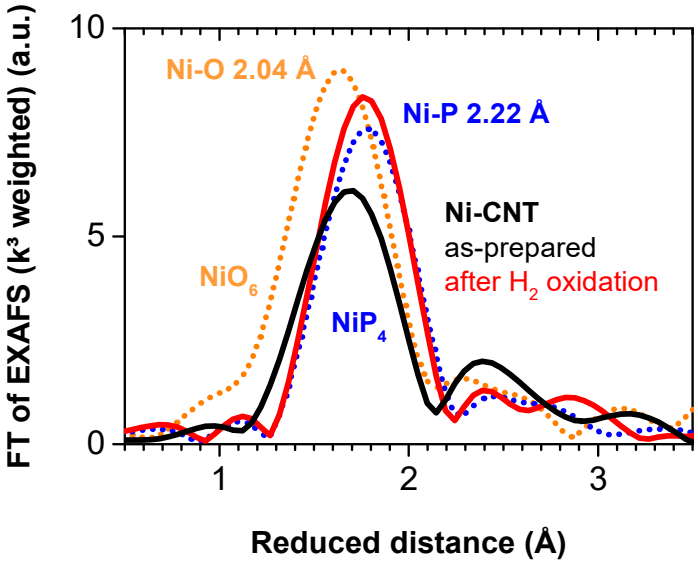

Figure 58

Fourier-transformed EXAFS spectra (k^3 weighted, k range = 2 - 13 Å^{-1}) collected at the Ni *K*-edge for the Ni-CNT material as prepared (**black** solid line), and after 1 h of H_2 oxidation (**red** solid line). The spectra of pristine $[Ni(P_2^{Ph}N_2^{CH_2Pyrene})_2]^{2+}$ (**blue** dotted line) and of $[Ni(OH_2)_6]^{2+}$ (**orange** dotted line) are shown for comparison. Their main peaks are labelled with the corresponding Ni-ligand distance.

The extended X-ray absorption fine-structure (EXFAS) of the Ni-CNT material (Ni *K*-edge) confirms the deductions from the XANES analysis. The Fourier transform of the Ni-CNT spectrum (see **Figure 58**) shows a prominent peak located between the Ni-P peak of the NiP_4 reference and the Ni-O peak of the NiO_6 reference. This indicates that the Ni-CNT peak contains contributions of both reference peaks and, hence, two Ni species are present on the CNTs, one with a P_4 and the other with $(O/N)_6$ ligand environment similar to the references. After 1 h of H_2 oxidation, the peak of the Ni-CNT shifts to the position of the Ni-P and exhibits a comparable amplitude, indicating the exclusive presence of the NiP_4 species on the CNTs after H_2 oxidation. Corresponding EXAFS simulations (see **Figure 61**) of the Ni-CNT peak lead to the same conclusions. Before H_2 oxidation, the Ni-CNT peak can be simulated with a Ni-P and a Ni-O coordination yielding the same Ni-P and Ni-O distances as in the NiP_4 and NiO_6 references (see **Table 18**). The simulated P and O coordination numbers are lower than in the references, indicating that the Ni species on the CNTs is split into a NiP_4 and a $Ni(O/N)_6$ fraction. The fractional P coordination number is closer to the complete number in the reference than the fractional O coordination number, suggesting that the NiP_4 fraction is more abundant on the CNTs than the NiO_6 fraction. After H_2 oxidation, the Ni-CNT peak can only be simulated with a Ni-P coordination, indicating

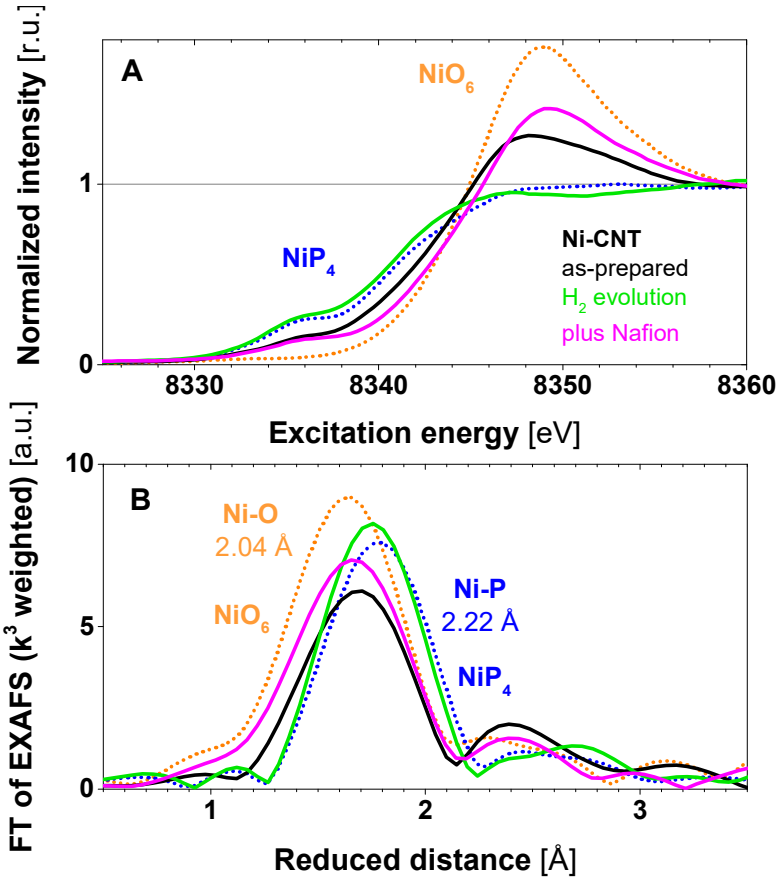

Figure 59

XANES spectra (**A**) and Fourier-transformed EXAFS spectra (k^3 weighted, k range = 2 - 13 Å^{-1}) (**B**) collected at the Ni *K*-edge. **Black** solid line: Ni-CNT material as prepared. **Magenta** solid line: Ni-CNT coated onto a *Nafion* membrane after 1 h of H_2 evolution. **Green** solid line: Ni-CNT in direct contact with the electrolyte (aqueous 0.5 M H_2SO_4) after 1 h of H_2 evolution. **Blue** dotted line: pristine $[Ni(P^{Ph}{}_2N^{CH2Pyrene}{}_2)_2]^{2+}$. **Orange** dotted line: $[Ni(OH_2)_6]^{2+}$. In **B**, the main peaks of $[Ni(P^{Ph}{}_2N^{CH_2Pyrene}{}_2)_2]^{2+}$ and $[Ni(OH_2)_6]^{2+}$ are labelled with the corresponding Ni-ligand distance.

the exclusive presence of the NiP_4 species on the CNTs. The structure of the NiP_4 catalysts seems to withstand an extended operation, as after 1 h of H_2 oxidation the simulated Ni-P distance and coordination number are close to the values of the NiP_4 reference (see **Table 18**).

In summary, the XANES and EXAFS analysis indicate that the Ni-CNT material consists of a planar-tetrahedral $Ni^{II}P_4$ species similar to the original NiP_4 catalyst and an octahedral $Ni^{II}(O/N)_6$ species similar to $Ni(OH_2)_6$. During H_2 oxidation, the NiP_4 species maintains its P_4 ligand environment and the $Ni(O/N)_6$ species is removed from the CNTs. Analogous effects for the Ni-CNT material can be also observed after 1 h of H_2 evolution (see **Figure 59** and **Table 18**) or after equilibration with a few cyclic

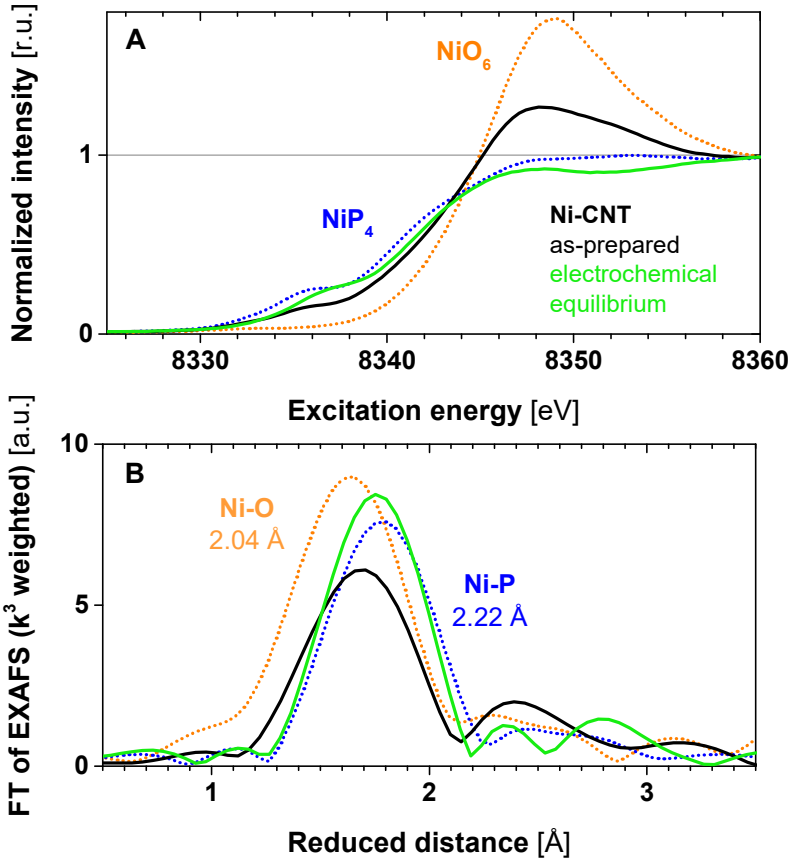

Figure 60

XANES spectra (**A**) and Fourier-transformed EXAFS spectra (k^3 weighted, k range = 2 - 13 Å^{-1}) (**B**) collected at the Ni *K*-edge. **Black** solid line: Ni-CNT as prepared. **Green** solid line: Ni-CNT after equilibration with a few cyclic voltammograms. **Blue** dotted line: pristine $[Ni(P_2^{Ph}N_2^{CH_2Pyrene})_2]^{2+}$. **Orange** dotted line: $[Ni(OH_2)_6]^{2+}$. In **B**, the main peaks of $[Ni(P_2^{Ph}N_2^{CH_2Pyrene})_2]^{2+}$ and $[Ni(OH_2)_6]^{2+}$ are labelled with the corresponding Ni-ligand distance.

voltammograms (see **Figure 60** and **Table 18**). The catalytic activity of the Ni-CNT material, however, does not decrease by the removal of the $Ni(O/N)_6$ species as shown by co-workers in (Tran, Morozan et al. 2015). This confirms that the NiP_4 species is the catalytic species of the Ni-CNT material.

In an advanced half-cell configuration, the Ni-CNT material was coated with a *Nafion* membrane as in the fuel-cell. In contrast to the previous configurations, the Ni-CNT material is not anymore in direct contact with the electrolyte, aqueous 0.5 M H_2SO_4. The Ni XANES and EXAFS of the Ni-CNT material with *Nafion* do not exhibit a removal of the $Ni(O/N)_6$ species after 1 h of H_2 evolution as observed for the other half-cell configurations. In the XANES (see **Figure 59**), the increased amplitude of the Ni absorption edge, indicative for a Ni-O/N coordination, remains after H_2 evolution. In the EXAFS (see Fourier transform in **Figure 59**), the Ni-CNT peak stays in a position close to the Ni-O peak after H_2 evolution and the simulated coordination number of O is not diminished (see **Table 18**). The *Nafion* membrane seems to prevent a removal of the $Ni(O/N)_6$ species, indicating that a direct contact of the Ni-CNT material with the H_2SO_4 electrolyte might be necessary for this process. In the fuel-cell, the removal of the $Ni(O/N)_6$ species is possibly inhibited, since the used Ni-CNT material is coated with a *Nafion* membrane as well.

	mean **Ni-ligand distance [Å]**		mean **coordination number**	
	Ni-O	Ni-P	Ni-O	Ni-P
$[Ni(OH_2)_6]^{2+}$	2.03 ± 0.01		6	
$[Ni(P^{Ph}{}_2N^{CH_2Pyrene}{}_2)_2]^{2+}$		2.22 ± 0.01		4
Ni-CNT as prepared	2.04 ± 0.01	2.23 ± 0.01	2.0 ± 0.2	1.9 ± 0.2
Ni-CNT in direct contact with the electrolyte (aqueous 0.5M H_2SO_4)				
after electrochemical equilibration		2.18 ± 0.01		3.5 ± 0.4
after 1h H_2 oxidation		2.19 ± 0.01		3.6 ± 0.2
after 1h H_2 evolution		2.19 ± 0.01		3.9 ± 0.3
Ni-CNT coated with a *Nafion* membrane				
after 1h H_2 evolution	2.00 ± 0.01	2.25 ± 0.01	2.5 ± 0.2	1.6 ± 0.2
E_0=1.6 eV S_0^2=0.76	Ni-O $2\sigma^2$=0.009 Å^2 Ni-P $2\sigma^2$=0.004 Å^2			

Table 18

Overview of the Ni-P distances and coordination P numbers of the $[Ni(P^{Ph}{}_2N^{CH_2Pyrene}{}_2)_2]^{2+}$ catalyst ("NiP_4") in its pristine state, grafted on CNT (= Ni-CNT material), after electrochemical equilibration, after H_2 oxidation and after H_2 evolution. It is differentiated between conditions where the Ni-CNT material was in direct contact with the electrolyte or coated with a Nafion® membrane. If a Ni-O/N species is significantly present besides the NiP_4 catalyst, then its Ni-O distance and O coordination number is given. The Ni-P/O distances and coordination numbers were determined by fitting the corresponding EXAFS spectra with two phase-functions: one for P and one for O. The functions were calculated from crystal structures similar to $[Ni(P^{Ph}{}_2N^{CH_2Pyrene}{}_2)_2]^{2+}$ or $[Ni(OH_2)_6]^{2+}$, respectively. For all fits, the energy offset, E_0, the amplitude reduction factor, S_0, and the Debye-Waller parameters, σ, of P and O were fixed at values determined from fits of the corresponding references, $[Ni(P^{Ph}{}_2N^{CH_2Pyrene}{}_2)_2]^{2+}$ or $[Ni(OH_2)_6]^{2+}$. For E_0 and S_0, the averages of the yielded values from the reference fits were applied. The use of an average but suboptimal S_0 leads to erroneous coordination numbers due to a correlation between those two fit parameters. In this case, the coordination numbers of P are suppressed and the ones of O are amplified. For compensation, all coordination numbers were multiplied by specific scale factors for P and O. These factors were determined via fitting the references with the average values for E_0 and S_0 and dividing the correct coordination numbers for P (N=4) and O (N=6) by the yielded coordination numbers. The simulated EXAFS spectra are presented in **Figure 61**.

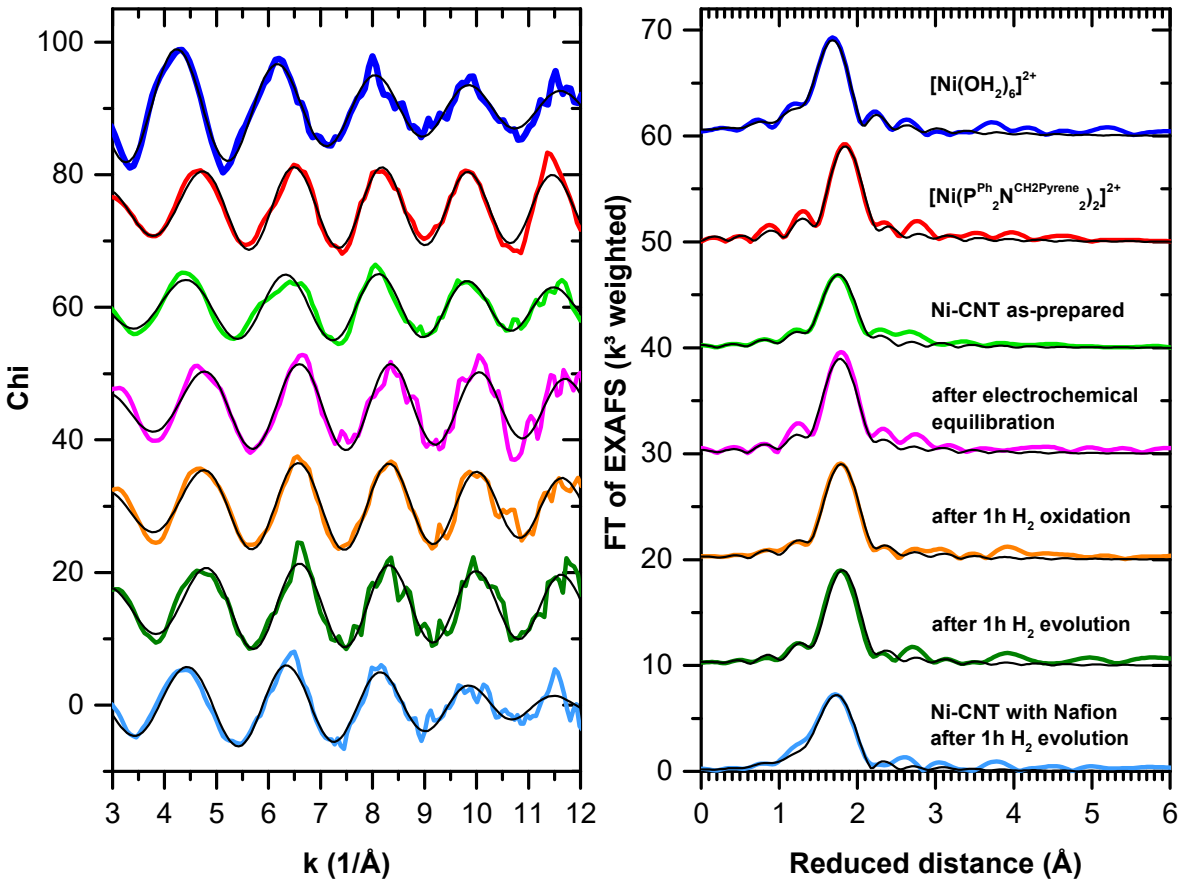

Figure 61

EXAFS simulations (**black** line) of the experimental spectra of the $[Ni(P^{Ph}_2N^{CH_2Pyrene}_2)_2]^{2+}$ catalyst in its pristine state (**red** line), grafted on CNT (= Ni-CNT as-prepared) (**light green** line), after electrochemical equilibration (**magenta** line), after H_2 oxidation (**orange** line) and after H_2 evolution (**dark green** line and, with Nafion membrane, **light blue** line); and of the $[Ni(OH_2)_6]^{2+}$ reference (**dark blue** line). **Left** side: the EXAFS represented as χ spectra. **Right** side: Fourier transforms (FT) of the k^3 weighted EXAFS spectra. The EXAFS simulations correspond to the structural parameters presented in **Table 18**. Only the first coordination sphere of the Ni-ligand environment is simulated.

The X-ray absorption near-edge structure (XANES) of the catalytic Co-N-C material (Co *K*-edge, see **Figure 62**) exhibit a mixture of features from a Co-O/N coordination similar to $[Co^{II}(OH_2)_6]^{2+}$, and from a contribution of metallic Co^0. During O_2 reduction in 1 h of fuel-cell operation, the Co-O/N coordination becomes more prominent and the metallic contribution diminishes. This can be deduced from a comparison with the XANES spectra of $[Co^{II}(OH_2)_6](NO_3)_2$ and Co^0 metal (see **Figure 62**). Before O_2 reduction, the position and the shape of the Co absorption edge of the Co-N-C spectrum are closer to the metal than to the $Co(OH_2)_6$ spectrum, in particular the prominent pre-edge. The amplitude of

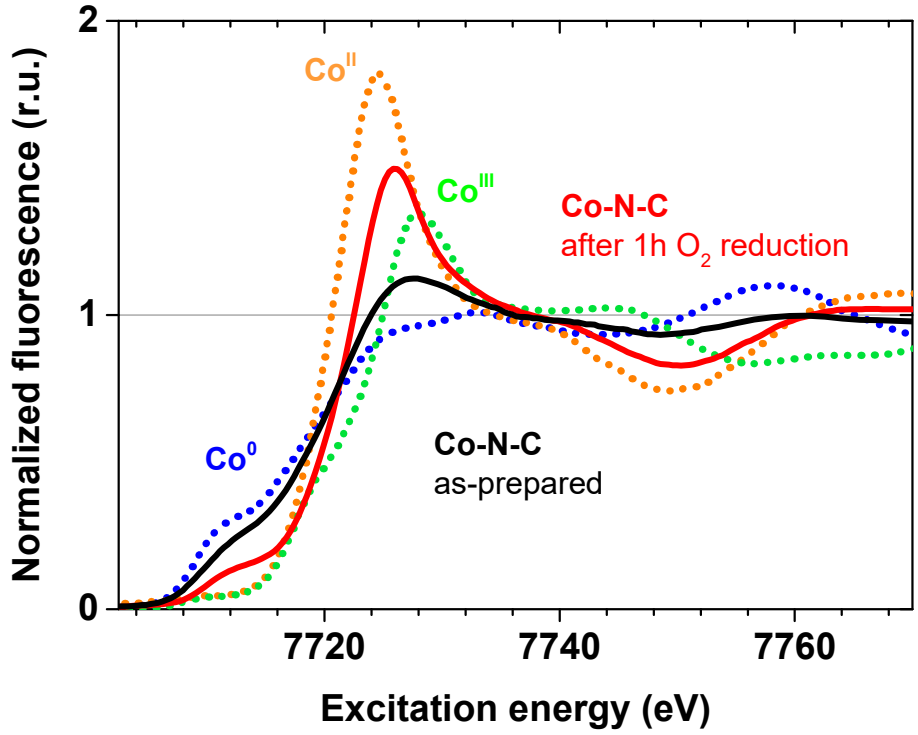

Figure 62

XANES/EXAFS spectra collected at the Co *K*-edge for the Co–N–C material as-prepared (**black** solid line) and after 1 h of O_2-reduction (**red** solid line). The spectra of metallic Co (**blue** dotted line), $[Co^{II}(H_2O)_6](NO_3)_2$ (**orange** dotted line) and $LiCo^{III}O_2$ (**green** dotted line) references are also shown for comparison.

the absorption edge, however, is higher than in the metal spectrum, indicating the presence of a Co-O/N coordination similar to $Co(OH_2)_6$. After O_2 reduction, the Co-N-C spectrum tends to contour the $Co(OH_2)_6$ spectrum: the metallic pre-edge is significantly diminished, the amplitude of the edge is further increased and the oscillations after the edge show a similar frequency as in $Co(OH_2)_6$. During O_2 reduction, the Co of the Co-N-C material is oxidized, indicated by a shift in the edge position towards higher excitation energies. The new position of the edge is located between the edges of the $[Co^{II}(OH_2)_6](NO_3)_2$ and $LiCo^{III}O_2$ references, indicating a mean oxidation state of Co between II and III in

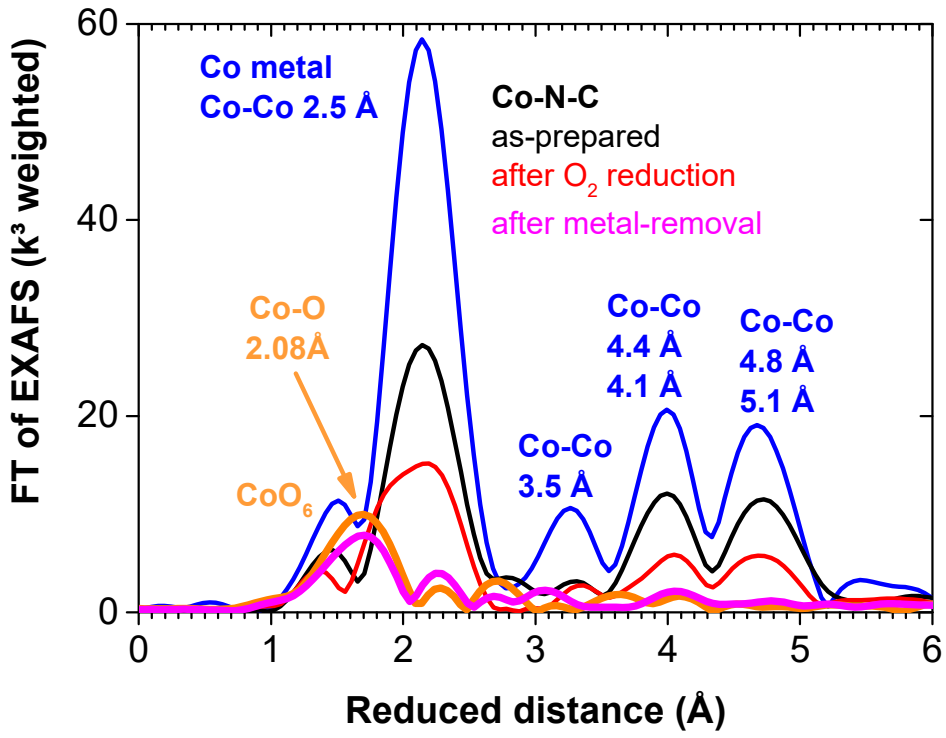

Figure 63

Fourier-transformed Co EXAFS (k^3 weighted, *k* range = 2 - 13 $Å^{-1}$) of the Co-N-C material as-prepared (**black** line) and after 1 h of O_2 reduction (**red** line), compared to metallic Co^0 (**blue** line) and $[Co^{II}(OH_2)_6](NO_3)_2$ (**orange** line). The **magenta** line was obtained by subtraction of the appropriately weighted metal spectrum from the spectrum of the Co-N-C material after catalytic operation. The resulting difference spectrum was renormalized and Fourier-transformed. The optimal weighting factor was determined by minimizing the oscillations in the metallic energy range of the Co-N-C spectrum. The peaks in the EXAFS spectra are labelled with the corresponding Co-ligand distances.

the Co-N-C material after O_2 reduction. It seems that, during O_2 reduction, the metallic Co contribution is removed from the Co-N-C material. Whether the Co-N-C material itself experiences modifications is unclear, since the metallic contribution in the XANES before O_2 reduction obscures the actual spectrum of the Co-N-C material. XAS emphasizes metallic contributions, as they consist of heavy back-scatterers and exhibit a significant long-range order.

The extended X-ray absorption fine-structure (EXAFS) of the Co-N-C material (Co *K*-edge) support the deductions from the XANES analysis. The Fourier transformed spectra of the Co-N-C material as-prepared and after 1 h of O_2 reduction (see **Figure 63**) exhibit significant peaks of metallic Co-Co distances (see structure scheme of Co metal in **Figure 48**). The amplitude of the peaks, however, is diminished by ≈50 - 70 % in comparison to the Co metal reference. This damping indicates the presence of a non-metallic Co contribution that possibly can be assigned to the catalytic Co-N-C species. The

Co-N-C material after O_2 reduction shows a stronger damping than the as-prepared material, indicating a diminishment of the metal contribution during the catalytic reaction. To gain more insight into the structure of the Co-N-C species, the obscuring metallic contribution is artificially removed from the EXAFS spectrum of the Co-N-C material. This was achieved by subtracting a weighted Co metal spectrum from the XANES/EXAFS of the Co-N-C material (after O_2 reduction) and renormalizing the difference spectrum (see **Equation 5**). The optimal weighting factor was determined by minimizing the metallic EXAFS oscillations in the higher energy range (from 7900 to 8750 eV) of the difference spectrum (for a more detailed description of the metal-subtraction method, see section *Subtraction of metal contribution from spectrum* in chapter *Methods*). The resulting weighting factor of 0.28 ± 0.15 indicates that on third of the Co-N-C material consists of metallic Co. The difference spectrum represents the non-metallic contribution of the Co–N-C material. The Fourier transform of the spectrum (see **Figure 63**) exhibits a prominent peak at short distances that, compared to the $Co(OH_2)_6$ reference, can be assigned to a Co-O coordination. EXAFS simulations indicate a Co-O distance of 2.08 ± 0.01 Å that falls into the range of O distances present in $Co(OH_2)_6$. This indicates that, in line with the XANES analysis, the Co-N-C species consists of Co ions coordinated to O and N atom in their first coordination sphere similar to $Co(OH_2)_6$. A deeper analysis with EXAFS simulations is prevented by the high noise level of the difference spectrum and the uncertainties of the method for artificially removing the metal contribution from the spectrum.

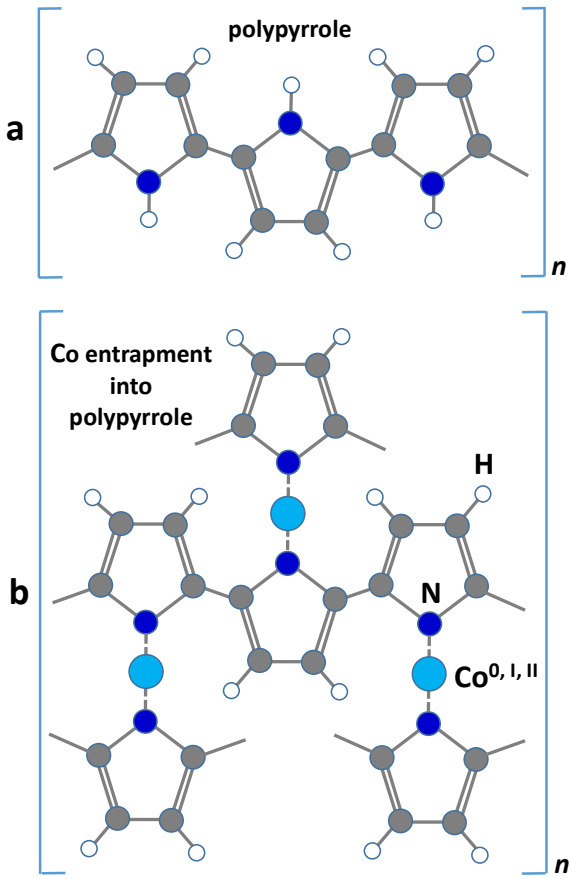

Figure 64

Schematic representation of the Co-polypyrrole composite catalyst reported by (Bashyam and Zelenay 2006). In **a**, polypyrrole structure. In **b**, presumed configuration of the catalyst after the entrapment and reduction of the cobalt precursor, $Co(NO_3)_2{\cdot}6H_2O$, into polypyrrole. Schemes in **a** and **b** based on illustration in (Bashyam and Zelenay 2006).

The oxidative transformation of the Co-N-C material during catalytic O_2-reduction from metallic Co to $Co^{II, III}$ ions with O/N coordination is similar to the behaviour of the cobalt-polypyrrole composite material reported by (Bashyam and Zelenay 2006) (see **Figure 64**), a O_2-reduction catalyst for polymer electrolyte fuel cells. The transformation does not lower the catalytic activity of the Co-N-C material as shown by co-workers in (Tran, Morozan et al. 2015).

CONCLUSIONS

The noble metal-free PEM fuel cell of *Tran et al.* consists of a layer of Ni-CNT material (CNT = carbon nanotube) catalytic for H_2 oxidation attached to a layer of Co-N-C material catalytic for O_2 reduction via an interfacing *Nafion* membrane only permeable for protons (Tran, Morozan et al. 2015). Our X-ray absorption spectroscopy (XAS) investigation give insight into the atomic structure of the catalytic

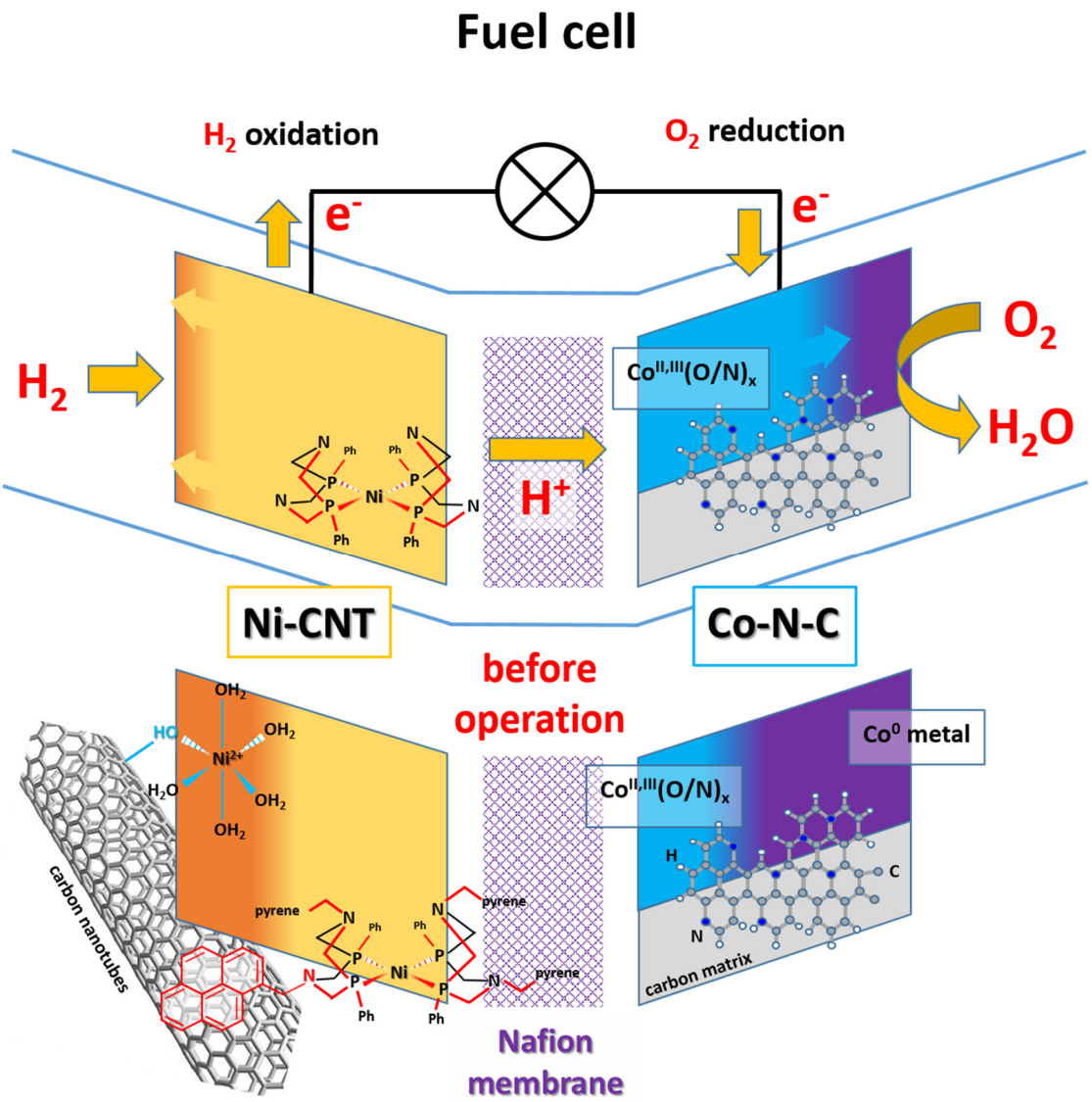

Figure 65

Schematic representation of the fuel cell before and during operation. The Ni-CNT material is the catalyst for the H_2 oxidation and the Co-N-C material for the O_2 reduction. The composition of both materials changes during operation. In the Ni-CNT material, the fraction of the $Ni^{II}(O/N)_6$ species (**orange**) diminishes and the catalytic "NiP_4" complexes (**yellow**) remain. In the Co-N-C material, the metallic Co^0 contribution (**violet**) decreases in favour of the catalytic $Co^{II,\,III}(O/N)_x$ species (**blue**).

materials and address the question whether the structure is modified under conditions of fuel-cell operation.

Our X-ray absorption spectroscopy (XAS) analysis shows that the Ni-CNT material consists of two Ni^{II} species (see **Figure 57**). One possesses a planar-tetrahedral P_4 ligand environment as in the original molecular Ni catalyst, a $[Ni(P_2^{Ph}N_2^{CH_2Pyrene})_2]^{2+}$ complex (= "NiP_4"), and the other an octahedral coordination to six light ligands (O or N) similar in structure to $[Ni(OH_2)_6]^{2+}$ (= "NiO_6") (see **Figure 65**). The proportion between the NiP_4 and NiO_6 species in the Ni-CNT material is about 2 : 1 (see detailed analysis in chapter *Molecular Ni catalyst grafted on a carbon-nanotube cathode*). After 1 h of H_2 oxidation under fuel-cell conditions (half-cell measurements), the Ni-CNT material exhibits a significant diminishment in the amount of NiO_6 species while the structure of the NiP_4 species remains unmodified. The catalytic activity of the Ni-CNT material, however, does not decrease, as shown by our co-workers (Tran, Morozan et al. 2015), confirming that the NiP_4 species is the catalytic species.

For the Co-N-C material, our XAS analysis indicates a mixture of a non-metallic $Co^{II, III}$ species with a metallic Co^0 contribution (see **Figure 62** and **Figure 65**). The non-metallic Co species consists of Co ions coordinated to O or N atoms (distance 2.08 Å) in their first coordination sphere similar to $[Co(OH_2)_6]^{2+}$. After 1 h of O_2 reduction in a fuel-cell, the previously major metallic contribution is significantly diminished. The new molar ratio between the non-metallic and metallic Co contributions is about 2 : 1. The diminishment of the metallic Co contribution, however, does not lead to a decrease in catalytic activity as shown by our co-workers (Tran, Morozan et al. 2015). The oxidative transformation of the Co-N-C material during catalysis, from metallic Co to $Co^{II, III}$ ions with O/N coordination, is similar to the behaviour of the cobalt-polypyrrole composite material (Bashyam and Zelenay 2006) (see **Figure 64**), an O_2-reduction catalyst for polymer electrolyte fuel cells. Possible alterations in the structure of the non-metallic Co-N-C material during catalysis could not be determined, since the state of the non-metallic material before O_2 reduction was obscured in XAS by a significant Co-metal contribution.

5. Catalytic Cu electrode for CO_2 reduction

The X-ray absorption spectroscopy (XAS) data and analysis shown in this chapter are published in (Huan, Andreiadis et al. 2015):

"From molecular copper complexes to composite electro-catalytic materials for selective reduction of CO_2 to formic acid"
Tran Ngoc Huan, Eugen. S. Andreiadis, Jonathan Heidkamp, Philippe Simon, Etienne Derat, Saioa Cobo, Guy Royal, Arno Bergmann, Peter Strasser, Holger Dau, Vincent Artero and Marc Fontecave
Journal of Materials Chemistry A 2015, **Vol 3**, 3901-3907
http://dx.doi.org/10.1039/c4ta07022d

Contributions:

- J. Heidkamp – X-ray absorption spectroscopy: entire data analysis and all measurements (samples were provided by co-workers)
- Co-workers – synthesis of the catalytic Cu electrode (development and execution); sample preparation, measurement and data analysis for all other used techniques aside from XAS

INTRODUCTION

Renewable energy sources as solar or wind are subject to temporal fluctuations. A possible approach is to store excess energy as chemical energy. The conversion of CO_2 into energy dense compounds (fuels) via solar or wind power is a potential storage technology (Morris, Meyer et al. 2009, Appel, Bercaw et al. 2013, Centi, Quadrelli et al. 2013, Costentin, Robert et al. 2013, Kondratenko, Mul et al. 2013, Reske, Duca et al. 2013, Mistry, Reske et al. 2014, Qiao, Liu et al. 2014, Reske, Mistry et al. 2014). The implementation of this technology could enable a global carbon-neutral and circular energy system and a slow-down of the accumulation of CO_2 (a greenhouse gas) in the atmosphere. A way to convert CO_2 is via electro-reduction in an electrochemical cell (Wu, Risalvato et al. 2013). However, the method requires an electro-catalyst that overcomes the very low kinetics of this multiple-electron reaction and exhibits a high selectivity. The reduction of CO_2 can form a variety of CO_2-derived products (CO, HCOOH, oxalate and, to lower extents, methanol or hydrocarbons) and, at the same time, molecular hydrogen (parallel reduction of the protons required for CO_2 activation) (Qiao, Liu et al. 2014). In the optimal case, an electro-catalyst for CO_2 reduction exclusively promotes the formation of liquid fuels as formic acid (Agarwal, Zhai et al. 2011) and methanol (Summers, Leach et al. 1986), which are compatible with the existing infrastructure for fuel transportation and distribution.

In recent studies, electro-catalytic material for CO_2 reduction has been investigated in non-aqueous media like organic solvents or ionic liquids (DiMeglio and Rosenthal 2013, Asadi, Kumar et al. 2014, Medina-Ramos, DiMeglio et al. 2014, Nakata, Ozaki et al. 2014, Oh, Vrubel et al. 2014). Non-aqueous media enables a higher solubility of CO_2 and a convenient control of H_2 evolution via adjusting the water concentration. Novel catalytic materials were developed based on MoO_2 (Oh, Vrubel et al. 2014), Bi (DiMeglio and Rosenthal 2013, Medina-Ramos, DiMeglio et al. 2014) and B-doped diamond (Nakata, Ozaki et al. 2014) or consist of molecular metal complexes (Morris, Meyer et al. 2009, Appel, Bercaw et al. 2013, Costentin, Robert et al. 2013, Qiao, Liu et al. 2014) whose activity is adjustable via ligand variations. So far, only one copper coordination compound has been reported as an electro-catalyst for CO_2 reduction (Angamuthu, Byers et al. 2010).

Huan et al. report a novel Cu material that is electro-catalytic for the reduction of CO_2 into formic acid (liquid fuel), showing remarkable activity, selectivity and stability (Huan, Andreiadis et al. 2015). The material is prepared via electro-deposition and operates in a non-aqueous medium (dimethylformamide). The organic ligand from the copper precursor (Cu cyclam) is preserved in the final catalyst material.

We perform X-ray absorption spectroscopy on the catalytic Cu material to gain insights in the atomic structure of the catalytic species.

This introduction text is based on a co-authored article (Huan, Andreiadis et al. 2015)

.

PREPARATION

Preparation of Cu electrode for XAS measurement

For the X-ray absorption spectroscopy (XAS) measurements, the Cu material was electro-deposited at -1.29 V *vs.* normal hydrogen electrode (NHE) on a glass substrate coated with fluorine-doped tin-oxide (FTO) (7 Ω sheet resistance) until 1 C/cm^2 of deposited charge was reached. The deposition solution consisted of dimethylformamide (DMF) (40 ml) containing the pre-cursor [Cu(cyclam)]$(ClO_4)_2$ (cyclam = 1,4,8,11-tetraazacyclotetradecane) (1.3 mM), a supporting electrolyte of *n*-Bu_4NBF_4 (0.1 M) and 3 % of bi-distilled water. The DMF solution was saturated with CO_2 gas before and during deposition via permanent sparging with a flow of CO_2 gas. After deposition, the resulting electrode was immediately dipped in a Cu-free DMF solution, then attached to a XAS sample holder and finally stored in liquid N_2. The electro-deposition was performed in a three-electrode system with an Ag/AgCl reference electrode (3 M KCl, +0.21 V *vs.* NHE) and a shielded counter electrode of Pt mesh. The used potentiostat was a *Biologic SP200* or *SP300*. *The deposition of the Cu material was developed and performed by co-workers in (Huan, Andreiadis et al. 2015)*

.

The X-ray absorption near-edge structure (XANES) of the Cu material on the electrode exhibit a mixture of features from Cu^0 metal, Cu^I oxide and from various Cu^{II} compounds as Cu malachite, Cu oxalate and Cu^{II} oxide. This suggests that the Cu material contains, besides the metallic contribution, a species of Cu^I ions most likely coordinated to two light atoms (O or N) in the first coordination sphere as in

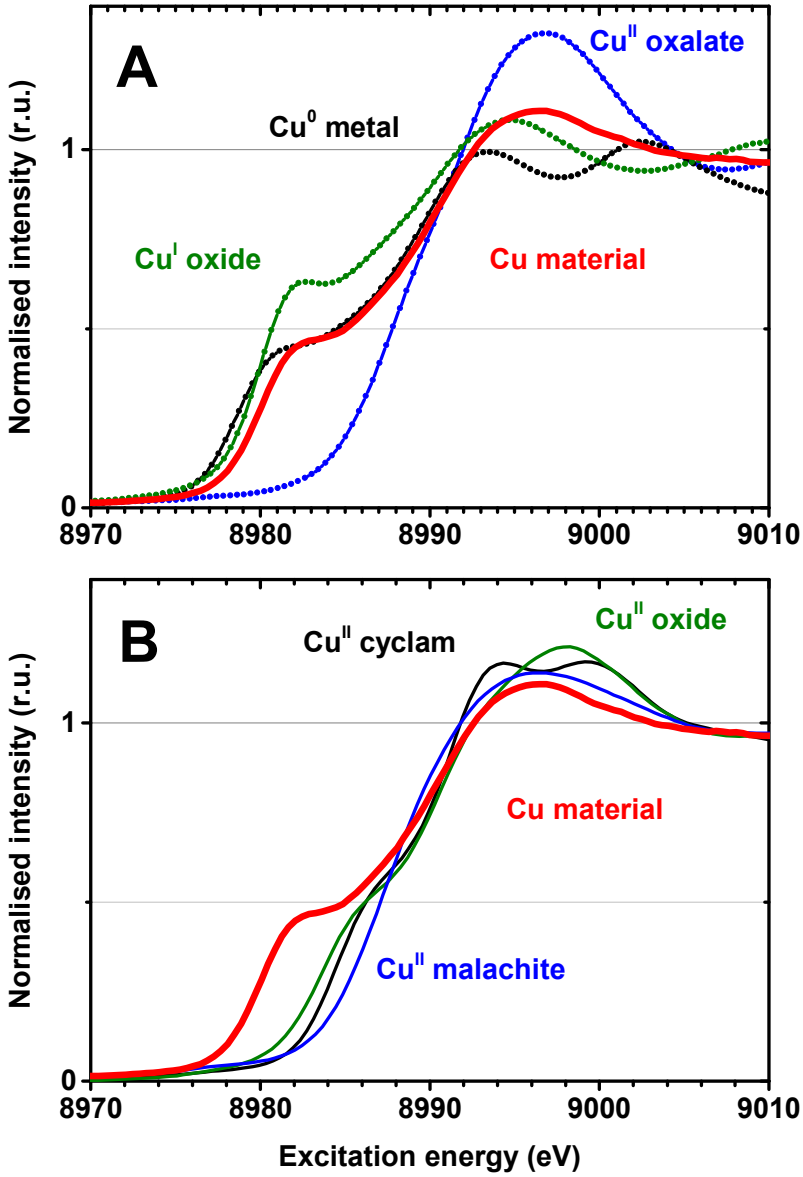

Figure 66

XANES spectra recorded at the Cu *K*-edge. (**A**) (**red** trace) catalytic Cu material, (**black** trace) metallic Cu^0, (**green** trace) Cu^I oxide and (**blue** trace) Cu^{II} oxalate. (**B**) (**red** trace) catalytic Cu material, (**green** trace) Cu^{II} oxide, (**blue** trace) Cu^{II} malachite and (**black** trace) the pre-cursor $[Cu(cyclam)](ClO_4)_2$.

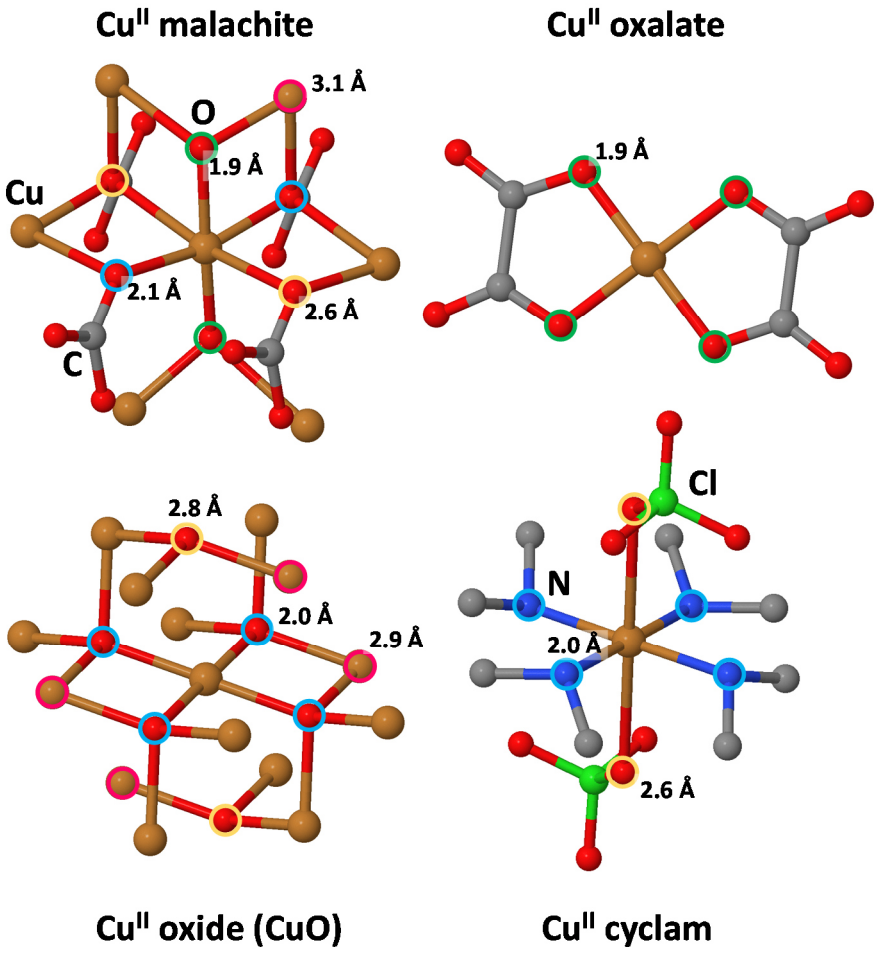

Figure 67

Schematic structures of Cu^{II} malachite, Cu^{II} oxalate, Cu^{II} oxide (CuO) and Cu^{II} cyclam with denoted Cu-O and Cu-Cu distances. O/N and Cu atoms with the same distance to the central Cu atom are marked with circles of the same colour. In the case of the Cu atoms, only the atoms with the shortest distance to the Cu centre are indicated. Images based on crystal data published for Cu malachite in (Zigan, Joswig et al. 1977), for Cu oxalate in (Gajapathy, Govindarajan et al. 1983, Schonfeld, Huang et al. 1983), for Cu^{II} oxide in (Niggli 1922) and for Cu cyclam in (Choi, Ryoo et al. 2007).

Cu^{I} oxide (see structure in **Figure 70**), and another species of Cu^{II} ions possibly with four light ligands (O, N or C) in the first sphere as in the mentioned Cu^{II} references (see structures in **Figure 67**). The possible ligand geometries for the Cu^{I} and Cu^{II} species in the first coordination sphere are, according to the references, linear or planar-tetrahedral planar, respectively. A XANES comparison with Cu^{I} oxide and Cu^{II} oxalate (see **Figure 66A**) suggests that the pre-edge of the Cu electrode spectrum (at higher energies than in Cu metal) is indicative for a Cu^{I} species, and that the increased amplitude of the main edge (at higher energies than in Cu^{I} oxide) is indicative for another Cu^{II} species. This is further confirmed by a comparison with other Cu^{II} references (see **Figure 66B**). Compared to Cu metal (see **Figure 66A**), the upper part of the edge of the Cu material (from 0.5 to 1 normalized intensity) seems to be of metallic nature.

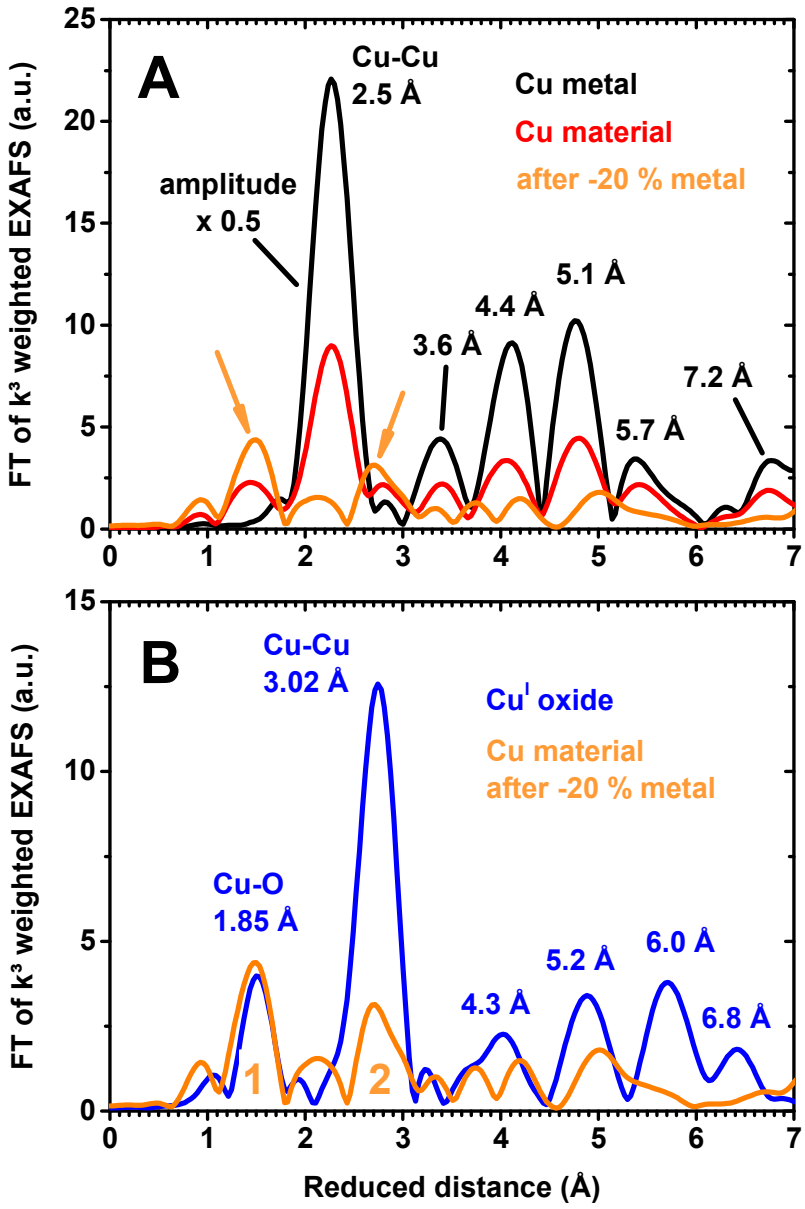

Figure 68

Fourier transforms (FT) of EXAFS spectra (k^3 weighted, k range = 2 - 16 Å^{-1}) recorded at the Cu K-edge. (**A**) (**red** trace) catalytic Cu material, (**orange** trace) after artificial removal of the metal contribution of 20 % and (**black** trace) metallic Cu^0. The FT amplitudes of the metal reference were multiplied by 0.5. The metal peaks are labelled by the corresponding Cu–Cu distances. The non-metallic peaks of the Cu material are marked by orange arrows. (**B**) (**orange** trace) catalytic Cu material after artificial removal of the metallic contribution of 20 % and (**blue** trace) Cu^I oxide. The peaks of Cu^I oxide are labelled with the corresponding Cu-O and Cu-Cu distances. The first and second main peak in the Cu-material spectrum are labelled with **1** and **2**.

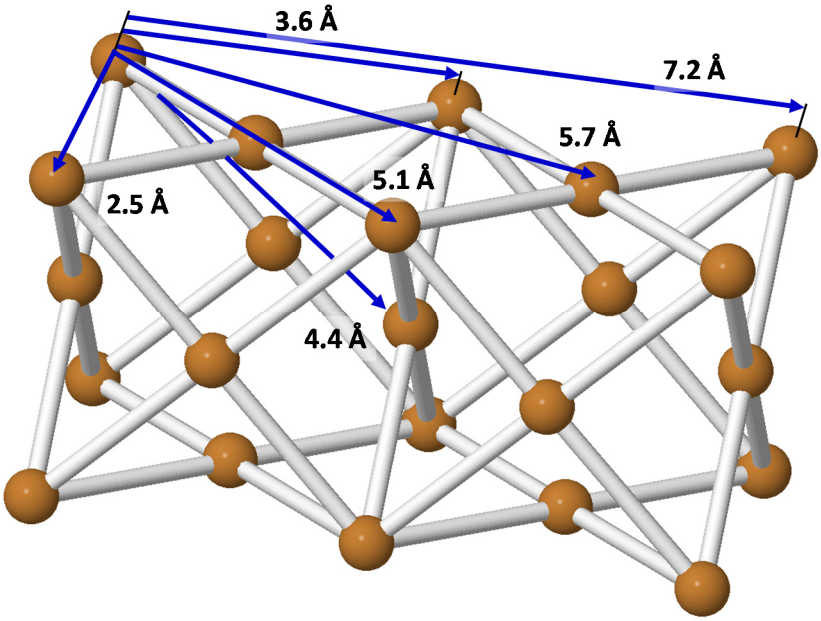

Figure 69

Schematic structure of metallic Cu^0 in the face-centred cubic phase with denoted Cu-Cu distances. Image based on crystal data of Cu metal published in (Otte 1961).

The XANES of the Cu material are well reassembled by a linear combination of weighted spectra of Cu metal, Cu^I oxide and Cu^{II} oxalate. This supports the proposed presence of the corresponding Cu^0, Cu^I and Cu^{II} species. The weighting factors of the optimal linear combination (see **Equation 6**) suggest that 24 ± 8 % of the Cu material on the electrode are metal, 48 ± 8 % Cu^I oxide and 28 ± 8 % Cu^{II} oxalate. For a more detailed description of the linear-combination method see section *Linear combination of spectra* in chapter *Methods*.

A XANES comparison with the pre-cursor of the Cu material, Cu cyclam, (see **Figure 66B** and **Figure 67**) suggests that the structure of the pre-cursor is modified in the Cu^{II} species of the material. The spectrum of the pre-cursor exhibits a unique edge with two summits that is not shared by the Cu material and by the other Cu^{II} references. The edge position of the Cu material in the XANES lies between the edges of the Cu^0, Cu^I and Cu^{II} references (see **Figure 66A**), indicating a mean oxidation state for Cu in the electrode between zero and II.

The extended X-ray absorption fine-structure (EXAFS) of the Cu material exhibits, as the XANES, a mixture of metallic and non-metallic features, indicating the presence of a Cu metal contribution and a non-metallic Cu species. An EXAFS comparison with Cu^0 metal (see Fourier-transforms in **Figure 68A** and **Figure 69**) shows that the spectrum of the Cu material contains all peaks of the metal reference (Cu-Cu coordinations) but with a ≈80 % lower amplitude. This damping indicates the presence of a non-metallic contribution in the Cu material. Furthermore, the spectrum of the Cu material exhibits two peaks at 1.5 Å and at 2.8 Å (see **Figure 68A**) that are not part of the metal spectrum and, hence, can be assigned to a non-metallic Cu species. To gain an unobscured view on the non-metallic contribution,

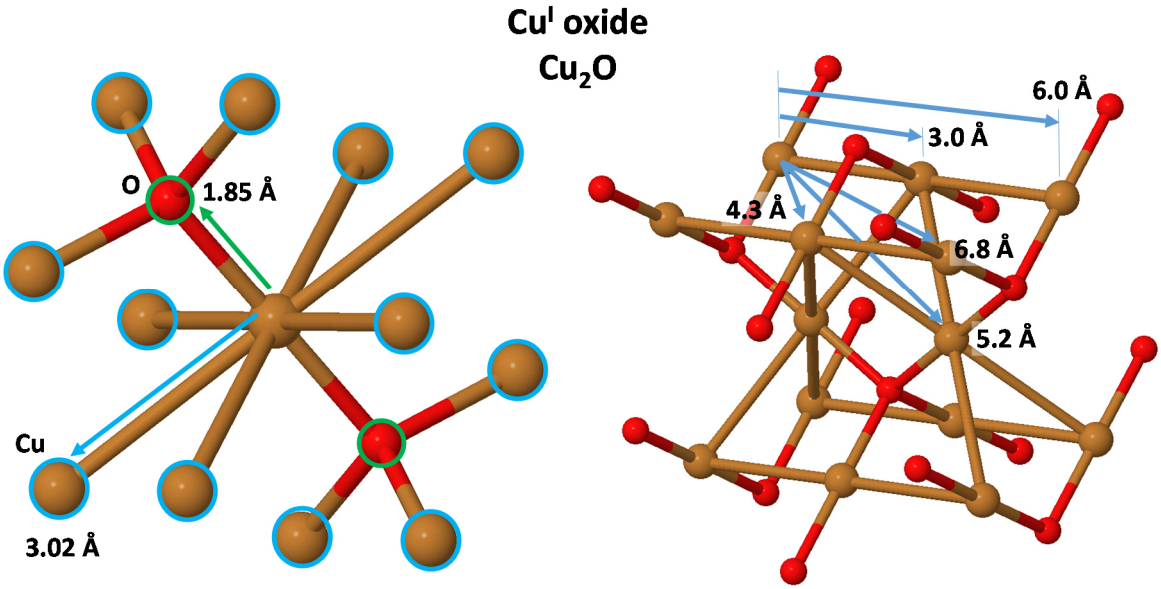

Figure 70

Schematic structure of Cu^{I} oxide (Cu_2O) with denoted Cu-O and Cu-Cu distances. **Left** side: first O (green circles) and Cu (blue circles) coordination sphere. **Right** side: Cu-Cu long-range structure. Images based on crystal data published in (Kirfel and Eichhorn 1990).

the metallic part of the spectrum was removed artificially. This was achieved by subtracting the EXAFS of the Cu material (not Fourier transformed) with a weighted Cu metal spectrum and subsequently re-normalizing the difference spectrum (see **Equation 5**). The optimal weighting factor was determined by minimizing the metallic EXAFS oscillations in the higher energy range (from 9170 to 10010 eV) of the Cu-material spectrum. The resulting weighting factor suggests that 20 ± 14 % of the Cu material are metallic. After the artificial removal of the metallic contribution, the spectrum of the Cu material (see Fourier transform in **Figure 68B**) lacks the metal peaks and exhibits magnified peaks of the non-metallic contribution. For more a detailed description of the metal-removal method see section *Subtraction of metal contribution from spectrum* in chapter *Methods*.

An EXAFS comparison with Cu^{I} oxide (see Fourier transform in **Figure 68B** and **Figure 70**) suggests that the non-metallic peak **1** of the Cu material can be assigned to a Cu-O coordination and peak **2** to a Cu-Cu coordination. EXAFS simulations (see **Figure 71**) of these peaks yield a Cu-O distance of 1.85 ± 0.01 Å and a Cu-Cu distance of 2.97 ± 0.02 Å that are close to the distances of Cu^{I} oxide as well as the simulated O coordination number of 2.4 ± 0.5 (see **Table 19**). Compared to the Cu^{I}-oxide spectrum, the low amplitude of peak **2** in the Cu-material spectrum and, at longer distances, the missing of prominent peaks (see **Figure 68B**) indicate that, at longer distances than 1.85 Å, the Cu^{I} species of the Cu material is very disordered and does not show a prominent long-range structure as in Cu^{I} oxide. The possible presence of an additional Cu^{II} species in the Cu material is indicated by the slightly higher O coordination number than in Cu^{I} oxide (see **Table 19**).

Compared to the molecular precursor, the Cu material shows a significantly shorter Cu-O distance than Cu cyclam and a Cu-Cu coordination not present in the pre-cursor (see **Table 19**). This indicates that the inner structure of the Cu cyclam is modified during the electro-deposition of the Cu material.

Cu compound	**Cu-O/N coordination** 1st coordination sphere		**Cu-Cu coordination** with the shortest distance	
	Distance [Å]	**Coordination number**	**Distance** [Å]	**Coordination number**
Catalytic Cu material // non-metallic Cu species	1.85 ± 0.01	2.4 ± 0.5	2.97 ± 0.02	2.4 ± 0.8
				EXAFS simulation
Cu^{I} oxide	1.84 – 1.85	2	3.01 – 3.02	12
Cu^{II} malachite	1.91 – 1.92 2.04 – 2.12	2 2	3.06	1
Cu^{II} oxalate	1.93 – 1.94	4		
Cu^{II} oxide	1.95 – 1.97	4	2.88 - 2.90	4
$[Cu(cyclam)]^{2+}$	2.01 – 2.05	4		
				Crystal structure (X-ray diffraction)

Table 19

Structural parameters of the Cu-O/N and Cu-Cu coordination in the non-metallic Cu species of the catalytic Cu material. The stated distances and coordination numbers for Cu-O/N and Cu-Cu were determined by EXAFS simulations of peak **1** (Cu-O/N) and **2** (Cu-Cu) in the Cu-material spectrum after the artificial removal of the metallic contribution of 20 % (see **Figure 68B**). The distances and coordination numbers of the Cu material are compared to the first Cu-O/N coordination sphere and the shortest Cu-Cu coordination (if present) of Cu^{I} oxide, Cu^{II} malachite, Cu^{II} oxalate, Cu^{II} oxide and the pre-cursor $[Cu(cyclam)]^{2+}$. The denoted values of these compounds were taken from the corresponding crystal structures. For the EXAFS simulations of the Cu material, the Debye-Waller factors of O and Cu ($2\sigma_O^2 = 0.002$ Å^2 and $2\sigma_{Cu}^2 = 0.011$ Å^2), the amplitude reduction factor ($S_0^2 = 0.6$) and the energy offset ($E_0 = 2.6$ eV) were fixed at values determined from simulations of the Cu^{I}-oxide spectrum. The used phase functions were calculated from the crystal structure of Cu^{I} oxide. The simulated EXAFS spectra are presented in **Figure 71**.

Crystal structure data for Cu^{I} oxide was obtained from (Neuburger 1930, Kirfel and Eichhorn 1990), for Cu^{II} malachite from (Süsse 1967, Zigan, Joswig et al. 1977), for Cu^{II} oxalate from (Gajapathy, Govindarajan et al. 1983), for Cu^{II} oxide from (Niggli 1922, Tunell, Posnjak et al. 1935, Smura, Parker et al. 2011) and for $[Cu(cyclam)]^{2+}$ from (Choi, Ryoo et al. 2007).

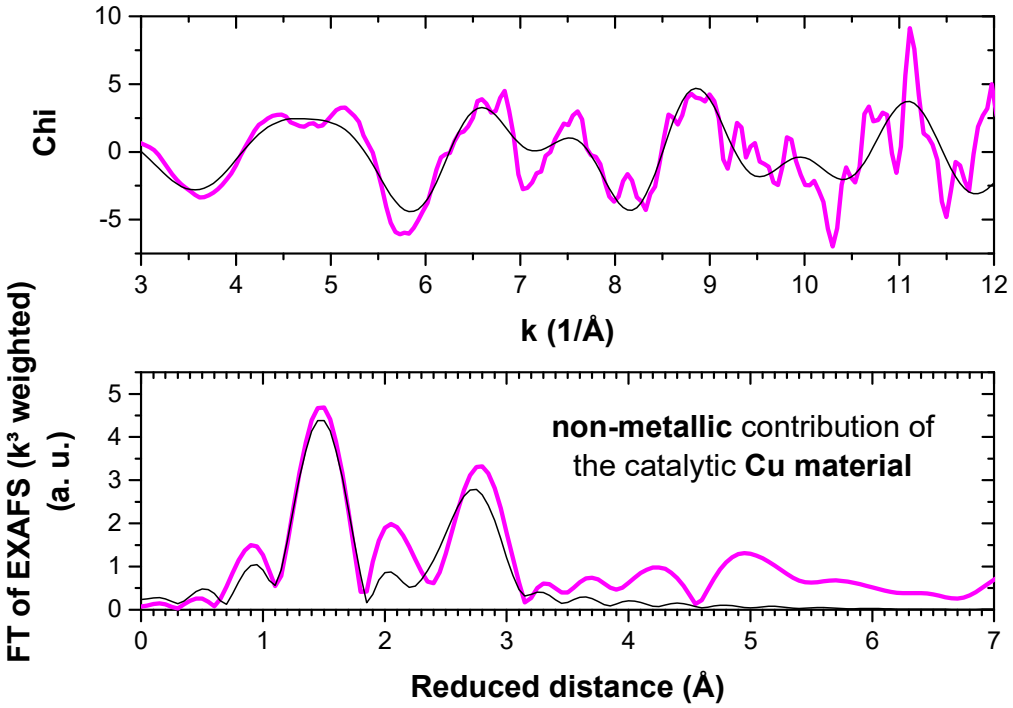

Figure 71

EXAFS simulations (**black** line) of the experimental spectrum of the non-metallic Cu species in the catalytic Cu material (**magenta** line). **Top**: the EXAFS represented as χ spectra. **Bottom**: Fourier transforms (FT) of the k^3 weighted EXAFS spectra. The EXAFS simulations correspond to the structural parameters presented in **Table 19**. Only the first Cu-O/N coordination sphere and the shortest Cu-Cu coordination are simulated.

CONCLUSIONS

The Cu material is a novel catalyst for CO_2 reduction and is prepared by simple electro-deposition from a dimethylformamide (DMF) solution of the precursor, $[Cu(cyclam)](ClO_4)_2$ (cyclam = 1,4,8,11-tetraazacyclotetradecane). Our X-ray absorption spectroscopy (XAS) investigations provide insight into the atomic structure of the Cu-based material.

The XAS analysis suggests that about one quarter of the Cu material (see **Figure 72**) consist of metallic Cu^0 and three quarter of a prominent non-metallic $Cu^{I, II}$ contribution. In the latter, the Cu^I ions are most likely coordinated to two light atoms (O or N) in the first coordination sphere and, at longer distances, to other Cu ions. The atomic structure of the Cu^I species is similar to Cu^I oxide (see extended X-ray absorption fine-structure (EXAFS) in **Figure 68B**) but does not exhibit a comparable long-range order. The Cu^{II} ions of the non-metallic contribution are possibly coordinated to four light ligands (O, N or C) as in Cu malachite, Cu oxalate or Cu^{II} oxide (see X-ray absorption near-edge structure (XANES) in **Figure 66B**). The Cu^{II} species is less abundant in the Cu material than the Cu^I species. The Cu material exhibits a higher selectivity for CO_2-derived products than pure Cu-metal or Cu^I-oxide electrodes, as shown by co-workers in (Huan, Andreiadis et al. 2015). The inner structure (Cu-O/N coordination) of the pre-cursor, Cu cyclam, is modified during electro-deposition of the Cu material.

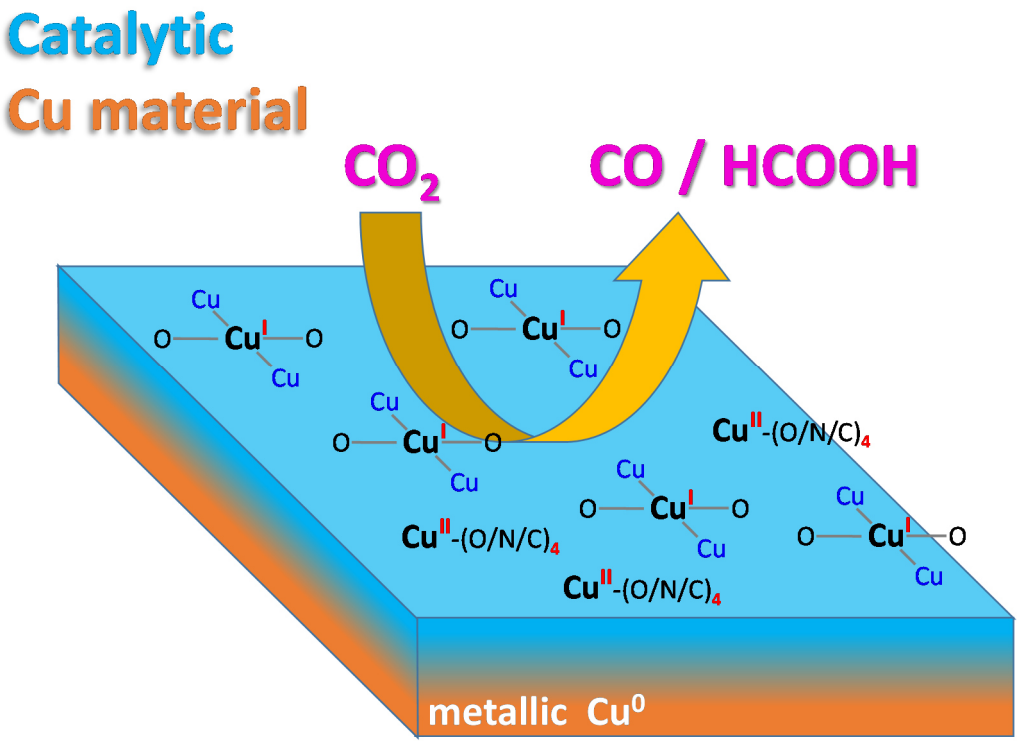

Figure 72

Schematic structure of the catalytic Cu material for CO_2 reduction. The material consists of metallic Cu^0 and a non-metallic contribution containing Cu^I and Cu^{II} ions coordinated to light atoms (O, N or C) in their first coordination sphere. The Cu^I ions also possess a Cu-Cu coordination and exhibit structural similarities to Cu^I oxide.

IV.SUMMARY

The amorphous MoS_x electrodes (x = 2 or 3) established by *Merki et al.* can be prepared by electro-deposition under ambient conditions and exhibit a high activity for the hydrogen-evolution reaction (HER) (Merki, Fierro et al. 2011, Merki, Vrubel et al. 2012). *Merki et al.* report that the doping of the electrodes with Co or Ni increases their catalytic activity for HER, as the dopants promote the catalytic load, the surface area and, at pH 7, the intrinsic activity of the electrodes (Merki, Vrubel et al. 2012).

We investigated the Co doped, Ni doped and undoped *Merki*-type MoS_x electrodes with X-ray absorption spectroscopy (XAS) at the Mo *K*-edge to gain insight into the atomic structure of their Mo sites. For the doped electrodes, additional XAS measurements were performed at the Co or Ni *K*-edge to obtain information about the atomic structure of the Co and Ni sites. The XAS spectra were recorded at electrode potentials of -0.80 V, -0.35 V and +1.40 V *vs.* normal hydrogen electrode (NHE) under neutral conditions (pH 7), to study structural differences between Mo, Co and Ni sites in a state of catalytic hydrogen-evolution reaction (HER) (-0.80 V), in a non-catalytic state (-0.35 V) and under conditions of water-oxidation (+1.40 V) (standard electrode potential of hydrogen reduction E^0_{H2} = -0.41 V and of water-oxidation E^0_{O2} = +0.82 V at pH 7).

Our XAS analysis indicates that the bulk of the Co/Ni doped and undoped *Merki* electrodes at pH 7 (Merki, Vrubel et al. 2012) comprises an amorphous MoS_x species (x = 2 or 3). For all electrodes, the atomic structure of the species is composed of Mo^{IV} ions coordinated to presumably five S atoms in the first coordination sphere and to a proximate Mo atom in the second sphere (see **Figure 35**). The Mo sites of the electrodes combine structural features of $Mo^{IV}S_2$ and MoS_3, as the mean Mo-S distance of 2.37 – 2.38 Å is typical for $Mo^{IV}S_2$ while the mean Mo-Mo distance of 2.79 – 2.81 Å as well as the low Mo coordination number are characteristic for MoS_3. The Mo-S coordination in the *Merki* electrodes exhibits a higher spatial disorder of the S coordination sphere (Debye-Waller parameter σ_S = ±0.08 Å) than in crystalline $Mo^{IV}S_2$ (σ_S = ±0.03 Å), suggesting a higher abundance of coordinatively unsaturated S sites. Furthermore, the Mo sites in the *Merki* electrodes seem to possess less S ligands (mean S coordination number N_S = 4.7 – 5.3) than in crystalline $Mo^{IV}S_2$ (N_S = 6), suggesting the presence of coordinatively unsaturated Mo sites. A six-fold S coordination of the Mo sites is not favoured by EXAFS simulations (EXAFS = extended X-ray absorption fine structure) (see **Table 2**) but cannot be excluded. The unsaturated S and Mo sites are possible adsorption sites for atomic hydrogen and, therefore, potential catalytic sites for HER. The higher density of unsaturated S and Mo sites in the *Merki* electrodes compared to bulk crystalline $Mo^{IV}S_2$ could explain the higher catalytic activity of the electrodes (Merki, Fierro et al. 2011, Merki, Vrubel et al. 2012). The presence of these unsaturated sites throughout the bulk of the *Merki* electrodes suggests that the bulk participates in the HER catalysis. This could be enabled via proton diffusion into the bulk (proposed by *Casalongue et al.*) supported by the porosity of the electrodes (Merki, Vrubel et al. 2012, Casalongue, Benck et al. 2014).

Our electrochemical studies on the *Merki* electrodes under neutral conditions (pH 7) also suggest a participation of the MoS_x bulk in HER catalysis. Cyclic voltammetry of the undoped *Merki* electrode (= pure MoS_x) under HER conditions shows redox currents (see **Figure 33**) that indicate the occurrence of redox equivalents approximately equal (order of magnitude estimate) in number to Mo and S atoms present in the electrode (see **Table 12**). Rather than the Mo ions itself, S sites appear to be crucial for the redox chemistry, since XAS analysis indicates only a minor change in mean oxidation state for the Mo ions when comparing non-catalytic and catalytic potentials (see **arrow** in **Figure 36**). This sub-

stoichiometric reduction of Mo^{IV} ions to Mo^{III} could be related to HER catalysis at the electrode surface as previously suggested by *Lassalle et al.* (Lassalle-Kaiser, Merki et al. 2015).

In the Co/Ni doped *Merki* electrodes, the MoS_x bulk is permeated by Co or Ni sites. Our XAS analysis indicates that the Co sites consist of $Co^{II,III}$ ions coordinated to six S atoms in the first coordination sphere while the Ni sites consist of $Ni^{I,II}$ ions coordinated to four S atoms (see **Figure 35**). The majority of the Co and Ni sites is directly coordinated to a neighbouring Mo atom, suggesting an incorporation of the sites in the MoS_x bulk. During HER catalysis at pH 7, the Co and Ni sites exhibit a decrease in S coordination number (see **Table 14**) and/or spatial order of the S coordination sphere, suggesting the formation of coordinatively unsaturated dopant sites and/or S sites. These sites are potential catalytic sites for HER, in analogy to the unsaturated S and Mo sites of the MoS_x bulk. This is especially evident for the Co sites, as their atomic structure likely is similar to the catalytic site of $CoMoS_2$ catalysts for hydrodesulphurisation. A direct involvement of the Co and Ni sites in HER catalysis is also supported by our electrochemical studies on the doped *Merki* electrodes, since cyclic voltammetry suggests (i) an influence of the dopant ions (Ni or Co) on the number of reducing equivalents accumulated when comparing catalytic with non-catalytic potentials (see **Table 12**), and (ii) a clear shift in the midpoint potential of the corresponding redox transition to less negative value by doping with Co or Ni ions (see **Figure 33**). The Co and Ni sites may be directly involved in active-site formation at catalytic potentials, since our XAS analysis suggests more significant structural modifications and oxidation state changes for the dopant sites than for the Mo sites (see **Figure 36** and **Figure 37**). The effect of the Co/Ni doping on the atomic structure of the MoS_x bulk material is small, leading only to a slight diminishment in density of unsaturated Mo or S sites for the doped *Merki* electrodes.

The intrinsic HER activity of the *Merki* electrodes under neutral conditions (pH 7) can be promoted by the doping with Co or Ni (Merki, Vrubel et al. 2012). The promotion effect in the doped electrodes could arise from the additional presence of unsaturated dopant and/or S sites and from the superior reactivity of the dopant sites in comparison to the Mo sites. The *Merki* electrodes possibly form a S-bound hydride whose reactivity and/or formation is promoted by the doping with Co or Ni. The HER mechanism of the electrodes most likely involves coordinatively unsaturated metal ions (Mo, Co and Ni) and S sites and could be analogous to the one in hydrogenases where molecular hydrogen is formed by the interplay between a hydride-binding metal site and a proton-binding pendant base in close proximity (Lubitz, Ogata et al. 2014).

Under conditions for water-oxidation (at pH 7), our electrochemical studies show only for the Co doped *Merki* electrode catalytic activity, indicated by a rise in anodic catalytic current at +1.25 V in cyclic voltammetry (see **Figure 46**). The Ni doped electrode does not exhibit significant catalytic currents under these conditions. Our XAS analysis (see **Figure 42** and **Figure 43**) indicates that, in the Co doped electrode, the *CoCat* is formed, which is a well-known Co-oxide catalyst for water oxidation (Kanan and Nocera 2008, Risch, Khare et al. 2009) while, in the Ni doped electrode, analogous Ni oxide cannot be formed due to the dissolution of Ni ions. The XAS analysis of the Mo sites (see **Figure 38** and **Figure 40**) indicates that in all electrodes, undoped and doped, the Mo sites experience a partial transformation of the original Mo-S species into a Mo-O species ($Mo^{VI}O_6$ octahedra coordinated to SO_x groups). However, both Mo species seem to be inactive under water-oxidation conditions, since the undoped electrode does *not* exhibit any significant catalytic current wave at potentials above +1.25 V (see **Figure 46**). The formation of the new Mo-O species can be assigned to an anodic current wave around +0.5 V (see **Figure 46** and **Figure 47**) that originates from a partial oxidation of the sulphur presumably via the

following reaction: $MoS_2 + 7H_2O \rightarrow MoO_3 + SO_4^{2-} + ½\ S_2^{2-} + 14H^+ + 11e^-$ (Bonde, Moses et al. 2008). The oxidation of the Mo-S species is irreversible and leads to a dissolving of the Mo film on the electrodes when the electrode potential is cycled repeatedly between -0.8 V and +1.4 V (see **Figure 47**).

CATALYTIC Co ELECTRODE ELECTRO-DEPOSITED UNDER REDUCTIVE CONDITIONS

The *H_2-CoCat* is a Co-based material electro-deposited under reductive conditions (deposition potential of -0.79 V *vs.* normal hydrogen electrode (NHE)) and exhibits a catalytic evolution of H_2 at -0.79 V and of O_2 at +1.37 V as verified by gas chromatography measurements (performed and analysed by our co-workers in France (Cobo, Heidkamp et al. 2012)). Our XAS investigation show that, in the state of H_2 evolution, about 60 % of the *H_2-CoCat* consists of a hexagonal close-packed phase of metallic Co^0 (see **Figure 48**) and about 40 % of a non-metallic species with Co ions coordinated to O, N or C ligands in their first coordination sphere (see **Figure 53**). The non-metallic contribution is crucial for the catalytic activity of the *H_2-CoCat*, since its electrochemical performance is much higher than of a pure metallic electrode (Cobo, Heidkamp et al. 2012). Together with evidence from X-ray photoelectron spectroscopy (XPS) measurements (performed and analysed by our co-workers (Cobo, Heidkamp et al. 2012)), it can be assumed that the *H_2-CoCat* is a combination of a Co^{II} phosphate with a Co oxo/hydroxo species formed on the surface of metallic Co. In the state of O_2 evolution, our XAS analysis shows that the *H_2-CoCat* (partly) transforms into a Co species similar to the *O_2-CoCat* (see **Figure 52**), an amorphous Co oxide catalyst for water oxidation (Kanan and Nocera 2008, Risch, Khare et al. 2009). The *O_2-CoCat*-like Co species consists of clusters of edge-sharing $Co^{III}O_6$ octahedra.

MOLECULAR Ni CATALYST GRAFTED ON A CARBON-NANOTUBE CATHODE

The $[Ni(P_2^{Ph}N_2^{CH_2Pyrene})_2]^{2+}$ complex ("NiP_4") is a molecular catalyst for H_2 formation (see **Figure 56**). Its structure is bioinspired by the active sites of hydrogenases, enzymes for H_2 oxidation and reduction. The NiP_4 complex is grafted on the multi-walled carbon-nanotubes (MWCNTs) surface of a gas diffusion layer (GDL) via noncovalent π-π stacking (Tran, Le Goff et al. 2011). Our X-ray absorption spectroscopy (XAS) investigation monitor the structure of the NiP_4 complex during the grafting on the MWCNTs/GDL electrode (see **Figure 54a** and **c**). Our XAS analysis indicates that one third of the complexes incorporates O/N ligands or transforms into an octahedral Ni^{2+} species with a coordination to six light atoms (O, N or C) similar to $[Ni^{II}(OH_2)_6]^{2+}$ (see **Figure 56**). The other two third maintain their original planar-tetrahedral P_4 ligand system. Simulations of the X-ray absorption near-edge structure (XANES) (see **Figure 55**) suggest that separate Ni-P and Ni-O species are formed on the MWCNTs without mixed P/O ligand environments. The Ni-O/N coordination could arise from a fraction of the NiP_4 complexes binding to water molecules, carboxylate, or hydroxo defects present at the surface of MWCNTs. Furthermore, the oxidation of a diphosphine ligand in the NiP_4 complex, either through the phosphine oxide function or through the amine function, could also lead to a Ni-O/N coordination as recently shown in a similar system (Yang, Bullock et al. 2010).

NOBLE METAL-FREE FUEL CELL

The noble metal-free fuel cell of *Tran et al.* utilizes a novel cobalt/nitrogen/Vulcan (Co-N-C) material as catalyst for O_2 reduction, and a previously studied carbon-nanotube material functionalized with biomimetic Ni complexes (Ni-CNT) as catalyst for H_2 oxidation (see chapter *Molecular Ni catalyst on a carbon-nanotube cathode*) (Tran, Le Goff et al. 2011). The fuel cell is based on proton exchange membrane (PEM) technology, using a *Nafion* membrane only permeable for protons as interface between the layer of Co-N-C material and the layer of Ni-CNT material (Tran, Morozan et al. 2015) (see **Figure 65**). Our X-ray absorption spectroscopy (XAS) investigation give insight into the atomic structure of the catalytic materials and address the question whether the structure is modified under conditions of fuel-cell operation.

Our X-ray absorption spectroscopy (XAS) analysis shows that the Ni-CNT material consists of two Ni^{II} species (see **Figure 57** and **Figure 58**). One possesses a planar-tetrahedral P_4 ligand environment as in the original molecular Ni catalyst, a $[Ni(P_2^{Ph}N_2^{CH_2Pyrene})_2]^{2+}$ complex (= "NiP_4"), and the other an octahedral coordination to six light ligands (O or N) similar in structure to $[Ni(OH_2)_6]^{2+}$ (= "NiO_6"). The proportion between the NiP_4 and NiO_6 species in the Ni-CNT material is about 2 : 1 (see detailed analysis in chapter *Molecular Ni catalyst grafted on a carbon-nanotube cathode*). After 1 h of H_2 oxidation under fuel-cell conditions (in half-cell measurements), the Ni-CNT material exhibits a significant diminishment in the amount of NiO_6 species while the structure of the NiP_4 species remains unmodified. The catalytic activity of the Ni-CNT material, however, does not decrease, as shown by our co-workers (Tran, Morozan et al. 2015), confirming that the NiP_4 species is the catalytic species.

For the Co-N-C material, our XAS analysis indicates a mixture of a non-metallic $Co^{II, III}$ species with a metallic Co^0 contribution (see **Figure 62** and **Figure 63**). The non-metallic Co species consists of Co ions coordinated to O or N atoms (distance 2.08 Å) in their first coordination sphere similar to $[Co(OH_2)_6]^{2+}$. After 1 h of O_2 reduction in a fuel-cell, the previously major metallic contribution is significantly diminished. The new molar ratio between the non-metallic and metallic Co contributions is about 2 : 1. The diminishment of the metallic Co contribution, however, does not lead to a decrease in catalytic activity as shown by our co-workers (Tran, Morozan et al. 2015). The oxidative transformation of the Co-N-C material during catalysis, from metallic Co^0 to $Co^{II, III}$ ions with O/N coordination, is similar to the behaviour of the cobalt-polypyrrole composite material (Bashyam and Zelenay 2006) (see **Figure 64**), an O_2-reduction catalyst for polymer electrolyte fuel cells. Possible alterations in the structure of the non-metallic Co-N-C material during catalysis could not be determined, since the state of the non-metallic material before O_2 reduction was obscured in XAS by a significant Co-metal contribution.

CATALYTIC Cu ELECTRODE FOR CO_2 REDUCTION

The Cu material is a novel catalyst for CO_2 reduction and is prepared by simple electro-deposition from a dimethylformamide (DMF) solution of the precursor, $[Cu(cyclam)](ClO_4)_2$ (cyclam = 1,4,8,11-tetraazacyclotetradecane) (Huan, Andreiadis et al. 2015). Our X-ray absorption spectroscopy (XAS) investigations provide insight into the atomic structure of the Cu-based material. The XAS analysis suggests that about one quarter of the Cu material consist of metallic Cu^0 and three quarter of a prominent non-metallic $Cu^{I, II}$ contribution (see **Figure 72**). In the latter, the Cu^I ions are most likely coordinated to two light atoms (O or N) in the first coordination sphere and, at longer distances, to

other Cu ions. The atomic structure of the Cu^{I}-species is similar to Cu^{I} oxide (see extended X-ray absorption fine-structure (EXAFS) in **Figure 68B**) but does not exhibit a comparable long-range order. The Cu^{II} ions of the non-metallic contribution are possibly coordinated to four light ligands (O, N or C) as in Cu malachite, Cu oxalate or Cu^{II} oxide (see X-ray absorption near-edge structure (XANES) in **Figure 66B**). The Cu^{II} species is less abundant in the Cu material than the Cu^{I} species. The Cu material exhibits a higher selectivity for CO_2-derived products than pure Cu-metal or Cu^{I}-oxide electrodes, as shown by co-workers in (Huan, Andreiadis et al. 2015). The inner structure (Cu-O/N coordination) of the pre-cursor, Cu cyclam, is modified during electro-deposition of the Cu material.

V. ABSTRACT

The amorphous MoS_x electrodes (x = 2 or 3) of *Merki et al.* are electro-deposited catalysts for the hydrogen-evolution reaction (HER) (Merki, Vrubel et al. 2012). The HER activity of the electrodes can be promoted by the doping with Co or Ni. Our X-ray absorption spectroscopy (XAS) investigations indicate that the MoS_x bulk of the *Merki* electrodes consists of directly interconnected Mo^{IV} ions coordinated to presumably five S atoms in the first coordination sphere. In the Co/Ni doped electrodes, the Co sites consist of $Co^{II,III}$ ions coordinated to six S atoms in the first coordination sphere while the Ni sites consist of $Ni^{I,II}$ ions coordinated to four S atoms. The dopant sites are incorporated into the MoS_x bulk via direct coordination to Mo atoms. The MoS_x bulk presumably participates in HER catalysis, suggested by the abundance of coordinatively unsaturated S and Mo sites (= potential adsorption sites for atomic hydrogen) throughout the bulk and the bulk-scale occurrence of redox equivalents during catalysis. The S sites appear to be more crucial for the redox chemistry than the Mo sites, since the latter exhibits only a minor change in mean oxidation state during HER. The promotion of the intrinsic HER activity by doping with Co or Ni presumably arises from the additional presence of unsaturated dopant and/or S sites and from the superior reactivity of the dopant sites in comparison to the Mo sites. The dopant ions (Ni or Co) have an influence on the number of reducing equivalents during HER, and shift the midpoint potential of the corresponding redox transition to less negative values. The HER mechanism of the *Merki* electrodes could be analogous to the one in hydrogenases where molecular hydrogen is formed by the interplay between a hydride-binding metal site (Mo, Co and/or Ni) and a proton-binding pendant base (S site) in close proximity. Under conditions for water-oxidation, only the Co doped *Merki* electrode exhibits catalytic activity, enabled by the formation of the *CoCat,* a well-known Co-oxide catalyst for water oxidation.

The *H_2-CoCat* of *Cobo et al.* is a Co-based catalyst for HER and OER (oxygen-evolution reaction) electro-deposited under reductive conditions (Cobo, Heidkamp et al. 2012). Our XAS investigations show that, in the state of HER, the *H_2-CoCat* consists of bulk metallic Co^0 and a catalytic non-metallic Co species on the surface that is presumably a Co^{II} phosphate mixed with a Co oxo/hydroxo species. In the state of OER, the *H_2-CoCat* (partly) transforms into the *O_2-CoCat* (= *CoCat*), a well-known Co-oxide catalyst for water oxidation.

The noble metal-free fuel cell of *Tran et al.* utilizes a novel cobalt/nitrogen/Vulcan (Co-N-C) material as catalyst for O_2 reduction, and a carbon-nanotube material functionalized with biomimetic Ni complexes (Ni-CNT) as catalyst for H_2 oxidation (Tran, Le Goff et al. 2011). Our XAS analysis shows that the Ni-CNT material consists of two Ni^{II} species. One possesses a planar-tetrahedral P_4 ligand environment as in the original molecular Ni catalyst, a $[Ni(P_2^{Ph}N_2^{CH_2Pyrene})_2]^{2+}$ complex (= "NiP_4"), and the other an octahedral coordination to six light ligands (O or N) similar in structure to $[Ni(OH_2)_6]^{2+}$ (= "NiO_6"). After fuel cell operation, the amount of NiO_6 species in the Ni-CNT material is diminished while the catalytic activity remains unmodified. For the Co-N-C material, our XAS analysis indicates a mixture of a non-metallic $Co^{II,III}$ species with a metallic Co^0 contribution. The non-metallic species consists of Co ions coordinated to O or N atoms in their first coordination sphere similar to $[Co(OH_2)_6]^{2+}$. After fuel cell operation, the previously major metallic contribution is significantly diminished.

The Cu material of *Huan et al.* is a novel catalyst for CO_2 reduction and is prepared by simple electro-deposition (Huan, Andreiadis et al. 2015). Our XAS investigation indicates that the Cu material consist of metallic Cu^0 and a prominent non-metallic $Cu^{I,II}$ contribution. The atomic structure of the Cu^I species is similar to Cu^I oxide but does not exhibit a comparable long-range order. The less abundant Cu^{II} ions of the non-metallic contribution are possibly coordinated to four light ligands (O, N or C) as in Cu malachite, Cu oxalate or Cu^{II} oxide.

VI. ZUSAMMENFASSUNG

Die amorphen MoS_x-Elektroden (x = 2 or 3) von *Merki et al.* sind elektrodeponierte Katalysatoren für die Wasserstoffentwicklung (HER) (Merki, Vrubel et al. 2012). Die katalytische Aktivität der Elektroden kann durch das Dotieren mit Co oder Ni verbessert werden. Unsere Röntgenabsorptionsspektroskopie-Untersuchungen (XAS) ergeben, dass der MoS_x-Film der *Merki*-Elektroden aus direkt miteinander verbundenen Mo^{IV}-Ionen besteht, die in der ersten Koordinationsschale vermutlich fünf S-Liganden besitzen. In den Co/Ni-dotierten Elektroden bestehen die Dotierungsstellen entsprechend aus $Co^{II,III}$-Ionen mit sechs S-Liganden in der ersten Koordinationsschale oder aus $Ni^{I,II}$-Ionen mit vier S-Liganden. Die Dotierungsstellen sind durch eine direkte Koordination mit Mo-Atomen in den MoS_x-Film integriert. Die HER-Katalyse involviert vermutlich einen Großteil des MoS_x-Filmvolumens, da während der Katalyse eine dem Filmvolumen entsprechende Anzahl an Redox-Äquivalenten beobachtet werden kann und das Filmvolumen mit koordinativ ungesättigten S- und Mo-Atomen durchzogen ist (potenzielle Adsorptionsstellen für atomaren Wasserstoff). Die S-Atome scheinen eine stärkere Bedeutung für die Redox-Chemie zu haben als die Mo-Atome, da Letztere nur eine geringe Änderung des Oxidationszustandes während der HER-Katalyse zeigen. Die Erhöhung der intrinsischen HER-Aktivität durch das Dotieren der *Merki*-Elektroden mit Co oder Ni wird vermutlich durch das zusätzliche Vorhandensein von ungesättigten Co-, Ni- und/oder S-Atomen verursacht sowie der höheren Reaktivität der Dotierungsstellen im Vergleich zu den Mo-Atomen. Des Weiteren beeinflussen die Dotierungsatome (Co oder Ni) die Zahl an Reduktionsäquivalenten, die während der HER-Katalyse auftreten, und verschieben das Elektrodenpotential für die entsprechenden Redox-Übergänge zu weniger negativen Werten. Der katalytische Mechanismus der *Merki*-Elektroden für HER könnte analog zu dem HER-Mechanismus in Hydrogenasen sein. Dort wird molekularer Wasserstoff durch das Zusammenspiel von hydrid-bindenden Metall-Atomen (Mo, Co und/oder Ni) und proton-bindenden Basen (S-Ligand), die sich in der Nähe der Metall-Atome befinden, gebildet. Unter Bedingungen für Wasseroxidation zeigen nur die Co-dotierten *Merki*-Elektroden katalytische Aktivität. Diese wird durch die Bildung eines bekannten Kobaltoxid-Katalysators (= *CoCat*) in den Elektroden ermöglicht.

Der *H_2-CoCat* von *Cobo et al.* ist ein auf Kobalt basierender Katalysator für HER (Wasserstoffentwicklung) und OER (Sauerstoffentwicklung), welcher durch Elektrodeponierung unter reduktiven Bedingungen hergestellt wird (Cobo, Heidkamp et al. 2012). Unsere XAS-Untersuchungen zeigen, dass im HER-Zustand der *H_2-CoCat* aus einem metallischen Co^0-Film mit einem bedeutenden nicht-metallischen Co-Beitrag besteht. Letzterer ist vermutlich ein Kobalt(II)-Phosphat mit Kobalt-Oxo/Hydroxo-Beiträgen in den Oberflächenschichten des Films. Im OER-Zustand wandelt sich der *H_2-CoCat* teilweise in den *O_2-CoCat* (= *CoCat*) um, einem bekannten Kobaltoxid-Katalysator für Wasseroxidation.

Die edelmetall-freie Brennstoffzelle von *Tran et al.* verwendet als Katalysator für die Sauerstoffreduktion ein neuartiges Kobalt/Stickstoff/Vulcan-Material (Co-N-C) und für die Wasserstoffoxidation ein katalytisches Kohlenstoffnanoröhrchen-Material, welches mit einem biomimetischen Ni-Komplex (Ni-CNT) funktionalisiert ist (Tran, Le Goff et al. 2011). Unsere XAS-Analyse ergibt, dass das Ni-CNT-Material aus zwei Ni^{II}-Spezies besteht. Eine der Ni^{II}-Spezies besitzt eine planar-tetrahedrale P_4-Ligandenumgebung wie in dem biomimetischen Ni-Komplex, $[Ni(P_2^{Ph}N_2^{CH_2Pyrene})_2]^{2+}$ (= "NiP_4"), und die andere Spezies zeigt eine oktahedrale Koordinierung zu sechs leichten Liganden (O oder N) ähnlich wie in $[Ni(OH_2)_6]^{2+}$ (= "NiO_6"). Nach einer Operation der Brennstoffzelle zeigt das Ni-CNT-Material einen verringerten Anteil der NiO_6-Spezies wodurch die katalytische Aktivität des Materials aber nicht beeinflusst wird. Unsere XAS-Analyse des Co-N-C-Materials ergibt, dass das Material aus einer nicht-metallischen $Co^{II,III}$-Spezies besteht, die mit einem metallischen Co^0-Beitrag gemischt ist. Die nicht-metallische Spezies besteht aus Co-Ionen mit einer Koordination zu O- oder N-Atomen in der ersten Koordinationssphäre ähnlich wie in $[Co(OH_2)_6]^{2+}$. Nach einer Operation der Brennstoffzelle verringert sich im Co-N-C-Material der zuvor dominierende Metallbeitrag deutlich.

Das Cu-Material von *Huan et al.* ist ein neuartiger Katalysator für die CO_2-Reduktion und wird durch einfache Elektrodeponierung hergestellt. Unsere XAS-Untersuchungen zeigen, dass das Cu-Material aus einem metallischen Cu^0- und einem bedeutendem nicht-metallischen $Cu^{I,II}$-Beitrag besteht. Die atomare Struktur der Cu^I-Spezies ist ähnlich zu Kupfer(I)-Oxid, zeigt aber keine vergleichbare Fernordnung der Struktur. Die weniger vorkommenden Cu^{II}-Ionen im nicht-metallischen Beitrag sind möglicherweise zu vier leichten Liganden (O, N oder C) koordiniert wie in Kupfermalachit, Kupferoxalat oder Kupfer(II)-Oxid.

VII. REFERENCES

Afanasiev, P. and Bezverkhy, I. (2002). "Synthesis of MoS_x (5 > x > 6) amorphous sulfides and their use for preparation of MoS_2 monodispersed microspheres." Chemistry of Materials **14**(6): 2826-2830.

Afanasiev, P., Jobic, H., Lorentz, C., Leverd, P., Mastubayashi, N., Piccolo, L. and Vrinat, M. (2009). "Low-Temperature Hydrogen Interaction with Amorphous Molybdenum Sulfides MoS_x." Journal of Physical Chemistry C **113**(10): 4139-4146.

Agarwal, A. S., Zhai, Y. M., Hill, D. and Sridhar, N. (2011). "The Electrochemical Reduction of Carbon Dioxide to Formate/Formic Acid: Engineering and Economic Feasibility." ChemSusChem **4**(9): 1301-1310.

Akashi, H., Shibahara, T. and Kuroya, H. (1990). "Isolation and x-ray structure determination of a sulfur-bridged incomplete cubane-type molybdenum(IV) aqua cluster, $[Mo_3S_4(H_2O)_9](CH_3*C_6H_4*SO_3)_4*9H_2O$." Polyhedron **9**(14): 1671-1676.

Alsen, N. (1925). "Röntgenographische Untersuchungen der Kristallstrukturen von Magnetkies, Breithauptit, Pentlandit, Millerit und verwandten Verbindungen." Geologiska Foereningens i Stockholm Foerhandlingar **47**: 19 - 73.

Angamuthu, R., Byers, P., Lutz, M., Spek, A. L. and Bouwman, E. (2010). "Electrocatalytic CO_2 Conversion to Oxalate by a Copper Complex." Science **327**(5963): 313-315.

Ankudinov, A. L., Ravel, B., Rehr, J. J. and Conradson, S. D. (1998). "Real-space multiple-scattering calculation and interpretation of X-ray-absorption near-edge structure." Physical Review B: Condensed Matter **58**(12): 7565-7576.

Appel, A. M., Bercaw, J. E., Bocarsly, A. B., Dobbek, H., DuBois, D. L., Dupuis, M., Ferry, J. G., Fujita, E., Hille, R., Kenis, P. J. A., Kerfeld, C. A., Morris, R. H., Peden, C. H. F., Portis, A. R., Ragsdale, S. W., Rauchfuss, T. B., Reek, J. N. H., Seefeldt, L. C., Thauer, R. K. and Waldrop, G. L. (2013). "Frontiers, Opportunities, and Challenges in Biochemical and Chemical Catalysis of CO_2 Fixation." Chemical Reviews **113**(8): 6621-6658.

Armaroli, N. and Balzani, V. (2011). "The hydrogen issue." Chemsuschem **4**(1): 21-36.

Artero, V., Chavarot-Kerlidou, M. and Fontecave, M. (2011). "Splitting water with cobalt." Angewandte Chemie International Edition **50**(32): 7238-7266.

Asadi, M., Kumar, B., Behranginia, A., Rosen, B. A., Baskin, A., Repnin, N., Pisasale, D., Phillips, P., Zhu, W., Haasch, R., Klie, R. F., Kral, P., Abiade, J. and Salehi-Khojin, A. (2014). "Robust carbon dioxide reduction on molybdenum disulphide edges." Nature Communications **5**.

Baffert, C., Artero, V. and Fontecave, M. (2007). "Cobaloximes as functional models for hydrogenases. 2. proton electroreduction catalyzed by difluoroborylbis(dimethylglyoximato)cobalt(II) complexes in organic media." Inorganic Chemistry **46**(5): 1817-1824.

Bard, A. J. and Faulkner, L. R. (1980). Electrochemical methods. Fundamentals and application, Wiley.

Baschuk, J. J. and Li, X. G. (2001). "Carbon monoxide poisoning of proton exchange membrane fuel cells." International Journal of Energy Research **25**(8): 695-713.

Bashyam, R. and Zelenay, P. (2006). "A class of non-precious metal composite catalysts for fuel cells." Nature **443**(7107): 63-66.

Bearden, J. A. and Burr, A. F. (1967). "Reevaluation of X-ray atomic energy levels." Reviews of Modern Physics **39**(1): 125-142.

Belanger, D., Laperriere, G. and Marsan, B. (1993). "The electrodeposition of amorphous molybdenum sulfide." Journal of Electroanalytical Chemistry **347**(1-2): 165-183.

Belougne, P., Chezeau, N. and Lapasset, J. (1976). "Nouvel affinement de la structure cristalline du thiomolybdate d'ammonium." Acta Crystallographica B **32**: 3087-3088.

Betke, U. and Wickleder, M. S. (2011). "Sulfates of the Refractory Metals: Crystal Structure and Thermal Behavior of $Nb_2O_2(SO_4)_3$, $MoO_2(SO_4)$, $WO(SO_4)_2$, and Two Modifications of $Re_2O_5(SO_4)_2$." Inorganic chemistry **50**: 858-872.

Bollinger, M. V., Jacobsen, K. W. and Norskov, J. K. (2003). "Atomic and electronic structure of MoS_2 nanoparticles." Physical Review B **67**.

Bonde, J., Moses, P. G., Jaramillo, T. F., Norskov, J. K. and Chorkendorff, I. (2008). "Hydrogen evolution on nano-particulate transition metal sulfides." Faraday discussions **140**: 219-231.

Bouwens, S. M. A. M., Koningsberger, D. C., De Beer, V. H. J., Louwers, S. P. A. and Prins, R. (1990). "EXAFS Study of the Local Structure of Ni in Ni-MoS_2/C Hydrodesulfurization Catalysts." Catalysis Letters **5**: 273-284.

Bouwens, S. M. A. M., van Veen, J. A. R., Koningsberger, D. C., de Beer, V. H. J. and Prins, R. (1991). "Extended X-ray Absorption Fine Structure Determination of the Structure of Cobalt in Carbon-Supported Co and Co-Mo Sulfide Hydrodesulfurization Catalysts." Journal of Physical Chemistry **95**(1): 123-134.

Brown, P. J. (1973). "The Crystal Structures of Solids." 129.

Bunker, G. (2010). Introduction to XAFS: A Practical Guide to X-ray Absorption Fine Structure Spectroscopy, Cambridge University Press.

Calvin, S. (2013). XAFS for Everyone, CRC Press.

Canaguier, S., Artero, V. and Fontecave, M. (2007). "Modelling NiFe hydrogenases: nickel-based electrocatalysis for hydrogen production." Dalton Transactions(3): 315-325.

Casalongue, H. G. S., Benck, J. D., Tsai, C., Karlsson, R. K. B., Kaya, S., Ng, M. L., Pettersson, L. G. M., Abild-Pedersen, F., Norskov, J. K., Ogasawara, H., Jaramillo, J. F. and Nilsson, A. (2014). "Operando Characterization of an Amorphous Molybdenum Sulfide Nanoparticle Catalyst during the Hydrogen Evolution Reaction." Journal of Physical Chemistry **118**: 29252-29259.

Centi, G., Quadrelli, E. A. and Perathoner, S. (2013). "Catalysis for CO_2 conversion: a key technology for rapid introduction of renewable energy in the value chain of chemical industries." Energy & Environmental Science **6**(6): 1711-1731.

Chen, Z. B., Cummins, D., Reinecke, B. N., Clark, E., Sunkara, M. K. and Jaramillo, J. F. (2011). "Core-shell MoO_3-MoS_2 Nanowires for Hydrogen Evolution: A Functional Design for Electrocatalytic Materials." Nano Letters **11**(10): 4168-4175.

Chien, F. Z., Moss, S. C., Liang, K. S. and Chianelli, R. R. (1984). "Local and intermediate-range structure of amorphous MoS_3 - model calculation study." Physical Review B **29**(8): 4606-4615.

Choi, J.-H., Ryoo, K. S. and Park, K.-M. (2007). "(5,16-Dimethyl-2,6,13,17-tetraazatricyclo[14.4.0(1,18).0(7,12)]docosane-kappa N-4)bis(perchlorato-kappa O)copper(II)." Acta Crystallographica, Section E **63**: M2674-U2436.

Chou, N. H., Ross, P. N., Bell, A. T. and Tilley, T. D. (2011). "Comparison of Cobalt-based Nanoparticles as Electrocatalysts for Water Oxidation." ChemSusChem **4**(11): 1566-1569.

Cobo, S., Heidkamp, J., Jacques, P.-A., Fize, J., Fourmond, V., Guetaz, L., Jousselme, B., Ivanova, V., Dau, H., Palacin, S., Fontecave, M. and Artero, V. (2012). "A Janus cobalt-based catalytic material for electro-splitting of water." Nature Materials **11**(9): 802-807.

Cook, T. R., Dogutan, D. K., Reece, S. Y., Surendranath, Y., Teets, T. S. and Nocera, D. G. (2010). "Solar energy supply and storage for the legacy and nonlegacy worlds." Chemical Reviews **110**(11): 6474-6502.

Costentin, C., Robert, M. and Saveant, J. M. (2013). "Catalysis of the electrochemical reduction of carbon dioxide." Chemical Society Reviews **42**(6): 2423-2436.

Craje, M. W. J., Louwers, S. P. A., de Beer, V. H. J., Prins, R. and van der Kraan, A. M. (1992). "An EXAFS Study on the So-Called "Co-Mo-S" Phase in Co/C and CoMo/C, Compared with a Mössbauer Emission Spectroscopy Study." Journal of Physical Chemistry **96**: 5445-5452.

Cramer, S. P., Liang, K. S., Jacobson, A. J., Chang, C. H. and Chianelli, R. R. (1984). "EXAFS studies of amorphous molybdenum and tungsten trisulfides and triselenides." Inorganic Chemistry **23**(9): 1215-1221.

Dau, H., Liebisch, P. and Haumann, M. (2003). "X-ray absorption spectroscopy to analyze nuclear geometry and electronic structure of biological metal centers—potential and questions examined with special focus on the tetra-nuclear manganese complex of oxygenic photosynthesis." Analytical and Bioanalytical Chemistry **376**(5): 562-583.

Dau, H., Limberg, C., Reier, T., Risch, M., Roggan, S. and Strasser, P. (2010). "The mechanism of water oxidation: from electrolysis via homogeneous to biological catalysis." ChemCatChem **2**(7): 724-761.

de Bont, P. W., Vissenberg, M. J., San de Beer, V. H. J., van Veen, J. A. R., van Santen, R. A. and van der Kraan, A. M. (1998). "An X-ray Absorption Fine Structure Study of the Sulfidation Behavior of CoNaY Prepared by Ion Exchange: The Influence of Physisorbed Water and Cobalt Loading." The Journal of Physical Chemistry B **102**(30): 5876-5885.

Dempsey, J. L., Winkler, J. R. and Gray, H. B. (2010). "Mechanism of H_2 Evolution from a Photogenerated Hydridocobaloxime." Journal of the American Chemical Society **132**(47): 16774-16776.

Dickinson, R. G. and Pauling, L. (1923). "The Crystal Structure of Molybdenite." Journal of the American Chemical Society **45**: 1466-1471.

DiMeglio, J. L. and Rosenthal, J. (2013). "Selective Conversion of CO_2 to CO with High Efficiency Using an Inexpensive Bismuth-Based Electrocatalyst." Journal of the American Chemical Society **135**(24): 8798-8801.

Dincă, M., Surendranath, Y. and Nocera, D. G. (2010). "Nickel-borate oxygen-evolving catalyst that functions under benign conditions." Proceedings of the National Academy of Sciences, USA **107**(23): 10337-10341.

Dugulan, A. I., van Veen, J. A. R. and Hensen, E. J. M. (2013). "On the structure and hydrotreating performance of carbon-supported CoMo- and NiMo-sulfides." Applied catalysis B: Environmental **142**: 178-186.

Eadie, W. T., Drijard, D., James, F. E., Roos, M. and Sadoulet, B. (1971). Statistical methods in experimental physics. Amsterdam, North Holland.

Eda, K., Kato, Y., Ohahiro, Y., Sugitani, T. and Whittingham, M. S. (2010). "Synthesis, crystal structure, and structural conversion of Ni molybdate hydrate $NiMoO_4 * nH_2O$." Journal of Solid State Chemistry **183**: 1334-1339.

Eda, K., Uno, Y., Nagai, N., Sotani, N. and Whittingham, M. S. (2005). "Crystal structure of cobalt molybdate hydrate $CoMoO_4 * nH_2O$." Journal of Solid State Chemistry **178**(9): 2791-2797.

Eijsbouts, S. (1997). "On the flexibility of the active phase in hydrotreating catalysts." Applied Catalysis A: General **158**: 53-92.

Fleet, M. E. (1977). "The crystal structure of heazlewoodite, and metallic bonds in sulfide minerals." American Mineralogist **62**: 341-345.

Fleet, M. E. (1987). "Structure of Godlevskite, Ni_9S_8." Acta Crystallographica **C43**: 2255-2257.

Fourmond, V., Jacques, P. A., Fontecave, M. and Artero, V. (2010). "H_2 Evolution and Molecular Electrocatalysts: Determination of Overpotentials and Effect of Homoconjugation." Inorganic Chemistry **49**(22): 10338-10347.

Furuseth, S., Kjekshus, A. and Andresen, A. F. (1969). "On the magnetic properties of $CoSe_2$, NiS_2, and $NiSe_2$." Acta Chemica Scandinavica **23**: 2325-2334.

Gajapathy, D., Govindarajan, S., Patil, K. C. and Manohar, H. (1983). "Synthesis, Characterisation and Thermal Properties of Hydrazinium Metal Oxalate Hydrates. Crystal and Molecular Structure of Hydrazinium Copper Oxalate Monohydrate." Polyhedron **2**: 865-873.

Gong, K. P., Du, F., Xia, Z. H., Durstock, M. and Dai, L. M. (2009). "Nitrogen-Doped Carbon Nanotube Arrays with High Electrocatalytic Activity for Oxygen Reduction." Science **323**(5915): 760-764.

Gordon, R. B., Bertram, M. and Graedel, T. E. (2006). "Metal stocks and sustainability." Proceedings of the National Academy of Science of the United States of America **103**(5): 1209-1214.

Gratzel, M. (2001). "Photoelectrochemical cells." Nature **414**(6861): 338-344.

Grice, J. D. and Ferguson, R. B. (1974). "Crystal structure refinement of millerite (B-NiS)." The Canadian Mineralogist **12**: 248-252.

Hassel, O. (1925). "Ueber die Kristallstruktur des Molybdaenglanzes." Zeitschrift fuer Kristallographie, Kristallgeometrie, Kristallphysik, Kristallchemie **61**: 92-99.

Haumann, M., Porthun, A., Buhrke, T., Liebisch, P., Meyer-Klaucke, W., Friedrich, B. and Dau, H. (2003). "Hydrogen-induced structural changes at the nickel site of the regulatory NiFe hydrogenase from Ralstonia eutropha detected by X-ray absorption spectroscopy (vol 42, pg 11004, 2003)." Biochemistry **42**(46): 13786-13786.

Hibble, S. J., Rice, D. A., Pickup, D. M. and Beer, M. P. (1995). "Mo K-edge EXAFS and S K-edge absorption studies of the amorphous molybdenum sulfides $MoS_{4.7}$, MoS_3, and MoS_3*nH_2O (n ~ 2)." Inorganic Chemistry **34**(21): 5109-5113.

Hill, B., Lerner, H.-W. and Bolte, M. (2010). "Redetermination of diammonium thiomolybdate." Acta Crystallographica Section E **66**(2).

Hinnemann, B., Moses, P. G., Bonde, J., Jorgenson, K. P., Nielsen, J. H., Horch, S., Chorkendorff, I. and Norskov, J. K. (2005). "Biomimetic hydrogen evolution: MoS_2 nanoparticles as catalyst for hydrogen evolution." Journal of the American Chemical Society **127**(15): 5308-5309.

Hu, X. L., Brunschwig, B. S. and Peters, J. C. (2007). "Electrocatalytic hydrogen evolution at low overpotentials by cobalt macrocyclic glyoxime and tetraimine complexes." Journal of the American Chemical Society **129**(29): 8988-8998.

Hu, X. L., Cossairt, B. M., Brunschwig, B. S., Lewis, N. S. and Peters, J. C. (2005). "Electrocatalytic hydrogen evolution by cobalt difluoroboryl-diglyoximate complexes." Chemical Communications(37): 4723-4725.

Huan, T. N., Andreiadis, E. S., Heidkamp, J., Simon, P., Derat, E., Cobo, S., Royal, G., Bergmann, A., Strasser, P., Dau, H., Artero, V. and Fontecave, M. (2015). "From molecular copper complexes to composite electrocatalytic materials for selective reduction of CO2 to formic acid." Journal of Materials Chemistry A **3**(7): 3901-3907.

IXAS (2000). Error reporting recommendations: A report of the standards and criteria committee, http://www.ixasportal.net/ixas/.

Jacques, P. A., Artero, V., Pecaut, J. and Fontecave, M. (2009). "Cobalt and nickel diimine-dioxime complexes as molecular electrocatalysts for hydrogen evolution with low overvoltages." Proceedings of the National Academy of Sciences of the United States of America **106**(49): 20627-20632.

Jaegermann, W. and Tributsch, H. (1988). "Interfacial properties of semiconducting transition-metal chalcogenides." Progress in Surface Science **29**(1-2): 1-167.

Jaramillo, T. F., Jorgensen, K. P., Bonde, J., Nielsen, J. H., Horch, S. and Chorkendorff, I. (2007). "Identification of active edge sites for electrochemical H_2 evolution from MoS_2 nanocatalysts." Science **317**(5834): 100-102.

Jiao, F. and Frei, H. (2010). "Nanostructured cobalt and manganese oxide clusters as efficient water oxidation catalysts." Energy & Environmental Science **3**(8): 1018-1027.

Kadono, T., Kubota, T., Hiromitsu, I. and Okamoto, Y. (2006). "Characterization of highly dispersed cobalt sulfide catalysts by X-ray absorption fine structure and magnetic properties." Applied Catalysis A: General **312**: 125-133.

Kanan, M. W. and Nocera, D. G. (2008). "In situ formation of an oxygen-evolving catalyst in neutral water containing phosphate and Co^{2+}." Science **321**(5892): 1072-1075.

Kanan, M. W., Surendranath, Y. and Nocera, D. G. (2009). "Cobalt-phosphate oxygen-evolving compound." Chemical Society Reviews **38**(1): 109-114.

Kibsgaard, J., Tuxen, A., Knudsen, K. G., Brorson, M., Topsoe, H., Laegsgaard, E., Lauritsen, J. V. and Besenbacher, F. (2010). "Comparative atomic-scale analysis of promotional effects by late 3d-transition metals in MoS_2 hydrotreating catalysts." Journal of Catalysis **272**(2): 195-203.

Kirfel, A. and Eichhorn, K. (1990). "Accurate structure analysis with synchrotron radiation. The electron density in Al_2O_3 and Cu_2O." Acta Crystallographica **A46**: 271-284.

Kissinger, P. T. and Heineman, W. R. (1983). "Cyclic Voltammetry." Journal of Chemical Education **60**(9): 702-706.

Kondratenko, E. V., Mul, G., Baltrusaitis, J., Larrazabal, G. O. and Perez-Ramirez, J. (2013). "Status and perspectives of CO_2 conversion into fuels and chemicals by catalytic, photocatalytic and electrocatalytic processes." Energy & Environmental Science **6**(11): 3112-3135.

Lassalle-Kaiser, B., Merki, D., Vrubel, H., Sheraz, G., Yachandra, V. K., Hu, X. and Yano, J. (2015). "Evidence from *in Situ* X-ray Absorption Spectroscopy for the Involvement of Terminal Disulfide in the Reduction of Protons by an Amorphous Molybdenum Sulfide Electrocatalyst." Journal of the American Chemical Society **137**: 314-321.

Lauritsen, J. V., Kibsgaard, J., Olesen, G. H., Moses, P. G., Hinnemann, B., Helveg, S., Norskov, J. K., Clausen, B. S., Topsoe, H., Laegsgaard, E. and Besenbacher, F. (2007). "Location and coordination of promoter atoms in Co- and Ni-promoted MoS_2-based hydrotreating catalysts." Journal of Catalysis **249**(2): 220-233.

Le Goff, A., Artero, V., Jousselme, B., Tran, P. D., Guillet, N., Metaye, R., Fihri, A., Palacin, S. and Fontecave, M. (2009). "From hydrogenases to noble metal-free catalytic nanomaterials for H2 production and uptake." Science **326**(5958): 1384-1387.

Lefevre, M., Proietti, E., Jaouen, F. and Dodelet, J. P. (2009). "Iron-Based Catalysts with Improved Oxygen Reduction Activity in Polymer Electrolyte Fuel Cells." Science **324**(5923): 71-74.

Lewis, N. S. and Nocera, D. G. (2006). "Powering the planet: chemical challenges in solar energy utilization." Proceedings of the National Academy of Sciences of the United States of America **103**(43): 15729-15735.

Li, Y. G., Wang, H. L., Xie, L. M., Liang, Y. Y., Hong, G. S. and Dai, H. J. (2011). "MoS_2 Nanoparticles Grown on Graphene: An Advanced Catalyst for the Hydrogen Evolution Reaction." Journal of the American Chemical Society **133**(19): 7292-7299.

Lindqvist, M. (1936). "The crystal structure of Co_9S_8 and of pentlandite $(NiFe)_9S_8$." Svensk Kemisk Tidskrift **48**: 156-160.

Liu, R. L., Wu, D. Q., Feng, X. L. and Müllen, K. (2010). "Nitrogen-Doped Ordered Mesoporous Graphitic Arrays with High Electrocatalytic Activity for Oxygen Reduction." Angewandte Chemie - International Edition **49**(14): 2565-2569.

Lubitz, W., Ogata, H., Rüdiger, O. and Reijerse, E. (2014). "Hydrogenases." Chemical Reviews **114**: 4081-4148.

Lundqvist, D. (1938). "Röntgenuntersuchung des Systems Co-S." Zeitschrift für Anorganische und Allgemeine Chemie **239**: 85-88.

Lundqvist, D. (1974). "X-ray studies on the binary system Ni-S." Arkiv for Mineralogi och Geologi **24**: 1-12.

Matsubara, Y., Fujita, E., Doherty, M. D., Muckerman, J. T. and Creutz, C. (2012). "Thermodynamic and Kinetic Hydricity of Ruthenium(II) Hydride Complexes." Journal of The American Chemical Society **134**(38): 15743-15757.

McKone, J. R., Warren, E. L., Bierman, M. J., Boettcher, S. W., Brunschwig, B. S., Lewis, N. S. and Gray, H. B. (2011). "Evaluation of Pt, Ni, and Ni-Mo electrocatalysts for hydrogen evolution on crystalline Si electrodes." Energy & Environmental Science **4**(9): 3573-3583.

Medici, L. and Prins, R. (1996). "The Influence of Chelating Ligands on the Sulfidation of Ni and Mo in $NiMo/SiO_2$ Hydrotreating Catalysts." Journal of Catalysis **163**: 38-49.

Medina-Ramos, J., DiMeglio, J. L. and Rosenthal, J. (2014). "Efficient Reduction of CO_2 to CO with High Current Density Using in Situ or ex Situ Prepared Bi-Based Materials." Journal of the Amercian Chemical Society **136**(23): 8361-8367.

Merki, D., Fierro, S., Vrubel, H. and Hu, X. (2011). "Amorphous molybdenum sulfide films as catalysts for electrochemical hydrogen production in water." Chemical Science **2**(7): 1262-1267.

Merki, D. and Hu, X. L. (2011). "Recent developments of molybdenum and tungsten sulfides as hydrogen evolution catalysts." Energy & Environmental Science **4**(10): 3878-3888.

Merki, D., Vrubel, H., Rovelli, L., Fierro, S. and Hu, X. (2012). "Fe, Co, and Ni ions promote the catalytic activity of amorphous molybdenum sulfide films for hydrogen evolution." Chemical Science **3**(8): 2515-2525.

Miller, J. T., Marschall, C. L. and Kropf, A. J. (2001). "$(Co)MoS_2$/Alumina Hydrotreating Catalysts: An EXAFS Study of the Chemisorption and Partial Oxidation with O_2." Journal of Catalysis **202**(1): 89-99.

Mistry, H., Reske, R., Zeng, Z. H., Zhao, Z. J., Greeley, J., Strasser, P. and Cuenya, B. R. (2014). "Exceptional Size-Dependent Activity Enhancement in the Electroreduction of CO_2 over Au Nanoparticles." Journal of the American Chemical Society **136**(47): 16473-16476.

Morozan, A., Jegou, P., Jousselme, B. and Palacin, S. (2011). "Electrochemical performance of annealed cobalt-benzotriazole/CNTs catalysts towards the oxygen reduction reaction." Physical Chemistry Chemical Physics **13**(48): 21600-21607.

Morozan, A., Jousselme, B. and Palacin, S. (2011). "Low-platinum and platinum-free catalysts for the oxygen reduction reaction at fuel cell cathodes." Energy & Environmental Science **4**(4): 1238-1254.

Morris, A. J., Meyer, G. J. and Fujita, E. (2009). "Molecular Approaches to the Photocatalytic Reduction of Carbon Dioxide for Solar Fuels." Accounts of Chemical Research **42**(12): 1983-1994.

Nakata, K., Ozaki, T., Terashima, C., Fujishima, A. and Einaga, Y. (2014). "High-Yield Electrochemical Production of Formaldehyde from CO_2 and Seawater." Angewandte Chemie - International Edition **53**(3): 871-874.

Neuburger, M. C. (1930). "Präzisionsmessung der Gitterkonstante von Cuprooxyd Cu_2O." Zeitschrift für Physik **67**: 845-850.

Niemann, W., Clausen, B. S. and Topsoe, H. (1990). "X-ray Absorption Studies of the Ni Environment in Ni-Mo-S." Catalysis Letters **4**: 355-364.

Niggli, P. (1922). "Die Kristallstruktur einiger Oxyde I." Zeitschrift für Kristallographie, Kristallgeometrie, Kristallphysik, Kristallchemie **57**: 253-299.

Nowack, E., Schwarzenbach, D., Gonschorek, W. and Hahn, T. (1989). "Deformationsdichten in CoS_2 and NiS_2 mit Pyritstruktur." Zeitschrift für Kristallographie **186**: 213-215.

Nowack, E., Schwarzenbach, D. and Hahn, T. (1991). "Charge densities in CoS_2 and NiS_2 (pyrite structure)." Acta Crystallographica, Section B, Structural Science **47**: 650-659.

Oh, Y., Vrubel, H., Guidoux, S. and Hu, X. L. (2014). "Electrochemical reduction of CO_2 in organic solvents catalyzed by MoO_2." Chemical Communications **50**(29): 3878-3881.

Okamoto, Y., Kato, A., Usman, Rinaldi, N., Fujikawa, T., Koshika, H., Hiromitsu, I. and Kubota, T. (2009). "Effect of sulfidation temperature on the intrinsic activity of Co-MoS_2 and Co-WS_2 hydrodesulfurization catalysts." Journal of Catalysis **265**(2): 216-228.

Otte, H. M. (1961). "Lattice parameter determinations with an X-ray spectrogoniometer by the Debye-Scherrer method and the effect of specimen condition." Journal of Applied Physics **32**: 1536-1546.

Parise, J. B. (1980). "Structure of hazelwoodite (Ni_3S_2)." Acta Crystallographica - Section B **36**: 1179-1180.

Penner-Hahn, J. E. (1999). "X-ray absorption spectroscopy in coordination chemistry." Coordination Chemistry Reviews **190-192**: 1101-1123.

Ponomarev, E. A., Neumann-Spallart, M., Hodes, G. and Levy-Clement, C. (1996). "Electrochemical deposition of MoS_2 thin films by reduction of tetrathiomolybdate." Thin Solid Films **280**(1-2): 86-89.

Pylypenko, S., Mukherjee, S., Olson, T. S. and Atanassov, P. (2008). "Non-platinum oxygen reduction electrocatalysts based on pyrolyzed transition metal macrocycles." Electrochimica Acta **53**(27): 7875-7883.

Qiao, J. L., Liu, Y. Y., Hong, F. and Zhang, J. J. (2014). "A review of catalysts for the electroreduction of carbon dioxide to produce low-carbon fuels." Chemical Society Reviews **43**(2): 631-675.

Rajamani, V. and Prewitt, C. T. (1974). "The crystal structure of millerite." The Canadian Mineralogist **12**: 253-257.

Raybaud, P., Hafner, J., Kresse, G., Kasztelan, S. and Toulhoat, H. (2000). "Structure, energetics, and electronic properties of the surface of a promoted MoS_2 catalyst: An ab initio local density functional study." Journal of Catalysis **190**(1): 128-143.

Razavet, M., Artero, V. and Fontecave, M. (2005). "Proton electroreduction catalyzed by cobaloximes: Functional models for hydrogenases." Inorganic Chemistry **44**(13): 4786-4795.

Reece, S. Y., Hamel, J. A., Sung, K., Jarvi, T. D., Esswein, A. J., Pijpers, J. J. H. and Nocera, D. G. (2011). "Wireless solar water splitting using silicon-based semiconductors and earth-abundant catalysts." Science **334**: 645-648

Rehr, J. J. and Albers, R. C. (2000). "Theoretical approaches to X-ray absorption fine structure." Reviews of Modern Physics **72**(3): 621-654.

Rehr, J. J., Kas, J. J., Prange, M. P., Sorini, A. P., Takimoto, Y. and Vila, F. (2009). "Ab initio theory and calculations of X-ray spectra." Comptes Rendus Physique **10**(6): 548-559.

Reske, R., Duca, M., Oezaslan, M., Schouten, K. J. P., Koper, M. T. M. and Strasser, P. (2013). "Controlling Catalytic Selectivities during CO_2 Electroreduction on Thin Cu Metal Overlayers." Journal of Physical Chemistry Letters **4**(15): 2410-2413.

Reske, R., Mistry, H., Behafarid, F., Cuenya, B. R. and Strasser, P. (2014). "Particle Size Effects in the Catalytic Electroreduction of CO_2 on Cu Nanoparticles." Journal of the American Chemical Society **136**(19): 6978-6986.

Risch, M., Khare, V., Zaharieva, I., Gerencser, L., Chernev, P. and Dau, H. (2009). "Cobalt-oxo core of a water-oxidizing catalyst film." Journal of the American Chemical Society **131**(20): 6936-6937.

Risch, M., Klingan, K., Ringleb, F., Chernev, P., Zaharieva, I., Fischer, A. and Dau, H. (2012). "Water oxidation by electrodeposited cobalt oxides - role of anions and redox-inert cations in structure and function of the amorphous catalyst." ChemSusChem **5**(3): 542-549.

Schonfeld, B., Huang, J. J. and Moss, S. C. (1983). "Anisotropic mean-square displacements (MSD) in single crystals of 2H- and 3R-MoS_2." Acta Crystallographica Section B **39**: 404-407.

Schweiger, H., Raybaud, P. and Toulhoat, H. (2002). "Promoter sensitive shapes of Co(Ni)MoS nanocatalysts in sulfo-reductive conditions." Journal of Catalysis **212**(1): 33-38.

Scott, R. A., Jacobson, A. J., Chianelli, R. R., Pan, W. H., Stiefel, E. I., Hodgson, K. O. and Cramer, S. P. (1986). "Reactions of MoS_3, WS_3, WSe_3, and $NbSe_3$ with lithium - metal cluster rearrangement revealed by EXAFS." Inorganic Chemistry **25**(9): 1461-1466.

Sgobba, V. and Guldi, D. M. (2009). "Carbon nanotubes-electronic/electrochemical properties and application for nanoelectronics and photonics." Chemical Society Reviews **38**(1): 165-184.

Shevchenko, D., Anderlund, M. F., Thapper, A. and Styring, S. (2011). "Photochemical water oxidation with visible light using a cobalt containing catalyst." Energy & Environmental Science **4**(4): 1284-1287.

Shibahara, T., Yamasaki, M., Akashi, H. and Katayama, T. (1991). "Cubane-type mixed-metal clusters with Mo_3NiS_4 cores - syntheses, characterization, and x-ray structures of $[Mo_3NiS_4(H_2O)_{10}](CH_3C_6H_4SO_3)_{4.7}H_2O$ and $Ca_{2.5}[Mo_3NiS_4(Hnta)(nta)_2Cl]*14H_2O$." Inorganic Chemistry **30**(12): 2693-2699.

Sitepu, H. (2009). "Texture and structural refinement using neutron diffraction data from molybdite (MoO3) and calcite (CaCO3) powders and a Ni-rich Ni50.7Ti49.30 alloy." Powder Diffraction **24**: 315-326.

Sitepu, H., O'Connor, B. H. and Li, D. (2005). "Comparative evaluation of the March and generalized spherical harmonic preferred orientation models using X-ray diffraction data for molybdite and calcite powders." Journal of Applied Crystallography **38**: 158-167.

Smith, G. W. and Ibers, J. A. (1965). "The Crystal Structure of Cobalt Molybdate, $CoMoO_4$." Acta Crystallographica **19**.

Smura, C. F., Parker, D. R., Zbiri, M., Johnson, M. R., Zoltan, A. G. and Clarke, S. J. (2011). "High-Spin Cobalt(II) Ions in Square Planar Coordination: Structures and Magnetism of the Oxysulfides $Sr_2CoO_2Cu_2S_2$ and $Ba_2CoO_2Cu_2S_2$ and Their Solid Solution." Journal of the American Chemical Society **133**: 2691-2705.

Stellmach, D. (2015). "Molybänsulfid-Nanopartikel als wasserstoffentwickelnder Elektrokatalysator für die lichtinduzierte Wasserspaltung." Dissertation.

Stern, E. A. (1993). "Number of relevant independent points in X-ray-absrption fine-structure spectra." Physical Review B **48**(13): 9825-9827.

Summers, D. P., Leach, S. and Frese, K. W. (1986). "The electrochemical reduction of aqueous carbon-dioxide to methanol at molybdenum electrodes with low overpotentials." Journal of Electroanalytical Chemistry **205**(1-2): 219-232.

Süsse, P. (1967). "Verfeinerung der Kristallstruktur des Malachits $Cu_2(OH)_2CO_3$." Acta Crystallographica **22**: 146.

Tang, M. L., Grauer, D. C., Lasalle-Kaiser, B., Yachandra, V. K., Amirav, L., Long, J. R., Yano, J. and Alivisatos, A. P. (2011). "Structural and Electronic Study of an Amorphous MoS_3 Hydrogen-Generation Catalyst on a Quantum-Controlled Photosensitizer." Angewandte Chemie - International Edition **50**(43): 10203-10207.

Taniguchi, M., Imamura, D., Ishige, H., Ishii, Y., Murata, T., Hidai, M. and Tatsumi, T. (1999). "Hydrodesulfurization of benzothiophene over zeolite-supported catalysts prepared from Mo and Mo-Ni sulfide clusters." Journal of Catalysis **187**(1): 139-150.

Tard, C. (2009). "Structural and Functional Analogues of the Active Sites of the [Fe]-, [NiFe]-, and [FeFe]-Hydrogenases." Chemical Reviews **109**(6): 2245-2274.

Tasis, D., Tagmatarchis, N., Bianco, A. and Prato, M. (2006). "Chemistry of carbon nanotubes." Chemical Reviews **106**(3): 1105-1136.

Teo, B. (1986). EXAFS: Basic principles and data analysis. Berlin, Germany, Springer Verlag.

Tran, P. D., Artero, V. and Fontecave, M. (2010). "Water electrolysis and photoelectrolysis on electrodes engineered using biological and bio-inspired molecular systems." Energy & Environmental Science **3**: 727-747.

Tran, P. D., Le Goff, A., Heidkamp, J., Jousselme, B., Guillet, N., Palacin, S., Dau, H., Fontecave, M. and Artero, V. (2011). "Noncovalent Modification of Carbon Nanotubes with Pyrene-Functionalized Nickel Complexes: Carbon Monoxide Tolerant Catalysts for Hydrogen Evolution and Uptake." Angew Chem Int Ed Engl **50**(6): 1371-1374.

Tran, P. D., Morozan, A., Archambault, S., Heidkamp, J., Chenevier, P., Dau, H., Fontecave, M., Martinent, A., Jousselme, B. and Artero, V. (2015). "A noble metal-free proton-exchange membrane fuel cell based on bio-inspired molecular catalysts." Chemical Science **6**(3): 2050-2053.

Tributsch, H. and Bennett, J. C. (1977). "Electrochemistry and photochemistry of MoS_2 layer crystals .1." Journal of Electroanalytical Chemistry **81**(1): 97-111.

Tunell, G., Posnjak, E. and Ksanda, C. J. (1935). "Geometrical and optical properties, and crystal structure of tenorite." Zeitschrift fuer Kristallographie, Kristallgeometrie, Kristallphysik, Kristallchemie **90**: 120-142.

Vrubel, H. and Hu, X. (2013). "Growth and Activation of an Amorphous Molybdenum Sulfide Hydrogen Evolving Catalyst." ACS Catalysis **3**: 2002-2011.

Walter, M. G., Warren, E. L., McKone, J. R., Boettcher, S. W., Mi, Q. X., Santori, E. A. and Lewis, N. S. (2010). "Solar Water Splitting Cells." Chemical Reviews **110**(11): 6446-6473.

Weber, T., Muijsers, J. C. and Niemantsverdriet, J. W. (1995). "Structure of amorphous MoS_3." Journal of Physical Chemistry **99**(22): 9194-9200.

Wee, T.-L., Sherman, B. D., Gust, D., Moore, A. L., Moore, T. A., Liu, Y. and Scaiano, J. C. (2011). "Photochemical synthesis of a water oxidation catalyst based on cobalt nanostructures." Journal of the American Chemical Society **133**(42): 16742-16745.

Westgren, A. (1938). "Die Kristallstruktur von Ni_3S_2." 1938 **239**: 82-84.

Wu, J. J., Risalvato, F. G., Sharma, P. P., Pellechia, P. J., Ke, F. S. and Zhou, X. D. (2013). "Electrochemical Reduction of Carbon Dioxide II. Design, Assembly, and Performance of Low Temperature Full Electrochemical Cells." Journal of the Electrochemical Society **160**(9): F953-F957.

Wu, Q. and van de Krol, R. (2012). "Selective Photoreduction of Nitric Oxide to Nitrogen by Nanostructured TiO_2 Photocatalysts: Role of Oxygen Vacancies and Iron Dopant." Journal of The American Chemical Society **134**: 9369-9375.

Wyckoff, R. W. (1931). "Structure of Crystals - Second Edition." The Chemical Catalog Company.

Wyckoff, R. W. (1963). "Crystal Structures - Second Edition." Interscience Publishers **1**.

Yang, J. Y., Bullock, R. M., Dougherty, W. G., Kassel, W. S., Twamley, B., DuBois, D. L. and DuBois, M. R. (2010). "Reduction of oxygen catalyzed by nickel diphosphine complexes with positioned pendant amines." Dalton Transactions **39**(12): 3001-3010.

Yin, Q., Tan, J. M., Besson, C., Geletii, Y. V., Musaev, D. G., Kuznetsov, A. E., Luo, Z., Hardcastle, K. I. and Hill, C. L. (2010). "A fast soluble carbon-free molecular water oxidation catalyst based on abundant metals." Science **328**: 342-345.

Zaharieva, I., Najafpour, M. M., Wiechen, M., Haumann, M., Kurz, P. and Dau, H. (2011). "Synthetic manganese-calcium oxides mimic the water-oxidizing complex of photosynthesis functionally and structurally." Energy and environmental sciences **4**(7): 2400-2408.

Zhao, Y.-L. and Stoddart, J. F. (2009). "Noncovalent Functionalization of Single-Walled Carbon Nanotubes." Accounts of Chemical Research **42**(8): 1161-1171.

Zigan, F., Joswig, W., Schuster, H. D. and Mason, S. A. (1977). "Verfeinerung der Struktur von Malachit, $Cu_2(OH)_2CO_3$, durch Neutronenbeugung." Zeitschrift für Kristallographie **145**: 412-426.

VIII. LIST OF PUBLICATIONS

I contributed to the following publications and patents during my PhD candidacy. In **1.** to **4.**, I designed and pursued the X-ray absorption spectroscopy (XAS) measurements as well as the XAS data evaluation. The results are presented in this thesis. In **4.** to **8.**, I contributed to XAS data collection and analysis. The respective results are not part of this thesis.

Publications

1. Cobo, S., **Heidkamp, J.**, Jacques, P. A., Fize, J., Fourmond, V., Guetaz, L., Jousselme, B., Ivanova, V., Dau, H., Palacin, S., Fontecave, M., Artero, V. (2012) A Janus cobalt-based catalytic material for electro-splitting of water, *Nature Materials 11*, 802-807.
   [chapter ***Catalytic Co electrode electrodeposited under reductive conditions***]

2. Tran, P. D.*, Morozan, A.*, Archambault, S.*, **Heidkamp, J.***, Chenevier, P., Dau, H., Fontecave, M., Martinent, A., Jousselme, B., Artero, V. (2015) A noble metal-free proton-exchange membrane fuel cell based on bio-inspired molecular catalysts, *Chemical Science 6*, 2050-2053. *These authors equally contributed to the work.
   [chapter ***Noble metal-free fuel cell***]

3. Huan, T. N., Andreiadis, E. S., **Heidkamp, J.**, Simon, P., Derat, E., Cobo, S., Royal, G., Bergmann, A., Strasser, P., Dau, H., Artero, V., Fontecave, M. (2015) From molecular copper complexes to composite electrocatalytic materials for selective reduction of CO_2 to formic acid, *Journal of Materials Chemistry A 3*, 3901-3907.
   [chapter ***Catalytic Cu electrode for CO_2 reduction***]

4. Tran, P. D., Le Goff, A., **Heidkamp, J.**, Jousselme, B., Guillet, N., Palacin, S., Dau, H., Fontecave, M., Artero, V. (2011) Noncovalent Modification of Carbon Nanotubes with Pyrene-Functionalized Nickel Complexes: Carbon Monoxide Tolerant Catalysts for Hydrogen Evolution and Uptake, *Angewandte Chemie – International Edition 50*, 1371-1374.
   [chapter ***Molecular Ni catalyst grafted on a carbon-nanotube cathode***]

---

5. Risch, M., Klingan, K., **Heidkamp, J.**, Ehrenberg, D., Chernev, P., Zaharieva, I., Dau, H. (2011) Nickel-oxido structure of a water-oxidizing catalyst film, *Chemical Communications 47*, 11912-11914.

6. Klingan, K., Ringleb, F., Zaharieva, I., **Heidkamp, J.**, Chernev, P., Gonzalez-Flores, D., Risch, M., Fischer, A., Dau, H. (2014) Water Oxidation by Amorphous Cobalt-Based Oxides: Volume Activity and Proton Transfer to Electrolyte Bases, *ChemSusChem* 7, 1301-1310.

7. Gonzalez-Flores, D., Sanchez, I., Zaharieva, I., Klingan, K., **Heidkamp, J.**, Chernev, P., Menezes, P. W., Driess, M., Dau, H., Montero, M. L. (2015) Heterogeneous Water Oxidation: Surface Activity versus Amorphization Activation in Cobalt Phosphate Catalysts, *Angewandte Chemie – International Edition 54*, 2472-2476.

8. Risch, M., Shevchenko, D., Anderlund, M. F., Styring, S.; **Heidkamp, J.**, Lange, K. M., Thapper, A., Zaharieva, I. (2012) Atomic structure of cobalt-oxide nanoparticles active in light-driven catalysis of water oxidation, *International Journal of Hydrogen Energy 37*, 8878-8888.

Patents

Method for preparing a catalyst mediating H_2 evolution, said catalyst and uses thereof

V. Artero, M. Fontecave, S. Cobo, P.-A. Jacques, H. Dau, **J. Heidkamp**, filed on 4/4/2013, published on 10/10/2013, WO 2013150116 A1

The present invention concerns a method for the preparation of a catalyst onto a solid support of a (semi-)conductive material consisting in depositing said catalyst onto said support from a nearneutral aqueous solution containing at least one nickel or cobalt organic complex and at least one basic oxoanion, by a method selected in the group consisting of reductive electrodeposition, photochemical electrodeposition and photoelectrochemical deposition. The present invention also concerns said catalyst and uses thereof.

IX. ACKNOWLEDGMENTS

First, I would like to thank Prof. Holger Dau for his continuous inspiration and support of my Ph. D. work as first supervisor.

I am grateful to Prof. Peter Strasser (*Technische Universität Berlin*), who kindly agreed to support me as second supervisor.

I am very thankful for the successful collaborations with Vincent Artero (*Laboratoire de Chimie et Biologie des M´etaux, Univ. Grenoble Alpes*) and his co-workers, in particular Saioa Cobo, Phong D. Tran and Tran Ngoc Huan.

I would like to thank Ivelina Zaharieva, Marcel Risch and Petko Chernev for introducing me into the experimental technique of X-ray absorption spectroscopy (XAS) and the corresponding data analysis, in particular simulations of extended X-ray absorption fine-structure (EXAFS). Special thanks to Michael Haumann for giving me helpful advice and insights with his XAS expertise. Furthermore, I like to thank Sebastian Horn for giving me a short introduction in simulations of X-ray absorption near-edge structure (XANES). I also have to thank all my colleagues who supported my X-ray absorption spectroscopy (XAS) measurements at the synchrotron in BESSY and SOLEIL: Petko Chernev, Ivelina Zaharieva, Marcel Risch, Katharina Klingan, Diego González-Flores, Elías Moreno-Martínez, Reza Mohammadi, Chiara Pasquini and Zhiyong Liang.

I would like to thank Katharina Klingan for introducing me into the experimental techniques of electrochemistry. Furthermore, I have to thank Diego Gonzáles-Flores, Stefan Loos and Paul Kubella for sharing with me their expertise in (electro)chemistry.

Many thanks go to Mikaela Görlin (*Technische Universität Berlin*, work group of Prof. Peter Strasser), who helped me to perform the ICP-OES measurements and executed the data evaluation.

I would like to thank the following people for proof-reading (parts of) this thesis: Prof. Holger Dau, Prof. Sebastian Fiechter (*Helmholtz-Zentrum Berlin*), Michael Haumann, Katharina Klingan, Diego González-Flores.

I kindly thank the *UniCat-Cluster of Excellence* for the financial support of my Ph. D. work.

Last but not least, I have to thank my family and my girlfriend Rebecca for their understanding and support.

X. SELBSTSTÄNDIGKEITSERKLÄRUNG

Ich erkläre gegenüber der Freien Universität Berlin, dass ich die vorliegende Doktorarbeit selbstständig und ohne Benutzung anderer als der angegebenen Quellen und Hilfsmittel angefertigt habe. Die vorliegende Arbeit ist frei von Plagiaten. Alle Ausführungen, die wörtlich oder inhaltlich aus anderen Schriften entnommen sind, habe ich als solche kenntlich gemacht. Diese Arbeit wurde in gleicher oder ähnlicher Form noch bei keiner anderen Universität als Prüfungsleistung eingereicht und ist auch noch nicht veröffentlicht.

Berlin, den

_____

(Jonathan Heidkamp)